

©Copyright 2016

Benjamin Mark Loren Drum

Three lenses into the cardiac dyad: calcium signaling,  
microtubule trafficking, and junctional sarcoplasmic reticular  
mobility

Benjamin Mark Loren Drum

A dissertation  
submitted in partial fulfillment of the  
requirements for the degree of

Doctor of Philosophy

University of Washington

2016

Reading Committee

Luis Fernando Santana, Chair  
Stanley Froehner  
Michael Regnier

Program Authorized to Offer Degree:

Physiology and Biophysics

# **University of Washington**

## **Abstract**

### **Three lenses into the cardiac dyad: calcium signaling, microtubule trafficking, and junctional sarcoplasmic reticular mobility**

**Benjamin Mark Loren Drum**

**Chair of the Supervisory Committee:**

**Professor Luis Fernando Santana  
Department of Physiology and Biophysics**

The cardiac dyad, the intersection between the sarcoplasmic reticulum and the sarcolemma in cardiac myocytes, is critically important for cellular contraction and function. It is the hub of calcium signaling where ryanodine receptors on the sarcoplasmic reticulum and L-type calcium channels on the sarcolemma interact. If the geometric distance between these two proteins is disrupted, calcium signaling will be impaired. In addition, these proteins are trafficked and maintained by microtubules. In this dissertation, I take a three-pronged approach to understanding the dyad. First, I use a mouse model of Timothy syndrome (TS), a disease created by an overactive L-type calcium channel, to examine the effects of the physiological calcium environment on calcium signaling. We find that the resting level of calcium in the cytosol is increased by 1.6-fold, calcium transients are increased by 1.8-fold, and sarcoplasmic reticulum load is increased by 1.5-fold in TS, leading to arrhythmogenicity. Secondly, I use an adeno-associated virus serotype 9 expressing a plus-end microtubule binding protein (AAV9-EB3-EGFP) to visualize microtubules in real time. I quantify microtubule dynamics in ventricular myocytes and find that

oxidative stress in myocardial infarction disrupts microtubules, leading to a decrease in the surface expression of  $K_{V4.2}$  and  $K_{V4.3}$  and decrease in  $I_{to}$ , also leading to arrhythmia by prolonging the action potential. I also show that microtubules and molecular motors, specifically kinesin-1, are responsible for trafficking the  $\beta_2$  subunit of  $Ca_v1.2$ , and that disruption of kinesin-1 results in a loss in current density of  $Ca_v1.2$  current. I also examine microtubule dynamics in atrial myocytes and use this research to probe the role of BIN1 in linking microtubule dynamics to the cardiac dyad. Lastly, I use an adeno-associated virus expressing triadin, a protein localized to the junctional sarcoplasmic reticulum (jSR) tagged with a photo-activatable GFP (AAV9-TRD-PAGFP) to directly monitor the movement of the jSR under normal physiology and find that 8% of jSR segments exert mobility. This movement is produced by molecular motors and is increased in the setting of myocardial infarction. By exploring the cardiac dyad through the lenses of calcium signaling, microtubule trafficking, and direct jSR movement, I am able to elucidate a multifaceted look at the regulation and function of the dyad as well as its importance in cardiac physiology.

## Table of Contents

<b>Table of Contents</b> .....	<b>i</b>
<b>List of Figures</b> .....	<b>vii</b>
<b>Preface</b> .....	<b>ix</b>
<b>Acknowledgements</b> .....	<b>xi</b>
<b>Dedication</b> .....	<b>xii</b>
<b>Copyright Permissions</b> .....	<b>xiii</b>
<b>Chapter 1: Introduction</b> .....	<b>1</b>
<b>1.1. Gross anatomy and physiology of the heart</b> .....	<b>1</b>
1.1.1. Anatomy of the heart.....	1
1.1.2. The cardiac cycle .....	5
<b>1.2. Electrical physiology of the heart</b> .....	<b>8</b>
1.2.1. The cardiac resting potential.....	8
1.2.2. Pace making and conduction.....	9
1.2.3. The electrocardiogram (ECG).....	13
<b>1.3. Cellular cardiac physiology</b> .....	<b>15</b>
1.3.1. The cardiac AP .....	15
1.3.2. Excitation-contraction (EC) coupling.....	17
1.3.3. L-type (Ca <sub>v</sub> 1.2) calcium channels.....	19
1.3.4. The fidelity of the heartbeat: local control theory of Ca <sup>2+</sup> signaling in ventricular myocytes .....	22
1.3.5. EC coupling in atrial myocytes.....	25

1.3.6. Microtubule (MT) physiology and protein trafficking .....	26
1.3.7. The junctional SR.....	31
<b>1.4. Arrhythmia: the denouement of diseased cardiomyocytes .....</b>	<b>35</b>
1.4.1. Pathology I: Timothy syndrome (TS) – the Ca <sup>2+</sup> overloaded heart .....	35
1.4.2. Pathology II: Myocardial infarction (MI).....	39
<b>1.5. Specific aims.....</b>	<b>42</b>
1.5.1. Aim 1.....	42
1.5.2. Aim 2.....	43
1.5.3. Aim 3.....	44
1.5.4. Aim 4.....	45
<b>Chapter 2: Cellular mechanisms of ventricular arrhythmias in a mouse</b>	
<b>model of Timothy syndrome (long QT syndrome 8).....</b>	<b>46</b>
<b>2. Summary.....</b>	<b>46</b>
<b>2.1. Introduction.....</b>	<b>48</b>
<b>2.2. Material and methods.....</b>	<b>51</b>
2.2.1. Isolation of ventricular myocytes.....	51
2.2.2. RT-PCR and Western blot analysis .....	52
2.2.3. Electrophysiology.....	52
2.2.4. Field Stimulation .....	55
2.2.5. Confocal Imaging of Ca <sup>2+</sup> signals.....	55
2.2.6. Statistics.....	58
<b>2.3. Results.....</b>	<b>59</b>
2.3.1. Higher resting sarcolemmal Ca <sup>2+</sup> leak and [Ca <sup>2+</sup> ] <sub>i</sub> transients in TS compared to WT ventricular myocytes.....	59

2.3.2. TS myocytes have a higher frequency of Ca <sup>2+</sup> sparks and waves than WT myocytes .....	64
2.3.3. Higher SR Ca <sup>2+</sup> load in TS than in WT ventricular myocytes.....	69
2.3.4. The large SR Ca <sup>2+</sup> release during EC coupling in TS cells increases the rate of inactivation of I <sub>Ca</sub> and hence limits Ca <sup>2+</sup> influx during membrane depolarization into these cells .....	70
2.3.5. Differences in AP waveform amplify differences in Ca <sup>2+</sup> influx between TS and WT myocytes .....	74
2.3.6. Differences in AP waveform contribute to differences in EC coupling between WT and TS cells .....	76
<b>2.4. Discussion .....</b>	<b>79</b>

<b>Chapter 3: Oxidative stress decreases microtubule growth and stability in ventricular myocytes .....</b>	<b>86</b>
<b>3. Summary .....</b>	<b>86</b>
<b>3.1. Introduction.....</b>	<b>88</b>
<b>3.2. Materials and methods.....</b>	<b>92</b>
3.2.1. Isolation of mouse ventricular myocytes .....	92
3.2.2. Myocardial infarction .....	92
3.2.3. Real Time qRT-PCR .....	93
3.2.4. Viral expression system .....	93
3.2.5. Immunocytochemistry and imaging .....	95
3.2.6. Fluorescent indicators.....	99
3.2.7. Image analysis .....	99
3.2.8. Immunoprecipitation Western blotting.....	101
3.2.9. Electrophysiology.....	102

3.2.10. Surface biotinylation.....	103
3.2.11. Statistics.....	104
<b>3.3. Results.....</b>	<b>105</b>
3.3.1. EB1 and tubulin co-localize in cardiomyocytes.....	105
3.3.2. Live imaging of MTs in ventricular myocytes .....	108
3.3.3. Oxidative stress disrupts MT dynamics .....	112
3.3.4. Live imaging of MTs in ventricular myocytes post-MI .....	114
3.3.5. Oxidative stress mimics MT dynamic disruptions seen after MI .....	118
3.3.6. MT dynamic disruptions reduce $I_{to}$ density .....	120
<b>3.4. Discussion .....</b>	<b>122</b>
<b>3.5. Limitations of the study .....</b>	<b>128</b>
<b>3.6. Summary and conclusions.....</b>	<b>129</b>
<b>Chapter 4: Bridging Integrator Protein 1 (BIN1) stabilizes microtubules on the T-tubules, enabling kinesin-1 (Kif5B) to traffic <math>Ca_v1.2\beta_2</math> in ventricular myocytes .....</b>	<b>130</b>
<b>4. Summary.....</b>	<b>130</b>
4.1. Introduction.....	132
4.2. Materials and methods.....	137
4.2.1. Isolation of mouse ventricular myocytes .....	137
4.2.2. Culturing mouse ventricular myocytes .....	137
4.2.3. Isolation of mouse atrial myocytes .....	138
4.2.4. Immunohistochemistry and imaging .....	139
4.2.5. Viral expression system .....	140
4.2.6. Imaging and fluorescent indicators .....	140
4.2.7. Image analysis .....	141

4.2.8. Electrophysiology.....	142
4.2.9. Co-immunoprecipitation Western blotting .....	143
4.2.10. Statistics.....	144
<b>4.3. Results.....</b>	<b>145</b>
4.3.1. BIN1 colocalizes with other proteins in T-tubules. ....	145
4.3.2. Cultured ventricular myocytes exhibit increased MT dynamic disruptions.....	147
4.3.3. Atrial myocytes have distinct expression of BIN1 and EB1 compared to ventricular myocytes. ....	150
4.3.4. Atrial myocytes exhibit increased MT dynamic disruptions.....	152
4.3.5. Kif5B colocalizes with other proteins in T-tubules.....	153
4.3.6. Kinesin-1 is the motor responsible for Ca <sub>v</sub> 1.2β <sub>2</sub> trafficking.....	155
<b>4.4. Discussion .....</b>	<b>157</b>
 <b>Chapter 5: Elucidating the biogenesis and role of junctional sarcoplasmic reticulum motility in normal and pathological Ca<sup>2+</sup> signaling .....</b>	 <b>162</b>
<b>5. Summary.....</b>	<b>162</b>
<b>5.1. Introduction.....</b>	<b>164</b>
<b>5.2. Methods.....</b>	<b>169</b>
5.2.1. Isolation of mouse ventricular myocytes .....	169
5.2.2. Myocardial infarction .....	169
5.2.3. Viral expression system .....	169
5.2.4. Immunocytochemistry and imaging .....	170
5.2.5. Image analysis .....	172
5.2.6. Real Time qRT-PCR.....	173
5.2.7. Detubulation.....	174

5.2.8. Statistics.....	174
<b>5.3. Results.....</b>	<b>175</b>
5.3.1. Triadin and Ca <sub>v</sub> 1.2 colocalize under super-resolution imaging .....	175
5.3.2. Virally-expressed TRD colocalizes with T-tubules and with the SR.....	176
5.3.3. The jSR is mobile and has several modalities of mobility.....	179
5.3.4. Dynein and kinesin 1 regulate jSR motility.....	180
5.3.5. The jSR and T-tubules can be uncoupled, leading to defects in Ca <sup>2+</sup> signaling.....	181
5.3.6. The jSR is disrupted and highly mobile after MI. ....	183
<b>5.4. Discussion .....</b>	<b>184</b>
<b>Chapter 6: Concluding Remarks .....</b>	<b>187</b>
<b>References .....</b>	<b>192</b>
<b>Curriculum Vitae .....</b>	<b>223</b>

## List of Figures

FIGURE 1.1. PRESSURE-VOLUME RELATIONSHIP OF CARDIAC BLOOD FLOW.....	6
FIGURE 1.2. IONIC CURRENTS OF SA NODE .....	10
FIGURE 1.3. NOMENCLATURE OF AN ECG.....	14
FIGURE 1.4. PHASES OF AN ACTION POTENTIAL IN A VENTRICULAR MYOCYTE .....	16
FIGURE 1.5. CARTOON OF THE JUNCTIONAL SARCOPLASMIC RETICULUM .....	34
FIGURE 2.1. LINEAR RELATIONSHIP OF RELATIVE mRNA AND PROTEIN EXPRESSION OF $Ca_v1.2$ -TS. ....	60
FIGURE 2.2. HIGHER DIASTOLIC, SYSTOLIC, AND RESTING $[Ca^{2+}]_i$ AND LARGER SARCOLEMMALEAK IN TS CELLS.....	62
FIGURE 2.4. HIGHER $Ca^{2+}$ WAVE ACTIVITY IN TS CELLS. ....	68
FIGURE 2.5. HIGHER RESTING AND PACED SR LOAD IN TS CELLS. ....	70
FIGURE 2.6. HIGHER SR $Ca^{2+}$ RELEASE DURING EC COUPLING IN TS CELLS INCREASES THE RATE OF INACTIVATION OF $I_{Ca}$ .....	72
FIGURE 2.7. DIFFERENCES IN AP WAVEFORM CONTRIBUTES TO DIFFERENCES IN L-TYPE $Ca^{2+}$ CURRENT BETWEEN WT AND TS MYOCYTES. ....	75
FIGURE 2.8. DIFFERENCES IN AP WAVEFORM CONTRIBUTES TO DIFFERENCES IN $[Ca^{2+}]_i$ BETWEEN WT AND TS MYOCYTES.....	77
FIGURE 3.1. JABLONSKI DIAGRAM ILLUSTRATING GROUND STATE DEPLETION. ....	97
FIGURE 3.2. EB1 AND TUBULIN CO-LOCALIZE IN PUNCTATE PATTERN IN VENTRICULAR MYOCYTES.....	107
FIGURE 3.3. EB3 AND TUBULIN COLOCALIZE UNDER SUPER-RESOLUTION. ....	108
FIGURE 3.4. LIVE IMAGING OF MTs IN VENTRICULAR MYOCYTES. ....	110
FIGURE 3.5. OXIDATIVE STRESS DISRUPTS MT DYNAMICS. ....	113
FIGURE 3.6. LIVE IMAGING OF MTs IN VENTRICULAR MYOCYTES POST-MYOCARDIAL INFARCTION. ....	115
FIGURE 3.7. NO MOLECULAR MECHANISM FOR INCREASED CATASTROPHE. ....	117
FIGURE 3.8. OXIDATIVE STRESS MIMICS MT DYNAMIC DISRUPTIONS SEEN AFTER MI. ....	118
FIGURE 3.9. REDUCTION IN $Kv4$ TRAFFICKING FROM MT DISRUPTION. ....	121
FIGURE 4.1. BIN1 COLOCALIZES WITH SEVERAL PROTEINS IN VENTRICULAR MYOCYTES. ....	146

FIGURE 4.2. LIVE IMAGING OF MICROTUBULES IN CULTURED VENTRICULAR MYOCYTES. ....	149
FIGURE 4.3. BIN1 AND EB1 HAVE VARIABLE EXPRESSION IN VENTRICULAR VS. ATRIAL MYOCYTES. ....	151
FIGURE 4.4. LIVE IMAGING OF MICROTUBULES IN ATRIAL MYOCYTES. ....	153
FIGURE 4.5. KIF5B COLOCALIZES WITH SEVERAL PROTEINS IN VENTRICULAR MYOCYTES. ....	154
FIGURE 4.6. KIF5B IS THE MOTOR TRANSPORTING $Ca_v1.2B_2$ . ....	156
FIGURE 4.7. PROPOSED MODEL OF $Ca_v1.2$ TRANSPORT. ....	158
FIGURE 5.1. CARTOON OF THE PROPOSED STRUCTURE OF THE JSR. ....	165
FIGURE 5.2. TRIADIN AND $Ca_v1.2$ CLUSTERING VISUALIZED BY GSD. ....	175
FIGURE 5.3. PHOTOACTIVATION OF AGFP-TRD IN A LIVE MYOCYTE. ....	177
FIGURE 5.4. DYNAMIC PROFILES OF MOTILE JSR SEGMENTS. ....	179
FIGURE 5.5. DYNEIN AND KINESIN ARE IMPLICATED IN JSR MOBILITY. ....	181
FIGURE 5.6. DETUBULATION RESULTS IN UNCOUPLING THE JSR FROM THE T-TUBULES. ....	182
FIGURE 5.7. JSR MOBILITY IS DECREASED AFTER MI. ....	183

## Preface

The only thing necessary for the triumph of evil is for good men to do nothing.

-Edmund Burke

Before you lies “Three lenses into the cardiac dyad: calcium signaling, microtubule trafficking, and junctional sarcoplasmic reticular mobility,” the final product of four years of research in the lab of Dr. L. Fernando Santana. I entered the lab after two years of medical school, excited about cardiovascular physiology but knowing very little about the scientific field. I emerge an expert, poised to return to medical school and finish my degree.

This research could not have been conducted without the help of the entire Santana lab. We functioned as a scientific community, geared towards each other’s successes. Fernando was also essential in the formation of this thesis—providing some of the sparks of my scientific progress and fanning the flames of my own. In addition, this thesis is the result of the scientific conversations of a few members of the department: Drs. Stanley Froehner, Linda Wordeman, Chip Asbury, and Chris Liu.

Looking retrospectively, it is remarkable that I was accepted and agreed to embark on an MD/PhD program, where I knew that I would spend the next 8 years of my life. It has been a steady, sometimes seemingly never-ending program, constantly changing in the transitions from MD to young graduate

student to experienced graduate student. I am still preparing myself for the next transition, back to medical school, but I am excited for the next challenge.

In these last four years, a tremendous amount of life has occurred. I was somehow fortunate enough to meet and marry Erin, the love of my life. Her tenacity and passions have driven me towards being my best, and her kindness and warmth have given me the safety and acceptance to fail and try again. For all friendships these last four years, whether still active or now memory, I owe thanks. And for Mosaic Community Church, I owe a tremendous amount of support and guidance.

Lastly, I thank God for giving me everything—every achievement, relationship, possession, and personality trait—in order to better serve His kingdom. May I always be one who actively perpetuates good, honoring Him in word and in deed, in my future as a medical scientist.

-Benjamin Drum  
Seattle, March 2016

## Acknowledgements

Thank you to Fernando for being my mentor for the past four years. He guided me through these projects and gave me the freedom to fail and learn while still investing in my success. Thank you to Drs. Stan Froehner, Fred Rieke, Bill Zagotta, and Michael Regnier for participating in my graduate committee. Thank you to Dr. Linda Wordeman for her expertise on microtubules. Thank you to Can Yuan for her molecular biology and virus management. Thank you to Drs. Rosie Dixon and Jose Mercado for helping me troubleshoot problems and teaching me heart physiology in the laboratory setting. Thank you to Jennifer Cabarrus for teaching me mouse cardiac isolations and for maintaining the lab excellently. I also owe thanks to my previous scientific mentors. Thank you to Dr. David Dawson for teaching me two-electrode voltage clamp as a college freshman and H. Peter Larsson for teaching me patch clamping as a college sophomore and for believing in me as a scientist. Thank you to Dr. Anne Carlson for teaching me the scientific method and for recommending the Santana lab to me.

## **Dedication**

To Erin

## Copyright Permissions

Portions of this dissertation have been previously published in separate manuscripts, and I have obtained all the proper permissions allowed me as a copyright holder to re-publish these works as parts of this dissertation.

Part of Chapter 1 was previously published as:  
BM Drum & LF Santana. "The long and winding road home: How junctin and triadin find their way to the junctional SR" *J Mol Cell Cardiol*, 2015 Apr; 81:15-17.

Chapter 2 was previously published as:  
BM Drum, RE Dixon, C Yuan, EP Cheng, & LF Santana. "Cellular mechanisms of ventricular arrhythmias in a mouse model of Timothy syndrome (long QT syndrome 8)" *J Mol Cell Cardiol*. 2014 Jan; 66:63-71.

Chapter 3 was previously published as:  
BM Drum, C Yuan, L Li, Q Liu, L Wordeman, & LF Santana. "Oxidative stress decreases microtubule growth and stability in ventricular myocytes" *J Mol Cell Cardiol* 2016 Apr; 93: 32-43.

Chapter 4 will be published as:  
BM Drum & LF Santana. "Bridging Integrator Protein 1 (BIN1) stabilizes microtubules on the T-tubules, enabling kinesin-1 (Kif5B) to traffic  $Ca_v1.2\beta_2$  in ventricular myocytes"

Chapter 5 will be published as:  
C Yuan, BM Drum & LF Santana. "Elucidating the biogenesis and role of junctional sarcoplasmic reticulum motility in normal and pathological  $Ca^{2+}$  signaling."

## **Chapter 1: Introduction**

### **1.1. Gross anatomy and physiology of the heart**

#### **1.1.1. Anatomy of the heart**

Consider for a moment the metaphor that the body is an army, with each organ system composing a different department. Perhaps the muscles are the soldiers, the digestive system the weapons factories, the brain the generals, etc. In order for the army to operate optimally, there must exist communication and transport between the different delegations of the army. For example, orders and supplies must get to the soldiers, and reports and injured soldiers must return from the front lines. Without constant communication, reinforcements, and supplies, the army would be compromised and fail. The heart serves as the supply system. Its function is to pump and circulate blood, meeting metabolic demands by providing oxygen and nutrients while removing waste. It also circulates hormones, to modulate organ activity, and immune cells, to heal injured areas to ensure the body is operating at its optimal capacity. The heart is steadfast, pumping approximately every second, every day of your life, to sustain this communication and supply. For a 72-year-old human (average life span), this means that the heart would have pumped 2-3 billion times.

The normal adult male human heart weighs only 300-350 grams. Unlike most other internal organs, the heart is essentially muscle, composed of striated cardiac myocytes. These myocytes are arranged in a spiral, complex orientation such that uniform contraction of the fibers collapses the internal chambers of the heart and forces blood into both the systemic and pulmonic circulation. The heart is situated between the lungs in the thorax in the mediastinum enclosed by a fibrous sack called the pericardium. Within the mediastinum, the heart sits in the center of the body below the sternum, with its apex towards the left. It can be approximated as a trigonal prism. The posterior surface consists of the left atrium, some of the right atrium, the superior and inferior vena cava, and the pulmonary vein (Drake, Vogl et al. 2005). It is fixed and extends from the fifth thoracic to the eighth thoracic vertebrae. Anteriorly (facing the sternum), the heart consists of the right ventricle, the rest of the right atrium, and a portion of the left ventricle. The inferior surface, facing the diaphragm, consists of portions of the left and right ventricles. The apex of the heart is composed of the left ventricle and can be found the fifth intercostal space on the left mid-clavicular line. Clinically, this point is referred to as the point of maximal impulse (PMI) and it is the only place on the body where one can take a pulse that is not paired/symmetrical to another pulse point (e.g., radial pulses from both right and left wrist or femoral pulses from both left or right thigh).

The heart consists of two atria, which collect blood from the body and lungs, and two ventricles, which eject blood out from the heart. The right side of the heart collects deoxygenated blood from the body and sends it to the lungs while the left side of the heart collects oxygenated blood from the lungs and sends it to the body in a closed loop system. The pulmonary system is lower in pressure ( $\approx 20$  mmHg) while the systemic circulation is higher in pressure ( $\approx 100$  mmHg). There are several reasons for this large discrepancy in pressure despite the fact that these two systems are in the same closed loop. One main difference is that systemic arterioles have more smooth muscle than pulmonic arterioles. Small arterioles are the main contributors to blood pressure, and they contract and relax to adjust blood pressure during stress or exercise. Another reason is that the pulmonic circulation carries much less volume than the systemic circulation. While the systemic circulation supplies the entire body, the pulmonic circulation saturates only two lungs, and so less pressure is needed to move the blood through this system. Lastly, the systemic circulation must overcome much more gravity, reaching both the head and the feet, whereas the lungs reside alongside the heart to minimize the forces exerted on the system by gravity. As a result, the right side of the heart is markedly more diminutive and less muscular than the left side.

Mechanically, the heart is simple. During diastole the atria empty into the ventricles, which relax to fill with blood. In systole the ventricles contract to send blood out of the heart and the atria receive blood. While there is an atrial septum

separating right and left atria as well as a muscular wall called the interventricular septum separating ventricles, the dividers between atria and ventricles need gates to be opened during diastole and closed during systole to ensure uniform directional flow of blood. These gates are called valves. The valve between the right atria and the right ventricle is called the tricuspid valve, named for its three leaves. This valve ensures that the blood pumped from the right ventricle goes through the pulmonary artery into the lungs instead of back into the right atrium and into the body. Similarly, the mitral valve between the left atrium and left ventricle closes during systole to ensure blood enters the aorta out into the body rather than regurgitating back into the left atrium and the lungs. In addition, there are two valves that sit at the exit of the ventricles. The pulmonic valve is at the interface of the pulmonary artery and the right ventricle and ensures that blood doesn't flow back into the right ventricle as it relaxes in diastole. Similarly, the aortic valve sits between the left ventricle and aorta and prevents blood from the body from returning to the left ventricle as it relaxes during diastole. Valvular diseases are a common source of pathology in humans. Valves can either become stiff and not open completely in a condition called valvular stenosis or can become unable to close completely, allowing backflow in a condition called valvular insufficiency or regurgitation. If left untreated, these conditions will increase the force needed to maintain the same work done by the heart, leading to first cardiac hypertrophy as heart muscle fibers grow to maintain work rate, followed by heart failure as the heart is unable to adjust to the increased demands in force production. In heart failure, the heart cannot completely

perfuse the body in order to meet metabolic demands, leading to increased fatigue, shortness of breath, and buildup of fluid in either the body or lungs.

The heart supplies itself with blood through the coronary circulation. The coronary arteries originate at the base of the aorta just above the aortic valve and supply blood to heart muscles. Contrary to the rest of the body, where blood enters tissue during systole, most of the blood supplying the heart reaches tissue during diastole because in systole the heart is maximally contracted and thus the blood vessels are collapsed. The vast majority of blood supplying the heart is gathered by the cardiac veins, which empties into the coronary sinus and later the right atrium to be re-oxygenated by the lungs. Coronary arteries are small and thus can be prone to development of plaques and thickening of the artery walls by cholesterol in a pathological process known as atherosclerosis. If the endothelial lining covering a cholesterol plaque ruptures, a thrombus quickly forms and can completely occlude the coronary artery, leading to hypoxia and infarct. Myocardial infarction, commonly known as a heart attack, is the leading cause of mortality and morbidity in the United States.

### 1.1.2. **The cardiac cycle**

The heart is constantly working, as evidenced by the presence of a heartbeat. The work done by the left ventricle can be quantified by plotting the change in the pressure of the left ventricle on the y-axis against the change in the volume of

blood in the left ventricle on the x-axis. Because the heart continuously beats, this graph can be visualized as a closed loop. The pressure-volume (PV) loop of the heart is shown below (Figure 1.1). The area of the circle is equal to the mechanical work performed during one heartbeat.

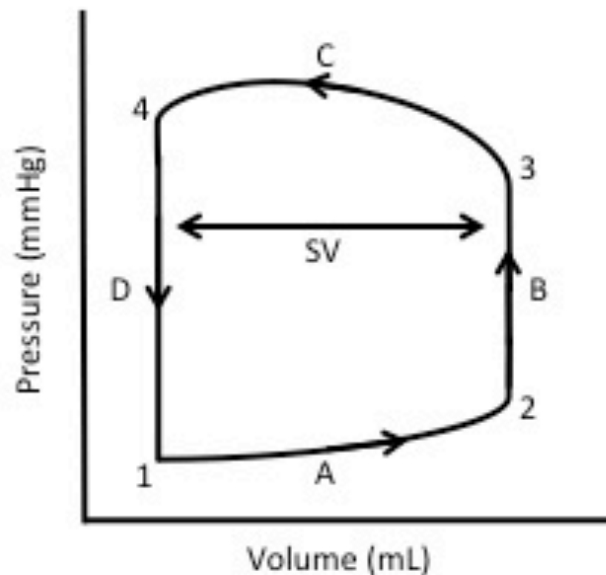


**Figure 1.1.** Pressure-volume relationship of cardiac blood flow

Let us start at point 1 on the PV loop. At this point, there is minimal blood and minimal pressure in the ventricle: the ventricle has just finished contracting and has yet to be filled again. At point 1, the mitral valve opens because the pressure in the left ventricle is less than that of the left atrium. During A, the ventricle fills with blood from the left atria. Because the wall of the left ventricle has some passive mechanical resistance against the blood as it expands, the pressure of the ventricle also increases along a curve. During A, the left atrium contracts to help fill the left ventricle. Although the left atrium is needed for optimum cardiac

function, it is not essential for cardiac function. Indeed, patients with complete heart block, a condition in which the atria beat independent of the ventricles, can survive without tight atria-ventricular communication because about 85% of the ventricular filling comes from gravity and bulk flow (Swinne, Shapiro et al. 1992). At point 2, the ventricle is full and starts to contract. The pressure of the left ventricle quickly increases, closing the mitral valve. The volume of the ventricle at the end of diastole is referred to as the preload. The ventricle increases the ejection fraction as preload increases in an effort to maintain homeostasis according to the Frank-Starling law.

During B, the ventricle is contracting while maintaining the same volume, thus increasing pressure until the pressure of the ventricle exceeds the pressure of the aorta, thus opening the aortic valve (point 3). The pressure needed to open the aortic valve is referred to as afterload, which is mostly determined by blood pressure and systemic blood volume. Once the aortic valve opens, blood flows into the aorta and the volume of the ventricle decreases until it is at its minimum volume. At point 4, the aortic valve closes as the pressure of the aorta supersedes the pressure of the ventricle. The ventricle continues to relax in an isovolumic manor during D (both valves are closed), dropping in pressure until the pressure is below atrial pressure and the mitral valve opens again at point 1. Note that, although this graph implies that systole and diastole occupy equal times, in actuality the heart spends two thirds of its time in diastole. The difference between maximum and minimum volume of the left ventricle is

referred to as the stroke volume (SV). One common measure of cardiac function is cardiac output (CO), which is calculated as the SV times the heart rate. An average CO is around 5.2 L/min. The average adult human male has 4.5 – 5.5 L of blood, which means the entire blood volume is circulated approximately once every minute in a healthy adult. Cardiac pathology often changes the shape of this PV loop. For example, in heart failure caused by hypertension, the afterload would be increased, the total area of the circle would be increased for a given SV due to the longer lengths of B and D, and the whole curve may be right shifted along the x-axis as ventricular wall hypertrophy could limit ventricular emptying and expand ventricular volume (Shah and Fifer 2007).

## 1.2. Electrical physiology of the heart

### 1.2.1. The cardiac resting potential

As stated previously, the heart is primarily composed of striated cardiac myocytes. Like all cells, these myocytes exhibit a resting membrane potential defined by the electrochemical gradient across the phospholipid membrane, called the sarcolemma in myocytes. At rest, the potential is approximately -90 mV, set by the large concentration differences in potassium and sodium, and, to a lesser extent, other select ions, according to the Nernst equation:

$$E = \frac{RT}{zF} \ln \frac{[ion]_{outside}}{[ion]_{inside}}$$

where R is the universal gas constant; T is the temperature in Kelvin; z is the charge of the ion; and F is the Faraday constant. The concentration of sodium extracellularly is 145 mM compared to 15 mM intracellularly, yielding a Nernst potential of +60 mV. Conversely, the concentration of potassium is 4 mM extracellularly and 150 mM intracellularly, yielding a Nernst potential of -94 mV. The large resting permeability of potassium ions compared to sodium ions yields a resting potential much closer to the potassium Nernst potential. It is also important to mention the calcium gradient in the cell: the extracellular concentration of calcium is 2 mM compared to  $1 \times 10^{-7}$  mM inside the cell, yielding a Nernst potential of +129 mV. Thus, there is a strong driving force for calcium to enter the cell when calcium channels are open. In addition, the minimal concentration of calcium inside the cell at rest means that calcium can be used as a powerful effector molecule inside the cell.

### 1.2.2. Pace making and conduction

Unlike the majority of other cells in the body, cardiac myocytes are never truly at rest. The necessity of the constant pumping of blood means that the heart is constantly beating, and thus, myocytes are constantly depolarizing to contract and repolarizing to relax. This electrical cycle is initiated not by the central nervous system as in the skeletal muscle system, but by pacemaker cells in the heart. These cells have inherently unstable resting potentials, causing them to

fire regularly. Thus, these cells are capable of automaticity. There are two main pacemaking centers in the cell: one is at the sinoatrial (SA) node, a spindle shaped structure that lies at the junction of the superior vena cava and the right atrium within the right atrial sulcus terminalis, and the other is at the atrioventricular (AV) node, which resides between the atria and the ventricles near the opening of the coronary sinus. In normal physiology, the SA node has a higher intrinsic rate of activity (60-100 beats per minute in resting adults), and suppresses the AV node through a mechanism known as overdrive suppression (Rolls 2007). If the SA node fails, then the AV node will drive the heart at a slower rate, approximately 40-60 beats per minute.

The unstable resting potential of these cells is dictated by ionic currents (Figure 1.2, (Klabunde 2005)).

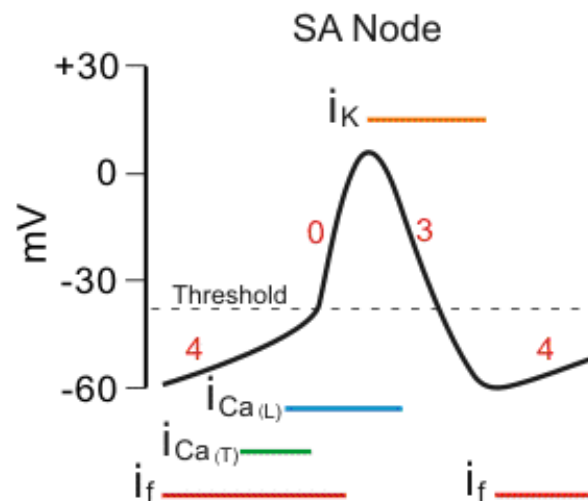


**Figure 1.2.** Ionic currents of SA node

The activation threshold of the cell is approximately -40 mV. Calcium currents from the opening of L-type and T-type channels underlie the upstroke of the

action potential, while potassium channels open and L-type  $\text{Ca}^{2+}$  channels inactivate to repolarize the cell. The unstable nature of the resting potential is due to the “funny current” ( $i_f$ ), a hyperpolarization-activated inward current which slowly depolarizes the cell between action potentials. This current is provided by a hyperpolarization-activated, cyclic-nucleotide gated HCN channel, which is permeable to sodium and potassium and is regulated by cyclic adenosine monophosphate (cAMP). Although these channels open by hyperpolarization, their S4 transmembrane is remarkably similar to that of the classic Shaker  $\text{K}_v$  channel and operate with similar kinetics (Trudeau 2012).

Once the SA node fires an action potential, that depolarization spreads into the atrial myocardium, spreading through connexin gap junction channels at the edges of myocytes. The depolarization of the atria is rapid, causing them to contract via excitation-contraction (EC) coupling. At the same time, depolarizing current is spreading through to the AV node, which is the sole connection between atria and ventricles under normal physiology. The AV node has a much slower conduction velocity compared to the atrial myocytes, and delays the depolarization signal by about 100 milliseconds. There are several reasons for this delay. Firstly, the junctional fibers of the AV node are very small in size, and thus higher resistance for electric impulses to move. Secondly, the membrane resting potential of AV node cells is much more negative than the SA node, meaning that the AV node must be depolarized more to reach the same threshold. Thirdly, there are few gap junctions between AV node cells, which also

increases resistance in conduction. Lastly, the AV node has a prolonged refractory period, which limits how quickly another action potential can depolarize the cells. This delay is physiologically critical, as it allows enough time for the atria to contract and fill the ventricles, before the depolarization signal spreads into the ventricles. After the AV node, the depolarization signal rapidly travels through specialized conduction fibers called the Bundle of His, and later the Purkinje fibers. These fibers are composed of specialized cardiac myocytes which cascade down the interventricular septum and then fan out along each ventricle. Ventricular myocytes are coupled to these fibers via connexin gap junctions and depolarize via EC coupling, similar to atrial myocytes.

Depolarization and contraction occurs from the endocardium to the epicardium and from the apex upwards. At the end of ventricular systole, repolarization of the ventricles progresses in the reverse direction such that the first cells to depolarize are also the last cells to repolarize, ensuring uniform flow of blood. After ventricular repolarization, the heart is poised and ready for another depolarization from the SA node and continuation of the heartbeat.

Pathology in the conduction pathway is common. Particularly after myocardial infarction, areas of the heart can be injured and have impaired conduction. Sometimes the main Purkinje fibers can be injured and impair ventricular contraction in either left or right bundle branch blocks. Other pathologies are arrhythmic and genetic in nature. For example, in Wolff-Parkinson-White syndrome (WPW), an abnormal conduction pathway exists between the atria and

the ventricles. Patients with WPW have a high risk of developing paroxysmal supraventricular tachycardia that leads to sudden cardiac death upon exercise, as the accessory conduction pathway can create a positive feedback pathway which escalates the heart rate past its limits.

### 1.2.3. The electrocardiogram (ECG)

By putting electric leads on the skin surface, clinicians can take a measurement of the electrical activity of the myocardium in a process called electrocardiography. The movement of ionic charge in the myocardium generates an electric field with measurable dipole moments. By attaching bipolar leads on axes  $60^\circ$  apart, these dipole moments can be recorded. Lead I lies along the horizontal axis, with the positive pole on the left arm and the negative pole on the right arm. Lead II is offset by  $60^\circ$ , with its positive pole on the leg and negative lead on the right arm. Lead III completes the triangle with its positive pole on the leg and negative pole on the left arm. This is known as the Einthoven triangle. These three leads can be viewed as vectors, and using vector mathematics the leads  $avR$ ,  $avL$ , and  $avF$  can be calculated, which bisect the angles formed by these standard leads. In addition, there are six precordial leads, which are important for localizing myocardial ischemia and infarction. A normal ECG can be seen in Figure 1.3 (Herman and Shelton 2010).

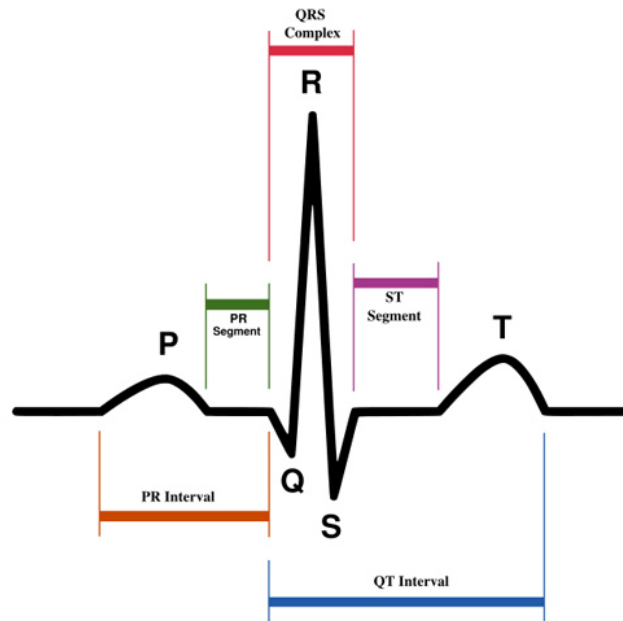


**Figure 1.3.** Nomenclature of an ECG

A positive deflection on the ECG represents a depolarization wavefront traveling towards its positive direction or a repolarization moving away from its positive direction. The P wave represents the atrial depolarization. Atrial repolarization cannot be seen in the ECG because it is obscured by the QRS complex. The PR interval represents the time from beginning of atrial depolarization to beginning of ventricular depolarization and the PR segment represents the delay in conduction through the AV node. The QRS complex signals the beginning of ventricular depolarization. The ST segment corresponds to the peak of the cardiac AP, and the T wave signals ventricular repolarization. Thus, the QT interval represents the duration of the ventricular AP. Both long and short QT intervals can signal pathology caused by congenital abnormalities, metabolic disturbances, and medication (Zimetbaum and Josephson 2008). A long QT,

representing prolonged depolarization of the ventricles, can lead to arrhythmia if the heart rate increases, causing the SA node to fire and spread a depolarizing impulse before the ventricle has repolarized. This condition, called torsades de pointes, is characterized by rapid, irregular QRS complexes which may degenerate into ventricular fibrillation resulting in SCD (Zimetbaum and Josephson 2008).

### **1.3. Cellular cardiac physiology**

#### **1.3.1. The cardiac AP**

Having described the heart on the macroscopic levels of conduction and propagation, let us now turn to the microscopic, molecular events required for cardiac contraction on a cellular level. The physiology of a cardiac AP is intricate and unique, as seen in figure 1.4.

As seen from the figure, there are five phases to the cardiac AP. The myocyte starts at its resting membrane potential, around -90 mV. At phase 0, the cell depolarizes sharply, at a rate of approximately 250 V/s, to a final level of approximately 30-50 mV (depending on the animal and location of myocyte in the heart). The main channels responsible for this opening are cardiac voltage-gated sodium channels ( $\text{Na}_v1.5$ ), and to a minor role, voltage-gated L-type calcium channels ( $\text{Ca}_v1.2$ ) (Nerbonne and Kass 2005). Phase 1, also called “the notch,”

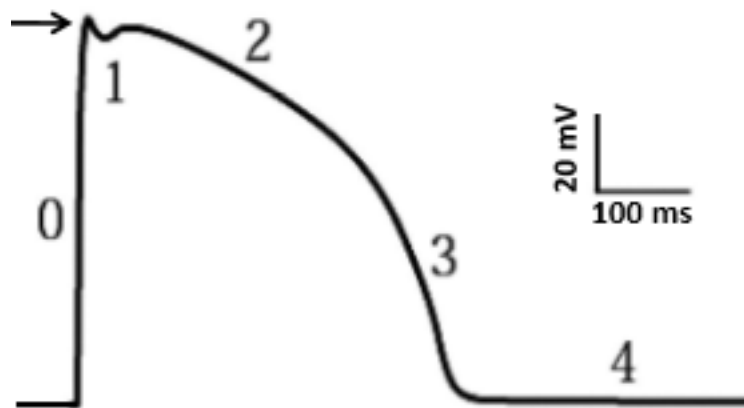


**Figure 1.4.** Phases of an action potential in a ventricular myocyte

occurs as a result of the fast inactivation of  $\text{Na}_v1.5$  channels combined with the activation of transient outward potassium current ( $I_{to}$ ) as well as current from the  $\text{Na}^+/\text{Ca}^{2+}$  exchanger ( $I_{\text{NCX}}$ ). The  $I_{to}$  currents have both a fast component, produced by  $\text{K}_v4.2$  and  $\text{K}_v4.3$  channels, and a slow component, produced by  $\text{K}_v1.4$  channels. In some pathologies, such as after myocardial infarction,  $\text{K}_v4.2$  and  $\text{K}_v4.3$  current decreases, leading to prolonged action potential duration and arrhythmogenesis (Rossow, Dilly et al. 2009, Cooper, Soeller et al. 2010).

Increased probability of arrhythmia is caused by both prolonged depolarization of the cell and inability for it to reach baseline before depolarizing again, increasing the driving force for calcium and leading to a calcium-overloaded myocyte.

The most unique phase of the cardiac AP is phase 2, which prolongs the action potential from approximately 3 ms to 300 ms in a stable depolarized plateau due largely to calcium influx into the cell.  $\text{Ca}_v1.2$  channels open, and, along with a

small amount of non-inactivated sodium current, provide the depolarizing force against a hyperpolarizing drive composed mostly of potassium current. Both hERG and  $K_vLQT1$  potassium channels open to rectify the current. The length of this plateau, and thus of the action potential, is determined by the balance of  $Ca_v1.2$  current against these potassium currents. Long QT syndrome, a set of pathologies in which the action potential duration is prolonged, usually is a result of potassium current disruption, either by drug blockade or congenital development. In particular, the hERG channel is easily blocked by drugs such as quinidine and rofecoxib and all drugs must be tested for their affinity to hERG before being approved for human use (Frolov, Ignatova et al. 2011). There is also a condition known as long QT 8 or Timothy's syndrome (TS), which causes long QT through a gain of function mutation delaying inactivation of  $Ca_v1.2$  channels. At phase 3, calcium and sodium currents decrease either by inactivation or closure as potassium currents continue to increase, thus repolarizing the myocyte. The threshold between relative and absolute refractory period is in phase 3. Absolute refractory period is the time in which no stimulus could elicit another action potential in the cell, regardless of stimulus severity. In relative refractory period, another action potential can be elicited but it requires a stronger than normal stimulus. Phase 4 is the return of the myocyte to rest. In phase 4, the cell is ready for another action potential.

### 1.3.2. Excitation-contraction (EC) coupling

EC coupling is the process by which the electrical stimulus of conduction results in mechanical contraction. The main molecular messenger in EC coupling is calcium. Calcium enters the cytoplasm via  $Ca_v1.2$  channels, which are coupled to other channels on the sarcoplasmic reticulum (SR) called ryanodine receptors (RyR). The SR is the main intracellular storage depot of calcium in the cell, containing many calcium-buffering proteins such as calsequestrin to increase its storage capacity. Whereas in skeletal muscle the membrane calcium sensor dihydropyridine receptor is physically coupled to the sarcoplasmic RyR, in the heart this relationship is not physical but chemical: calcium entering via  $Ca_v1.2$  activates RyRs to release intracellular calcium in a mechanism called calcium induced calcium release. Whereas during diastole, the concentration of calcium in the cytoplasm is only  $\approx 150$  nM, during an AP the concentration can reach  $\approx 1$   $\mu$ M. During this rise, approximately 1/3 of the  $[Ca^{2+}]$  elevation comes from  $Ca_v1.2$  whereas 2/3 of the  $[Ca^{2+}]$  rise is a result of RyR release. Thus,  $Ca_v1.2$  channels not only control the duration of the action potential but also regulate the amount of calcium entering the cell during that action potential.

Calcium is then intimately involved in myocyte contraction. Calcium binds to troponin-C, a protein attached to the actin filaments, and changes its conformation to move tropomyosin such that actin molecules are able to bind to the myosin head. The myosin head binds to actin, hydrolyzing ATP and supplying energy for the myosin head to cock, contracting the sarcomere length. New ATP then binds and changes the conformation of the myosin head back to

its original conformation. As long as the myosin-binding site on actin remains exposed, the myosin will ratchet up the actin molecule to shorten the sarcomere. As the cell starts to repolarize, calcium is removed from the cytoplasm via the SR calcium ATPase (SERCA) and extruded via the NCX, normalizing calcium levels. As a result, calcium unbinds from troponin-C and the myosin-binding site on actin is covered.

### 1.3.3. L-type ( $\text{Ca}_v1.2$ ) calcium channels

$\text{Ca}_v1.2$  channels open for long durations before inactivating, hence the name L-type (for Long-lasting). These channels are also sensitive to blocking by dihydropyridines such as nifedipine or nicardipine, thus giving them the name “dihydropyridine receptors” (DHPR). Structurally, these channels are composed of three subunits: the pore-forming  $\alpha_{1C}$ , as well as the accessory  $\beta$  and  $\alpha_2/\delta$  subunits. In non-cardiac tissue, there is also a  $\gamma$  subunit (Bodi, Mikala et al. 2005). The  $\alpha_{1C}$  subunit is the largest protein, about 2000 amino acids long with a molecular weight of 170 kDa. Structurally, it is divided into four domains, with each domain having six transmembrane  $\alpha$  helices (Catterall 2000, Catterall 2011). Like other voltage-gated channels, the S4 helix in each domain acts as the voltage sensor (Catterall 2011). The helix contains basic arginine or lysine residues every third or fourth residue, which forces the S4 segment to move outward into the extracellular space upon depolarization. This movement is coupled to the S5 and S6 domains, which make up the pore region, and opens

the channel (Bodi, Mikala et al. 2005). There is a cluster of glutamate residues in the loop connecting S5 and S6 that confers  $\text{Ca}^{2+}$  selectivity (Heinemann, Terlau et al. 1992).

$\text{Ca}_v1.2$  channels inactivate slowly, but they have two forms of inactivation. Voltage-dependent inactivation (VDI) is slower while  $\text{Ca}^{2+}$  dependent inactivation (CDI) is faster. In cardiac cells, CDI predominates (Treinys and Jurevicius 2008). CDI depends mostly on calcium released from the SR; thus RyR activity and SR content largely determine  $I_{\text{Ca}}$  in normal physiology. However, in some pathologies, any situation resulting in calcium excess could also increase CDI. Calmodulin (CaM), a  $\text{Ca}^{2+}$  sensor in cells, is also implicated in CDI. CaM binds to the part of the  $\text{Ca}_v1.2$  channel in the C-terminus called the pre-IQ and IQ domains (or the L and K domains). Mutation residues in this domain completely abolished CDI. There are two molecular reasons for CaM's involvement in CDI. First, the pre-IQ domain contains a  $\text{Ca}^{2+}$  sensor, and binding of this sensor modulates how CaM binds to the  $\alpha_{1C}$  subunit. In addition, the IQ domain binds CaM that is already loaded with  $\text{Ca}^{2+}$  in a way that might impede the pore (Soldatov and Cannell 1997, Soldatov, Zuhlke et al. 1997, Soldatov, Oz et al. 1998). However, it is currently unclear mechanistically how CaM binding in the IQ domain creates CDI.

Unlike the ball and chain model of sodium channels or the C-type inactivation of potassium channels, the mechanism of VDI in calcium channels is also unclear.

There is some evidence that the cytoplasmic loop between domains I and II can form a hinged lid that blocks the channel during activation (Zhang, Ellinor et al. 1994, Stotz and Zamponi 2001, Cens, Rousset et al. 2006, Liao and Soong 2010). On the other hand, other groups have provided evidence that the intracellular hydrophobic ring lining the lower vestibule of the pore may be implicated in VDI and CDI (Cens, Rousset et al. 2006). Furthermore, VDI might even be regulated or modulated by extrinsic factors of the channel such as phosphorylation by protein kinase A (PKA) or calmodulin kinase II (CaMKII).

Ca<sub>v</sub>1.2 channels are large protein complexes consisting of an  $\alpha$  subunit, which consists of 24 transmembrane segments which forms the pore and voltage sensors, as well as a  $\beta$  and  $\alpha_2\delta$  subunit in 1:1:1 stoichiometry. The accessory subunits also have important roles in Ca<sub>v</sub>1.2 physiology. The  $\alpha_2/\delta$  subunit is composed of two halves derived from a single gene: the  $\alpha_2$  resides extracellularly while the  $\delta$  subunit has a single transmembrane domain. The two segments are linked through a disulfide bridge (Bodi, Mikala et al. 2005). A glycoposphatidylinositol on the tail of the  $\delta$  segment anchors the  $\alpha_2/\delta$  subunit to the extracellular face of the membrane (Catterall 2011). There is evidence that this subunit can increase channel density, charge movement, and drug binding. The  $\beta$  subunit, on the other hand, is required for plasma membrane expression and proper gating (Lacerda, Kim et al. 1991). It is a hydrophilic, nonglycosylated protein that is entirely intracellular. It binds tightly to a highly conserved motif in the cytoplasmic linker between domains I and II in a region called the  $\alpha$

interaction domain. There are four subfamilies of the  $\beta$  subunit ( $\beta_1 - \beta_4$ ), with  $\beta_2$  being the predominant subunit in the heart (Colecraft, Alseikhan et al. 2002).

Without the  $\beta$  subunit,  $\text{Ca}_v1.2$  channels show little to no surface expression and produce very small or no current, indicating that the  $\beta$  subunit is also important for trafficking of the channel (Birnbaumer, Qin et al. 1998).

In general, coexpression of  $\beta$  subunits results in a left-shift of the I-V relationship, leading to the channel opening at more hyperpolarized voltages (Bodi, Mikala et al. 2005). Expression of  $\beta_2$  also results in slower inactivation kinetics of the channel (Cens, Rousset et al. 2006).

#### **1.3.4. The fidelity of the heartbeat: local control theory of $\text{Ca}^{2+}$ signaling in ventricular myocytes**

$\text{Ca}_v1.2$  channels open to let  $\text{Ca}^{2+}$  into the cell, thus opening RyRs and flooding the cell with calcium. However, this process is not a global phenomenon, spatially averaged in the cell. Rather, calcium release occurs on a local basis within the cell. In ventricular myocytes,  $\text{Ca}_v1.2$  channels are concentrated in transverse tubules (T-tubules), invaginations in the sarcolemma that run perpendicular to the long axis of the myocyte at regular intervals  $\approx 2 \mu\text{m}$ . T-tubules colocalize with Z-lines, which are the striations seen on confocal images of myocytes (Guatimosim, Dilly et al. 2002). T-tubules come in close apposition to a section of the sarcoplasmic reticulum called the junctional sarcoplasmic reticulum (jSR), and together these structures form the cardiac dyad. RyRs

populate the surface of the jSR, packed as a 30 nm wide quasi-crystalline array known as calcium release units (CRU). Franzini-Armstrong's widely cited EM study found that there are approximately 100 RyRs in a given CRU (Franzini-Armstrong, Protasi et al. 1999). However, recent super-resolution imaging has suggested that RyRs are packed into smaller clusters of about 13 channels, and that these small clusters communicate with other nearby clusters to create the CRU (Baddeley, Jayasinghe et al. 2009).

During phase II of the cardiac AP, the myocyte depolarizes, opening  $\text{Ca}_v1.2$  as  $\text{Ca}^{2+}$  enters the cytoplasm. The dyad limits the diffusional ability of  $\text{Ca}^{2+}$ , and so when a  $\text{Ca}_v1.2$  channel opens the local concentration of  $\text{Ca}^{2+}$  increases from  $\approx 150$  nM to  $>10$   $\mu\text{M}$  within 0.3 ms (Forbes and Sperelakis 1983, Cannell and Kong 2012). The increase in  $[\text{Ca}]_i$  leads to rapid openings of RyR. These molecular events can be visualized by loading the cell with a cytoplasmic fluorescent indicator that fluoresces upon binding of calcium. The openings of  $\text{Ca}_v1.2$  channels are called sparklets and the openings of RyR are called sparks (Cheng, Lederer et al. 1993, Navedo, Amberg et al. 2005, Cheng and Lederer 2008). The stoichiometry of the myocyte is such that clusters of  $\approx 10$   $\text{Ca}_v1.2$  channels on the T-tubules congregate opposite clusters of RyRs on the jSR. In the dyad, the surface and the jSR are separated by  $\approx 12$  nm. The entire  $\text{Ca}^{2+}$  transient, then, is the summation of these individual calcium events. This is called the local control theory of cardiac EC coupling: that SR  $\text{Ca}^{2+}$  release is controlled by  $\text{Ca}_v1.2$  current activating RyR clusters, and not by the average increase in

$\text{Ca}^{2+}$  concentration in a myocyte. In fact, a “common pool” model of EC coupling would lead to unstable, all-or-nothing behavior in  $\text{Ca}^{2+}$  transients (Cheng and Wang 2002). In addition, a global increase proved to be less effective than local  $I_{\text{Ca}}$  activation (Niggli and Lederer 1990).

During systole, it is estimated that approximately 10,000 sparks, each one evoked from a sparklet, result in a transient. However, there are also spontaneous sparks that occur during diastole. These sparks occur because there is a very small probability of RyRs opening at the resting calcium concentration. It is important to note that, although spark events are independent, there is evidence from Izu *et al* that sparks are able to increase the local frequency of other sparks 912-24 fold through local  $\text{Ca}^{2+}$  subspace elevation along a Z line (Izu, Banyasz et al. 2007). However, due to the structure of the T-tubule and distance between Z-lines, it is impossible for a spark to jump between Z-lines (Parker and Wier 1997).

The amount of  $\text{Ca}^{2+}$  released from a RyR depends on the  $\text{Ca}^{2+}$  load in the SR. If the SR is in a  $\text{Ca}^{2+}$ -overloaded state, there is more driving force for  $\text{Ca}^{2+}$  to exit the SR. In addition, excess  $\text{Ca}^{2+}$  in the SR increases the RyR sensitivity to  $\text{Ca}^{2+}$ -mediated opening through a currently unknown mechanism (Lukyanenko and Gyorke 1999). In extreme cases of  $\text{Ca}^{2+}$  overload, a spark can become self-regenerating and will eventually spread to adjacent sites, creating a  $\text{Ca}^{2+}$  wave. This wave would cause the myocyte to depolarize and contract as if in phase II of

the cardiac AP. Through connexin gap-junctions, this depolarization could spread to adjacent cells, creating a non-pacemaker generated contraction which could interact with the natural pacemaker depolarization to create arrhythmogenic activity (Cheng, Lederer et al. 1993, Diaz, O'Neill S et al. 2004).

As discussed earlier,  $\text{Ca}_v1.2$  channels inactivate by a combination of VDI and CDI, which terminates the  $\text{Ca}^{2+}$  sparklet, thus ending the initiative process of the global  $\text{Ca}^{2+}$  transient. The mechanism of spark termination remains unclear. RyR may inactivate either by undergoing CDI themselves or by depletion of SR  $\text{Ca}^{2+}$  reserves (Cheng and Lederer 2008). In any case, both  $\text{Ca}_v1.2$  and RyRs close, eliminating the influx of  $\text{Ca}^{2+}$  into the cytoplasm. However,  $\text{Ca}^{2+}$  must still be removed from the cytoplasm to prepare for the next cardiac cycle. SERCA pumps  $\text{Ca}^{2+}$  back into the SR to replenish the internal  $\text{Ca}^{2+}$  stores while the NCX transports  $\text{Ca}^{2+}$  extracellularly. The NCX operates at a stoichiometry of 3  $\text{Na}^+$ : 1  $\text{Ca}^{2+}$ , resulting in a net inward depolarization current.

#### 1.3.5. EC coupling in atrial myocytes

In contrast to ventricular myocytes, in most species atrial myocytes lack T-tubules. Rather than have invaginations of the sarcolemma at the Z-lines, atrial myocytes have outcroppings of the sarcoplasmic reticulum that approach the sarcolemma, called Z-tubules (Brette and Orchard 2003, Chung and Guarne 2008). The lack of T-tubules translates to drastic differences in  $\text{Ca}^{2+}$  handling

between the two cell types. In atrial cells, depolarization under normal physiological conditions only provokes  $\text{Ca}^{2+}$  signals around the periphery of the cell. These signals do not propagate into the center of the cell and do not fully engage the contractile machinery, thus resulting in only a modest contraction (Bootman, Smyrniak et al. 2011). There are many hypotheses for why the signal does not propagate into the cell interior, but the leading hypothesis involves a spatial gap between the RyRs at the cell periphery (named the junctional RyRs) and the RyRs deep inside the cell (the non-junctional RyRs) (Kawai, Hussain et al. 1999). Whereas the gap between RyR clusters along a Z-line is usually  $\approx 1 \mu\text{m}$ , the gap between junctional and non-junctional RyRs is  $> 2 \mu\text{m}$  (Robu, Pfeiffer et al. 2003, Fischmeister, Castro et al. 2006). However, when atrial myocytes are stimulated with inotropic agonists such as isoproterenol, the  $\text{Ca}^{2+}$  signal becomes globalized, which leads to increased contraction (Chen-Izu, McCulle et al. 2006, Smyrniak, Mair et al. 2010).

#### 1.3.6. Microtubule (MT) physiology and protein trafficking

Having thoroughly elucidated the role of calcium in the perpetual heartbeat, let us turn our attention towards some of the other cellular processes that support EC coupling, in particular the physiology of microtubules (MTs). MTs are long cytoskeletal fibers formed by the polymerization of  $\alpha\beta$  tubulin dimers. These  $\alpha\beta$  dimers join end-to-end to form a protofilament, which then associates with 12 other parallel protofilaments to form a hollow, helical structure approximately 24

nm in outer diameter and 12 nm in inner diameter with approximately a 12 nm helical pitch. Because the filaments assemble in like direction, MTs have polarity. The side that has the exposed  $\alpha$  tubulin ends is referred to as the (-) end and the side with exposed  $\beta$  tubulin is the (+) end. The (-) end is generally anchored to a MT nucleation site or MT organizing center (MTOC) while the (+) end projects outward towards the cell surface.

MTs have several functions in cellular processes, such as sustaining cell shape, mitosis, and intracellular trafficking of proteins (Gelfand and Bershadsky 1991). MTs are the major components of cilia and flagella, and also push against the cell membrane to provide structure. Perhaps the most research on MTs has been to understand their role in mitosis: they comprise the mitotic spindle, a structure used to segregate chromosomes, and are also found at kinetochores to pull chromosomes apart. In mitosis, two mitotic spindles, which also contain the MTOC and other microtubule associated proteins, separate to different sides of the cell and send out MTs to the midline to attach and align chromosomes. Other MTs go from the spindle towards the cell membrane to stabilize the position of the MTOC and provide cell structure. Because mitosis becomes misregulated in cancer, researching MTs in mitosis has been a significant research topic in recent years.

An important aspect of MT physiology is that MTs are in dynamic equilibrium. Assembly and disassembly of MTs is driven by the binding, hydrolysis, and

exchange of a guanine nucleotide on the  $\alpha$  tubulin monomer GTP hydrolysis. GTP is not required for MT assembly but is necessary for switching between catastrophe and rescue. Growing MTs are thus believed to maintain a 'cap' of tubulin-GTP subunits to stabilize growth (Akhmanova and Steinmetz 2008). At any time, MTs are either growing by assembling  $\alpha\beta$  tubulin dimers to their (+) tip or shrinking by instabilization of the (+) tip and loss of  $\alpha\beta$  dimers. The transition from growing to shrinking is called catastrophe, and the process from shrinking to growing is called rescue. This entire process is called dynamic instability.

There are several proteins that associate with the (+) end of MTs, either to stabilize and prevent it from catastrophe, to destabilize it and promote catastrophe, or for other functions such as recruiting MT regulators. Some of these proteins are called plus-end binding (EB) proteins. EBs are dimers and seem to require two tubulin binding sites in order to effectively track MT (+) ends (Slep and Vale 2007). EBs autonomously track growing MT ends and have been used with fluorescence imaging to track MT dynamics in real time in non-cardiac cells. Some other plus-end proteins, such as CLIP170, require EB1 to track MT growth (Dixit, Barnett et al. 2009). Meunier et al recently performed research on CLIP170 in HeLa cells and found that CLIP170 associates with a protein called bridging integrator 1 (BIN1), which is responsible for the formation of T-tubules in muscle. Moreover, CLIP170 was found to be essential for formation of T-tubules by BIN1. They suggest that BIN1 may be the anchoring point for CLIP170 on the

plasma membrane (Meunier 2009 (Meunier, Quaranta et al. 2009)). In addition, CLIP170 has been shown to pull on and anchor MTs (Tai, Dujardin et al. 2002).

MTs are also the highways of some molecular motors, proteins that walk or process along tracks using ATP hydrolysis. Molecular motors consist of 18 different class of myosins, 10 different families of kinesins, and 2 groups of dyneins, each with up to several dozen members. While myosins move along actin filaments, both kinesins and dyneins use MTs. Many kinesin superfamily proteins move processively towards the (+) end. On the other hand, dynein motors move towards the (-) end. The loss of the  $\gamma$ -phosphate group from ATP bound to a molecular motor leaves a space of approximately 0.5 nm, which causes a structural rearrangement of a conserved set of residues flanking the ATP-binding site. The rearrangement coordinates structural changes in the track-binding site of the motor (Murphy, Rock et al. 2002). The conformational changes are then transformed into a step of a lever arm onto the track, leading to an advance of the molecular motor on the track by about 15 nm (Schliwa and Woehlke 2003). These motors are important in transporting RNA, macromolecular complexes, mitochondria, or proteins such as ion channels to the membrane (Howard and Hyman 2003). Thus, disruption of MTs in pathology such as after MI could also impact the protein contents of the cell membrane.

Mature cardiac myocytes do not possess cilia or flagella, nor do they differentiate or undergo mitosis; however, MTs may still have important roles in the cell

(Kerfant, Vassort et al. 2001). However, little work has been done on MTs in muscle. Kerfant et al showed that MT disruption affected  $\text{Ca}^{2+}$  signaling, increasing the  $[\text{Ca}^{2+}]_i$  transient and preventing  $\beta$ -adrenergic signaling. A recent study by Oddoux et al imaged MTs in skeletal muscle using super resolution STED microscopy (Oddoux, Zaal et al. 2013). They found that, in contrast to the center-out formation of MTs in most cells, MTs in skeletal muscle formed a grid-like network that grew at  $9 \mu\text{m}/\text{min}$ , and that static Golgi elements are the major sites of MT nucleation. In addition, they found that EB3-GFP was localized not only to the tips but also along the entirety of the MT and that puncta moved mostly longitudinally or transversely with no regard to cell polarity at similar growth rates. Interestingly, their data indicate that MTs are most likely forming a dynamic lattice and that they grow over each other in bundles. Furthermore, Oddoux *et al* (Oddoux, Zaal et al. 2013) speculates that dystrophin may serve to guide and define regions of MT growth and propose that MT pathology may be implicated in muscular dystrophy.

The formation of reactive oxidative species (ROS) has also been implicated in disrupting MTs (Parker, Kavallaris et al. 2014). Hydrogen peroxide treatment has been shown to depolymerize and disorganize MTs in human osteosarcoma 143B cells, rat pheochromocytoma PC-12 cells, AR42J pancreatic epithelial cells, and human umbilical cord vein endothelial HUVEC cells (Hinshaw, Miller et al. 1993, Valen, Sonden et al. 1999, Lee, Liu et al. 2005, Hu and Lu 2014). In addition, oxidative stress has been implicated in inducing MT disassembly in the setting of

lung injury, resulting in pulmonary endothelial cell barrier dysfunction and increased inflammatory response (Kratzer, Tian et al. 2012). EB proteins are also disrupted during oxidative stress. Le Grand *et al* (Le Grand, Rovini et al. 2014) found that EB1 associates with MTs in a phosphorylation-dependent manner, which is affected by ROS. Smyth *et al* (Smyth, Hong et al. 2010) found that EB1 is displaced from MTs in oxidative stress, correlating with decreased surface connexin 43 expression in human and mouse cardiomyocytes. Lastly, Cartelli *et al* (Cartelli, Ronchi et al. 2010) showed that increased ROS production caused reversals of EB3 comets and growth cone collapse in PC-12 cells.

#### 1.3.7. The junctional SR

To sustain the structures and domains involved in the activation of contraction, cardiac myocytes, like all other cells in the body, must perform basic cellular functions such as protein synthesis and post-translational modification, phospholipid and steroid synthesis, and protein trafficking. In non-muscle cells, these vital functions are performed by the endoplasmic reticulum (ER). Cardiac myocytes have a specialized form of the ER called the sarcoplasmic reticulum (SR). The SR performs specialized roles in  $\text{Ca}^{2+}$  signaling, with the junctional SR (jSR) being important in  $\text{Ca}^{2+}$  release and the longitudinal SR in  $\text{Ca}^{2+}$  reuptake.

Excitation-contraction (EC) coupling is initiated in specialized regions (called “dyads”) where the jSR comes into close apposition (10-30 nm) to the

sarcolemma of cardiac myocytes. Activation of sarcolemmal voltage-gated  $\text{Ca}_v1.2$  channels during the action potential causes a small influx of  $\text{Ca}^{2+}$  that activates ryanodine receptors (RyR) expressed in the nearby jSR via the mechanism of  $\text{Ca}^{2+}$ -induced  $\text{Ca}^{2+}$  release. A central tenet of this model is that dyads must be structurally stable in order to ensure the fidelity and strength of EC coupling, and even small changes in the jSR molecular composition or geometry could induce dramatic changes in EC coupling (Gomez, Valdivia et al. 1997, Soeller and Cannell 1997). Thus, trafficking of jSR proteins could, at least in principle, have an impact on EC coupling.

Accordingly, the structure of both the jSR and sarcolemma is important for normal  $\text{Ca}^{2+}$  signaling. Clusters of  $\text{Ca}_v1.2$  channels localize to the T-tubule sarcolemma in the dyads. Addressing the mechanism of this clustering, Hong et al has shown that BIN1 anchors microtubules to the membrane and localizes  $\text{Ca}_v1.2$  channels to the T-tubules (Hong, Smyth et al. 2010). The study also showed that BIN1 was capable of anchoring and stabilizing microtubules (MTs). In addition, BIN1 has been shown to have a role in  $\text{Ca}^{2+}$  diffusion. The lumen of the T-tubules is continuous with the  $\text{Ca}^{2+}$ -rich extracellular space, and so a 'fuzzy space' of dense protective inner membrane folds in order to limit  $\text{Ca}^{2+}$  diffusion near the T-tubule-jSR zones (Lederer, Niggli et al. 1990, Shepherd and McDonough 1998, Pasek, Simurda et al. 2006, Swift, Stromme et al. 2006). BIN1 has recently been implicated in creating these folds and thus regulating  $\text{Ca}^{2+}$  flux into the cell (Hong, Yang et al. 2014). Lastly, BIN1 knockdown in the heart results

in cardiomyopathy, indicating that BIN1 may play a role in regulating the cardiac calcium current (Muller, Baker et al. 2003).

The jSR is a complex structure with several proteins contributing to its architecture and function. Figure 1.5 shows a cartoon of the proposed protein composition of the jSR. Junctophilin-2 (JP2) is a protein that is anchored to the jSR in its C-terminus and contacts the T-tubules through lipid-interacting motifs in its N-terminus (Garbino and Wehrens 2010). These proteins are hypothesized to provide a molecular bridge between the jSR and the T-tubules. Calsequestrin (CSQ) is a  $\text{Ca}^{2+}$ -binding protein that ensures high levels of  $\text{Ca}^{2+}$  close to RyRs (Rossi, Barone et al. 2008). Two proteins, junctin (JCT) and triadin (TRD), anchor calsequestrin to the SR membrane. junctin (26 kDa) (Jones, Zhang et al. 1995) and triadin (95 kDa) (Kim, Caswell et al. 1990) have a single trans-membrane domain. Because these proteins contain binding sites for the RyR as well as for calsequestrin, they allow conformational coupling between the  $\text{Ca}^{2+}$ -binding protein and the  $\text{Ca}^{2+}$  release channel (Beard, Laver et al. 2004). Triadin is hypothesized to maintain dyad structure, contribute to healthy EC coupling, and recruit microtubules and molecular motors. In addition, triadin is localized exclusively to the jSR (Fourest-Lieuvain, Rendu et al. 2012). Both triadin and junctin knockout mice show changes in the jSR architecture, and, with RyRs and calsequestrin, form the “core complex of proteins required for  $\text{Ca}^{2+}$  release” (Zhang, Kelley et al. 1997, Glover, Quinn et al. 2002).

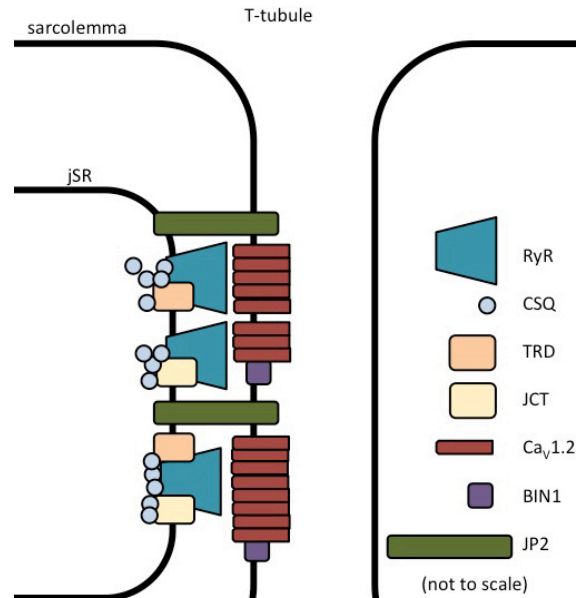


**Figure 1.5.** Cartoon of the junctional sarcoplasmic reticulum

Work by Sleiman *et al* adds to a growing body of evidence that suggests that the SR is a dynamic organelle. They found that triadin and junctin moved radially away from the nuclei, developing a punctate pattern in the cell body over 48 hours. Vega *et al* (Vega and Santana 2011) found that SR “boutons” expressing functional RyRs can move throughout the cell, approaching or moving away from the sarcolemma of ventricular myocytes. Another interesting finding is the implication of the microtubule network in jSR protein trafficking. As mentioned previously, there are several molecular motors, both kinesins and dyneins, which are expressed in the heart. Microtubules and the molecular motors dynein and kinesin 1 (Kif5b) have been proposed to be important regulators of SR motility. Microtubule-mediated defects in junctophilin-2 trafficking has been implicated in  $Ca^{2+}$  handling dysfunction and heart failure (Zhang, Chen et al. 2014). It has yet to be seen if triadin and junctin trafficking may also impair  $Ca^{2+}$  signaling and

have a role in pathology. The roles the molecular motors might have in this trafficking pathway and other pathways in the heart are unknown.

Interestingly, new research shows that changes in the dyad structure can likely contribute to  $\text{Ca}^{2+}$  instability during pathology. Zhang *et al* (Zhang, Li et al. 2013) found that T-tubules and SR physically uncouple in human heart failure. Song *et al* (Song, Sobie et al. 2006) found that remodeled T-tubules move away from the Z-lines in heart failure, leading to loss of local control and  $\text{Ca}^{2+}$  instability. Recently, Zhang *et al* (Zhang, Chen et al. 2014) has shown that microtubule densification is implicated in T-tubule remodeling and disruption of dyadic proteins in heart failure. Similar studies have been done in other pathological states besides heart failure. Wagner *et al* (Wagner, Lauterbach et al. 2012), for example, used STED nanoscopy to assay remodeling post-myocardial infarction (MI) and found proliferative membrane changes, early EC uncoupling, and SR network fracturing.

#### **1.4. Arrhythmia: the denouement of diseased cardiomyocytes**

##### **1.4.1. Pathology I: Timothy syndrome (TS) – the $\text{Ca}^{2+}$ overloaded heart**

Cardiac arrhythmia is a significant cause of mortality, causing 300,000-400,000 deaths in the United States every year (Rubart and Zipes 2005). The cause of arrhythmia can be extremely varied, and the breadth of the pathophysiology can

be seen in this thesis by comparing 1.4.1 and 1.4.2. Despite the variance, all arrhythmias share some commonalities.

All arrhythmias fundamentally arise from disorders in the ionic currents that shape the cardiac action potential, generally prolonging the AP such that the cell does not fully recover to baseline before being stimulated again to depolarize. Arrhythmias can be divided into two mechanistic classes. The first mechanism is triggered activity, by which abnormal foci of automaticity—groups of myocytes undergoing synchronized early afterdepolarizations (EADs) or delayed afterdepolarizations (DADs)—develop and create a competing pacemaking unit in the cell (Rubart and Zipes 2005, Sato, Xie et al. 2009, Weiss, Nivala et al. 2011). DADs are depolarizations of the cell that occur during the normally quiescent phase 4 of the AP. In DAD, myocytes undergo spontaneous  $\text{Ca}^{2+}$  release often in the form of  $\text{Ca}^{2+}$  waves that propagate through the cell during SR  $\text{Ca}^{2+}$  overload rather than the uniform depolarization seen during normal physiology (Sipido, Volders et al. 2002, Rubart and Zipes 2005, Weiss, Nivala et al. 2011). The  $\text{Ca}^{2+}$  release from the SR creates a depolarizing current due to  $\text{Ca}^{2+}$  extrusion through the NCX, which transfers 3  $\text{Na}^+$  into the cell for every 1  $\text{Ca}^{2+}$  extruded. EADs are depolarizations that occur at the end of phase 2 of the AP. EAD can be caused by several mechanisms, including  $\text{Ca}_v1.2$  channels reactivating during a prolonged APD or by spontaneous SR  $\text{Ca}^{2+}$  release similar to DAD (Choi, Burton et al. 2002, Rubart and Zipes 2005).

Long QT syndromes are a principal cause of triggered activity, as myocytes can stay depolarized longer than they should and may not completely repolarize before the next AP comes, resulting in abnormal depolarization. Long QT syndromes carry an increased rate of arrhythmia, syncope, and sudden cardiac death. Congenital long QT syndromes are largely channelopathies, that is, caused by abnormally functioning ion channels. In the vast majority of long QT syndromes,  $K^+$  currents are reduced, resulting in decreased or delayed repolarization. This is the cause of LQT1 and LQT2 syndromes, which are responsible for 65% of all congenital long QT syndromes. However, there are several other pathophysiological possibilities that result in long QT, including increased  $Na^+$  current (LQT3) or deficiencies in ankyrin, a protein involved in function of the sodium-calcium exchanger (Kaufman, 2009).

One rare form of long QT syndrome, known as long QT 8 or Timothy syndrome (TS), is caused by defects not in  $K^+$  or  $Na^+$  current but in  $Ca^{2+}$  signaling. TS is caused by the G1216A point mutation in exon 8A of the CACNA1C gene that encodes the human L-type  $Ca_v1.2$  calcium channel, which causes a glycine to arginine substitution in position 406 (G406R) located on the cytoplasmic side of internal segment 6 (Splawski et al., 2004). Exon 8A is a mutually exclusive, alternatively spliced form of exon 8, which has a prevalence of 20% in cardiac  $Ca_v1.2$  mRNA (Splawski et al., 2005). Thus, in TS, myocytes have approximately 80% functioning  $Ca_v1.2$  and 20% mutant  $Ca_v1.2$ . In a variant of TS, two individuals have the identical G406R mutation in exon 8, and they

exhibited more severe symptoms, presumably due to dose dependent effect of the mutation (Splawski et al., 2005). It is hypothesized that the mutation, at the cytoplasmic loop linking DI and DII (I-II loop), plays an important role in delaying or stopping an inactivation lid on the channel. Indeed, the mutation causes a dominant, gain-of-function mutation that significantly delays open state VDI in  $Ca_v1.2$  channels and prolongs APD (Splawski, Timothy et al. 2004, Tadross and Yue 2010). When the ratio of repolarizing to depolarizing current is decreased in cardiac myocytes, as in TS, EADs can occur (Sato, Xie et al. 2009). In whole heart preparations, EAD leads to ventricular fibrillation (VF) (Sato, Xie et al. 2009).

A case report from Reichenbach et al., first identified the spectrum of symptoms associated with TS clinically in 1992, and in 2004, Splawski et al. identified its genetic etiology—a point mutation in exon 8A of the *CACNA1C* gene encoding the human  $Ca_v1.2$  channel (Reichenbach, Meister et al. 1992, Splawski, Timothy et al. 2004). In addition to being a long QT syndrome, TS also causes disorders in multiple organ systems, including congenital heart disease, cardiomegaly, syndactylyl, facial dysmorphia, immune deficiency, intermittent hypoglycemia, and neurological disorders such as autism spectrum disorder (ASD) and cognitive deficits (Splawski, Timothy et al. 2004). Half of known TS patients have died by the age of ~2.5 years (Splawski, Timothy et al. 2004). Because of the autosomal dominant nature of the TS mutation and lethality before reaching reproductive maturity, most documented cases of TS have been *de novo*

mutations, with the exception of cases where a parent is mosaic for TS (Splawski, Timothy et al. 2004). The multisystem nature of TS gives us insight into the importance of  $Ca_v1.2$  channels in development, in addition to its primary role in EC coupling in the cardiac system. Although many details of the  $Ca_v1.2$ -TS channels are known, the cellular mechanisms by which they induce arrhythmogenic changes in intracellular  $Ca^{2+}$  remain unclear. In the studies I present in this dissertation, I demonstrate through a thorough set of experiments the physiological cause of arrhythmia in TS and the result of  $Ca^{2+}$  overload in this pathology.

#### 1.4.2. Pathology II: Myocardial infarction (MI)

The second class of arrhythmia is reentry. Reentry results from aberrant or blocked conduction of the depolarization wavefront through the myocardium, creating an island of unexcited myocardium, which becomes excited and conducts a retrograde depolarization wavelet once the main front has bypassed it (Bonow, Mann et al. 2011). The backward propagation can cause a self-propagating ring of depolarizing myocytes. Reentry is caused by variations in refractoriness across the myocardium, and is often caused by tissue damage to the heart, especially after myocardial infarction (Rubart and Zipes 2005). Myocytes exhibit spontaneous SR  $Ca^{2+}$  release as well as EADs (Huffaker, Lamp et al. 2004, Rubart and Zipes 2005). A very deadly example of a reentry arrhythmia is ventricular fibrillation, which requires immediate cardioversion in

patients (Bonow, Mann et al. 2011). Reentry arrhythmia is the leading cause of death acutely after an MI as well as in heart failure (Zachariah, Vasan et al. 2011).

Myocardial infarction (MI) occurs when a vascular occlusion reduces coronary blood flow, resulting in ischemia and necrosis (Diaz-Munoz, Alvarez-Perez et al. 2006). There are many mechanisms involved in injury during MI. Ischemia results in an absence of oxidative phosphorylation and thus a depletion of high-energy phosphates, which is accompanied by cellular and subcellular alterations in cardiac myocytes (de Zwaan, Daemen et al. 2001). Because of the lack of energy, the myocardium can accumulate a variety of metabolic substrates such as fatty acids and ketone bodies, thus increasing the osmolarity of the cell. In order to compensate, the cell swells, leading to osmotic cell stress, reducing myocardial function and activating the renin-angiotensin-aldosterone system, which leads to myocardial fibrosis (de Zwaan, Daemen et al. 2001). In addition, the loss of ATP also slows the  $\text{Na}^+/\text{K}^+$  ATPase, leading to an increase in intracellular  $\text{Na}^+$  which leads to an increase in intracellular  $\text{Ca}^{2+}$  due to reversing activity of the  $\text{Na}^+/\text{Ca}^{2+}$  exchanger. This increases baseline  $\text{Ca}^{2+}$  levels, thus decreasing the gain of CICR and EC coupling.

MI enacts other changes on myocytes as well. In long lasting ischemia, lysosomes may be activated, hydrolyzing the cell membrane and contents by exposing them to the destructive enzymes inside, leading to lysosomal cell death

(de Zwaan, Daemen et al. 2001). There is also evidence that hypoxia can induce apoptosis (Wride, Lapchak et al. 1994). Lastly, MI leads to an increase in inflammation. Acute MI induces activation of the complement system, which causes pro-inflammatory cytokines. In addition, the injury leads to migration and infiltration by activated neutrophils, leading to secondary inflammatory components (Pierce, Mustoe et al. 1989, Pierce, Brown et al. 1991, Boyle and Weisman 1993).

Prolonged hypoxia can lead to formation of free radicals and oxidative stress in cardiomyocytes (Hori and Nishida 2009). Post-infarction, myocytes can lose their structure and display abnormal protein expression, which could be a result of MT disruption (Iwai, Hori et al. 1990, Heling, Zimmermann et al. 2000). It has also been shown that tubulin levels are increased in hypertrophied and failing myocardium (Aquila-Pastir, DiPaola et al. 2002, Zhang, Chen et al. 2014). MT content is increased in pressure-overload cardiac hypertrophy, lending support to the idea that compensatory increases in MT density enhances the rigidity of ventricular myocytes in heart failure (Tsutsui, Ishihara et al. 1993, Tagawa, Koide et al. 1998).

MI also changes the surface expression of several proteins on cardiomyocytes. A set of key proteins, whose expression is decreased after MI, is the voltage-gated  $K_v4$  channels.  $K_v4.2$  and  $K_v4.3$  are the pore-forming subunits responsible for the fast component of the transient outward  $K^+$  current ( $I_{to}$ ). Previous research has

shown that  $I_{to}$  is markedly reduced after MI and in hypertrophied hearts, leading to changes in action potential waveform in failing cardiomyocytes (Nabauer, Beuckelmann et al. 1993, Wagner, Goltz et al. 2007). There is evidence that  $K_v4.2$  and  $K_v4.3$  are trafficked to the membrane via kinesin-2 (Kif17) and that interrupting dynein function can also alter expression of these channels (Chu, Rivera et al. 2006, Loewen, Wang et al. 2009). Reduction in  $I_{to}$  prolongs action potential duration, which influences  $Ca^{2+}$  transient amplitude, delays repolarization, and contributes to intracellular  $Ca^{2+}$  overload. By increasing  $Ca^{2+}$  and reducing diastole, the myocyte becomes prone to over-excitability and being unable to recover in time for the next action potential. Thus, reducing  $I_{to}$  contributes to arrhythmogenesis.

## 1.5. Specific aims

### 1.5.1. Aim 1

**To test the hypothesis that  $Ca_v1.2$ -TS channels increase  $[Ca^{2+}]$  in the cytosol and the SR, creating a  $Ca^{2+}$  overloaded state that increases the probability of arrhythmogenic spontaneous SR  $Ca^{2+}$  release in ventricular myocytes.**

I use a  $Ca_v1.2$ -LQT8 transgenic mouse model to study the effects of the TS mutation. I measure the level of diastolic  $Ca^{2+}$  in TS myocytes as well as SR  $Ca^{2+}$  leak. I quantify SR  $Ca^{2+}$  load,  $Ca^{2+}$  spark activity,  $Ca^{2+}$  transients, and  $Ca^{2+}$  waves

in order to provide a comprehensive picture of  $\text{Ca}^{2+}$  signaling in TS myocytes. In addition, I measure kinetics and magnitude of  $\text{Ca}_v1.2$  current both with and without intracellular  $\text{Ca}^{2+}$  buffers to determine the effect of intracellular  $\text{Ca}^{2+}$  on  $\text{Ca}^{2+}$  current. By measuring  $\text{Ca}^{2+}$  levels with corresponding  $\text{Ca}_v1.2$  current, I measured ECC gain. In order to determine whether the  $\text{Ca}^{2+}$  environment or the prolonged AP of TS was most important in  $\text{Ca}^{2+}$  mishandling, I depolarized WT cardiomyocytes with a TS AP waveform and depolarized TS cardiomyocytes with a WT AP waveform. I expect to find increased levels of  $\text{Ca}^{2+}$  in TS mice in both the cytosol and the SR, which is sufficient for formation of arrhythmogenic events such as  $\text{Ca}^{2+}$  waves.

#### 1.5.2. Aim 2

**To test the hypothesis that MT growth in ventricular myocytes is dynamic and that increased ROS production during MI disrupts MT dynamics, decreasing  $\text{K}^+$  channel trafficking.**

I use an adeno-associated viral vector expressing the MT-associated protein plus end binding protein 3 (EB3) tagged with EGFP to perform live imaging and thus capture and quantify MT dynamics in ventricular myocytes in real time under physiological conditions. I also use super-resolution GSD imaging to visualize EB1 expression in myocytes. I quantify MT growth and expression patterns in ventricular myocytes. I measure catastrophe and rescue rates in control conditions as well as in conditions of oxidative stress and myocardial infarction. I

measure  $K_{v4.2}$  and  $K_{v4.3}$  current and surface expression before and after MI and oxidative stress. I expect to see a disruption in MT dynamics under MI and oxidative stress which results in a decrease in  $K_{v4.2}$  and  $K_{v4.3}$  current and surface expression due to defects in membrane trafficking.

### 1.5.3. Aim 3

**To test the hypothesis that BIN1 stabilizes microtubules on the T-tubules, enabling kinesin-1 to traffic  $Ca_v1.2 \beta_2$  in ventricular myocytes.**

I use an adeno-associated viral vector expressing the MT-associated protein plus end binding protein 3 (EB3) tagged with EGFP to perform live imaging and thus capture and quantify MT dynamics in atrial myocytes in real time under physiological conditions. I quantify MT growth and expression patterns in atrial and cultured myocytes. I use dual-antibody staining to assay the expression patterns of BIN1 and EB1 in both ventricular and atrial myocytes. In ventricular myocytes, BIN1 associates with CLIP170, EB1, and  $Ca_v1.2$ , suggesting MT trafficking of the channel. Using an adeno-associated viral vector expressing a dominant negative version of the molecular motor kinesin-1 (Kif5B-DN), I demonstrate that kinesin-1 is implicated in  $Ca_v1.2$  current density and trafficking. I use co-immunoprecipitation to show that kinesin-1 binds the  $\beta_2$  subunit of  $Ca_v1.2$ . I expect to find that BIN1, CLIP 170, and EB1 form a complex at the cardiac dyad that facilitates MT anchoring and  $Ca_v1.2$  trafficking.

#### 1.5.4. Aim 4

**To test the hypothesis that the SR of adult ventricular myocytes is a dynamic structure.**

Using adeno-associated viral vectors, I visualize triadin with a photo-activatable GFP, the SR with RFP, and the T-tubules with di-8-ANNEPS in order to verify that triadin is expressed on the jSR and that the jSR comes in close apposition to the T-tubules. Using this imaging, I visualize and quantify jSR movement to test the hypothesis that the jSR is dynamic and that there are multiple modalities of jSR biogenesis. Using additional viral vectors disrupting molecular motors, either by expressing a dominant negative form of kinesin 1 or by using shRNA to reduce expression of dynein, I tested the hypothesis that dynein and kinesin 1 regulate SR motility. Using detubulating agents, I will test the hypothesis that the jSR and T-tubules can be uncoupled, leading to defects in  $\text{Ca}^{2+}$  signaling. I expect to find mobile units of jSR that are regulated by molecular motors.

## Chapter 2: Cellular mechanisms of ventricular arrhythmias in a mouse model of Timothy syndrome (long QT syndrome 8)

### 2. Summary

$\text{Ca}^{2+}$  flux through L-type  $\text{Ca}_v1.2$  channels shapes the waveform of the ventricular action potential (AP) and is essential for excitation-contraction (EC) coupling. Timothy syndrome (TS) is a disease caused by a gain-of-function mutation in the  $\text{Ca}_v1.2$  channel ( $\text{Ca}_v1.2\text{-TS}$ ) that decreases inactivation of the channel, which increases  $\text{Ca}^{2+}$  influx, prolongs APs, and causes lethal arrhythmias. Although many details of the  $\text{Ca}_v1.2\text{-TS}$  channels are known, the cellular mechanisms by which they induce arrhythmogenic changes in intracellular  $\text{Ca}^{2+}$  remain unclear. We found that expression of  $\text{Ca}_v1.2\text{-TS}$  channels increased sarcolemmal  $\text{Ca}^{2+}$  “leak” in resting TS ventricular myocytes. This resulted in higher diastolic  $[\text{Ca}^{2+}]_i$  in TS ventricular myocytes compared to WT. Accordingly, TS myocytes had higher sarcoplasmic reticulum (SR)  $\text{Ca}^{2+}$  load and  $\text{Ca}^{2+}$  spark activity, larger amplitude  $[\text{Ca}^{2+}]_i$  transients, and augmented frequency of  $\text{Ca}^{2+}$  waves. The large SR  $\text{Ca}^{2+}$  release in TS myocytes had a profound effect on the kinetics of  $\text{Ca}_v1.2$  current in these cells, increasing the rate of inactivation to a high, persistent level. This limited the amount of influx during EC coupling in TS myocytes. The relationship between the level of expression of  $\text{Ca}_v1.2\text{-TS}$  channels and the probability of  $\text{Ca}^{2+}$  wave occurrence was non-linear, suggesting that even low

levels of these channels were sufficient to induce maximal changes in  $[Ca^{2+}]_i$ . Depolarization of WT cardiomyocytes with a TS AP waveform increased, but did not equalize,  $[Ca^{2+}]_i$  compared to depolarization of TS myocytes with the same waveform. We propose that  $Ca_v1.2$ -TS channels increase  $[Ca^{2+}]$  in the cytosol and the SR, creating a  $Ca^{2+}$  overloaded state that increases the probability of arrhythmogenic spontaneous SR  $Ca^{2+}$  release.

## 2.1. Introduction

The function of the heart is to pump blood. To achieve this function, the heart chambers must contract in a specific, electrically coordinated sequence. The cardiac electrical cycle starts with the firing of an action potential (AP) by sinoatrial node cells. This AP propagates via gap junctions to neighboring atrial myocytes and the atrio-ventricular node, eventually reaching the ventricles. Excitation-contraction (EC) coupling is the coordinated process by which this AP triggers cell contraction.

During the AP, depolarization of the sarcolemma briefly opens L-type  $\text{Ca}_v1.2$  channels, thus allowing a small amount of  $\text{Ca}^{2+}$  to enter the cytosol (Niggli and Lederer 1990, Cannell, Cheng et al. 1995, López-López, Shacklock et al. 1995, Santana, Cheng et al. 1996). The increased  $[\text{Ca}^{2+}]_i$  in the cytosol activates ryanodine-sensitive  $\text{Ca}^{2+}$  channels in the sarcoplasmic reticulum (SR) via the mechanism called “ $\text{Ca}^{2+}$ -induced  $\text{Ca}^{2+}$  release” (CICR) (Fabiato 1983). This results in the production of a “ $\text{Ca}^{2+}$  spark” (Cheng, Lederer et al. 1993).

Synchronous activation of thousands of  $\text{Ca}^{2+}$  sparks throughout the myocytes causes a cell-wide increase in  $[\text{Ca}^{2+}]_i$  that triggers contraction. Closure of  $\text{Ca}_v1.2$  channels, due to inactivation and membrane repolarization, terminates both  $\text{Ca}^{2+}$  influx and release. Re-sequestration of  $\text{Ca}^{2+}$  into the SR by the  $\text{Ca}^{2+}$  ATPase and  $\text{Ca}^{2+}$  extrusion by the sarcolemmal  $\text{Na}^+/\text{Ca}^{2+}$  exchanger (NCX) restores  $[\text{Ca}^{2+}]_i$  to diastolic levels.

This process of  $\text{Ca}^{2+}$  release and recovery is critical for the physiological heartbeat. Disruption of the cycle via prolongation of the AP can lead to an inability of the cell to return to diastolic levels before the next systole, thus creating spontaneous  $\text{Ca}^{2+}$  release and fatal arrhythmia. Long QT syndrome is one set of disorders in which ventricular repolarization is prolonged. Timothy syndrome (TS), also known as long QT syndrome 8, is a rare childhood disorder caused by a single amino acid substitution (G406R) in exon 8 of  $\text{Ca}_v1.2$ , creating a mutant channel ( $\text{Ca}_v1.2\text{-TS}$ ) (Splawski, Timothy et al. 2005). It is an autosomal dominant, multisystem disorder, leading to congenital heart disease, syndactyly, immunodeficiency, cognitive abnormalities, and autistic spectrum defects. TS patients commonly suffer sudden cardiac death as a result of lethal cardiac arrhythmias characterized by a long QT interval (Splawski, Timothy et al. 2005).

In the sarcolemma,  $\text{Ca}_v1.2$  channels can exist in 3 gating modes: 0, 1, and 2.  $\text{Ca}_v1.2$  channels in mode 0 are closed (Hess, Lansman et al. 1984). In mode 1,  $\text{Ca}_v1.2$  channels have a low open probability ( $P_o$ ) and undergo brief openings (<1 ms). In contrast,  $\text{Ca}_v1.2$  channels in mode 2 have a high  $P_o$  and relatively long open times (>10 ms).  $\text{Ca}_v1.2$  channels in this mode of operation allow relatively large amounts of  $\text{Ca}^{2+}$  to enter the cell (Tsien, Bean et al. 1986, Erxleben, Liao et al. 2006).  $\text{Ca}_v1.2\text{-TS}$  channels exhibit increased “mode 2” gating, and undergo a slower voltage-dependent inactivation (VDI). Together, these properties

contribute to a longer mean open time of these channels compared to WT channels (Splawski, Timothy et al. 2004, Barrett and Tsien 2008).

We generated transgenic mice expressing variable levels of  $Ca_v1.2$ -TS solely in cardiac myocytes (TS mice) (Cheng, Yuan et al. 2011). TS mice have a long QT interval and increased arrhythmia frequency despite having similar resting and exercise heart rates (Cheng, Yuan et al. 2011). Two studies have investigated the effects of  $Ca_v1.2$ -TS channels on  $[Ca^{2+}]_i$  in cultured inducible pluripotent stem cell-derived cardiomyocytes and rat ventricular myocytes (Thiel, Chen et al. 2008, Yazawa, Hsueh et al. 2011). Although important, these studies focused on  $Ca^{2+}$  current changes, leaving some biophysical aspects of EC coupling unexplored, which are difficult to study in cultured adult or immature myocytes due to absence or loss of transverse tubules. Thus, the mechanisms by which  $Ca_v1.2$ -TS causes arrhythmogenic changes in  $[Ca^{2+}]_i$  remain unclear. In the present study, we found that even a low level of expression of  $Ca_v1.2$ -TS is sufficient to dramatically alter  $[Ca^{2+}]_i$  in ventricular myocytes.  $Ca_v1.2$ -TS channels increased resting  $[Ca^{2+}]_i$ , SR load,  $Ca^{2+}$  spark frequency and amplitude, AP-evoked  $[Ca^{2+}]_i$  transients, and probability of  $Ca^{2+}$  waves, providing evidence that  $[Ca^{2+}]$  increases in both the cytosol and SR. We propose that  $Ca_v1.2$ -TS channels create a  $Ca^{2+}$  overloaded state that increases the probability of arrhythmogenic events due to spontaneous SR  $Ca^{2+}$  release.

## 2.2. Material and methods

### 2.2.1. Isolation of ventricular myocytes

Mice (TS and WT controls) were euthanized with a lethal dose of sodium pentobarbital administered intraperitoneally as approved by the University of Washington Institutional Animal Care and Use Committee. Ventricular myocytes were isolated using a Langendorff perfusion apparatus as previously described (Rossow, Dilly et al. 2006, Shioya 2007). Digestion buffer (DB) was prepared containing (mM): 130 NaCl, 5 KCl, 3 pyruvic acid, 25 HEPES, 0.5 MgCl<sub>2</sub>, 0.33 NaH<sub>2</sub>PO<sub>4</sub>, 22 dextrose, pH = 7.4 with NaOH. DE was made by adding 75 µL of 100 mM EGTA to 50 mL of DB. DCP was made by adding 1.25 µL of 1M CaCl<sub>2</sub>, 1 mg protease from Streptomyces, and 35 mg collagenase type II to 25 mL DB. POT was made by adding 1.25 µL of 1M CaCl<sub>2</sub>, 0.5 mg protease from Streptomyces, and 15 mg collagenase type II, and 125 mg BSA to 12.5 mL DB. Wash buffer was made by adding 6.25 µL of 1M CaCl<sub>2</sub> and 250 mg BSA to 25 mL DB. Heart was isolated and placed in ice cold DE to isolate and cannulate aorta. Cannula was secured with suture and then heart was hung on gravity perfusion system and perfused with 35 °C DE followed by 35 °C DCP. After heart had digested, ventricles were cut off and placed into POT and mixed with plastic pipette to isolate cells. Cells were pelleted by gravity and then washed with wash buffer once. The isolated ventricular myocytes were kept at room temperature (22-25 °C) in Tyrode's solution containing (mM): 140 NaCl, 5 KCl, 10 HEPES, 10

glucose, 2 CaCl<sub>2</sub>, and 1 MgCl<sub>2</sub>; pH 7.4 with NaOH, and used 0.5-8 hours after isolation.

### 2.2.2. RT-PCR and Western blot analysis

For this study, Ca<sub>v</sub>1.2-TS and Ca<sub>v</sub>1.2-WT channel mRNA was quantified using qPCR as previously described (Amberg and Santana 2003). In addition, protein expression was determined by Western blot, performed as previously described (Cheng, Yuan et al. 2011). Briefly, proteins were extracted from WT and TS mice hearts and run on an SDS-page. A WT brain, which has high expression of Ca<sub>v</sub>1.2, was used as a positive control for the WT band and tsA-201 cells transfected with Ca<sub>v</sub>1.2-TS plasmids were used as a positive control for the TS band. Electrophoresed proteins were then transferred to PVDF membranes. After blocking with 5% normal donkey serum, membranes were probed with Ca<sub>v</sub>1.2 primary antibody (Alomone, cat#ACC-003). Alkaline phosphatase-conjugated donkey anti-rabbit secondary antibody (Jackson Immunoresearch) was used for detection using ECF substrate (GE healthcare). Ca<sub>v</sub>1.2-WT (240 kDa) and TS channels (270 kDa) could be discerned on the blot because Ca<sub>v</sub>1.2-TS channels are fused to a red fluorescent protein (tagRFP<sup>®</sup>; Evrogen) (30 kDa).

### 2.2.3. Electrophysiology

All electrophysiological recordings were performed while cells were superfused with saline solutions at room temperature ( $\approx 22$  °C). Pipettes were pulled using a Flaming-Brown type puller (Sutter Instruments) with nominal resistance of 1-2 M $\Omega$  and filled with solutions as described below.

To record action potentials, the current-clamp mode of the Axopatch 200B amplifier was used. APs were recorded while cells were superfused with Tyrode's solution. The patch-pipette solution used to record APs contained (mM): 110 potassium aspartate, 30 KCl, 10 HEPES, 5 MgATP and 10 NaCl; pH 7.2 with KOH. APs were evoked by a brief (5ms) injection of depolarizing current (7 nA). Membrane voltage records were sampled at 10 kHz and low-pass filtered at 2 kHz.

We used the AP clamp technique to measure  $[Ca^{2+}]_i$  during the physiological WT and TS AP by using stored APs as the voltage command to depolarize myocytes. The representative APs used in these experiments were recorded from WT and TS cells at a frequency of 1 Hz as described above. In some experiments, after stimulating the cell to a steady state, 20 mM caffeine was suddenly applied to assay SR  $Ca^{2+}$  content.

We also used the AP clamp technique to measure L-type  $Ca^{2+}$  currents during the physiological WT and TS AP. Once whole-cell configuration was successfully established in myocytes perfused with Tyrode's solution, the extracellular

solution was exchanged for one with the following constituents (mM): 140 NMDG, 5 CsCl<sub>2</sub>, 2 CaCl<sub>2</sub>, 1 MgCl<sub>2</sub>, 10 glucose, 10 HEPES; pH 7.4 with HCl, and 10 μM tetrodotoxin was added to block sodium channels. The pipette solution used in these experiments contained (mM): 87 CsAsp, 20 CsCl, 10 EGTA, 1 MgCl<sub>2</sub>, 5 Mg-ATP and 10 HEPES; pH 7.2 with CsOH. Cells were stimulated with either the WT or TS APs.

To record  $I_{Ca}$ , membrane potential was controlled via the patch-clamp technique using an Axopatch 200B amplifier (Molecular Devices). Data were acquired at 10 kHz and low-pass filtered at 2 kHz. Ventricular myocytes were continuously perfused with Tyrode's solution. Once whole-cell configuration was successfully established in myocytes, an extracellular solution with the following constituents (mM) was exchanged: 140 NMDG, 5 CsCl<sub>2</sub>, 2 CaCl<sub>2</sub>, 1 MgCl<sub>2</sub>, 10 glucose, 10 HEPES; pH 7.4 with HCl, and 10 μM tetrodotoxin was added to block sodium channels. The pipette solution used in experiments designed to record  $I_{Ca}$  during EC coupling contained (mM): 130 CsCl, 10 TEA-Cl, 5 Mg-ATP and 10 HEPES; pH 7.2 with CsOH.  $I_{Ca}$  was evoked by 200 ms long depolarization pulses from -80 mV to potentials ranging from -40 to +60 mV (10 mV increment). In other experiments, 10 mM EGTA was included in the pipette solution to maintain low global  $[Ca^{2+}]_i$  and eliminate SR  $Ca^{2+}$  release. For these experiments the pipette solution contained (mM): 87 CsAsp, 20 CsCl, 10 EGTA, 1 MgCl<sub>2</sub>, 5 Mg-ATP and 10 HEPES; pH 7.2 with CsOH.

To calculate the kinetics of  $I_{Ca}$ , the 0 mV trace was analyzed in pClamp and fit to the double exponential transient decay equation:

$$y = Ae^{\frac{-x}{\tau_{fast}}} + Be^{\frac{-x}{\tau_{slow}}}$$

where A is the amplitude of the fast decay component (pA),  $\tau_{fast}$  is the time constant of the fast component (ms), B is the amplitude of the slow decay component (pA), and  $\tau_{slow}$  is the time constant of the fast component (ms).

Current density (pA/pF) was obtained by dividing current (pA) by cell capacitance (pF). Integrals of the current density were calculated in pClamp by integrating the area above the current (and below baseline, since  $I_{Ca}$  is inward).

#### 2.2.4. Field Stimulation

Field stimulation was performed via two platinum wires (0.5 cm separation) placed at the bottom of the perfusion chamber. An IonOptix Myopacer (IonOptix Corp, Milton, MA, USA) was used to deliver square voltage pulses (4 ms duration) with an amplitude of 5 V at a frequency of 1 Hz. After reaching steady state, SR  $Ca^{2+}$  load was assayed by measuring the caffeine-induced  $Ca^{2+}$  transient evoked by rapid application of 20 mM caffeine to the cells via a picospritzer.

#### 2.2.5. Confocal Imaging of $Ca^{2+}$ signals

For ratiometric data, Asante Calcium Red (ACaR) was prepared and calibrated as described by Ljubojevic *et al.* (Ljubojevic, Walther et al. 2011). Briefly, ACaR was suspended in a solution of 0.02% pluronic F-127 in DMSO and added to cells to a concentration of 10  $\mu\text{M}$ . Cells were incubated for 1 hour to pellet, then resuspended in Tyrode's solution for use. Excitation occurred at 488 nm and emission was collected at  $>650$  nm ( $F_1$ ) and 525 nm ( $F_2$ ). Absolute  $[\text{Ca}^{2+}]$  was calculated according to the equation:

$$[\text{Ca}^{2+}] = K_d \beta \frac{(R - R_{\min})}{(R_{\max} - R)}$$

where  $R = F_1/F_2$ ,  $R_{\min} = F_1/F_2$  in the absence of  $\text{Ca}^{2+}$ ,  $R_{\max} = F_1/F_2$  in the presence of 20 mM  $[\text{Ca}^{2+}]$  and 10  $\mu\text{M}$  ionomycin,  $K_d = 1336 \pm 38$  nM in the cytoplasm, and  $\beta$  = the proportionality factor determined by the ratio of the  $F_2$  intensities of free and  $\text{Ca}^{2+}$ -bound dye, respectively (Ljubojevic, Walther et al. 2011).

Ventricular myocytes were loaded with the membrane-permeable acetoxymethyl-ester form of Fluo-4 (Fluo-4 AM) for measurement of  $[\text{Ca}^{2+}]_i$  as previously described (Santana et al. 2002). Experiments to measure  $\text{Ca}^{2+}$  waves and sparks were performed on the stage of an Olympus Fluo View 1000 confocal microscope. All other experiments were performed using a BioRad Radiance 2000 confocal system coupled to a Nikon TE300 inverted microscope equipped with a Nikon 60x oil immersion lens. All images were analyzed using ImageJ.  $\text{Ca}^{2+}$  sparks were identified using the computer algorithm SparkMaster on ImageJ (Picht, Zima et al. 2007). Fluorescence signals were calibrated using the  $F_{\max}$  equation (Maravall, Mainen et al. 2000):

$$[Ca^{2+}] = K_d \frac{\left( \frac{F}{F_{\max}} - \frac{1}{R_f} \right)}{\left( 1 - \frac{F}{F_{\max}} \right)}$$

where  $F$  is fluorescence,  $F_{\max}$  is the fluorescence intensity of Fluo-4 AM in the presence of a saturating free  $Ca^{2+}$  concentration,  $K_d$  is the dissociation constant of Fluo-4 AM (1100 nM), and  $R_f$  (255) is this indicator's  $F_{\max}/F_{\min}$ .  $F_{\min}$  is the fluorescence intensity of Fluo-4 in a solution where the  $Ca^{2+}$  concentration is 0.  $K_d$  and  $R_f$  values for Fluo-4 were determined in vitro using standard methods (Woodruff, Sampath et al. 2002).

To determine diastolic  $Ca^{2+}$  for TS cells,  $F_{\max}$  was determined by (1) obtaining stable field transients in Tyrode's; (2) exposing cells to Tyrode's solution with 20 mM 2,3-butanedione monoxime (BDM) and 0 mM  $Ca^{2+}$  until no transients could be induced; (3) exposing cells to 20 mM  $Ca^{2+}$  and 10  $\mu$ M ionomycin until the fluorescence signal was saturated.

To quantify sarcolemmal leak for WT and TS myocytes, cells incubated with 1  $\mu$ M thapsigargin were exposed to solution containing (in mM): 140 NMDG, 5 KCl, 10 HEPES, 10 glucose, 10 EGTA, and 1  $MgCl_2$  until stable calcium levels were reached. Cells were then exposed to the same solution except without EGTA and with 2 mM  $CaCl_2$  added until the cell reached a new steady state level of calcium.

### 2.2.6. Statistics

Data are presented as mean  $\pm$  standard error of the mean (S.E.M.). Two-sample comparisons were made using a Student's *t* test (\*  $P < 0.05$ , \*\*  $0.001 < P \leq 0.01$ , \*\*\*  $P \leq 0.001$ ).

## 2.3. Results

### 2.3.1. Higher resting sarcolemmal $\text{Ca}^{2+}$ leak and $[\text{Ca}^{2+}]_i$ transients in TS compared to WT ventricular myocytes

We have three TS mouse lines. Real time PCR was used to quantify  $\text{Ca}_v1.2\text{-TS}$  transcript expression in these lines (Figure S1A). Data were normalized to  $\beta$ -actin mRNA levels because it was expressed to a similar extent in WT and TS lines. Using this analysis, we found increasing levels of  $\text{Ca}_v1.2\text{-TS}$  channels in our 3 TS lines with line 1 expressing the lowest and 3 the highest mRNA ( $n = 3$  mice per group;  $P < 0.01$ ) (Figure 1A). We also quantified relative protein expression of  $\text{Ca}_v1.2\text{-TS}$  compared to  $\text{Ca}_v1.2\text{-WT}$  in these lines and found that line 1 expression was  $0.20 \pm 0.04$ , line 2 was  $0.40 \pm 0.3$ , and line 3 expression was  $1.54 \pm 0.68$  ( $n = 4$  mice per group;  $P < 0.05$ ) (Figure 1B). The relationship between  $\text{Ca}_v1.2\text{-TS}$  mRNA and protein was linear, suggesting that higher mRNA translated into higher  $\text{Ca}_v1.2\text{-TS}$  protein expression in ventricular myocytes (Figure 1C). Unless specified, TS line 1 was used in the experiments described below because the expression level of this channel is similar in humans with TS (Splawski, Timothy et al. 2004).

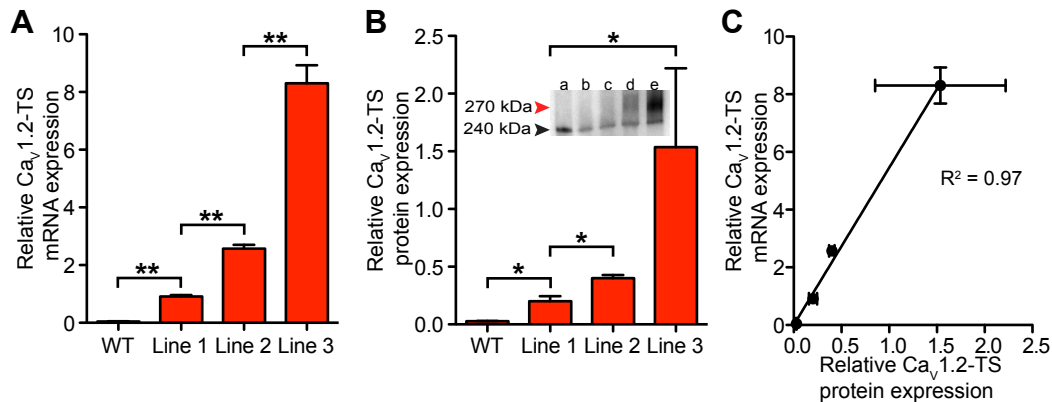


**Figure 2.1.** Linear relationship of relative mRNA and protein expression of  $Ca_V1.2-TS$ .

**A**, plot of relative  $Ca_V1.2-TS$  mRNA expression normalized to expression of  $\beta$ -actin. **B**, plot of relative  $Ca_V1.2-TS$  protein expression normalized to expression of  $Ca_V1.2-WT$  protein. *Inset*, example Western blot: *a*, WT mouse brain (high  $Ca_V1.2-WT$  expression); *b*, WT mouse heart; *c*, TS line 1 mouse heart; *d*, TS line 3 mouse heart; *e*, tsA-201 cells transfected with  $Ca_V1.2-TS$  plasmids. Black arrow at 240 kDa indicates expected  $Ca_V1.2$  channel, red arrow at 270 kDa indicates expected  $Ca_V1.2-TS$  channel fused with tagRFP. **C**, linear fit of relative  $Ca_V1.2-TS$  protein expression, x-axis, vs. relative  $Ca_V1.2-TS$  mRNA expression, y-axis,  $R^2 = 0.97$ .

To examine  $[Ca^{2+}]_i$  in WT and TS myocytes, cells were loaded with the fluorescent  $Ca^{2+}$  indicators Asante  $Ca^{2+}$  Red (ACaR) or Fluo-4 AM and imaged using a confocal microscope. ACaR is a ratiometric  $Ca^{2+}$  indicator that can be excited with 488 nm light. The emission spectrum of the  $Ca^{2+}$ -free and -bound forms of ACaR peak at 525 and 650 nm, respectively. The ratio ACaR fluorescence at 650 and 525 nm increases  $\approx 35$ -fold when  $[Ca^{2+}]$  goes from  $Ca^{2+}$ -free to saturating levels. Like ACaR, the single wavelength indicator Fluo-4 was excited with 488 nm light. Fluo-4 emission was measured at 525 nm. Fluo-4 undergoes much larger changes in fluorescence than ACaR in response to changes in  $Ca^{2+}$ , increasing  $\approx 255$ -fold when  $[Ca^{2+}]$  is elevated from  $Ca^{2+}$ -free to saturating levels.

The relationship between the fluorescence intensities of ACaR or Fluo-4 and  $[Ca^{2+}]_i$  is non-linear. Thus, ACaR and Fluo-4 fluorescence values were converted to concentration (nM) units as described by Grynkiewicz *et al.* (Grynkiewicz, Poenie *et al.* 1985) and Maravall *et al.* (Maravall, Mainen *et al.* 2000), respectively. The rationale for using these two indicators in the initial set of experiments was manifold. Although the ratiometric ACaR has a lower dynamic range than Fluo-4, it has the advantage that its calibration is not affected by dye concentration or photo-bleaching rates. Fluo-4's large dynamic range makes it a better choice for the detection of small  $[Ca^{2+}]_i$  levels than ACaR in TS and WT myocytes. However, because Fluo-4 is a single wavelength indicator, calibrating it assumes no change in laser intensity, photomultiplier gain, pinhole size, and indicator concentration during the experiment. By comparing the  $[Ca^{2+}]_i$  values obtained using ACaR or Fluo-4, we tested the assumption that these parameters did not change during Fluo-4 experimentation, which would validate the calibration of this indicator.

We recorded action potential (AP)-evoked  $[Ca^{2+}]_i$  transients in TS and WT myocytes. APs were evoked via field stimulation at a frequency of 1 Hz. Figure 2A-B shows representative AP-evoked  $[Ca^{2+}]_i$  transients in WT and TS cells under steady-state conditions. The amplitude of the global  $[Ca^{2+}]_i$  transient was larger in TS than in WT cells whether it was measured using ACaR (WT =  $560 \pm 46$  nM,  $n = 8$  vs. TS =  $1003 \pm 151$  nM,  $n = 10$ ;  $P < 0.05$ ) or Fluo-4 (WT =  $600 \pm 40$

nM,  $n = 49$  vs. TS =  $1000 \pm 62$  nM,  $n = 56$ ;  $P < 0.001$ ). Diastolic  $[Ca^{2+}]_i$  — defined as the  $[Ca^{2+}]_i$  measured at the end of the 1 s interval between APs — was also higher in TS than in WT cells in ACaR (WT =  $152 \pm 17$  nM,  $n = 8$  vs. TS =  $237 \pm 15$  nM,  $n = 10$ ;  $P < 0.01$ ) and Fluo-4-loaded cells (WT =  $158 \pm 8$  nM,  $n = 9$  vs. TS =  $215 \pm 7$  nM,  $n = 10$ ;  $P < 0.001$ ).  $[Ca^{2+}]_i$  in non-stimulated, resting myocytes (measured at least 2 seconds after the cessation of stimulation) was also higher in TS (ACaR =  $222 \pm 13$  nM,  $n = 10$  vs. Fluo-4 =  $215 \pm 15$  nM,  $n = 10$ ) than in WT myocytes (ACaR =  $144 \pm 12$  nM,  $n = 8$  vs. Fluo-4 =  $150 \pm 6$  nM,  $n = 7$ ; ACaR  $P < 0.001$ , Fluo-4  $P < 0.01$ ) (Figure 2C).

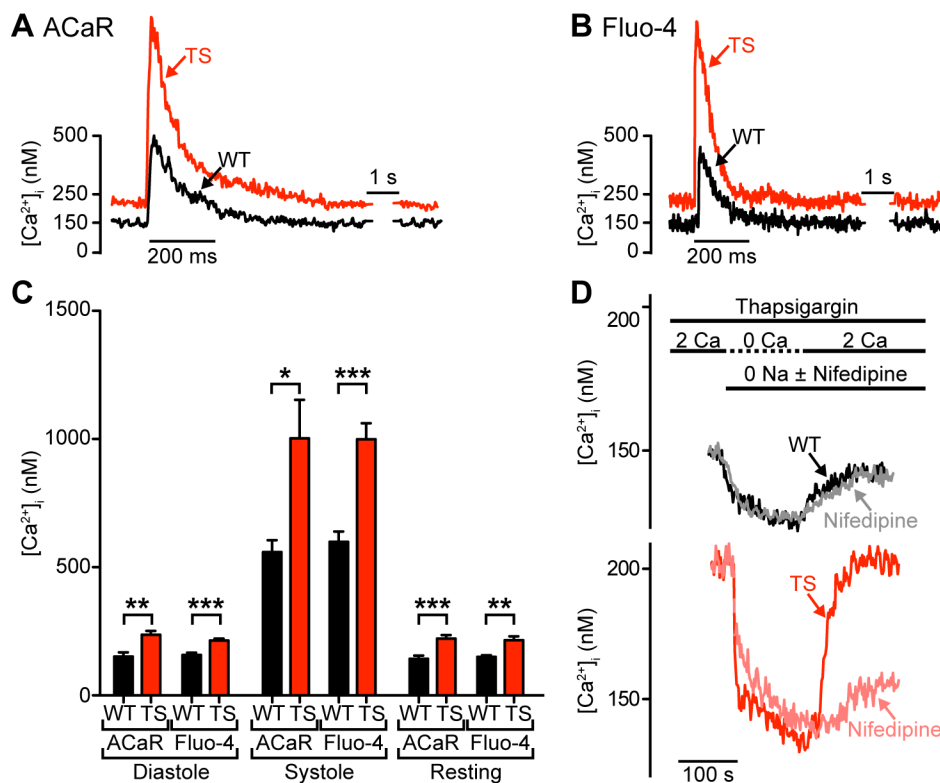


**Figure 2.2.** Higher diastolic, systolic, and resting  $[Ca^{2+}]_i$  and larger sarcolemmal leak in TS cells.

**A-B**, representative  $[Ca^{2+}]_i$  (nM) traces of WT (*black*) and TS (*red*) cells in diastole, systole, and at rest measured using the indicators ACaR (**A**) and Fluo-4 (**B**). **C**, bar plots of the mean  $\pm$  S.E.M. of the diastolic, systolic, and resting  $[Ca^{2+}]_i$

(nM) levels of WT and TS cells measured using each indicator. **D**, representative time courses of WT (*black*) and TS (*red*) cell sarcolemmal  $[Ca^{2+}]_i$  (nM) leak (upon application of thapsigargin and removal of  $Na^+$  and  $Ca^{2+}$  from bath) and recovery (upon restoration of 2 mM  $Ca^{2+}$  to bath). Grey and pink traces indicate same experiment upon application of nifedipine.

We tested the hypothesis that higher “ $Ca^{2+}$  leak” through sarcolemmal  $Ca_v1.2$  channels contributes to higher resting  $[Ca^{2+}]_i$  in TS than in WT myocytes (Figure 2D). To test this hypothesis, we recorded  $[Ca^{2+}]_i$  in resting TS and WT myocytes before and after the application of a 0  $Na^+$ /0  $Ca^{2+}$  external solution in the presence or absence of the  $Ca_v1.2$  channel blocker nifedipine (10  $\mu$ M). All solutions in these experiments contained the SERCA pump inhibitor thapsigargin (1  $\mu$ M) to eliminate SR  $Ca^{2+}$  release. As shown in the representative traces in Figure 2D, application of the 0  $Na^+$ /0  $Ca^{2+}$  external solution decreased  $[Ca^{2+}]_i$  in TS and WT myocytes, presumably due to the termination of  $Ca^{2+}$  leak via  $Na^+$ / $Ca^{2+}$  exchanger and  $Ca^{2+}$ -permeable channels and extrusion via the sarcolemmal  $Ca^{2+}$  pump. In the WT myocyte, return to the  $Ca^{2+}$  containing extracellular solution increased resting  $[Ca^{2+}]_i$  to control levels ( $150 \pm 4$  nM,  $n = 6$ ) even in the presence of nifedipine ( $153 \pm 4$  nM,  $n = 6$ ,  $P > 0.05$ ). This suggests that  $Ca^{2+}$  flux via  $Ca_v1.2$  channels does not contribute to resting  $[Ca^{2+}]_i$  in WT myocytes. However, in TS myocytes,  $[Ca^{2+}]_i$  increased only to  $160 \pm 4$  nM upon return to control conditions in the presence of nifedipine compared to  $207 \pm 13$  nM without nifedipine ( $P < 0.05$ ).

We differentiated these records to determine the rate of change in resting  $[Ca^{2+}]_i$  during the switch from the 0  $Na^+$ /0  $Ca^{2+}$  to the 2 mM external  $Ca^{2+}$  solution. The

maximum  $d[Ca^{2+}]_i/dt$  was  $0.0010 \pm 0.0001$  nM/ms and  $0.004 \pm 0.001$  nM/ms in WT and TS myocytes ( $P < 0.05$ ), respectively. By contrast, the maximum  $d[Ca^{2+}]_i/dt$  of the AP-evoked  $[Ca^{2+}]_i$  transients in the presence of  $1 \mu\text{M}$  thapsigargin was  $2.5 \pm 0.1$  nM/ms ( $n = 8$  WT cells). Thus, while the maximum rate of  $Ca^{2+}$  influx at rest is faster in TS than in WT myocytes, it is about three orders of magnitude slower than the rate of  $Ca^{2+}$  influx into a ventricular myocyte during EC coupling.

Collectively, these data suggest that TS myocytes have a higher resting, diastolic, and systolic  $[Ca^{2+}]_i$  than WT myocytes. Although  $Ca^{2+}$  influx through  $Ca_v1.2$  channels does not contribute to resting  $[Ca^{2+}]_i$  in WT cells, expression of  $Ca_v1.2$ -TS channels results in higher resting sarcolemmal leak and consequently higher  $[Ca^{2+}]_i$  in TS than in WT cells. Furthermore, our data indicate that ACaR and Fluo-4 report similar  $[Ca^{2+}]_i$  in ventricular myocytes, suggesting that laser intensity, photomultiplier gain, pinhole size, and Fluo-4 concentration did not change under our experimental conditions. Thus, calibration of Fluo-4 using the Maravall *et al.* (Maravall, Mainen *et al.* 2000) method is valid. Based on this, and the higher dynamic range of Fluo-4, this indicator was used in the experiments presented below.

### **2.3.2. TS myocytes have a higher frequency of $Ca^{2+}$ sparks and waves than WT myocytes**

We investigated the mechanisms underlying higher  $[Ca^{2+}]_i$  transients in TS myocytes. Experiments tested the hypothesis that RyR activity is higher in TS myocytes than in WT myocytes. A testable prediction of this hypothesis is that spontaneous  $Ca^{2+}$  spark activity is higher in TS myocytes than in WT myocytes.

Figure 3A shows representative confocal line-scan images of  $Ca^{2+}$  sparks in quiescent/resting WT and TS cells. Consistent with our hypothesis, we found that spontaneous  $Ca^{2+}$  spark frequency was  $\approx 3.5$ -fold higher in TS ( $3.8 \pm 0.6$  sparks/100  $\mu\text{m/s}$ ,  $n = 11$  cells) than in WT cells ( $1.1 \pm 0.2$  sparks/100  $\mu\text{m/s}$ ,  $n = 15$  cells;  $P < 0.01$ ) (Figure 3B).  $Ca^{2+}$  sparks in TS cells also had larger amplitude ( $401 \pm 3$  nM,  $n = 1602$  vs.  $297 \pm 2$  nM,  $n = 1782$ ,  $P < 0.01$ ) (Figure 3C) and full width at half-maximal amplitude ( $4.0 \pm 0.1$  ms,  $n = 1602$  vs.  $3.6 \pm 0.1$  ms,  $n = 1782$ ;  $P < 0.05$ ) (Figure 3D) compared to WT cells.  $Ca^{2+}$  spark duration, however, was similar in these cells (WT =  $45 \pm 1$  ms,  $n = 1782$  vs. TS =  $44 \pm 1$  ms,  $n = 1602$ ;  $P > 0.05$ ) (Figure 3E).

If higher  $Ca^{2+}$  channel activity is sufficient to increase resting  $[Ca^{2+}]_i$  and thus induce higher  $Ca^{2+}$  spark activity in TS than in WT ventricular myocytes, exposing WT cells to a  $Ca_v1.2$  channel opener should increase  $Ca^{2+}$  spark frequency in these cells to a level similar to that of TS cells. Figure 3F shows a representative line-scan image of a quiescent WT cell exposed to 1  $\mu\text{M}$  FPL 64176, a drug known to increase the open probability of  $Ca_v1.2$  channels. Consistent with our hypothesis, FPL 64176 increased resting  $[Ca^{2+}]_i$  (from  $150 \pm$

16 to  $209 \pm 26$  nM) and  $\text{Ca}^{2+}$  spark frequency in WT cells to a level similar to the one observed in TS cells ( $3.0 \pm 0.4$  sparks/100  $\mu\text{m}^2/\text{s}$ ,  $n = 10$  cells;  $P < 0.05$ ) (Figure 3H).

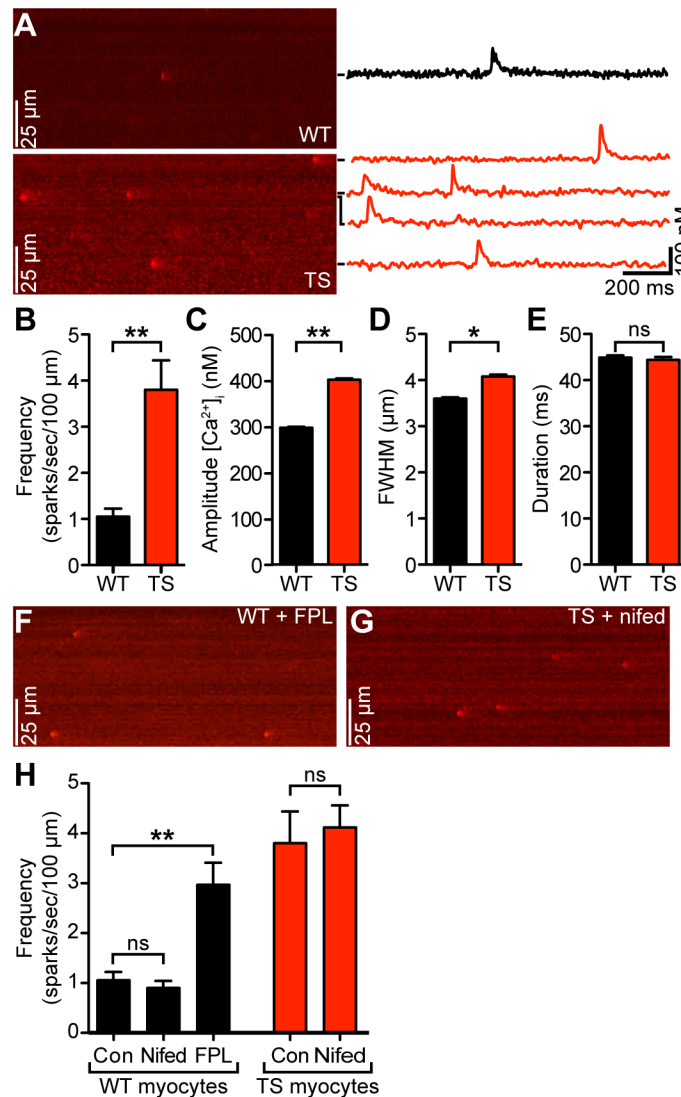


**Figure 2.3.** Higher  $\text{Ca}^{2+}$  spark activity in TS cells.

**A**, representative confocal line-scan images from WT (*above*) and TS (*below*) cells. [ $\text{Ca}^{2+}$ ]<sub>i</sub> (nM) plotted to the right for each spark seen, marked by black bars. **B-E**, bar plots of the mean  $\pm$  S.E.M. of the frequency (**B**), amplitude (**C**), full width at half-maximal amplitude (**D**), and duration (**E**) of  $\text{Ca}^{2+}$  sparks in WT and TS myocytes. **F**, representative confocal line-scan image of a WT cell upon long-term application of FPL 64176. **G**, representative confocal line-scan image of a TS cell upon short-term application of nifedipine. **H**, bar plots of the mean  $\pm$

S.E.M. frequency of  $\text{Ca}^{2+}$  sparks in WT myocytes upon application of FPL 64176 and nifedipine and TS myocytes upon application of nifedipine.

Application of 1  $\mu\text{M}$  FPL 64176 to TS cells invariably induced  $\text{Ca}^{2+}$  waves and cell death. It is important to note, that the effects of FPL 64176 on WT and TS myocytes were not rapid. Rather, the effects of FPL 64176 on  $\text{Ca}^{2+}$  spark (or waves) activity were seen approximately 3 minutes after exposure to the drug, during which time the cell was not stimulated. Similarly, short-term application (i.e., <20 s) of nifedipine (10  $\mu\text{M}$ ) did not affect  $\text{Ca}^{2+}$  spark frequency in WT and TS cells ( $P > 0.05$ ) (Figure 3G-H). This suggests that spontaneous  $\text{Ca}^{2+}$  sparks are not directly activated or produced by the opening of  $\text{Ca}_v1.2$  channels in TS or WT myocytes.

Having determined that TS myocytes have a higher propensity to undergo spontaneous SR  $\text{Ca}^{2+}$  release than WT myocytes, we performed a quantitative analysis of arrhythmogenic spontaneous  $\text{Ca}^{2+}$  waves in these cells. Figure 4A shows representative line-scan images of a large, non-propagated  $\text{Ca}^{2+}$  spark in a WT myocyte and a  $\text{Ca}^{2+}$  wave in a TS cell. Indeed, we found that while in WT cells  $\text{Ca}^{2+}$  waves are rare (1 wave per  $308 \pm 166$  s,  $n = 25$ ), the frequency of  $\text{Ca}^{2+}$  waves is dramatically higher in TS myocytes (1 wave per  $49.4 \pm 16.8$  s,  $n = 37$ ;  $P < 0.05$ ) (Figure 4B). This relationship is maintained even upon application of 100 nM of the  $\beta$  adrenergic receptor agonist isoproterenol (WT, 1 wave per  $31.7 \pm 9.0$  s,  $n = 17$  vs. TS,  $17.1 \pm 2.7$  s,  $n = 22$ ;  $P < 0.05$ ) (Figure 4C). Analysis of the  $\text{Ca}^{2+}$

waves suggested that they propagate at a faster rate in TS ( $87.4 \pm 1.7 \mu\text{m/s}$ ,  $n = 147$ ) than in WT cells ( $77.7 \pm 2.6 \mu\text{m/s}$ ,  $n = 25$ ;  $P < 0.05$ ) (Figure 4D).

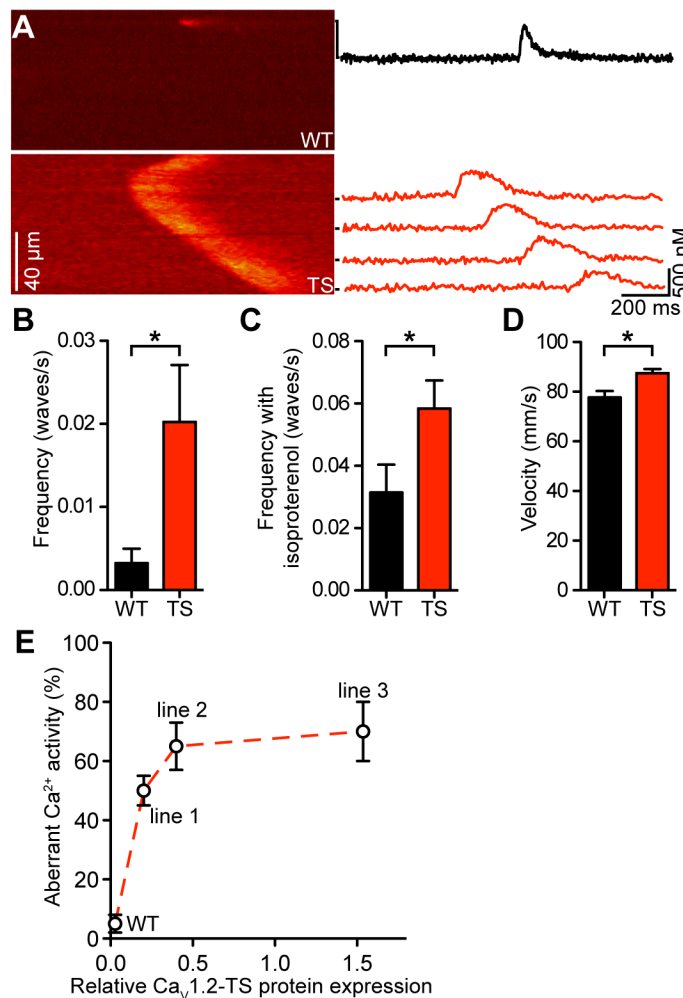


**Figure 2.4.** Higher  $\text{Ca}^{2+}$  wave activity in TS cells.

**A**, representative confocal line-scan images of a large spark in a WT cell (*above*) and a  $\text{Ca}^{2+}$  wave in a TS cell (*below*).  $[\text{Ca}^{2+}]_i$  (nM) plotted to the right for each line marked by black bars. **B-D**, bar plots of the mean  $\pm$  S.E.M. of the frequency (**B**), frequency upon application of 100 nM isoproterenol (**C**), and velocity (**D**) of  $\text{Ca}^{2+}$  waves in WT and TS myocytes. **E**, plot of relative  $\text{Ca}_v1.2\text{-TS}$  expression (x-axis) vs. frequency of aberrant  $\text{Ca}^{2+}$  activity (%) (y-axis).

We extended this  $\text{Ca}^{2+}$  analysis to the other two  $\text{Ca}_v1.2\text{-TS}$  mouse lines to investigate the relationship between  $\text{Ca}_v1.2\text{-TS}$  expression and arrhythmogenic  $\text{Ca}^{2+}$  wave activity in ventricular myocytes. Interestingly, although only  $5 \pm 3\%$  of

the WT myocytes ( $n = 12$ ) had spontaneous  $\text{Ca}^{2+}$  waves,  $50 \pm 3$  ( $n = 16$ ),  $65 \pm 8$  ( $n = 19$ ), and  $70 \pm 10\%$  ( $n = 22$ ) of the myocytes isolated from TS mice lines 1-3 had  $\text{Ca}^{2+}$  waves (Figure 4E). This suggests a nonlinear relationship between TS expression and aberrant  $\text{Ca}^{2+}$  wave activity in a cell.

### 2.3.3. Higher SR $\text{Ca}^{2+}$ load in TS than in WT ventricular myocytes

A potential mechanism for a higher frequency of spontaneous  $\text{Ca}^{2+}$  sparks,  $\text{Ca}^{2+}$  waves, and larger AP-evoked  $[\text{Ca}^{2+}]_i$  transients is an elevation in the SR  $\text{Ca}^{2+}$  load. Thus, we tested the hypothesis that SR  $\text{Ca}^{2+}$  content was higher in TS than in WT myocytes. We used a pico-spritzer to rapidly apply a  $\text{Na}^+$ - and  $\text{Ca}^{2+}$ -free saline solution containing 20 mM caffeine to both paced and quiescent/resting WT and TS cells. Figure 5A shows caffeine-induced  $[\text{Ca}^{2+}]_i$  transients from representative resting TS and WT myocytes. Under these experimental conditions, the amplitude of the caffeine induced  $[\text{Ca}^{2+}]_i$  transient was  $\approx 1.5$ -fold higher in TS ( $1666 \pm 109$  nM,  $n = 11$ ) compared to WT cells ( $1090 \pm 66$  nM,  $n = 17$ ;  $P < 0.01$ ) (Figure 4C), suggesting that TS myocytes have a higher SR  $\text{Ca}^{2+}$  load than WT myocytes.

Figure 5B shows caffeine-induced  $[\text{Ca}^{2+}]_i$  transients from representative TS and WT myocytes which had been paced at 1 Hz until reaching steady-state. At this frequency, the amplitude of the  $[\text{Ca}^{2+}]_i$  transient of TS and WT myocytes reached steady state after 7 APs. On average, the amplitude of the caffeine-induced

$[Ca^{2+}]_i$  transient in paced cells was  $\approx 1.4$ -fold higher in TS ( $1207 \pm 66$  nM,  $n = 60$ ) compared to WT cells ( $828 \pm 59$  nM,  $n = 49$ ;  $P < 0.01$ ) (Figure 5C).

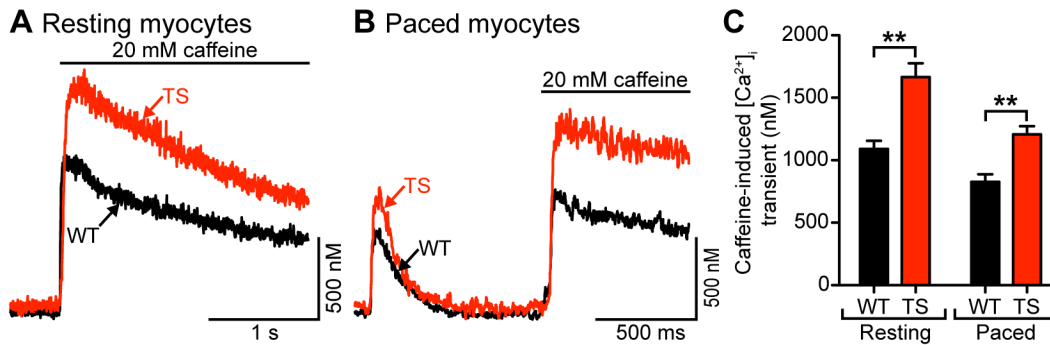


**Figure 2.5.** Higher resting and paced SR load in TS cells.

**A**, representative SR  $Ca^{2+}$  release upon application of 20 mM caffeine in resting WT (*black*) and TS (*red*) cells. **B**, representative SR  $Ca^{2+}$  release upon application of 20 mM caffeine in WT (*black*) and TS (*red*) cells paced at 1 Hz. **C**, bar plot of the mean  $\pm$  S.E.M. of SR  $Ca^{2+}$  release upon application of 20 mM caffeine in resting and paced WT and TS myocytes.

#### 2.3.4. The large SR $Ca^{2+}$ release during EC coupling in TS cells increases the rate of inactivation of $I_{Ca}$ and hence limits $Ca^{2+}$ influx during membrane depolarization into these cells

In the heart, the  $Ca^{2+}$  current ( $I_{Ca}$ ) triggers SR  $Ca^{2+}$  release during EC coupling. Membrane depolarization opens  $Ca_v1.2$  channels, but these channels inactivate due to  $Ca^{2+}$ -dependent and voltage-dependent mechanisms (Catterall 2000). SR  $Ca^{2+}$  release is a major contributor to  $Ca^{2+}$ -dependent inactivation of  $I_{Ca}$  (Adachi-Akahane, Cleemann et al. 1996). Although  $Ca_v1.2$ -TS currents inactivate at a

slower rate than WT channels, the effects of SR  $\text{Ca}^{2+}$  release on these currents are unknown.

Figure 6A shows representative  $I_{\text{Ca}}$  records from TS and WT myocytes dialyzed with an intracellular solution containing 10 mM of the  $\text{Ca}^{2+}$  chelator EGTA to maintain low global  $[\text{Ca}^{2+}]_i$  and eliminate SR  $\text{Ca}^{2+}$  release. Peak  $I_{\text{Ca}}$  at 0 mV was  $-1154 \pm 202$  pA in WT ( $n = 5$ ) and  $-1734 \pm 541$  pA in TS cells ( $n = 6$ ). However, because TS cells ( $214 \pm 25$  pF) had a higher capacitance than WT cells ( $171 \pm 25$  pF),  $I_{\text{Ca}}$  density (i.e., pA/pF) was similar in these cells (WT =  $-6.9 \pm 1.1$  pA/pF vs. TS =  $-7.7 \pm 1.8$  pA/pF;  $P > 0.05$ ). We fitted the decaying phase of these currents with the sum of two exponential functions. The time constants of the fast ( $\tau_{\text{fast}}$ ; WT =  $26 \pm 4$  ms vs. TS =  $38 \pm 4$  ms;  $P < 0.05$ ) and slow component ( $\tau_{\text{slow}}$ ; WT =  $84 \pm 7$  ms vs. TS =  $136 \pm 13$  ms;  $P < 0.01$ ) were larger in TS than in WT cells. Accordingly, the total charge associated with the  $I_{\text{Ca}}$  recorded from EGTA-dialyzed cells (determined by integrating these currents) was  $-688 \pm 208$  fC/pF in TS ( $n = 6$ ) compared to  $-455 \pm 98$  fC/pF in WT cells ( $n = 5$ ) (Figure 6A).

Figure 6C shows line-scan images,  $I_{\text{Ca}}$  densities, and the time course of the spatially-averaged  $[\text{Ca}^{2+}]_i$  of TS and WT cells depolarized to the test potential of 0 mV. EGTA was absent from the patch pipette solution to ensure normal SR  $\text{Ca}^{2+}$  release during membrane depolarization. To achieve steady-state SR  $\text{Ca}^{2+}$  load, 10 pre-conditioning pulses (100 ms duration) from -80 to 0 mV (1 Hz) were applied just prior to the test pulse. Control experiments showed that TS myocytes

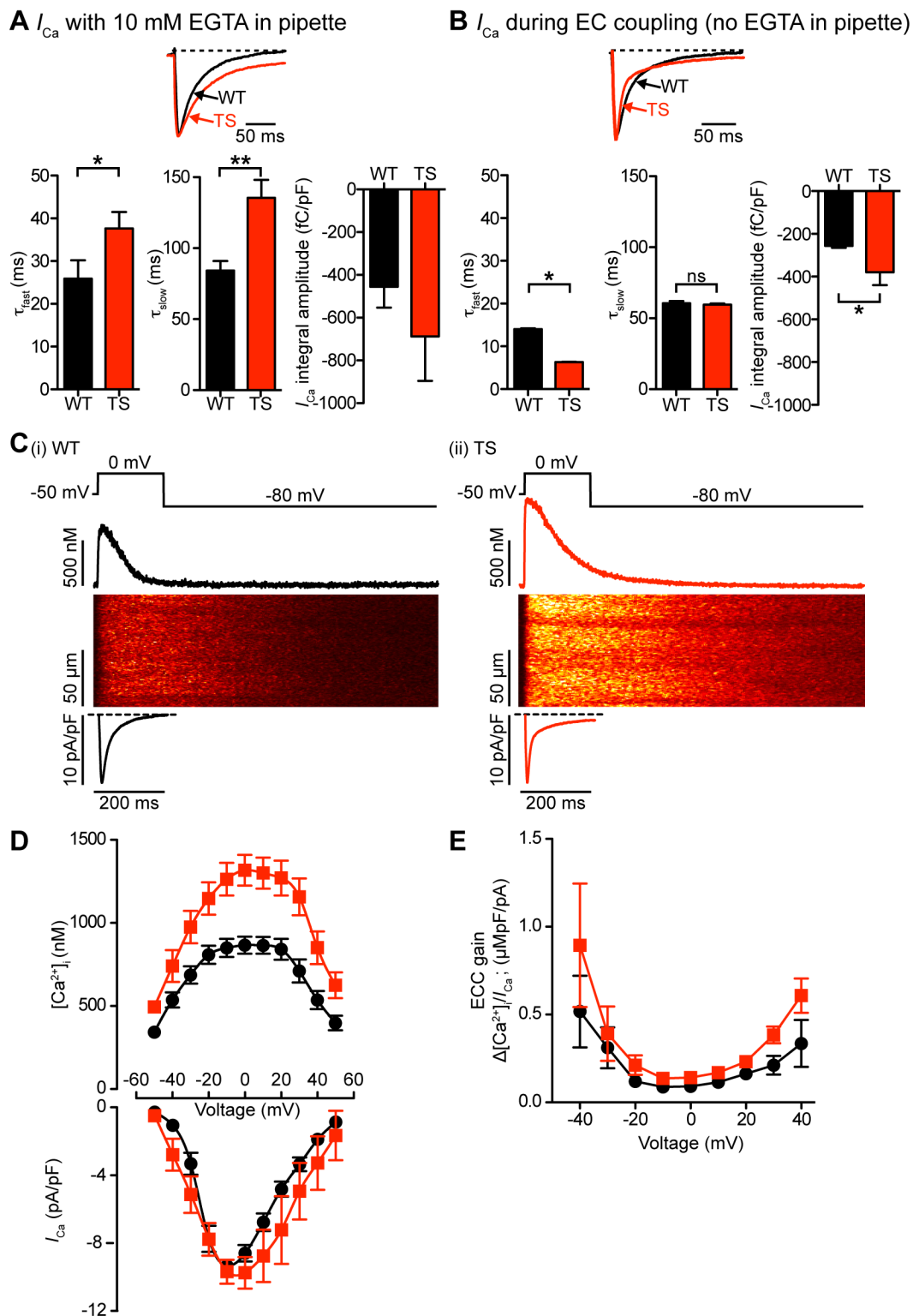


**Figure 2.6.** Higher SR  $Ca^{2+}$  release during EC coupling in TS cells increases the rate of inactivation of  $I_{Ca}$ .

**A-B**, representative  $I_{Ca}$  records normalized to peak from TS and WT myocytes dialyzed with an intracellular solution containing (**A**) or lacking (**B**) 10 mM of the  $Ca^{2+}$  chelator EGTA. Currents were evoked by a voltage step from -50 mV to 0 mV in the presence of 2 mM external  $Ca^{2+}$ . *Below*, bar plots of the mean  $\pm$  S.E.M. of the inactivation components of  $I_{Ca}$ :  $T_{fast}$  (ms),  $T_{slow}$  (ms), and current integral (fC/pF) in WT and TS myocytes. **C**, representative  $I_{Ca}$  and confocal line-scan images from WT (i) and TS (ii) cells.  $I_{Ca}$  and  $[Ca^{2+}]_i$  transients were evoked by a 200 ms voltage step from -50 to 0 mV. Traces showing the time course of  $I_{Ca}$  and  $[Ca^{2+}]_i$  in these cells are shown below and above the line-scan images, respectively. **D**, voltage dependence of the amplitude of the  $[Ca^{2+}]_i$  transient on positive y-axis, current-voltage relationship of  $I_{Ca}$  on negative y-axis, for both WT (*black*) and TS (*red*) cells. **E**, voltage dependence of EC coupling (ECC) gain for WT (*black*) and TS (*red*).

(amplitude of the caffeine-induced transient =  $1224 \pm 74$  nM) had a higher SR  $Ca^{2+}$  load than WT cells (amplitude of the caffeine-induced transient =  $828 \pm 59$  nM) when depolarized with a similar waveform ( $P < 0.05$ ). Test pulses began with a slow ramping depolarization (0.08 mV/ms) from -80 mV to -50 mV, where the cell was held for 50 ms to inactivate  $Na^+$  channels. In addition, to ensure no contaminating  $Na^+$  channel currents, 10  $\mu$ M tetrodotoxin was added to the perfusion solution. Cells were then depolarized for 200 ms from this interim holding potential to voltages ranging from -40 to +60 mV.

Although, on average, peak  $I_{Ca}$  density was similar in WT and TS cells, the  $[Ca^{2+}]_i$  transients these currents evoked were larger in TS ( $n = 7$ ) than in WT myocytes ( $n = 7$ ) at all voltages examined (Figure 6D;  $P < 0.05$ ). Consequently, EC coupling gain, defined here as the maximum change in  $[Ca^{2+}]_i$  divided by the peak  $I_{Ca}$  density at a given voltage, tended to be higher in TS than in WT cells over a broad range of voltages (Figure 6E).

Interestingly, with SR  $\text{Ca}^{2+}$  release enabled,  $I_{\text{Ca}}$  inactivated at a faster rate in TS than in WT cells. This was largely due to a faster first component in TS ( $\tau_{\text{fast}} = 6 \pm 1$  ms,  $n = 6$ ) than in WT cells ( $\tau_{\text{fast}} = 14 \pm 2$  ms,  $n = 5$ ;  $P < 0.05$ ), as  $\tau_{\text{slow}}$  was similar in these cells (WT =  $61 \pm 17$  ms,  $n = 5$  vs. TS =  $60 \pm 11$  ms,  $n = 6$ ;  $P > 0.05$ ). However, because TS cells had a larger non-inactivating component, total  $\text{Ca}^{2+}$  flux during the 200 ms pulse was  $\approx 1.5$ -fold higher in TS cells ( $-389 \pm 60$  fC/pF,  $n = 3$ ) than WT cells ( $-256 \pm 8$  fC/pF,  $n = 5$ ;  $P < 0.05$ ) (Figure 6B).

Taken together, the data in Figure 6 suggest that SR  $\text{Ca}^{2+}$  release and EC coupling gain are larger in TS than in WT myocytes. SR  $\text{Ca}^{2+}$  release has a profound impact on the kinetics of  $I_{\text{Ca}}$  in TS cells. In the absence of EC coupling  $I_{\text{Ca}}$  inactivates at a slower rate in TS than in WT myocytes. However, with SR  $\text{Ca}^{2+}$  release,  $I_{\text{Ca}}$  inactivates faster, but to a sustained current level in TS cells.

### 2.3.5. Differences in AP waveform amplify differences in $\text{Ca}^{2+}$ influx between TS and WT myocytes

Although the use of square voltage pulses to evoke  $I_{\text{Ca}}$  is convenient for technical and analytical purposes, they do not provide information on  $\text{Ca}^{2+}$  influx during the physiological AP. We used the AP clamp technique to test the hypothesis that  $\text{Ca}^{2+}$  influx is larger in TS than in WT myocytes during the AP. Myocytes were depolarized with a previously recorded WT or TS AP (Figure 7A). Figure 7B-C shows averaged AP-evoked  $\text{Ca}^{2+}$  current traces from WT and TS myocytes in the

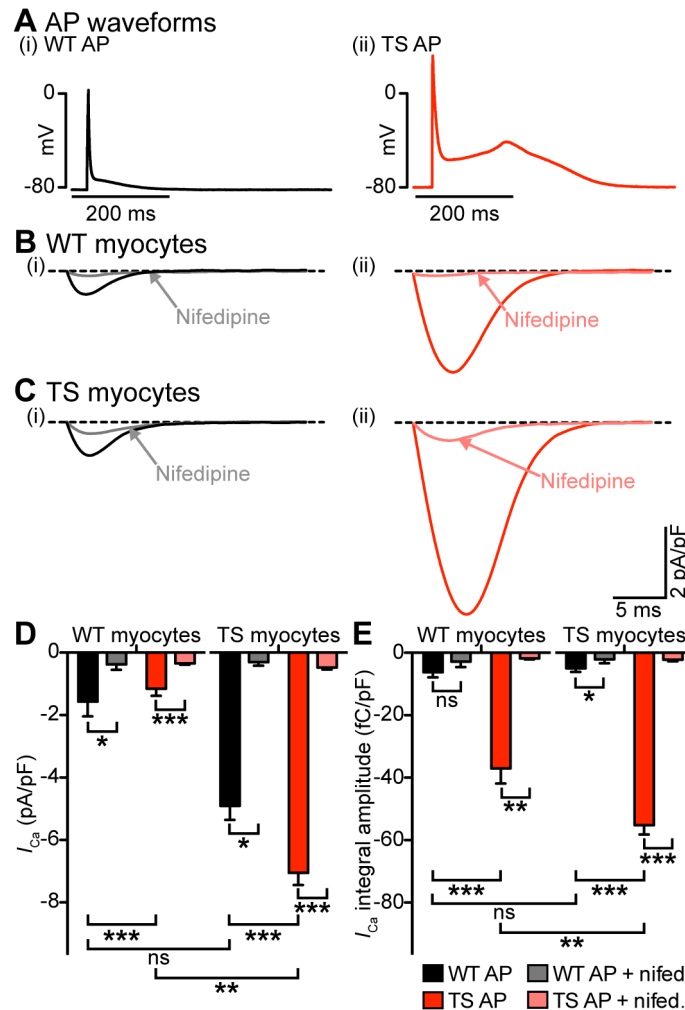


**Figure 2.7.** Differences in AP waveform contribute to differences in L-type  $Ca^{2+}$  current between WT and TS myocytes.

**A**, representative WT (i) and TS (ii) APs. **B-C** Current traces from a representative WT myocyte (**B**) and a TS myocyte (**C**) stimulated with the WT AP (i) or TS AP (ii). Traces recorded in the presence of 10  $\mu$ M nifedipine are labeled and indicated with arrows. **D-E**, bar plots of the mean  $\pm$  S.E.M. of the amplitude of  $I_{Ca}$  (**D**) and the current integral (**E**) in WT and TS myocytes stimulated with the WT or TS APs with and without 10  $\mu$ M nifedipine.

absence or presence of 10  $\mu$ M nifedipine. In WT cells, the TS AP evoked currents with a larger peak ( $-4.9 \pm 0.5$  pA/pF,  $n = 9$ ) and integral ( $-37.0 \pm 4.9$  fC/pF,  $n = 9$ ) than the WT AP (peak,  $-1.6 \pm 0.5$  pA/pF,  $n = 11$ ; integral,  $-6.2 \pm 1.7$  fC/pF,  $n = 11$ ;  $P < 0.001$ ) (Figure 7D-E). Similarly, in TS cells, the TS AP evoked

currents with a larger peak ( $-7.0 \pm 0.4$  pA/pF,  $n = 11$ ) and integral ( $-55.2 \pm 2.9$  fC/pF,  $n = 11$ ) than the WT AP (peak,  $-1.1 \pm 0.2$  pA/pF,  $n = 11$ ; integral,  $-5.0 \pm 1.2$  fC/pF,  $n = 11$ ;  $P < 0.001$ ). Interestingly, applying the TS AP evoked a greater response from TS myocytes ( $-55.2 \pm 2.9$  fC/pF,  $n = 11$ ) than WT myocytes ( $-37.0 \pm 4.9$  fC/pF,  $n = 9$ ;  $P < 0.01$ ) (Figure 7B-E). Strong reduction of these AP-evoked currents with 10  $\mu$ M nifedipine suggests that these currents are produced by  $\text{Ca}^{2+}$  influx via  $\text{Ca}_v1.2$  channels (Figure 7B-E). Importantly, these data suggest that both AP waveform and  $\text{Ca}_v1.2$ -TS gating properties contribute to the increase in  $I_{\text{Ca}}$  seen in TS.

#### 2.3.6. Differences in AP waveform contribute to differences in EC coupling between WT and TS cells

Next, we tested the hypothesis that differences in the AP waveform between WT and TS cells contribute to differences in  $[\text{Ca}^{2+}]_i$  between these cells. A testable prediction of this hypothesis is that if differences in  $[\text{Ca}^{2+}]_i$  between WT and TS cells were due exclusively to differences in AP waveform, then  $[\text{Ca}^{2+}]_i$  transients of WT cells stimulated with TS APs should resemble TS cells and vice versa. Thus, we recorded  $[\text{Ca}^{2+}]_i$  transients while using a AP clamp to again apply WT or TS AP waveforms.

Figure 8A-B shows a set of confocal line-scan images and  $[\text{Ca}^{2+}]_i$  transients from representative WT and TS cells depolarized with WT and TS APs. As expected, WT cells stimulated with a WT AP had smaller  $[\text{Ca}^{2+}]_i$  transients ( $717 \pm 35$  nM,  $n$

= 13) compared to TS cells stimulated with a TS AP ( $1144 \pm 35$  nM,  $n = 13$ ;  $P < 0.01$ ). In addition, we found that WT cells stimulated with TS APs had larger  $[Ca^{2+}]_i$  transients than when stimulated with WT APs, and TS cells stimulated with WT APs had smaller  $[Ca^{2+}]_i$  transients than when stimulated with TS APs. Interestingly, however, the amplitudes of these transients were not recapitulations of WT or TS cells. Rather, the  $[Ca^{2+}]_i$  transient of WT cells depolarized with a WT AP ( $717 \pm 35$  nM,  $n = 13$ ) was smaller in amplitude

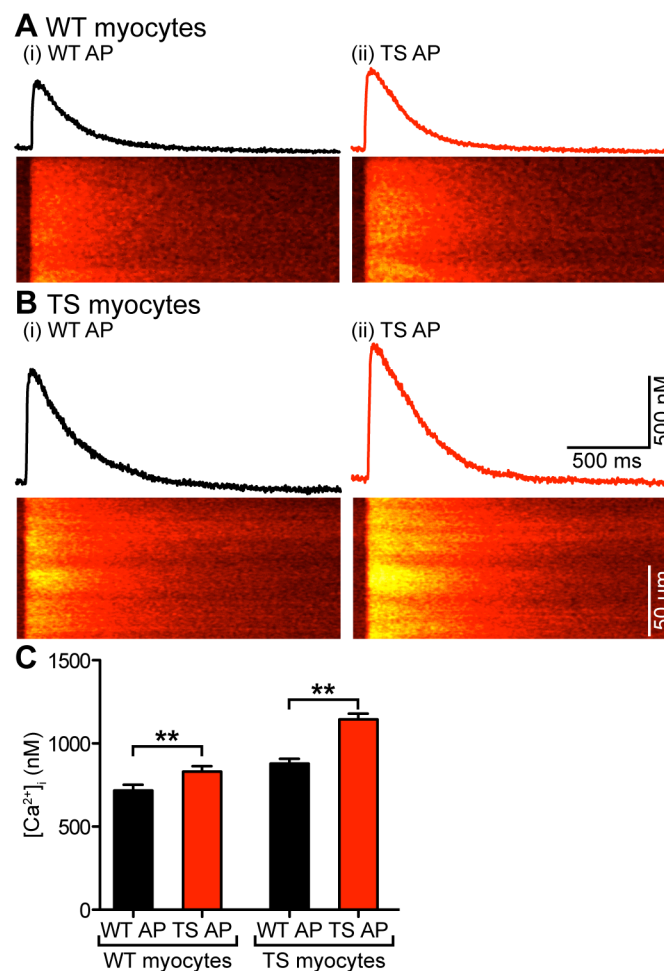


**Figure 2.8.** Differences in AP waveform contribute to differences in  $[Ca^{2+}]_i$  between WT and TS myocytes.

**A-B,**  $[Ca^{2+}]_i$  transients and confocal line-scan images from a representative WT (**A**) and TS myocyte (**B**) stimulated with the WT AP (i) or TS AP (ii). **C,** bar plot of

the mean  $\pm$  S.E.M. of the amplitude of the  $[Ca^{2+}]_i$  transient in WT and TS myocytes stimulated with the WT or TS APs.

compared to the  $[Ca^{2+}]_i$  transients of TS cells depolarized with a WT AP ( $878 \pm 29$  nM,  $n = 11$ ;  $P < 0.05$ ). Similarly, the  $[Ca^{2+}]_i$  transient of TS cells depolarized with a TS AP ( $1144 \pm 35$  nM,  $n = 13$ ) was larger in amplitude compared to the  $[Ca^{2+}]_i$  transients of WT cells depolarized with a TS AP ( $831 \pm 33$  nM,  $n = 13$ ;  $P < 0.05$ ) (Figure 8C). These data indicate that differences in AP waveform contribute to, but do not sufficiently account for the differences in  $[Ca^{2+}]_i$  transients observed between WT and TS cells.

## 2.4. Discussion

We performed a detailed biophysical analysis of the functional consequences of  $\text{Ca}_v1.2\text{-TS}$  channel expression on EC coupling in adult ventricular myocytes. On the basis of these data, we propose a mechanistic model for how  $\text{Ca}_v1.2\text{-TS}$  channels alter  $[\text{Ca}^{2+}]_i$  and EC coupling in ventricular myocytes. Our data indicate that expression of  $\text{Ca}_v1.2\text{-TS}$  increases resting and AP-evoked  $\text{Ca}^{2+}$  influx into ventricular myocytes. This is associated with an increase in diastolic  $[\text{Ca}^{2+}]_i$  and SR  $\text{Ca}^{2+}$  load that likely augments the frequency and amplitude of spontaneous  $\text{Ca}^{2+}$  sparks in TS cells. Accordingly, AP-evoked  $[\text{Ca}^{2+}]_i$  transients were larger in TS than in WT myocytes. Furthermore, we found that there is a non-linear relationship between the expression of  $\text{Ca}_v1.2\text{-TS}$  channel and  $\text{Ca}^{2+}$  wave frequency, suggesting that relatively low levels of  $\text{Ca}_v1.2\text{-TS}$  expression induces a disproportionately large increase in the probability of arrhythmogenic SR  $\text{Ca}^{2+}$  release events in ventricular myocytes.

The mouse model of TS we generated expresses WT  $\text{Ca}_v1.2$  channels and mutant  $\text{Ca}_v1.2$  channels with the glycine at position 406 substituted with an arginine, which promotes mode 2 gating of  $\text{Ca}_v1.2\text{-TS}$  channels (Erxleben, Liao et al. 2006). Recent studies suggest two potential mechanisms by which the G406R substitution alters  $\text{Ca}_v1.2\text{-TS}$  gating. Erxleben *et al.* (Erxleben, Liao et al. 2006) suggested that this G406R mutation creates a new phosphorylation site for the CaMKII. In their experiments in HEK293 cells, CaMKII was critical for mode 2

gating by  $\text{Ca}_v1.2$ -TS channels. Thiel *et al.* (Thiel, Chen *et al.* 2008) reached a similar conclusion using cultured ventricular myocytes. Others, however, suggest that phosphorylation by CaMKII may not be necessary for  $\text{Ca}_v1.2$ -TS channels to have a slower rate of inactivation than WT channels (Yarotsky, Gao *et al.* 2009, Cheng, Yuan *et al.* 2011).

Cheng *et al.* (Cheng, Yuan *et al.* 2011) proposed an alternative model for  $\text{Ca}_v1.2$ -TS channel dysfunction during Timothy syndrome. In this model, the anchoring protein AKAP150 and  $\text{Ca}_v1.2$ -TS form a complex that is necessary for aberrant  $\text{Ca}_v1.2$ -TS channel gating and arrhythmias.  $\text{Ca}_v1.2$ -TS channels likely interact with AKAP150 via leucine zipper motifs in the C-terminals of these proteins (Oliveria, Dell'Acqua *et al.* 2007). AKAP150 functions like an allosteric modulator of  $\text{Ca}_v1.2$ -TS channels, increasing  $\text{Ca}_v1.2$ -TS currents by stabilizing the open conformation (i.e., mode 2 gating) and increasing the probability of coupled gating between  $\text{Ca}_v1.2$ -TS channels (Shioya 2007, Navedo, Cheng *et al.* 2010, Cheng, Yuan *et al.* 2011). The longer openings of  $\text{Ca}_v1.2$ -TS channels are due, at least in part, to decreased voltage-dependent inactivation of these channels (Barrett and Tsien 2008). This leads to increased  $\text{Ca}^{2+}$  influx, AP prolongation, cardiac hypertrophy, and arrhythmias. Coupled gating of  $\text{Ca}_v1.2$ -TS channels presumably occurs because AKAP150 promotes physical interactions of adjacent channels via their C-tails (Oliveria, Dell'Acqua *et al.* 2007, Navedo, Cheng *et al.* 2010, Gold, Stengel *et al.* 2011). Thus, a combination of frequent, longer, and coupled openings of  $\text{Ca}_v1.2$ -TS channels increases  $\text{Ca}^{2+}$  influx even

with shorter APs. Furthermore, although increasing  $K^+$  channel conductance is likely to decrease  $Ca^{2+}$  influx, it may not be sufficient to eliminate the pathology.

Our data suggest that the impact of  $Ca_v1.2$ -TS channels on myocyte  $[Ca^{2+}]_i$  extends beyond the AP. Indeed, we found that resting and diastolic  $[Ca^{2+}]_i$  was higher in TS than in WT myocytes. In quiescent myocytes,  $[Ca^{2+}]_i$  is largely determined by the balance between  $Ca^{2+}$  extrusion and influx through the sarcolemma. The two primary pathways of  $Ca^{2+}$  influx are  $Ca_v1.2$  channels and the  $Na^+/Ca^{2+}$  exchanger (NCX) in its “reverse mode” of operation.  $Ca^{2+}$  is extruded by the NCX in its forward mode and, to a much lower extent, by the sarcolemmal  $Ca^{2+}$  pump (Bers, Bassani et al. 1993, Balke, Egan et al. 1994). Because at the diastolic potential of ventricular myocytes (-80 mV) the open probability of WT  $Ca_v1.2$  channels is very low,  $Ca^{2+}$  influx through these channels is also minimal. Consistent with this, we found that application of nifedipine does not alter resting  $[Ca^{2+}]_i$  in WT ventricular myocytes. However,  $Ca_v1.2$ -TS channels have a higher level of activity than WT channels even at diastolic membrane potentials (Navedo, Cheng et al. 2010, Cheng, Yuan et al. 2011). Accordingly, nifedipine-sensitive  $Ca^{2+}$  influx — presumably via  $Ca_v1.2$ -TS channels — contributes to higher resting  $[Ca^{2+}]_i$  in TS than in WT myocytes. Thus, while in WT myocytes resting  $[Ca^{2+}]_i$  is largely determined by the NCX and to a lesser extent the sarcolemmal  $Ca^{2+}$  pump, in TS cells  $Ca_v1.2$ -TS channels represent a new  $Ca^{2+}$  “leak” pathway at rest. Yet, our analysis indicate that this  $Ca^{2+}$  leak is likely due to a relatively low number of persistently open  $Ca_v1.2$ -TS

channels open at rest, as the rate of  $\text{Ca}^{2+}$  influx at these potentials is orders of magnitude lower than during the AP.

Our results show that the TS phenotype not only increases cytosolic  $[\text{Ca}^{2+}]$  directly via increased flux through TS channels, it also increases the SR load and causes the SR to be more leaky. As noted above, CaMKII signaling has been implicated in SR leak, has been found to be activated in TS (Maier, Zhang et al. 2003, Guo, Zhang et al. 2006, Thiel, Chen et al. 2008). Bradshaw *et al.* (Bradshaw, Kubota et al. 2003) found that CaMKII activation is relatively insensitive to resting  $[\text{Ca}^{2+}]$ . Indeed, they found that a  $[\text{Ca}^{2+}]_i \approx 3.2 \mu\text{M}$  is needed to activate 50% CaMKII *in vitro*. Consistent with this, the Bers group (Saucerman and Bers 2008, Song, Saucerman et al. 2008) found that the majority of CaMKII activation in ventricular myocytes was found in areas of local high  $[\text{Ca}^{2+}]_i$ , such as the dyadic cleft. Thus, we speculate that these high  $\text{Ca}^{2+}$  areas would be both more abundant and richer in  $\text{Ca}^{2+}$  in TS due to increased  $\text{Ca}^{2+}$  sparklets (Navedo, Cheng et al. 2010, Cheng, Yuan et al. 2011),  $\text{Ca}^{2+}$  spark activity, higher  $\text{Ca}^{2+}$  transients, and  $\text{Ca}^{2+}$  wave activity. CaMKII activation in these areas could further augment SR leak and increase mode 2 gating of TS and WT channels in TS cells, creating a feed-forward mechanism that could increase the probability of arrhythmogenic changes in  $\text{Ca}^{2+}$  signaling. Furthermore, it is intriguing to speculate that the seemingly contradictory reports (Yarotsky, Gao et al. 2009, Cheng, Yuan et al. 2011) on the role of CaMKII on  $\text{Ca}_v1.2$ -TS channel function

may reflect differences in local  $\text{Ca}^{2+}$  signaling and thus the activity of this kinase. Future experiments should examine this issue in detail.

Our data suggest that SR  $\text{Ca}^{2+}$  release had a profound impact on the kinetics of  $I_{\text{Ca}}$  in TS cells, greatly accelerating the rate of inactivation of this current. This is important because SR  $\text{Ca}^{2+}$  release increased CDI, limiting  $\text{Ca}^{2+}$  influx into TS myocytes. Because CDI is unaffected in TS channels (Barrett and Tsien 2008), the faster rate of inactivation is likely due to the faster CDI of WT and TS  $\text{Ca}_v1.2$  channels in TS cells. Note, however, that while  $I_{\text{Ca}}$  inactivates at a much lower rate in TS than in WT in the absence of EC coupling, with SR  $\text{Ca}^{2+}$  release enabled, TS  $I_{\text{Ca}}$  inactivates faster than WT cells, albeit to a higher sustained level. We propose that SR  $\text{Ca}^{2+}$  release forms part of a negative feedback mechanism that decreases  $\text{Ca}^{2+}$  influx in TS cells by increasing CDI of WT and TS  $\text{Ca}_v1.2$  channels.

An important observation in this study is that the relationship between the level of expression of  $\text{Ca}_v1.2$ -TS channels and the probability of  $\text{Ca}^{2+}$  wave occurrence was non-linear. This suggests that even low levels of these channels are sufficient to induce maximal changes in  $[\text{Ca}^{2+}]_i$ . A potential mechanism by which a relatively small number of  $\text{Ca}_v1.2$  channels could have a disproportionately large effect on  $[\text{Ca}^{2+}]_i$  was proposed by Dixon *et al.* (Dixon, Yuan *et al.* 2012), who found that  $\text{Ca}_v1.2$ -TS channels can physically interact with WT  $\text{Ca}_v1.2$  channels. When they do, WT channel activity increases to a level similar to that of TS

channels. In this context, even a small level of expression of functional TS channels could have a disproportionately large effect on  $\text{Ca}^{2+}$  influx by making adjoined WT channels function like TS channels. Fusion of channels increases  $I_{\text{Ca}}$  by increasing the open probability of adjoining channels. It is intriguing to speculate that in heterozygous humans expressing G406R  $\text{Ca}_v1.2$ -TS channels, where these channels account for only ~12% of  $\text{Ca}_v1.2$  channels, coupling of WT and TS channels amplifies  $\text{Ca}^{2+}$  influx and thus increases the probability of SR  $\text{Ca}^{2+}$  overload and arrhythmias (Splawski, Timothy et al. 2004).

Furthermore, the relationship between  $[\text{Ca}^{2+}]_i$  and  $\text{Ca}^{2+}$  overload has been well characterized and shown to be highly nonlinear. A two-fold increase in diastolic  $[\text{Ca}^{2+}]_i$  could lead to up to an 84-fold increase in pathological  $\text{Ca}^{2+}$  activity such as  $\text{Ca}^{2+}$  waves (Cheng, Lederer et al. 1996). This non-linear relationship between  $\text{Ca}_v1.2$ -TS expression and  $\text{Ca}^{2+}$  waves arises from an increase in basal  $[\text{Ca}^{2+}]_i$ , SR  $\text{Ca}^{2+}$  content, and  $\text{Ca}^{2+}$  spark properties such as frequency and amplitude as well as the non-linear combinatorics of these properties' influence (e.g., RyR  $\text{Ca}^{2+}$  sensitivity) on  $\text{Ca}^{2+}$  wave development. In line with these results, we have found that even low levels of TS expression lead to a  $\approx 1.4$ -fold increase in diastolic  $[\text{Ca}^{2+}]_i$ , a  $\approx 3$ -fold increase in  $\text{Ca}^{2+}$  spark frequency, and a  $\approx 10$ -fold increase in  $\text{Ca}^{2+}$  wave frequency. Furthermore, it is important to note that potential changes in the electrical properties of the TS cells (e.g., decreased inward rectifying  $\text{K}^+$  currents) could conspire with higher  $[\text{Ca}^{2+}]_i$  to increase the probability of arrhythmogenic voltage fluctuations in these cells.

To conclude,  $\text{Ca}_v1.2\text{-TS}$  channels exhibit greater  $\text{Ca}^{2+}$  flux, which increases  $[\text{Ca}^{2+}]$  in both the cytosol and the SR. This  $\text{Ca}^{2+}$ -overloaded state leads to increases in  $\text{Ca}^{2+}$  spark frequency and amplitude, AP-evoked  $[\text{Ca}^{2+}]_i$  transients, and probability of  $\text{Ca}^{2+}$  waves. The increase in  $\text{Ca}_v1.2\text{-TS}$   $\text{Ca}^{2+}$  flux also leads to increased SR  $\text{Ca}^{2+}$  load, thus increasing EC coupling gain. The non-linear relationship between  $\text{Ca}_v1.2\text{-TS}$  expression and  $\text{Ca}^{2+}$  waves shows that even low levels of  $\text{Ca}_v1.2\text{-TS}$  can induce dramatic effects on cell  $\text{Ca}^{2+}$  levels. These conditions combine to create a cell environment prone to arrhythmogenic spontaneous SR  $\text{Ca}^{2+}$  release.

## Chapter 3: Oxidative stress decreases microtubule growth and stability in ventricular myocytes

### 3. Summary

Microtubules (MTs) have many roles in ventricular myocytes, including structural stability, morphological integrity, and protein trafficking. However, despite their functional importance, dynamic MTs had never been visualized in living adult myocytes. Using adeno-associated viral vectors expressing the MT-associated protein plus end binding protein 3 (EB3) tagged with EGFP, we were able to perform live imaging and thus capture and quantify MT dynamics in ventricular myocytes in real time under physiological conditions. Super-resolution nanoscopy revealed that EB1 associated in puncta along the length of MTs in ventricular myocytes. The vast (~80%) majority of MTs grew perpendicular to T-tubules at a rate of  $0.06 \mu\text{m}\cdot\text{s}^{-1}$  and growth was preferentially (82%) confined to a single sarcomere. Microtubule catastrophe rate was lower near the Z-line than M-line. Hydrogen peroxide increased the rate of catastrophe of MTs ~7-fold, suggesting that oxidative stress destabilizes these structures in ventricular myocytes. We also quantified MT dynamics after myocardial infarction (MI), a pathological condition associated with increased production of reactive oxygen species (ROS). Our data indicate that the catastrophe rate of MTs increases following MI. This contributed to decreased transient outward  $\text{K}^+$  currents by decreasing the surface expression of  $\text{K}_v4.2$  and  $\text{K}_v4.3$  channels after MI. On the basis of these data, we conclude that, under physiological conditions, MT growth

is directionally biased and that increased ROS production during MI disrupts MT dynamics, decreasing K<sup>+</sup> channel trafficking.

### 3.1. Introduction

After conducting a thorough study on the machinery of calcium signaling and becoming interested in the close interaction of RyRs and  $Ca_v1.2$  channels, I turned my interest towards regulation and biogenesis of the cardiac dyad, that is, how the proteins in the dyad are trafficked and maintained in such precise geometry to ensure faithful EC coupling. These processes are dependent on microtubules and molecular motors.

Microtubules (MTs) are cytoskeletal fibers formed by the polymerization of  $\alpha\beta$  tubulin dimers. They have several functions in cellular processes, such as sustaining cell shape, mitosis, and intracellular trafficking of proteins (Gelfand and Bershadsky 1991). In mature non-differentiating ventricular myocytes, MTs cannot play a role in mitosis, but still maintain important functions in the cell (Kerfant, Vassort et al. 2001). MTs are dynamically active and switch between phases of growth and shrinking, a process called dynamic instability (Mitchison and Kirschner 1984). MT dynamics can be characterized by measuring the growth rate and shrinkage rate, as well as the frequency of catastrophe (i.e., the transition from growth to shrinkage) and rescue (i.e., the transition from shrinkage to growth) (Desai and Mitchison 1997). Although MTs have been visualized in fixed tissue, they have not been seen assembling in live cardiac myocytes.

Plus-end binding (EB) proteins constitute a unique group of structurally and functionally diverse proteins that target the plus ends of growing MTs. These proteins orchestrate MT growth and recruit MT regulators. EBs are also implicated in MT-based transport (Gu, Zhou et al. 2006, Shaw, Fay et al. 2007). EBs autonomously track growing MT ends and are involved in many MT-based processes (Akhmanova and Steinmetz 2008). Three EB (EB1-3) isoforms have been identified to date. Of these proteins, EB1 (30 kDa) has previously been identified as expressed in the heart (Zhang and Shaw 2013).

The formation of reactive oxidative species (ROS) has been implicated in disrupting MTs (Parker, Kavallaris et al. 2014). Hydrogen peroxide treatment depolymerizes and disorganizes MTs in human osteosarcoma 143B cells, rat pheochromocytoma PC-12 cells, AR42J pancreatic epithelial cells, and human umbilical cord vein endothelial HUVEC cells (Hinshaw, Miller et al. 1993, Valen, Sonden et al. 1999, Lee, Liu et al. 2005, Hu and Lu 2014). In addition, oxidative stress has been implicated in inducing MT disassembly in the setting of lung injury, resulting in pulmonary endothelial cell barrier dysfunction and increased inflammatory response (Kratzer, Tian et al. 2012). EB proteins are also disrupted during oxidative stress. Le Grand *et al* (Le Grand, Rovini et al. 2014) found that EB1 associates with MTs in a phosphorylation-dependent manner, which is affected by ROS. Smyth *et al* (Smyth, Hong et al. 2010) found that EB1 is displaced from MTs in oxidative stress, correlating with decreased surface connexin 43 expression in human and mouse cardiomyocytes. Lastly, Cartelli *et*

*al* (Cartelli, Ronchi et al. 2010) showed that increased ROS production caused reversals of EB3 comets and growth cone collapse in PC-12 cells.

Myocardial infarction (MI) occurs when a vascular occlusion reduces coronary blood flow, resulting in ischemia and necrosis (Diaz-Munoz, Alvarez-Perez et al. 2006). The prolonged hypoxia can lead to formation of free radicals and oxidative stress in cardiomyocytes (Hori and Nishida 2009). Post-infarction, myocytes can lose their structure and display abnormal protein expression, which could be a result of MT disruption (Iwai, Hori et al. 1990, Heling, Zimmermann et al. 2000). It has also been shown that tubulin levels are increased in hypertrophied and failing myocardium (Aquila-Pastir, DiPaola et al. 2002, Zhang, Chen et al. 2014). Finally, MT content is increased in pressure-overload cardiac hypertrophy, lending support to the idea that compensatory increases in MT density enhances the rigidity of ventricular myocytes in heart failure (Tsutsui, Ishihara et al. 1993, Tagawa, Koide et al. 1998). However, because these studies examined MT structure in fixed myocytes or used *in vitro* biochemical approaches, it is not known how MT dynamics change after MI, if oxidative stress might be implicated in these changes, and if these changes would have measurable physiological effects in the cell.

A set of key proteins, whose traffic to the membrane from the Golgi apparatus has been linked to MT movement, is the voltage-gated  $K_v4$  channels.  $K_v4.2$  and  $K_v4.3$  are the pore-forming subunits responsible for the transient outward  $K^+$

current ( $I_{to}$ ). There is evidence that  $K_{V4.2}$  and  $K_{V4.3}$  are trafficked to the membrane via kinesin-2 (Kif17) and that interrupting dynein function can also alter expression of these channels (Chu, Rivera et al. 2006, Loewen, Wang et al. 2009). Previous research has shown that  $I_{to}$  is markedly reduced after MI and in hypertrophied hearts, leading to changes in action potential waveform in failing cardiomyocytes (Nabauer, Beuckelmann et al. 1993, Wagner, Goltz et al. 2007). At present, however, it is unclear if alterations in MTs during MI are implicated in the change in  $K_{V4.2}$  and  $K_{V4.3}$  expression seen after MI.

In this report, we take a direct approach to MT cardiac physiology. Confocal imaging showed that EB1 was localized on the Z-lines as well as along the length of MTs. Furthermore, using super-resolution nanoscopy, we found that the protein EB1 expresses along MTs in a punctate pattern. We quantified MT dynamics and found that MT growth was temperature dependent. Interestingly, most MTs assembled from one end of the sarcomere to the other. Under control conditions, MT catastrophe rate was low and occurred mostly near the M-line. We found that MT dynamics are severely disrupted in MI, and that this disruption is due to the increase in oxidative stress in the cellular environment. Furthermore, we find that this disruption on MT physiology results in  $I_{to}$  and  $K_{V4.2}$  and  $K_{V4.3}$  density reduction, thus increasing action potential length after infarction.

## 3.2. Materials and methods

### 3.2.1. Isolation of mouse ventricular myocytes

Mice were euthanized with a lethal dose of sodium pentobarbital administered intra-peritoneally as approved by the University of Washington Institutional Animal Care and Use Committee. Ventricular myocytes were isolated using a Langendorff perfusion apparatus as previously described (Drum, Dixon et al. 2014). The isolated ventricular myocytes were kept either at room temperature (22 °C) or at 37 °C in Tyrode's solution containing (mM): 140 NaCl, 5 KCl, 10 HEPES, 10 glucose, 2 CaCl<sub>2</sub>, and 1 MgCl<sub>2</sub>; pH = 7.4 with NaOH, and used 0.5–8 h after isolation.

### 3.2.2. Myocardial infarction

The myocardial infarction model was produced as described previously (Kolk, Meyberg et al. 2009). Briefly, mice were anesthetized by isoflurane and non-invasively intubated. A left lateral thoracotomy was performed to expose the heart and the associated vasculature. The left ascending coronary artery was permanently ligated with a silk ligature and the thoracotomy was then closed. The infarct was obvious upon gross examination and myocytes were isolated from the left ventricle 48-72 h after the procedure.

### 3.2.3. Real Time qRT-PCR

For this study, EB1 and EB3 mRNA was quantified using real time quantitative RT-PCR as previously described (Amberg, Bonev et al. 2003, Amberg and Santana 2003). Total RNA was purified from mouse left ventricle, brain, or isolated cardiomyocytes using TRIzol reagent (Invitrogen, Waltham, MA) and RNeasy Mini Kit (Qiagen). The RNA was reverse transcribed using Super Script III First-Strand Synthesis System (Invitrogen). qPCR was used to confirm the expression of EB1 and EB3. EB1 and EB3 qPCR primers were ordered from Qiagen (EB1 Cat. No. QT01169189, EB3 Cat. No. QT00168224) and compared using GAPDH (QT01658692) as a reference. The same procedure was used with tubulin (QT01060311), Kif2a (QT00174993), Katna1 (QT00107296), Kif18b (QT00115178), and Kif2c (Cat. No. QT00148708) to determine expression levels in the left ventricle and in isolated cardiomyocytes after infarction using GAPDH (QT01658692) as a reference.

### 3.2.4. Viral expression system

In order to better probe cellular protein dynamics, we needed to fluorescently image proteins to see them real time in living cells. Traditionally, this would be accomplished by transfecting cultured cells with a virus, usually lentivirus, adenovirus, or adeno-associated virus, which has been engineered to express the protein of interest with a fluorescent tag. This virus would infect the cells and

thus enable imaging. However, mouse myocytes cannot be successfully cultured because they lose their structure and T-tubules soon after plating. Thus, we needed to develop a method in order to expose myocytes to virus in live animals. Previous work has shown that the serotype AAV9 displays robust, efficient cardiac gene transfer in mice (Inagaki, Fuess et al. 2006, Bish, Morine et al. 2008). Mice were injected retro-orbitally with AAV9 constructs and then myocytes were isolated 4 weeks after injection to allow time for viral infection. We generated the following viruses: AAV9-TRD-AGFP; AAV9-ER-TRFP; AAV9-Kif5B-DN-RFP; AAV9-Dynch1h1-shRNA-RFP; AAV9- $\beta_2$ -AGFP; AAV9-EB3-GFP; AAV9-EB3-mCherry.

By using a variety of fluorescent tags, we were able to image multiple proteins in the same cell, such as AAV9-TRD-AGFP and AAV8-Kif5B-DN-RFP. We were also able to use calcium imaging dyes and oxidative stress indicators with our viruses to yield more information about these proteins.

For these experiments, adeno-associated virus serotype 9 (AAV9) expressing EB3-EGFP was generated by Vector Biolabs. Mice were anesthetized by isoflurane and injected retro-orbitally with AAV9 encoding the protein EB3 tagged with EGFP (AAV9-EB3-EGFP) (Inagaki, Fuess et al. 2006, Bish, Morine et al. 2008). To allow expression of the protein, experiments were performed at least 3 weeks after virus injection.

### 3.2.5. Immunocytochemistry and imaging

Ventricular myocytes were imaged using an Olympus FluoView 1000 confocal microscope equipped with an Olympus 60x (NA = 1.49) oil immersion lens (Drum, Dixon et al. 2014). Super-resolution imaging was performed as described previously (Mercado, Baylie et al. 2014, Dixon, Moreno et al. 2015). Briefly, cardiomyocytes were fixed by incubating in 4% paraformaldehyde in PBS at 37 °C for 30 m, then washed with PBS and blocked for 1 h at room temperature in 50% SEA BLOCK (Thermo Fisher Scientific Waltham, MA) and 0.5% w/v Triton X-100 in PBS (blocking buffer). MTs were probed with a rat (Harlan, Indianapolis, IN, MAS 077) or mouse (Sigma, St. Louis, MO, T-9026) anti-tubulin antibody and mouse anti-EB1 antibody (BD transduction, San Jose, CA, 610534) or rat anti-EB3 antibody (Abcam, Cambridge, UK, ab53360) diluted to 1 µg/mL in blocking buffer by incubating overnight at 4 °C. Cells were washed extensively with 20% Sea Block three times. Cells were then incubated for 1 h at room temperature with donkey anti-rat Alexa Fluor 647 and goat anti-mouse Alexa Fluor 568 in blocking buffer. Myocytes were washed with 20% Sea Block three times and then mounted for imaging.

For immunocytochemistry, cells were mounted with PBS and sealed with nail polish. For super-resolution, the cells were mounted with imaging buffer containing: MEA-GLOX (MEA is cysteamine, GLOX is 0.56 mg/mL glucose oxidase, 34 µg/mL catalase, 10% w/v glucose), TN buffer (50 mM Tris pH 8.0, 10

mM NaCl). Slides were sealed with Twinsil (Picodent, Wipperfürth, Germany) sealant.

GSD is a new microscopy technique which allows visualization below the diffraction limit of conventional confocal microscopy. In order to thoroughly explain its theory, one must first understand conventional microscopy methods. Wide-field microscopy is the most basic system of visualization. In wide-field microscopy, the entire sample is flooded evenly with light. Because all parts of the sample are excited at the same time, the measured fluorescence includes not just the part of the sample in focus but also all of the fluorescence from the unfocused sections of the sample. Thus, there is a large background component to the image which limits the clarity of the image. Improvements in visualization were needed to limit the amount of background fluorescence. In confocal microscopy, a pinhole was used to eliminate the amount of the sample that was excited by the light source. As a result, only light produced by fluorescence very close to the focal plane could be detected. One disadvantage of the pinhole was that, due to the decrease in illumination, the image also had decreased signal intensity. As a result, longer exposures were required to create an image. However, the optical sectioning allowed by the pinhole greatly enhanced image resolution. The confocal microscopes used on cardiomyocytes are laser-scanning, in which a laser is focused by an objective lens into a small focal volume on the surface of the sample through a pinhole. The laser excites electrons, which then release photons as they transition back to the ground state.

The light intensity is detected by a photomultiplier tube, which transforms the light into an electrical signal which can be read by the computer. This electron cycling occurs within nanoseconds; however, the image is acquired in the time scale of milliseconds. Thus, many photons are captured in every image acquisition and all the overlap of the photons is seen at once. The limit to resolution, thus, became the diffraction of light, the slight bending of light as it passes around the edge of an object. The limitations of diffraction vary based on the size of the objective and the inverse of the wavelength ( $\lambda$ ) of the light being observed, but the lower limit of resolution corresponded to  $\lambda$  divided by 2, which is about 200-250 nm.

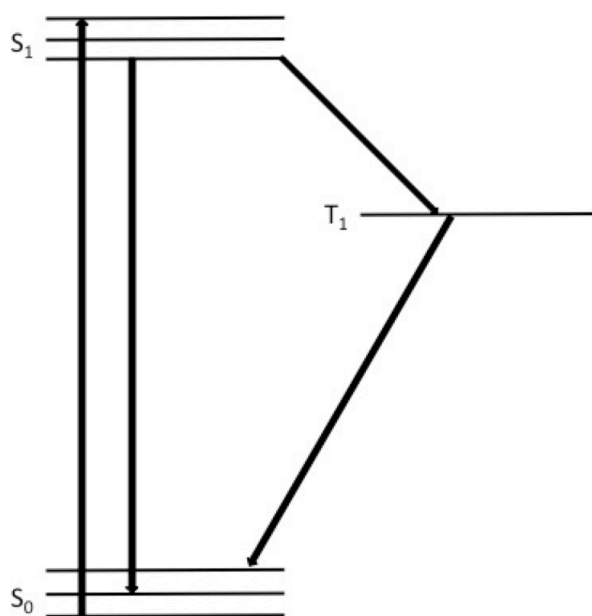


**Figure 3.1.** Jablonski diagram illustrating ground state depletion.

$S_0$  are the ground states,  $S_1$  are the first singlet states, and  $T_1$  is the triplet/dark state.

GSD was first theorized in 1995, but was not practically invented until 2007 (Hell and Kroug 1995, Bretschneider, Eggeling et al. 2007). In GSD microscopy,

resolution is improved by limiting the amount of overlapping signals. Instead of simply moving the electrons between singlet/excited and ground states, GSD pushes the electrons into another state, called the triplet or dark state (See Figure 3.1). Because the electrons must spin-flip to enter this dark state, it is conventionally a rare occurrence. However, in GSD the laser is very strong and pushes electrons into the dark state where they are hidden. This state is stable and electrons stay in the dark state for seconds before returning to the ground state. Once an electron escapes the dark state, it is free to cycle between excited and ground states as before. In GSD, only a few electrons at a time leave the dark state to cycle, thus eliminating the overlap of signal seen in confocal laser scanning microscopy. As expected, because of the delay in electrons leaving the dark state and only recording from a few electrons at a given time, these images take a longer time to acquire, usually 5-10 minutes. But they give a resolution up to 20 nm, far exceeding the resolution of diffraction-limited images. These images serve as maps, giving precise locations of where proteins are localized in cells.

GSD super-resolution images of MTs and EB1 in fixed ventricular myocytes were generated with a Leica SR GSD 3D system consisting of a Leica DMI6000 B TIRF microscope equipped with a Leica oil-immersion HC PL APO 160x (NA = 1.43) objective, four laser lines (405 nm/30 mW, 488 nm/300 mW, 532 nm/500mW, and 642 nm/600mW), and an Andor iXon3 EM-OCD. Images were

collected in TIRF mode with a 100 Hz frame rate for 20,000-100,000 frames using Leica Application Suite (LAS AF) software.

### 3.2.6. Fluorescent indicators

Some myocytes were loaded with 10  $\mu$ M di8-ANEPPS (ThermoFisher) to label the location of T-tubules. In other experiments, myocytes were exposed to various concentrations of hydrogen peroxide ( $H_2O_2$ ) while being imaged for EB3-EGFP movement or incubated for Western Blot protein expression experiments. To quantify oxidative stress, myocytes were loaded with 5  $\mu$ M MitoSox-Red (ThermoFisher), a fluorescent indicator that localizes to the mitochondria and increases in fluorescence in response to oxidative species (e.g., superoxide,  $H_2O_2$ ). We excited the indicator at 510 nm to yield a uniform signal assaying intracellular ROS (Zielonk, Vasquez-Vivar et al. 2008, Kalyanaraman, Darley-Usmar et al. 2012).

### 3.2.7. Image analysis

Colocalization was analyzed using the ImageJ plugin “JaCoP” after applying a threshold to eliminate noise. MT diameter data was generated on ImageJ by drawing a line perpendicular to the MT signal in an area where there was clear background signal on both sides and measuring the width of the signal. Each MT was measured 5 times and averaged to give an accurate measurement.

Each cell was scanned in the z-axis and recorded at a plane where the predominant number of MTs could be seen and tracked, usually in the midsection of the cell. MTs were tracked manually by generating a kymograph for each MT with strict parameters. For readers not familiar with this, kymographs can be conceptualized as an x-t scan, where the intensity along a given line is plotted for all images of a stack. We constructed kymographs by tracing the path of an MT throughout the image stack to form the x-axis of the kymograph image. The lines are then stacked along the y-axis for all frames in the image stack. In this paradigm, a growing MT will appear as a line oriented downward and to the right and a shrinking MT will appear as a line oriented downward and to the left. A catastrophe would be seen as a left facing angle ( $>$ ) and a rescue is seen as a right facing angle ( $<$ ). A pause is visualized as a vertical line.

Growth and shrinkage were evaluated only in linear circumstances ( $R^2 < 0.85$  in linear regression analysis) as seen in many other studies (Tirnauer, O'Toole et al. 1999, Kosco, Pearson et al. 2001, Tanaka, Kitamura et al. 2007). MT pause was characterized by a MT tip moving less than  $0.5 \mu\text{m}$  in 30 s (Kline-Smith and Walczak 2002). Catastrophe and rescue were counted if: (1) they persisted for more than 15 s; (2) clear growth, shrinkage, or pause could be seen surrounding the event; and (3) movement exceeded that of pausing conditions. MTs were analyzed blind to experimental condition via name randomization (Labbe, Maddox et al. 2003, Peris, Wagenbach et al. 2009). EB3-monitored dynamics

was measured by counting the number of EB3-marked MTs in a given cell area, corrected for photobleaching using the Histogram Matching feature of Photocorrection in ImageJ (Montenegro Gouveia, Leslie et al. 2010).

### 3.2.8. Immunoprecipitation Western blotting

Protein expression for Kif2c was determined by Western blot, performed as previously described (Cheng, Yuan et al. 2011). Briefly, proteins were extracted from control and MI mice left ventricle or cardiomyocytes and run on SDS-PAGE. To check Kif2c expression in cardiomyocytes, we immunoprecipitated Kif2c with Kif2c antibody in order to maximize possibility of seeing a band as the initial Western blot did not reveal protein expression. IgG was used as a negative control and testis tissue was used as a positive control. Cardiomyocyte protein lysates were incubated with anti-Kif2c antibody at 4°C for 2 hours and protein-antibody complexes were precipitated with protein-A/G-coupled agarose beads (Santa Cruz Biotech, Dallas, TX) at 4°C for overnight. The agarose beads were washed 4 times with IP-buffer and proteins were eluted by incubation at 100°C for 10 min in 2 × Laemmli sample buffer (Bio-Rad, Hercules, CA) supplemented with 5% 2-mercaptoethanol. The supernatants were then run on SDS-PAGE and proteins were transferred to PVDF membranes. After blocking with 5% normal donkey serum (Jackson ImmunoResearch, West Grove, PA), membranes were probed with anti-Kif2c primary antibody (Novus Biologicals, Littleton, CO, cat# NB100-2588) at room temperature for 2 h, followed by incubation with donkey

anti-rabbit IgG alkaline phosphatase conjugated secondary antibody (Jackson ImmunoResearch) at room temperature for 1 h. The blots were developed with ECF (Amersham Biosciences, Piscataway, NJ) and imaged with Bio-Rad ChemiDoc XRS+ system.

### 3.2.9. Electrophysiology

Cells were kept at 37 °C during the day of the experiment. All electrophysiological recordings were performed while cells were superfused with saline solutions  $\approx$ 37 °C. Pipettes were pulled using a Flaming-Brown type puller (Sutter Instruments, Novato, CA) with nominal resistance of 1-2 M $\Omega$  and filled with solutions as described below.

To record  $I_{to}$ , membrane potential was controlled via the patch-clamp technique using an Axopatch 200B amplifier (Molecular Devices, Sunnyvale, CA). Data were acquired at 10 kHz and low-pass filtered at 2 kHz. Myocytes were perfused with Tyrode's solution while patched. After a G $\Omega$  seal was formed, a small amount of negative pressure was applied through the pipette to break the membrane and achieve a whole cell configuration. Once whole-cell configuration was successfully established in myocytes perfused with Tyrode's solution, the extracellular solution was exchanged for one with the following constituents (mM): 140 N-methyl-D-glucamine, 5.5 KCl, 10 HEPES, 0.1 CaCl<sub>2</sub>, 2 MgCl<sub>2</sub>, and 10 glucose; pH 7.4 with HCl. The pipette solution used in these experiments

contained (mM): 110 K-aspartate, 30 KCl, 10 HEPES, 5 EGTA, and 4 Mg-ATP; pH 7.3. Cells were dialyzed with this solution. After a 100ms step to -50 mV to inactivate voltage-gated Na<sup>+</sup> channels,  $I_{to}$  was evoked by 2 s long depolarization pulses from -70 mV to potentials ranging from -70 to +80 mV (10 mV increment).

#### 3.2.10. Surface biotinylation

Surface biotinylation was performed using a protocol adapted from Huang *et al* (Huang, Zeng et al. 2006). Briefly, cells were incubated with external control, colchicine, or H<sub>2</sub>O<sub>2</sub> treatment for 4 h. After treatment, cells were exposed to 1 mg/mL of EZ-link sulfo-NHS-LC-LC-biotin (ThermoScientific) and incubated at room temperature for 30 m. Cells were washed with PBS + 100 mM glycine three times, then lysed using CHAPS lysis & IP buffer (FIVEphoton Biochemicals, San Diego, CA) with protease (Roche, Risch-Rotkreuz, Switzerland), sonicated, and centrifuged at 4 °C for 10 min. Total protein concentrations were determined and normalized between samples. Supernatant was mixed with immobilized Neutraavidin beads (ThermoScientific) and rotated at 4 °C overnight. Beads were washed with 4 °C PBS 3 times and then combined with 2x Laemmli sample loading buffer (Bio-Rad) supplemented with 5% 2-mercaptoethanol. Beads were incubated for 10 m at 65 °C to elute proteins. Eluted proteins were then run on a 4-15% TGX precast gradient gel (Bio-Rad) and then electrophoresed proteins were transferred to a PVDF membrane. The membrane was blocked with 10% skim milk in TBST, then stained with K<sub>v</sub>4.2 & K<sub>v</sub>4.3 anti-rabbit primary antibody

(Santa Cruz, Cat. No. sc-28634) in TBST with 1% BSA followed by goat anti-rabbit secondary antibody (Santa Cruz, Cat. No. sc-2057) in 5% skim milk in TBST before exposure.

### 3.2.11. Statistics

Data are presented as mean  $\pm$  standard error of the mean (S.E.M.). Two-sample comparisons were made using a Student's *t* test (\* $P < 0.05$ , \*\* $0.001 < P \leq 0.01$ , \*\* $P \leq 0.001$ ).

### 3.3. Results

#### 3.3.1. EB1 and tubulin co-localize in cardiomyocytes

We began our study by determining the level of expression of EB1 and EB3 transcript in ventricular myocytes using quantitative real time PCR (qRT-PCR). This analysis revealed that both of these genes were expressed in ventricular myocytes using GAPDH as a standard. However, EB1 was expressed to a larger extent than EB3 in heart. Expression in brain tissue was used for comparison (Figure 3.2A-B). These data suggest that EB1 is the predominant MT plus end binding protein in heart.

Thus, we investigated the spatial distribution of EB1 in ventricular myocytes using confocal and super-resolution microscopy. Figure 3.1C shows a confocal image of a ventricular myocyte labeled with EB1 (green) and tubulin-specific antibodies. Tubulin-associated fluorescence was located in tubules in the cytosol of the cell. Most MTs ran along the longitudinal axis of the cell. Figure 3.2D shows periodicity to the EB1 signal at intervals of  $\approx 2 \mu\text{m}$ , suggesting a relationship to the Z-lines. We determined the Pearson's coefficient of EB1 and tubulin fluorescence signals (the merged image in Figure 3.2C) to provide a quantitative analysis of the degree of overlap between these two proteins. The Pearson co-efficient ranges from 0 (for non co-localized) to 1 (for fully co-localized) fluorescent signals. Indeed, we found that the Pearson's coefficient

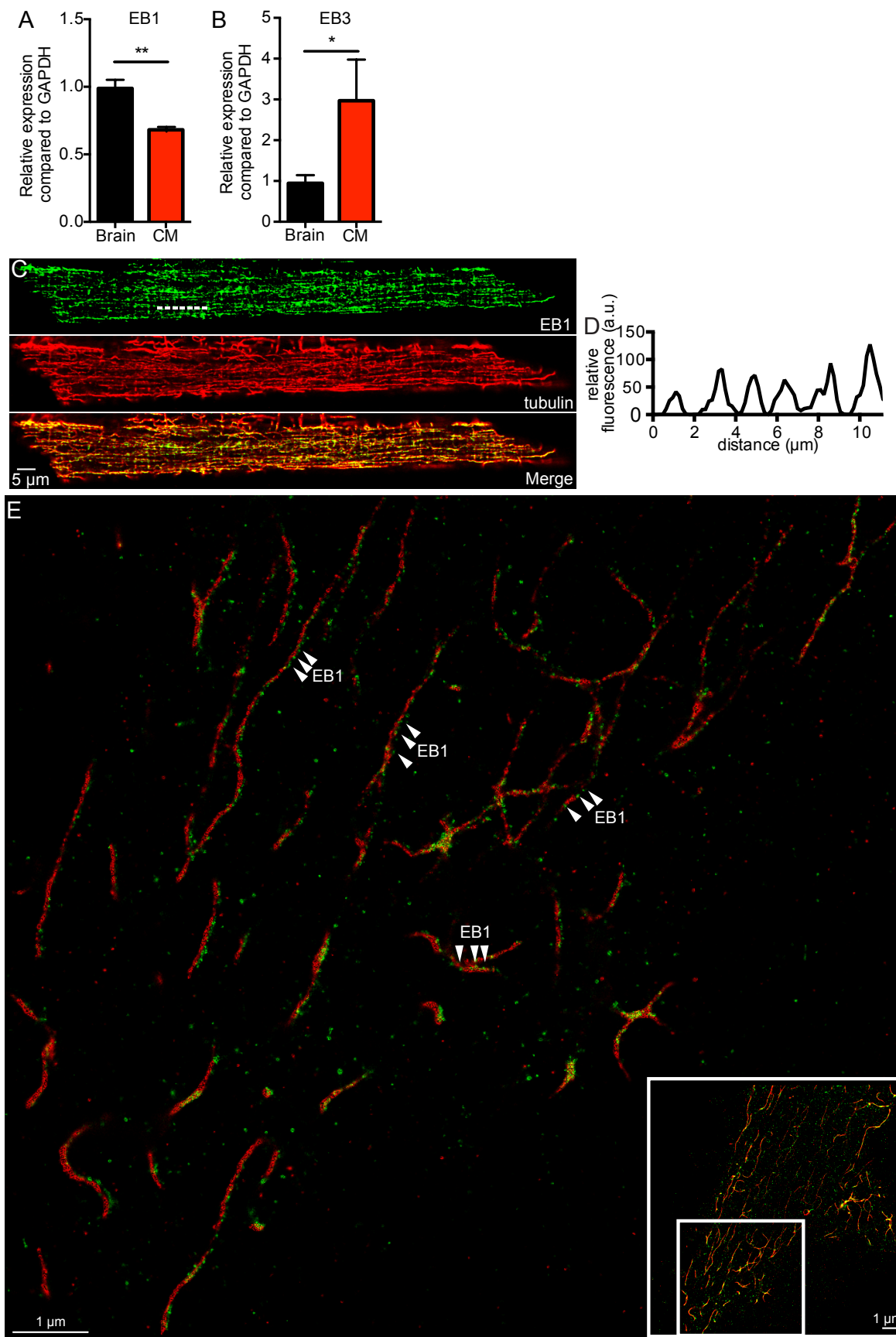


**Figure 3.2.** EB1 and tubulin co-localize in punctate pattern in ventricular myocytes.

**A**, bar plot of the mean  $\pm$  S.E.M. of relative real time qRT-PCR expression compared to GAPDH of EB1 in brain (*black*) and ventricular myocytes (*red*). **B**, bar plot of the mean  $\pm$  S.E.M. of relative real time qRT-PCR expression compared to GAPDH of EB3 in brain (*black*) and cardiomyocytes (*red*). **C**, representative confocal image of a myocyte showing EB1 imaged with EGFP (*green*), tubulin imaged with RFP (*red*), and both signals merged, scale bar = 5  $\mu$  m. **D**, fluorescent line profile of dashed line shown in EB1 signal of **C**, indicating Z-line periodicity. **E**, zoomed-in section of representative super-resolution image of myocyte showing tubulin stained with Alexa647 (*red*) and EB1 stained with Alexa568 (*green*) via a dual-antibody staining, scale bar = 1  $\mu$ m. Arrowheads highlight prominent areas of punctate staining. Inset shows location of zoomed-in section in relation to full image, scale bar = 1  $\mu$ m.

between EB1 and tubulin was  $0.8 \pm 0.1$  ( $n = 5$ ), indicating that at the level of resolution of our confocal microscope ( $\sim 250$  nm) these two proteins have a high degree of co-localization in ventricular myocytes, as most EB1 can be found along the length of the MTs.

We used ground state depletion (GSD) nanoscopy of EB1 and tubulin to obtain higher resolution maps of the localization of these proteins in ventricular myocytes. The resolution of the super-resolution GSD microscope is  $\sim 30$  nm. Figure 3.2E shows a representative super-resolution localization map of tubulin (red) and EB1 (green) in a section of a ventricular myocyte. The inset shows the full image as well as the location of the zoomed in region. We detected a punctate pattern of EB1 localization along the MT lattice. We saw a similar expression profile and co-localization with tubulin when imaging endogenous EB3 using our super-resolution system (Figure 3.3). The diameter of these MTs was  $42.0 \pm 2.8$  nm ( $n = 9$ ). We calculate that our primary and secondary antibody

staining system on average adds about 17 nm to our measurements, which means that we imaged MTs to be ~25 nm thick, which is consistent with the literature (Vaughan, Jia et al. 2012).

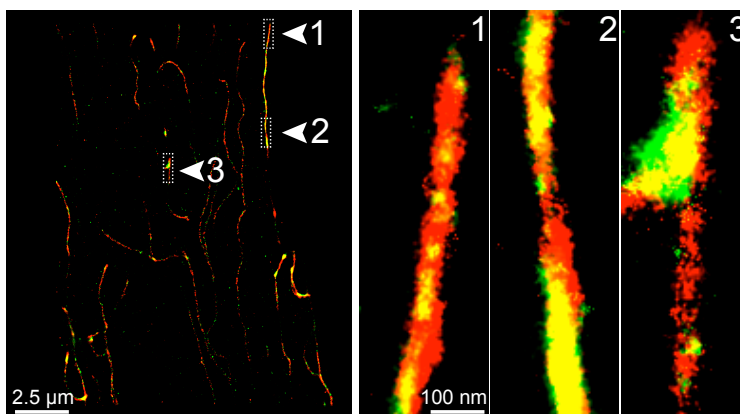


**Figure 3.3.** EB3 and tubulin colocalize under super-resolution.

A representative super-resolution image of a myocyte showing tubulin stained with Alexa647 (*red*) and EB3 stained with Alexa568 (*green*) via a dual-antibody staining, scale bar = 2.5  $\mu\text{m}$ . Arrowheads highlight prominent areas of colocalized staining. Zoomed-in images of areas indicated by arrowheads shown on right, scale bar = 100 nm

### 3.3.2. Live imaging of MTs in ventricular myocytes

Having shown that EB1 is expressed in small puncta along MTs in ventricular myocytes, we investigated MT dynamics in these cells. Although EB1 is more prevalent in the heart and better for native protein fixed cell imaging, we chose to use EB3 for our viral vector expression system because it is functionally similar to EB1 and because it is widely regarded to be superior in live imaging studies (Sironi, Solon et al. 2011).

We generated an AAV9-EB3-EGFP viral vector and injected it retro-orbitally into live mice, allowing sufficient time for the virus to infect live ventricular myocytes before isolating cells. In addition to labeling the MT ends and lattice, we also saw the presence of bands oriented transversely along the cell (Figure 3A). These bands were periodic in nature at  $\approx 2 \mu\text{m}$  apart. In order to determine their relation to the sarcomere, we stained myocytes with di8-ANEPPS, a marker of T-tubules. The di8-ANEPPS signal and EB3-EGFP bands co-localize perfectly, showing that cytoplasmically expressed EB3 also localizes to the T-tubules/Z-lines.

In addition to being localized to the T-tubules/Z-lines, the EB3-EGFP protein also labeled MT ends, enabling us to image MTs in acutely dissociated adult ventricular myocytes. We used these data to analyze MT tip translocation, and thus MT dynamics, by recording 2D images of the cell at a frequency of 1 frame every  $\approx 5\text{-}10$  s and creating kymographs. Kymographs like the ones shown in Figure 2B were generated from the image stack (Figure 3A).

Figure 2B shows two kymographs from a representative myocyte showing MT growth at 22 (top) and physiological 37 °C (bottom). Labels show areas of growth, shrinkage, pause, rescue, and catastrophe. At 22 °C, this MT grew at a rate that ranged from  $0.01\text{-}0.02 \mu\text{m}\cdot\text{s}^{-1}$ . There was one rescue event in this MT kymograph. The MT we recorded at 37 °C had a much higher rate of growth ( $0.08 \mu\text{m}\cdot\text{s}^{-1}$ ) than the one recorded at 22 °C.

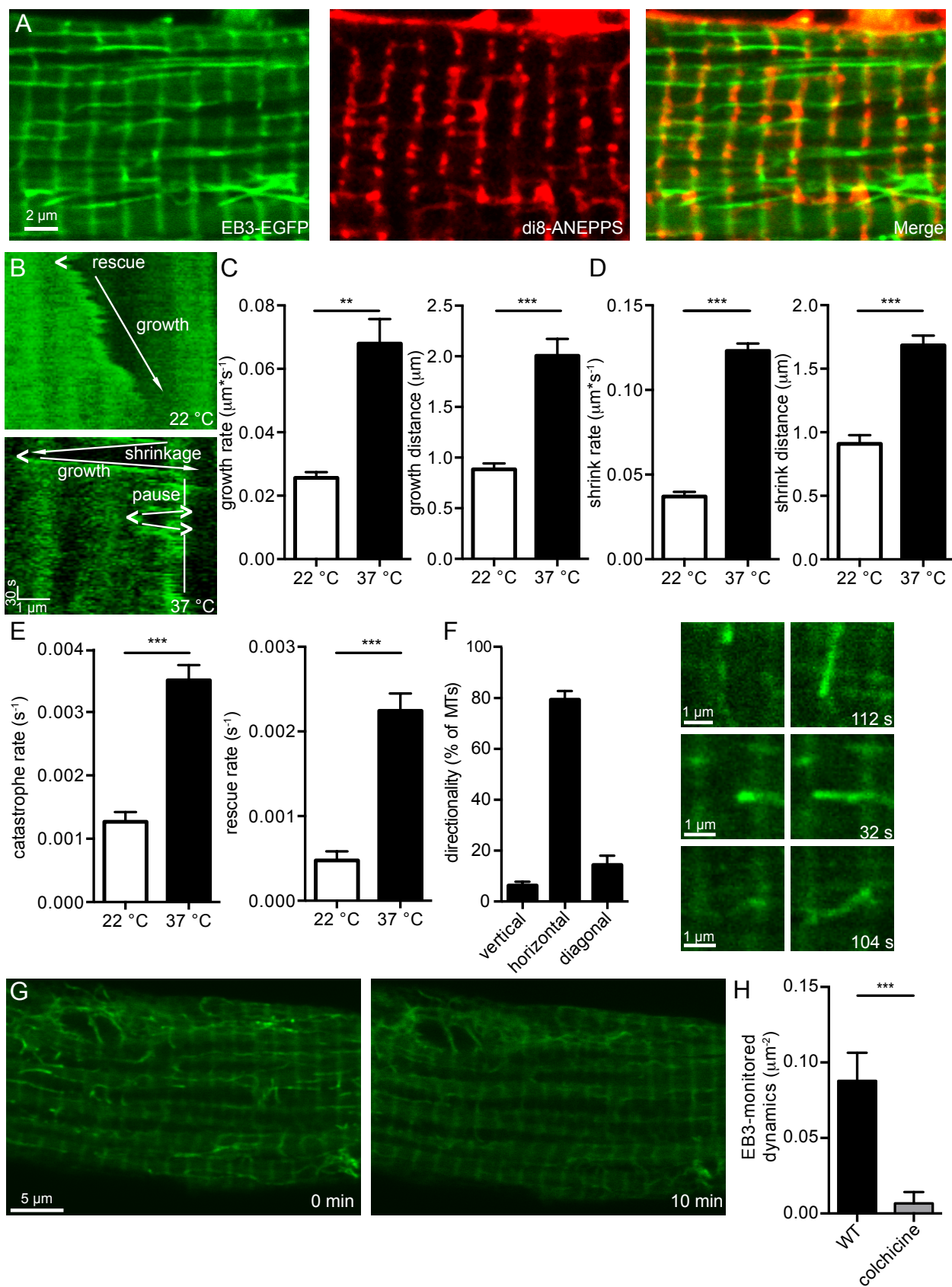


**Figure 3.4.** Live imaging of MTs in ventricular myocytes.

**A**, representative 2D We used analysis from several kymographs generated from images of MTs growing at 22 °C to quantify multiple MT dynamics: growth rate and distance, shrinkage rate and distance, catastrophe rate, and rescue rate (Figure 3C-E). While dynamic MTs could be scored at 22 °C, at physiological 37 °C, MTs were much more dynamic. MT growth rate and shrink rate were greatly increased, as was growth distance and shrink distance. Lastly, catastrophe rate rescue rate were also increased. These data show that, in confocal image of a ventricular myocyte expressing Eb3-EGFP (*left*) and stained with di8-ANEPPS (*middle*), with overlaid signals (*right*), scale bar = 2µm. **B**, representative kymographs of a MT taken from a myocyte recorded at 22 °C (*above*) and a myocyte recorded at 37 °C (*below*), scale bars = 1µm horizontally and 30 s vertically. Growth directions indicated by arrows and rescue indicated by “<”. The kymograph recorded from the MT at 37 °C also features a section of MT pausing, labeled with vertical line, and catastrophes indicated by “>”. **C**, bar plots of the mean ± S.E.M. of average growth rate (*left*) and growth distance (*right*) of MTs from myocytes recorded at 22 °C (*white*) and cardiomyocytes recorded at 37 °C (*black*). **D**, bar plots of the mean ± S.E.M. of average shrink rate (*left*) and shrink distance (*right*) of MTs from cardiomyocytes recorded at 22 °C (*white*) and cardiomyocytes recorded at 22 °C (*black*). **E**, bar plots of the mean ± S.E.M. of average catastrophe rate (*left*) and rescue rate (*right*) of MTs from cardiomyocytes recorded at 22 °C (*white*) and myocytes recorded at 37 °C (*black*). **F**, bar plot of the percentage of MTs moving vertically, horizontally, or diagonally (*left*) to the longitudinal axis of the cell, and representative examples of each type of movement. The first column of images is taken from start of cell recording, while the time points of the second column are indicated on the lower right in seconds, scale bar = 1µm. **G**, representative confocal image of a myocyte before (*left*) and after (*right*) application of colchicine, scale bar = 5 µm. **H**, bar plot of the mean ± S.E.M. of the average EB3-monitored dynamics of cardiomyocytes before (*black*) and after (*gray*) 10 min application of colchicine.

every parameter, the dynamicity of MTs was significantly increased between room temperature and physiological temperature (Figure 3C-E).

We quantified the directionality of MT growth at physiological temperature (Figure 3.4F). The vast majority (~80%) of all MTs grew along the horizontal axis of the cardiomyocytes, traversing between T-tubules. We calculated the ratio between leftward growing and rightward growing horizontal MTs to be  $0.97 \pm 0.05$  ( $n =$

176), indicating that MT polarity was evenly mixed relative to the horizontal axis of the cell. Thirteen percent of MTs grew diagonally, usually around nuclei. A small fraction of MTs (7%) grew vertically, almost always along the Z-line, both upward and downward. In addition, 91% of the time that a MT paused, that is, rested between two growth periods or shrink periods, it was on a Z-line, suggesting that the Z-line provides some mechanism of stability for the MT. Lastly, 82% of MTs were confined to a single sarcomere for the duration of our recordings (at least 10 min). 14% of MTs spanned 2 sarcomeres, 2.4% spanned 3 sarcomeres, and 1.7% spanned over 3 sarcomeres.

We also applied 1  $\mu$ M colchicine, a MT depolymerizer, to the myocytes (Figure 3.4G). As expected, the MTs underwent catastrophe and depolymerized. After ten minutes, a significant loss in EB3-monitored dynamics was observed, thus showing in real time the use of colchicine as an artificial inducer of MT catastrophe and depolymerization (Figure 3.4H). Lastly, we were able to compare MTs in ventricular myocytes to those in other cells by transfecting EB3-EGFP into human embryonic (tSA-201) cells and assaying dynamics. We found no significant difference between MT growth and shrinkage rates in either cell model ( $p > 0.05$ ).

### 3.3.3. Oxidative stress disrupts MT dynamics

Next, we tested the hypothesis that oxidative stress disrupts MT dynamics. To do this, we recorded EB3-EGFP images before and after application of 200  $\mu\text{M}$   $\text{H}_2\text{O}_2$ , an inducer of oxidative stress at a concentration known to induce injury in ventricular myocytes (Xie, Zhou et al. 2013). The myocytes used in these experiments were loaded with MitoSox Red, a mitochondrial-targeted indicator that increases in fluorescence intensity based on the amount of ROS (e.g., super oxide and  $\text{H}_2\text{O}_2$ ) present in a given cell (Figure 3.5). Figure 3.5A shows an exemplary cell with EB3-EGFP in green and the MitoSox Red signal in red inset.

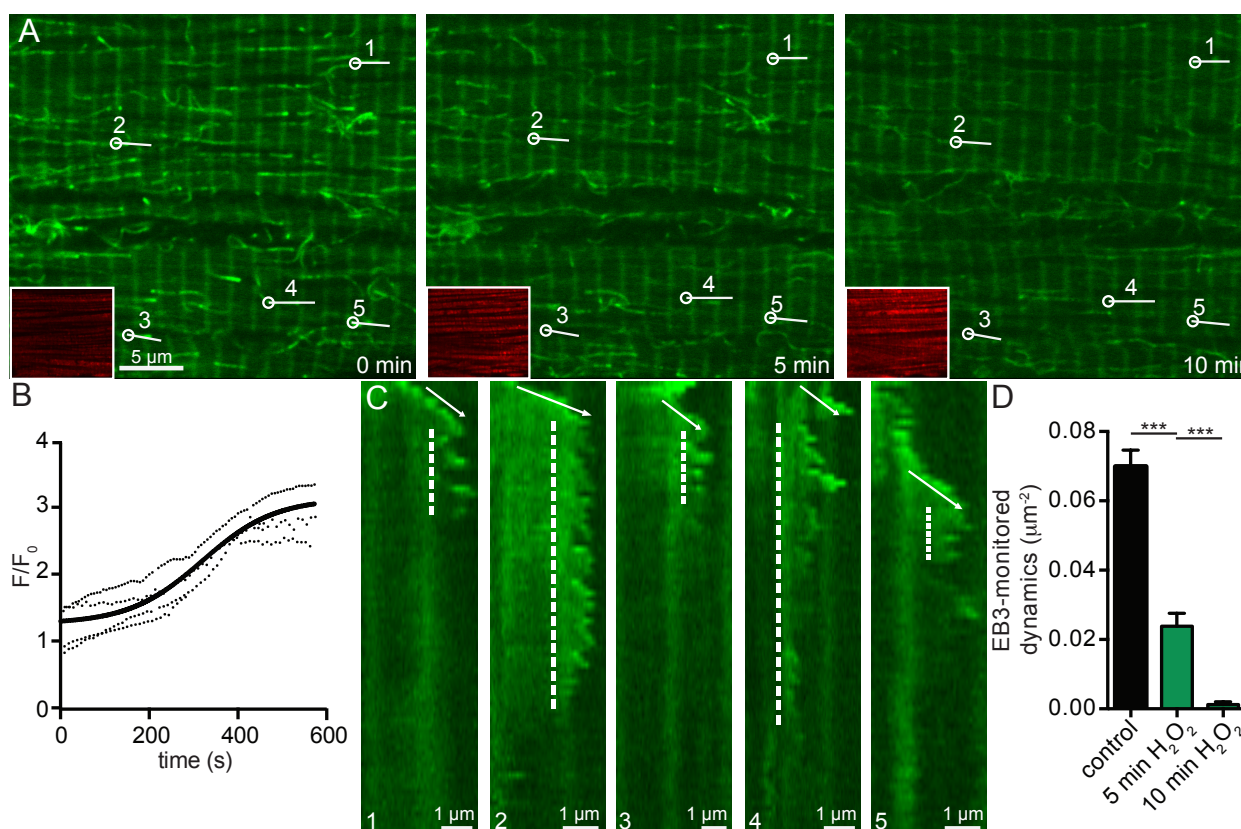


**Figure 3.5.** Oxidative stress disrupts MT dynamics.

A, representative confocal images of a cell before (*left*) and after 5 min (*center*) and 10 min (*right*) application of 200  $\mu\text{M}$   $\text{H}_2\text{O}_2$ , scale bar = 5  $\mu\text{m}$ . Lower left inset shows MitoSox Red channel. Numbers and lines indicate MTs shown in kymographs in C. B, representative plots of MitoSox Red fluorescence over time upon application of 200  $\mu\text{M}$   $\text{H}_2\text{O}_2$  fit to sigmoidal curve. C, five kymographs of MTs over 10 min application. Entire kymograph image is 10 min, scale bar = 1

$\mu\text{m}$ . Regions of growth are indicated by arrows and regions of instability by dashed lines. D, bar plot of the mean  $\pm$  S.E.M. of average EB3-monitored dynamics of cardiomyocytes before (*black*) and after 5 min (*green*) and 10 min (*dark green*) application of 200  $\mu\text{M}$   $\text{H}_2\text{O}_2$ .

Superfusion with an external solution containing 200  $\mu\text{M}$   $\text{H}_2\text{O}_2$  progressively increased the MitoSox Red signal, showing an increase in cell oxidative stress, and also altered MT dynamics. On average ( $n = 5$ ), the MitoSox Red signal's change in fluorescence upon application of 200  $\mu\text{M}$   $\text{H}_2\text{O}_2$  shows that the cell's level of oxidative stress increases in a seemingly sigmoidal fashion that plateaus around 10 minutes, reaching a level of  $\approx 3 F/F_0$  (Figure 3.5B). Over the course of these 10 minutes, similar to colchicine, we saw MTs undergo catastrophe and depolymerize.

Figure 3.5C shows five example kymographs of MTs from the cell shown in Figure 4A. In each kymograph, the MTs grow, and then undergo a period of dynamic instability and catastrophe before depolymerizing. In most cases (kymographs 1-4), the MT depolymerizes soon after application of 200  $\mu\text{M}$   $\text{H}_2\text{O}_2$ . The period of instability is also variable, lasting anywhere from less than a minute (kymograph 5) to over 7 minutes (kymograph 4). Through this time course, EB3-monitored dynamics decreased and became completely absent after 10 minutes of 200  $\mu\text{M}$   $\text{H}_2\text{O}_2$  application in a similar fashion to that seen upon colchicine application (Figure 3.5D).

#### 3.3.4. Live imaging of MTs in ventricular myocytes post-MI

Because oxidative stress increases following MI (Hori and Nishida 2009), we tested the hypothesis that MI would alter MT dynamics. We performed total left

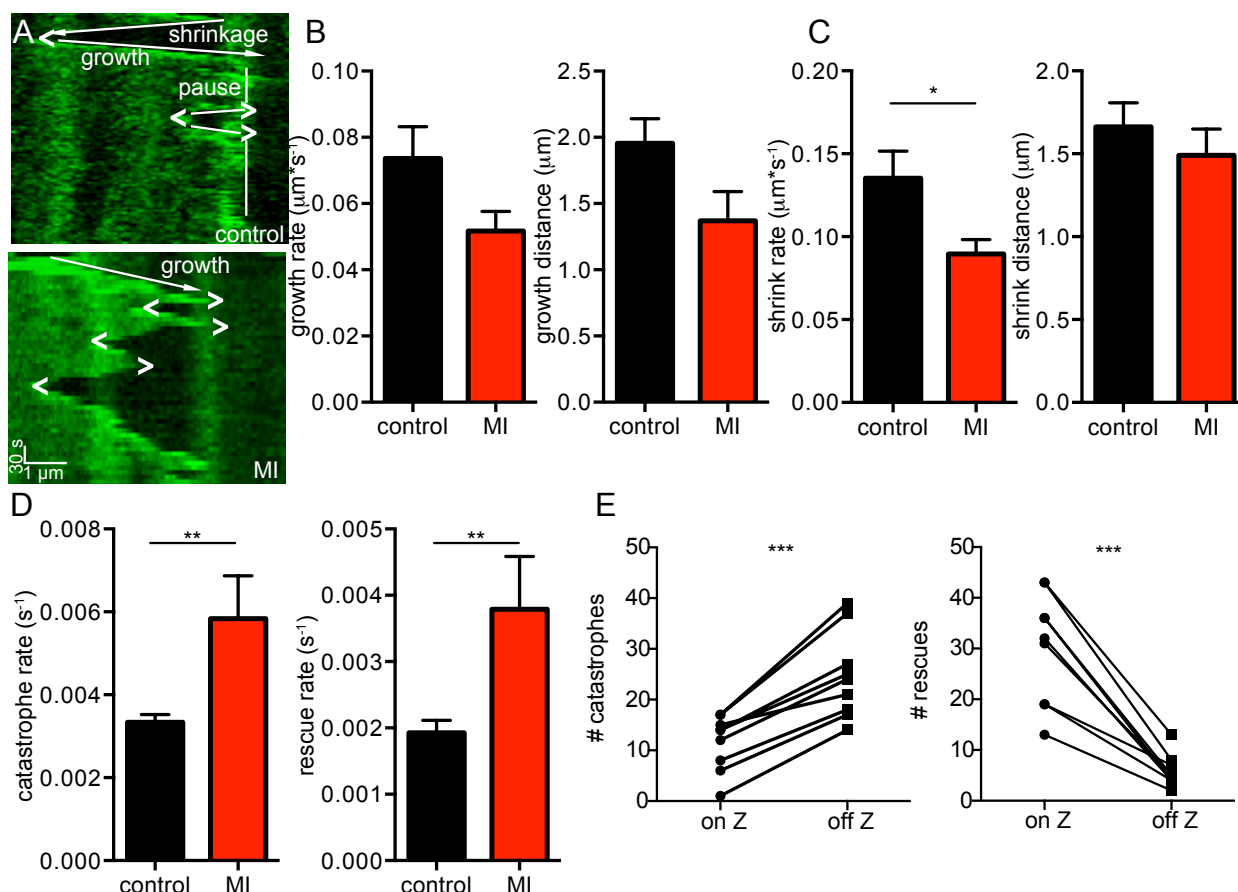


**Figure 3.6.** Live imaging of MTs in ventricular myocytes post-myocardial infarction.

**A**, representative kymographs of a MT taken from a control myocyte (*above*) and an infarcted myocyte (*below*), scale bars =  $1\mu\text{m}$  horizontally and 30 s vertically. Growth directions indicated by arrows, pausing by vertical line, catastrophes indicated by “>”, and rescues indicated by “<”. **B**, bar plots of the mean  $\pm$  S.E.M. of average growth rate (*left*) and growth distance (*right*) of MTs from control (*black*) and infarcted (*red*) cells. **C**, bar plots of the mean  $\pm$  S.E.M. of average shrink rate (*left*) and shrink distance (*right*) of MTs from control (*black*) and infarcted (*red*) cells. **D**, bar plots of the mean  $\pm$  S.E.M. of average catastrophe rate (*left*) and rescue rate (*right*) of MTs from control (*black*) and infarcted (*red*) cells. **E**, bar plots tracking paired responses for each cell of the number of catastrophes (*left*) and rescues (*right*) occurring on and off of the Z-line.

ascending coronary occlusion in mice injected with AAV9-EB3-EGFP to mimic MI and isolated cardiomyocytes 48-72 hours later (Figure 3.6). Similar to application

of 200  $\mu\text{M}$   $\text{H}_2\text{O}_2$ , MT dynamics were significantly altered. Figure 3.6A shows kymographs of a MT imaged in a control vs. infarcted mouse. In this MI sample, kymograph, there were 3 catastrophic events and 3 rescue events.

Taking an ensemble of MT kymographs from MI mice shows that while growth rate, growth distance, and shrink distance were unchanged between control and infarcted mice, shrinkage rate, catastrophe rate, and rescue rate were significantly higher (Figure 3.6B-D). Figure 3.6E shows a quantification of catastrophe and rescue in regards to the position of the head of the MT on the Z-line by cell. In every cell, there were more catastrophic events when the head of the MT was between rather than on a Z-line and more rescue events when the head of the MT was on rather than between Z-lines. Overall, 68% of catastrophic events occurred between Z-lines and 84% of rescue events occurred on Z-lines.

We explored possible explanations for the increase in catastrophic events seen after MI (Figure 3.7). A quantitative real time qRT-PCR screen of molecular inducers of catastrophe between control vs. infarcted cells revealed no change in RNA expression for Kif2a, Katna1, or Kif18b relative to GAPDH (Ganem and Compton 2004, Stout, Yount et al. 2011, Zhang, Grode et al. 2011). There was a non-significant trend towards increased tubulin expression ( $p < 0.08$ ). There was a significant increase in Kif2c protein expression (Figure 3.7A) (Newton, Wagenbach et al. 2004). However, on Western blot, there was no band seen in either control or infarcted cells (data not shown). We also performed a co-IP blot

using Kif2c to try and use a more sensitive technique to assay protein

expression, which showed a prominent band when using the entire left ventricle

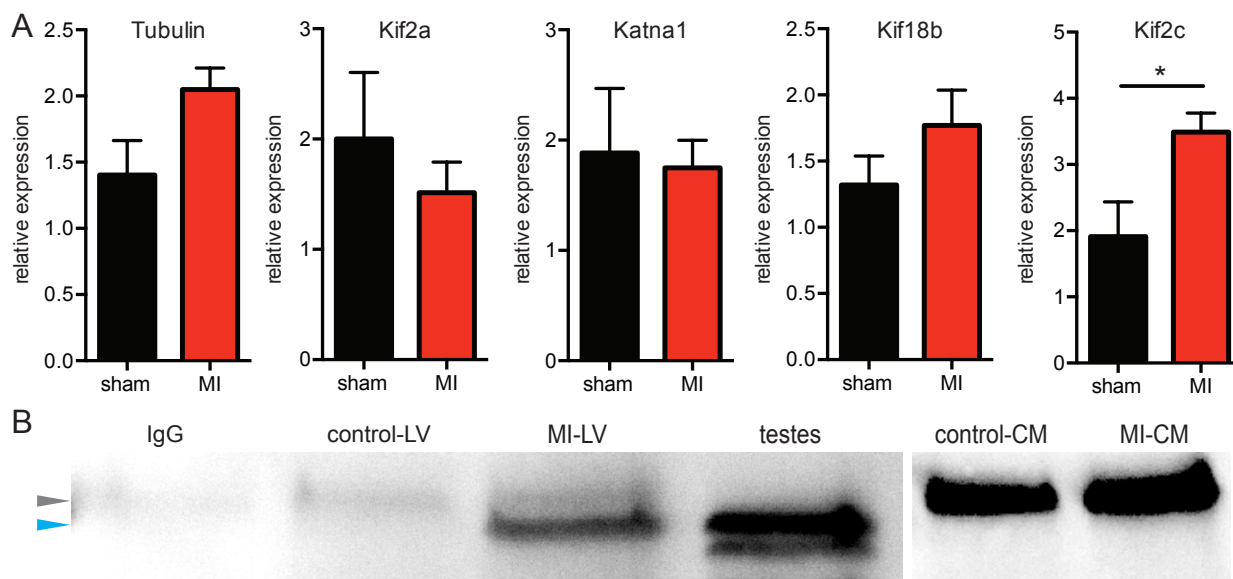


**Figure 3.7.** No molecular mechanism for increased catastrophe.

**A**, bar plots the mean  $\pm$  S.E.M. of relative real time qRT-PCR expression compared to GAPDH for tubulin, Kif2a, Katna1, Kif18b, and Kif2c in cardiomyocytes from mice undergoing a sham operation (*black*) or myocardial infarction (*red*). **B**, co-immunoprecipitation Western blot showing self-binding Kif2c expression in IgG (negative control) (*lane 1*), the left ventricle sham operation mice (*lane 2*), the left ventricle of infarcted mice (*lane 3*), mouse testis (positive control) (*lane 4*), isolated myocytes from sham operation mice (*lane 5*), and isolated myocytes from infarcted mice (*lane 6*). Gray arrow shows location of nondescript cardio-specific band. Blue arrow shows location of Kif2c band.

after MI but no band with isolated cardiomyocytes (Figure 3.7B). In addition, we were unable to visualize Kif2c with antibody-mediated imaging on control or infarcted cells. Kif2c has only been reported to be associated with dividing cells and has never been found in terminally differentiated cardiac tissue.

Furthermore, Kif2c expression is lost from postmitotic C2C12 cells as they undergo myofibrillogenesis (Ginkel and Wordeman 2000). Thus, we conclude that the increase seen in Kif2c transcript after MI is likely due to fibroblasts and

other dividing cells migrating into the infarcted region rather than novel expression of this molecular inducer of catastrophe in ventricular myocytes.

### 3.3.5. Oxidative stress mimics MT dynamic disruptions seen after MI

After discovering and quantifying MT dynamic disruptions in our model of MI, we tested the hypothesis that oxidative stress was responsible for this change in MT

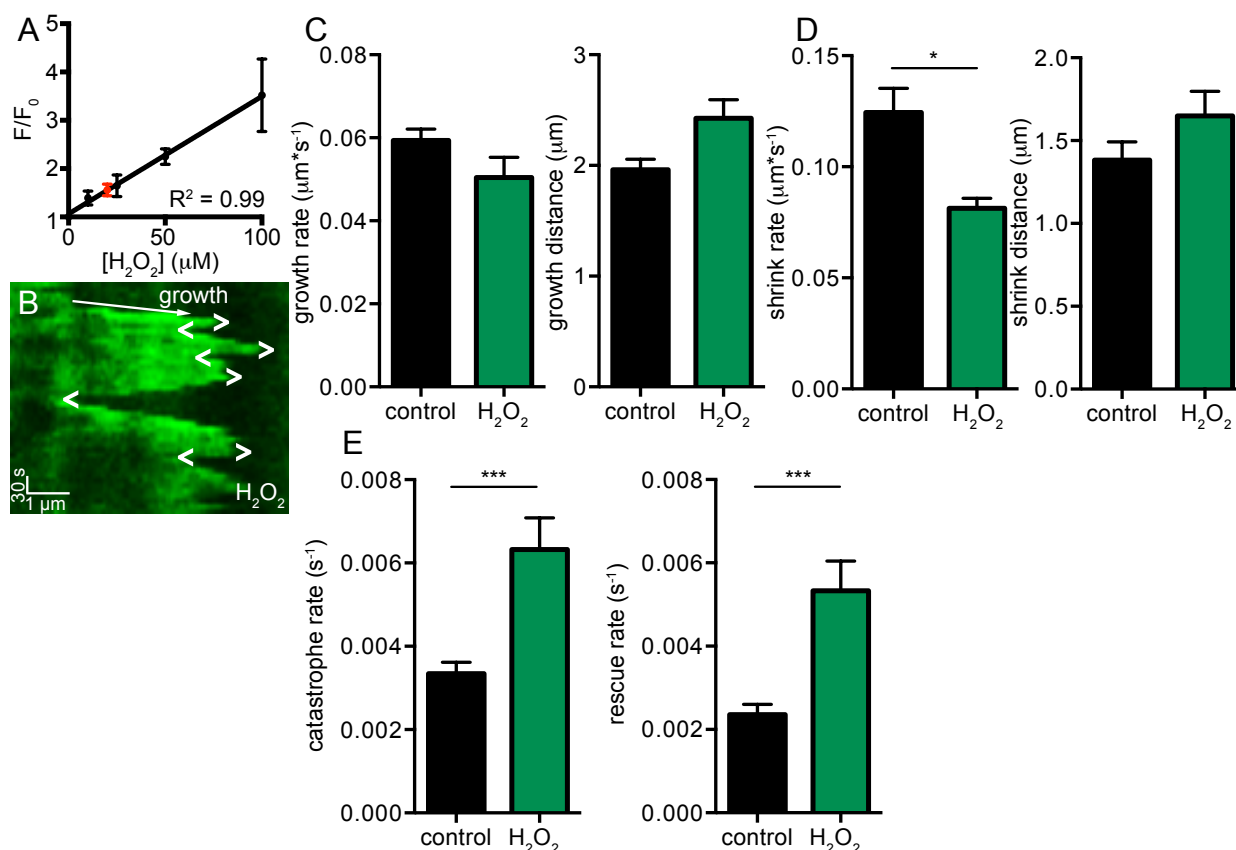


**Figure 3.8.** Oxidative stress mimics MT dynamic disruptions seen after MI.

**A**, x-y plot of the mean  $\pm$  S.E.M. of the relative fluorescence of MitoSox Red signal of cardiomyocytes exposed to various concentrations of H<sub>2</sub>O<sub>2</sub> fit to linear model. Red circle shows mean  $\pm$  S.E.M. of relative fluorescence of cardiomyocytes from MI model. **B**, representative kymograph of MT imaged from cardiomyocyte exposed to 10  $\mu$ M H<sub>2</sub>O<sub>2</sub>, scale bars = 1 $\mu$ m horizontally and 30 s vertically. Growth directions indicated by arrow, catastrophes indicated by “>”, and rescues indicated by “<”. **C**, bar plots of the mean  $\pm$  S.E.M. of average growth rate (*left*) and growth distance (*right*) of MTs from control cells (*black*) and cells treated with 10  $\mu$ M H<sub>2</sub>O<sub>2</sub> (*green*) cells. **D**, bar plots of the mean  $\pm$  S.E.M. of

average shrink rate (*left*) and shrink distance (*right*) of MTs from control cells (*black*) and cells treated with 10  $\mu\text{M}$   $\text{H}_2\text{O}_2$  (*green*) cells. **E**, bar plots of the mean  $\pm$  S.E.M. of average catastrophe rate (*left*) and rescue rate (*right*) of MTs from control cells (*black*) and cells treated with 10  $\mu\text{M}$   $\text{H}_2\text{O}_2$  (*green*) cells. dynamics. Using myocytes loaded with MitoSox Red and solutions with varied  $\text{H}_2\text{O}_2$  concentrations, we performed a concentration response curve to assay the effect of  $\text{H}_2\text{O}_2$  on cell oxidative stress. We found that MitoSox Red fluorescence increased linearly over the range of  $\text{H}_2\text{O}_2$  concentrations (0-100  $\mu\text{M}$ ) used in these experiments (Figure 3.8A). We measured the average fluorescence of MitoSox Red in MI cardiomyocytes and found that the amount of oxidative stress was equivalent to application of about 10-20  $\mu\text{M}$   $\text{H}_2\text{O}_2$  to control (i.e., non-MI) myocytes.

Many of the cells died or became unhealthy after prolonged (>30 min) exposure to 20  $\mu\text{M}$   $\text{H}_2\text{O}_2$ , so we assayed and quantified MT dynamics at 10  $\mu\text{M}$   $\text{H}_2\text{O}_2$  (Figure 3.8). Figure 3.8B shows a kymograph of a MT from a cell exposed to 10  $\mu\text{M}$   $\text{H}_2\text{O}_2$ , with 4 catastrophic events and 4 rescues present. We found that growth rate, growth distance, and shrink distance were similar to control cells. However, like infarcted cells, the shrink rate, catastrophe rate, and rescue rate were significantly different from control ventricular myocytes (Figure 3.8C-E). From these data, we conclude that 10  $\mu\text{M}$   $\text{H}_2\text{O}_2$  application, which induces the level of oxidative stress within the range seen in our MI model, is also able to replicate the disruptions in MT dynamics seen during this pathological condition.

### 3.3.6. MT dynamic disruptions reduce $I_{to}$ density

Lastly, we tested the impact of MT dynamics on ventricular myocyte physiology by testing the hypothesis that changes in MT dynamics would inhibit trafficking of ion channels, namely  $K_{V4.2}$  and  $K_{V4.3}$ , to the membrane. We quantified  $I_{to}$  density as well as  $K_{V4.2}$  and  $K_{V4.3}$  surface expression in control and MI cells (Figure 3.9). We found that  $I_{to}$  density was significantly reduced in MI cells at all positive voltages (Figure 3.9A-B). Application of 10  $\mu$ M  $H_2O_2$  to control cells

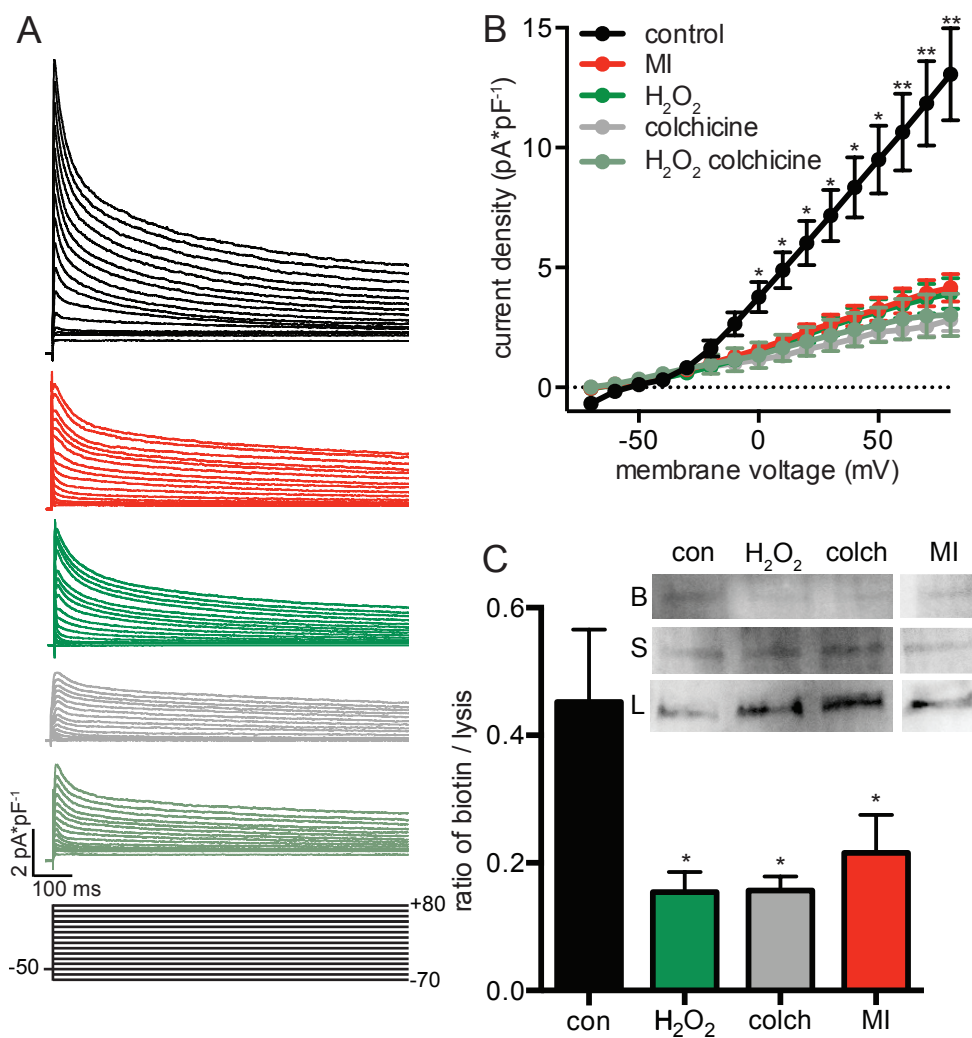


**Figure 3.9.** Reduction in Kv4 trafficking from MT disruption.

**A**, representative currents from mouse cardiomyocytes under control conditions (*black*), after infarct (*red*), and after treatment with H<sub>2</sub>O<sub>2</sub> (*dark green*), colchicine (*gray*), and both H<sub>2</sub>O<sub>2</sub> and colchicine (*green-gray*). Scale bars = 100 ms horizontally and 2 pA·pF<sup>-1</sup> vertically. Voltage protocol shown below, 10 mV separating each line. **B**, x-y plot of the mean ± S.E.M. of the average current density of control, infarcted, H<sub>2</sub>O<sub>2</sub>, colchicine, and colchicine + H<sub>2</sub>O<sub>2</sub> treated cells for a given voltage. **C**, bar plot of the mean ± S.E.M. of the average surface expression of K<sub>v</sub>4.2 and K<sub>v</sub>4.3 channels under control conditions, after 4 hour treatment with H<sub>2</sub>O<sub>2</sub>, after 4 hour treatment with colchicine, and from infarcted cells. Inset shows representative Western blot. B indicates biotinylated band, S indicated supernatant band, and L indicates lysis band. Lane 1 is control (*con*), lane 2 treated with H<sub>2</sub>O<sub>2</sub> (*H<sub>2</sub>O<sub>2</sub>*), lane 3 treated with colchicine (*colch*) and lane 4 infarcted (*MI*).

recapitulated the decrease in  $I_{t0}$  density seen in MI, as did application of 1  $\mu$ M colchicine. Co-application of H<sub>2</sub>O<sub>2</sub> and colchicine did not further reduce  $I_{t0}$ , lending support to the argument that both reagents are working by the same mechanism of MT polymer loss and that H<sub>2</sub>O<sub>2</sub> application is not causing a decrease in  $I_{t0}$  by other mechanisms. Using surface biotinylation binding with Western blot, we assayed surface expression of K<sub>v</sub>4.2 and K<sub>v</sub>4.3 in control and MI ventricular myocytes as well as after application of 10  $\mu$ M H<sub>2</sub>O<sub>2</sub> and application of 1  $\mu$ M colchicine (Figure 3.9C). After isolation, cells were incubated for 4 hours to allow time for MT trafficking defects to be seen. By quantifying the amount of protein bound to biotin in ratio to the amount of total protein found in the cell lysis, we found that surface expression of K<sub>v</sub>4.2 and K<sub>v</sub>4.3 was significantly decreased in infarcted cells as well as after application of H<sub>2</sub>O<sub>2</sub> and colchicine. This is consistent with the view that the reduction in  $I_{t0}$  seen was due to defects in K<sub>v</sub>4.2 and K<sub>v</sub>4.3 trafficking rather than any other mechanism.

### 3.4. Discussion

In this study, we were able to visualize dynamic MTs in living, acutely dissociated ventricular myocytes and made fundamental observations regarding these cytoskeletal structures. Our data suggest that EB proteins accumulate in bands at or near the Z-lines/T-tubules that run perpendicular to the longitudinal axis of ventricular myocytes. MTs are highly dynamic, growing, and shrinking within ventricular myocytes. MTs grow from Z-line-to-Z-line in ventricular myocytes and appear to be stabilized at the Z line, as evidenced by decreased catastrophe rate, increased rescue rate, and the prevalence of pausing. Finally, we found that increased oxidative stress during MI increases the catastrophe rate of MTs, decreasing  $l_{10}$  in ventricular myocytes. The physiological implications of these findings are discussed below.

Super-resolution and confocal imaging revealed EB1 punctate localization along the MT lattice. Interestingly, we also found that EB1 and transfected EB3 accumulated in the Z-lines of ventricular myocytes, which is where most MTs start growing. Although the molecular mechanisms causing EB1 and EB3 expression in the Z-line are unclear, protein-protein interaction may be important here. For example, it is possible that EB proteins link with proteins on the Z-line for MT stability, cargo transfer, or other cellular processes. Future studies should investigate these issues in detail.

A recent study by Oddoux *et al* (Oddoux, Zaal et al. 2013) imaged MTs in live skeletal muscle cells using super resolution STED microscopy. Similar to our findings, they found that EB3-GFP was localized not only to the tips, but also along the entirety of the MT and that puncta moved mostly longitudinally or transversely with no regard to cell polarity at similar growth rates. Furthermore, EB3 movement was localized to Z-lines of skeletal muscle. Interestingly, their data indicate that MTs are most likely forming a dynamic lattice and that they grow over each other in bundles. Furthermore, Oddoux *et al* (Oddoux, Zaal et al. 2013) speculates that dystrophin may serve to guide and define regions of MT growth and propose that MT pathology may be implicated in muscular dystrophy. Similarly, Belanto *et al* showed that dystrophin is capable of pausing MTs in vitro (Belanto, Mader et al. 2014). As ROS is also implicated in several muscular dystrophies, these studies appear to be synergistic. In combination, our data and that of Oddoux *et al* (Oddoux, Zaal et al. 2013), suggest that MTs in striated muscle (i.e., cardiac and skeletal) have similar structural and dynamic properties.

MTs in ventricular myocytes grow at a rate of  $\approx 0.07 \mu\text{m}\cdot\text{s}^{-1}$  at physiological temperatures. This means that a MT could move from one Z-line to another in about 30 seconds, assuming it does not pause. Considering that most molecular motors translocate along MT lattice faster, for example, kinesin 1 and dynein both process at a rate of  $\approx 1 \mu\text{m}\cdot\text{s}^{-1}$  depending on their load, MT growth would be the limiting factor in organelle and protein transport in ventricular myocytes (Muller, Klumpp et al. 2008). Interestingly, the direction of MT growth did not

appear to be random, as the vast majority of the time MTs grew from Z-line-to-Z-line without preference to cell polarity. This is distinctly different from non-muscle cells, where MTs grow in multiple directions (Howard and Hyman 2003). Indeed, the average growth distance we observed in ventricular myocytes was about 2  $\mu\text{m}$ , roughly the distance between Z-lines.

Related to this, Hong *et al* (Hong, Smyth *et al.* 2010) have supplied evidence that bridging indicator protein 1 (BIN1), the protein which localizes  $\text{Ca}_v1.2$  to the surface membrane and induces formation of T-tubules, also stabilizes MTs. It is possible that MTs may be involved in transporting proteins to the dyad for use in excitation-contraction coupling, moving horizontally from dyad to dyad to optimize each dyad for  $\text{Ca}^{2+}$  signaling. More work needs to be done to determine why T-tubules seem to stabilize MTs, and what physiological roles this stabilization plays in excitation-contraction coupling. Nevertheless, our data suggests that if MTs are involved in trafficking proteins to and from the T-tubule and SR dyad, then rapid changes in MT dynamics could alter the protein composition in these compartments in a matter of minutes.

Our data, in combination with the findings of a recent study, provide insights into the molecular mechanisms underlying increased MT catastrophe in ventricular myocytes isolated from infarcted hearts. We, as others (Kukielka, Smith *et al.* 1999, von Knethen, Callsen *et al.* 1999, Hori and Nishida 2009), found that oxidative stress increases after MI. Phosphorylation of EB1 by the glycogen

synthase kinase 3 $\beta$  (GSK3 $\beta$ ) increases binding of EB1 to the MT plus tip (Le Grand, Rovini et al. 2014). ROS inhibits GSK3 $\beta$  and EB1 accumulation in the MT plus end. Together, these findings suggest that higher oxidative stress after MI inhibits GSK3 $\beta$ , which decreases EB phosphorylation and thus promotes EB dislocation from the MTs, which destabilizes these cytoskeletal structures.

The increase in catastrophes seen after MI has significant implications for ventricular myocyte physiology. As our data suggest, it strongly correlates with decreases in K<sub>v</sub>4.2 and K<sub>v</sub>4.3 channels in the membrane and thus decreases  $I_{to}$  density after MI. K<sub>v</sub> channels may not be the only K<sup>+</sup> channels regulated by MT dynamics, however. The mechanism linking increased MT catastrophe to decreased K<sub>v</sub> currents likely involves the disruption of the “tracks” by which vesicles containing these channels are transported by kinesin-2 (Kif17) and dynein to and from the membrane (Chu, Rivera et al. 2006, Zadeh, Cheng et al. 2009). Recently, Arakel *et al* (Arakel, Brandenburg et al. 2014) showed that ATP-sensitive K<sup>+</sup> channels (K<sub>ATP</sub>) are held at the Golgi and released under  $\beta$ -adrenergic stimulation in ventricular myocytes. As MTs are nucleated at the Golgi in striated muscle (Oddoux, Zaal et al. 2013), it is intriguing to speculate that transport of vesicles containing K<sub>ATP</sub> channels is activated by protein kinase A during  $\beta$ -adrenergic signaling, thereby increasing the incorporation of these channels into the sarcolemma of ventricular myocytes.

Our study investigated MT dynamics during acute MI, when most ventricular myocyte remodeling is electrophysiological. However, our findings suggest that increasing MT dynamics could also impact the long-term (i.e., >1 week) structural stability of these cells post-infarction. It is established that MI results in a loss of T-tubules (Brette and Orchard 2003, Louch, Mork et al. 2006, Lyon, MacLeod et al. 2009). If MTs are stabilized by BIN1 and thus by T-tubules, the loss of T-tubules would create areas in the cell where MTs would be unstable and unable to grow. These would represent areas of most severe injury. As a result, proteins might be trafficked preferentially to areas of the cell that are healthier, and thus this reorganization might facilitate cellular recovery. Indeed in our data, we saw areas where catastrophe seemed to be more prevalent after MI. On the other hand, many proteins would be unable to get to the surface membrane, resulting in a significant loss of resources and inefficiency for an injured cell. Restoring MT dynamics after MI, using pharmacology or other means, may help increase the surface expression of trafficked proteins and help stabilize cell physiology in the critical time period after infarction.

At present, the mechanism for directional (i.e., Z-line-to-Z-line) MT growth in heart is unclear. One possibility is that MTs are “forced” to grow in a specific direction due to structural constraints. In this model, MTs would be able to grow primarily between myosin-actin fibers within each sarcomere. These inter-fiber “tunnels” would provide access to growing MTs and their cargo for delivery. Furthermore, it raises the possibility that MTs also provide additional structural

support to the sarcomere. Future studies, should examine this intriguing possibility.

All MT parameters we examined in ventricular myocytes were temperature-dependent: growth, shrink, catastrophe and rescue. This finding is relevant because most MT studies in ventricular myocytes have been traditionally performed at temperatures typically ranging from 21-23 °C. Our study suggests that drawing conclusions from MT-related processes from studies at these temperatures could be misleading. Increasing temperature to physiological levels resulted in a significant increase in MT dynamics. This finding is important for the entire cardiac electrophysiological field moving forward, as the vast majority of experiments are conducted at room temperature. If cardiomyocytes sit at room temperature throughout the experimental day, it is likely that their MTs are less dynamic, leading to changes in protein trafficking. Our data suggests that cardiomyocytes should be incubated at 37 °C after being isolated in order to approximate normal cell physiology.

### 3.5. Limitations of the study

All studies that investigate the effects of myocardial infarction and involve expression of endogenous proteins on a wild type background should be interpreted cautiously. For example, although endogenous EB1, EB3, and exogenous EB3-EGFP are expressed on the on the MTs as well as on the t-tubules/Z-lines of ventricular myocytes, expression of EB3-EGFP in these structures could be potentially higher than under control conditions. Furthermore, in our MI studies we did not segregate cells based on their proximity to the infarct zone. Thus, we likely recorded cells in various levels of injury. In spite of these limitations, we contend that novel insights into the bases of MT dynamics in ventricular myocytes have been obtained in the present experiments. These insights should form the bases of new hypotheses that can be best tested in appropriate animal models.

### 3.6. Summary and conclusions

To conclude, MTs have important roles in cardiomyocytes. By live-imaging MTs, we were able to assay their dynamics and provide valuable insights regarding how MTs move within cardiomyocytes. We also quantified how oxidative stress disrupts MTs in the setting of MI. We showed that this disruption in MTs has direct impacts on cell physiology, decreasing  $I_{to}$  by reducing  $K_v4.2$  and  $K_v4.3$  surface expression.

## **Chapter 4: Bridging Integrator Protein 1 (BIN1) stabilizes microtubules on the T-tubules, enabling kinesin-1 (Kif5B) to traffic $\text{Ca}_v1.2\beta_2$ in ventricular myocytes**

### **4. Summary**

Recently, using adeno-associated viral vectors expressing the microtubule (MT)-associated protein plus end binding protein 3 (EB3) tagged with EGFP, MT dynamics were captured and quantified in ventricular myocytes in real time under physiological conditions. However, the dynamics of MTs in atrial myocytes remained a mystery. We quantified MT dynamics in both atrial myocytes as well as in cultured ventricular myocytes lacking T-tubules. Catastrophe and rescue rates were increased in both of these experimental paradigms. In addition, directionality of MTs became more variable and MT pausing was disrupted, suggesting that T-tubules are important for MT stability. We performed dual-antibody staining and found that the protein bridging integrator protein 1 (BIN1) and EB1 have differential expression in atrial contrasted with ventricular myocytes. In ventricular myocytes, BIN1 associates with MT-associated protein CLIP170 as well as EB1, suggesting that BIN1 may help stabilize MTs on the T-tubules. In addition, BIN1 colocalizes with  $\text{Ca}_v1.2$ , suggesting MT trafficking of the channel. Using a virus that expressed a dominant negative version of the kinesin-1 motor as well as co-immunoprecipitation results, we found that kinesin-

1 is the molecular motor responsible for trafficking the  $\beta_2$  subunit of  $\text{Ca}_v1.2$  to the membrane.

#### 4.1. Introduction

In order for heart to circulate blood throughout the body, it must reliably and consistently beat. As a corollary, cardiac myocytes must contract with every action potential (AP). The chain of events that couple an AP to contraction is collectively known as excitation-contraction (EC) coupling. In EC coupling, the opening of sarcolemmal voltage-gated calcium channels ( $Ca_v1.2$ ) during the AP causes a small influx of  $Ca^{2+}$  that activates ryanodine receptors (RyRs) on the sarcoplasmic reticulum (SR) to open and release large amounts of  $Ca^{2+}$ , flooding the cell to enable faithful contraction. EC coupling, then, relies on the faithful interaction between  $Ca_v1.2$ , which predominate in T-tubules, periodic invaginations of the plasma membrane, and RyRs in the junctional sarcoplasmic reticulum (jSR), the region of the sarcoplasmic reticulum that sits in close apposition to the T-tubules, to enable high fidelity calcium release from ryanodine receptors after opening of  $Ca_v1.2$  channels. If  $Ca_v1.2$  channels are not trafficked to the T-tubules, the  $Ca^{2+}$  influx from their opening would diffuse and weaken before reaching RyRs, resulting in insufficient activation.

In contrast to ventricular myocytes, most atrial myocytes do not possess T-tubules. Rather than have invagination of plasma membrane, atrial myocytes have outcroppings of sarcoplasmic reticulum at periodic intervals of  $\approx 2 \mu\text{m}$ , called Z-tubules (Bootman, Higazi et al. 2006, Chen-Izu, McCulle et al. 2006). In addition, there is a gap of  $\approx 2 \mu\text{m}$  between RyRs close to the sarcolemma

(junctional RyRs) and those on the inner Z-tubules (non-junctional RyRs) (Carl, Felix et al. 1995, Mackenzie, Bootman et al. 2001). As a result,  $Ca^{2+}$  influx is generally limited to only the periphery of atrial cells during normal physiology and only uniform upon adrenergic stimulation (Mackenzie, Roderick et al. 2004, Bootman, Higazi et al. 2006).

The protein bridging integrator 1 (BIN1) has been shown to be implicated in the formation of T-tubules in both skeletal and cardiac muscle (Lee, Westenbroek et al. 2002, Hong, Yang et al. 2014). Recently, Hong et al furthered the role of BIN1 by showing it has a role in localizing  $Ca_v1.2$  to the T-tubules (Hong, Smyth et al. 2010). In addition, the study showed that BIN1 was capable of anchoring and stabilizing microtubules (MTs). However, the molecular mechanisms behind this finding were not elucidated. In addition, the role of BIN1 in atrial myocytes is unknown.

$Ca_v1.2$  channels are large protein complexes consisting of an  $\alpha$  subunit, which consists of 24 transmembrane segments which forms the pore and voltage sensors, as well as a  $\beta$  and  $\alpha_2\delta$  subunit in 1:1:1 stoichiometry. The  $\beta$  subunit is required for plasma membrane expression and proper gating (Lacerda, Kim et al. 1991). There are four subfamilies of the  $\beta$  subunit ( $\beta_1 - \beta_4$ ), with  $\beta_2$  being the predominant subunit in the heart (Colecraft, Alseikhan et al. 2002). Without the  $\beta$  subunit,  $Ca_v1.2$  channels show little to no surface expression and produce very

small or no current, indicating that the  $\beta$  subunit is also important for trafficking of the channel (Birnbaumer, Qin et al. 1998).

Microtubules (MTs) are cytoskeletal fibers formed by polymerization of  $\alpha\beta$  tubulin dimers required for correct protein trafficking. Their diverse functions in cellular processes include sustaining cell shape, mitosis, and intracellular trafficking of proteins (Gelfand and Bershadsky 1991). Despite their mature non-differentiating nature, it has been recently shown that MTs maintain important functions in the ventricular myocytes (Kerfant, Vassort et al. 2001). MTs are dynamically active and switch between phases of growth and shrinking in a process called dynamic instability (Mitchison and Kirschner 1984). Plus-end binding (EB) proteins constitute a unique group of structurally and functionally diverse proteins that target the plus ends of MTs, orchestrate MT growth, and recruit MT regulators. EBs are also implicated in MT-based transport (Gu, Zhou et al. 2006, Shaw, Fay et al. 2007). Some plus-end proteins, such as CLIP170, require EB1 to track MT growth (Dixit, Barnett et al. 2009). CLIP170 has also recently been shown to interact with BIN1 (Meunier, Quaranta et al. 2009). Recently, Drum et al used an adeno-associated virus expressing a MT plus-end protein to visualize MT dynamics in live cardiomyocytes for the first time, characterizing the growth rate and shrinkage rate, as well as the frequency of catastrophe (i.e., the transition from growth to shrinkage) and rescue (i.e., the transition from shrinkage to growth) (Desai and Mitchison 1997, Drum, Yuan et al. 2016). In addition, the study found that MTs could be disrupted in pathology

such as oxidative stress and myocardial infarction and implicated MTs in the trafficking of the  $K_v4$  channel family. However, the role of MTs in protein trafficking of the machinery of EC coupling is yet to be determined. In addition, the dynamics of MTs in atrial myocytes is unknown.

Molecular motors are proteins that move along MTs using ATP and are involved in protein and vesicle trafficking (Schliwa and Woehlke 2003). Most kinesins walk towards the positive ends of MTs in a process called anterograde transport. The first discovered kinesin, kinesin-1, consists of 2 identical heavy chains, which are the motor subunits, and 2 light chains. In the heart, the heavy chain is encoded by the gene *Kif5B*. Kinesin-1 is responsible for the trafficking of several proteins in cardiomyocytes.

In this report, we explore MT function in atrial myocytes and trafficking of proteins involved in EC coupling. Confocal imaging showed that BIN1 associated with dyadic proteins  $Ca_v1.2\alpha$  and  $Ca_v1.2\beta_2$  as well as MT-associated proteins CLIP170 and EB1 in ventricular myocytes. We also imaged BIN1 and EB1 in atrial myocytes and found distinct differences compared to expression in ventricular myocytes. We quantified MT dynamics in conditions without T-tubules including in atrial myocytes and found that the loss of T-tubules disrupted MT stability, dynamics, and directionality. Furthermore, we used confocal imaging combined with co-immunoprecipitation to find that kinesin-1 serves as the

molecular motor for  $\text{Ca}_v1.2\beta_2$ , and that disrupting kinesin-1 results in a loss of  $I_{\text{Ca}}$  current density.

## 4.2. Materials and methods

### 4.2.1. Isolation of mouse ventricular myocytes

Mice were euthanized with a lethal dose of sodium pentobarbital administered intra-peritoneally as approved by the University of Washington Institutional Animal Care and Use Committee. Ventricular myocytes were isolated using a Langendorff perfusion apparatus as previously described (Drum, Dixon et al. 2014). The isolated ventricular myocytes were kept either at room temperature (22 °C) or at 37 °C in Tyrode's solution containing (mM): 140 NaCl, 5 KCl, 10 HEPES, 10 glucose, 2 CaCl<sub>2</sub>, and 1 MgCl<sub>2</sub>; pH = 7.4 with NaOH, and used 0.5–8 h after isolation.

### 4.2.2. Culturing mouse ventricular myocytes

After isolation, myocytes were resuspended in plating media (Minimal Essential Media (MEM) with 5% bovine calf serum, 2 mM L-glutamine, 10 mM BDM, and 1% penicillin/streptomycin) and plated in petrie dishes. 2 mL of culture media consisting of MEM with 0.1mg/mL bovine serum albumin, 2 mM L-glutamine, 10 mM BDM, and 1% penicillin/streptomycin, was added to each dish and myocytes were incubated at 37° C with 2% CO<sub>2</sub> for 24h, 48h, or 72h before imaging (Graham, Balla et al. 2013).

#### 4.2.3. Isolation of mouse atrial myocytes

Mice were euthanized with a lethal dose of sodium pentobarbital administered intra-peritoneally as approved by the University of Washington Institutional Animal Care and Use Committee. Atrial myocytes were isolated by modifying previous protocols (Temple, Frias et al. 2005). Mouse hearts were removed and placed into Tyrode's solution warmed to 37° C, pH = 7.4. Atria were removed and cut into strips and transferred to a solution containing (in mM) 140 NaCl, 5.4 KCl, 0.07 CaCl<sub>2</sub>, 0.5 MgCl<sub>2</sub>, 1.2 KH<sub>2</sub>PO<sub>4</sub>, 50 taurine, 5.5 D-glucose, 1 mg/mL bovine serum albumin (BSA), and 5 HEPES; pH = 7.4. Atria strips were washed three times in these solution and then digested by addition of 10 mg collagenase type II (125 U/mg, Worthington Biochemical; Lakewood NJ) and 0.5 mg protease type XIV (3.5 U/mg, Sigma; Oakville, Ontario, Canada). Enzymatic digestion took place for 30 min at 37° C with manual agitation every 5 min. Tissue strips were then washed five times in a modified Kraftbrühe solution containing (in mM): 100 K<sup>+</sup> glutamate, 10 K<sup>+</sup> aspartate, 25 KCl, 10 KH<sub>2</sub>PO<sub>4</sub>, 2 MgSO<sub>4</sub>, 20 taurine, 5 creatine base, 0.5 EGTA, 5 HEPES, 20 D-glucose, and 1 mg/mL BSA; pH = 7.2 with KOH. Single atrial myocytes were isolated by gentle trituration at room temperature with a set of fire-polished Pasteur pipettes of decreasing diameter size (6 mm – 2 mm). Myocytes were slowly readapted to 0.5 mM Ca<sup>2+</sup> concentration by dropwise addition of Ca<sup>2+</sup> and then suspended in recording solution containing (in mM): 140 NaCl, 5 KCl, 0.5 CaCl<sub>2</sub>, 1 MgCl<sub>2</sub>, 10 HEPES, 10 D-glucose, and 1 mg/mL BSA.

#### 4.2.4. Immunohistochemistry and imaging

Ventricular myocytes were imaged using an Olympus FluoView 1000 confocal microscope equipped with an Olympus 60x (NA = 1.49) oil immersion lens (Drum, Dixon et al. 2014). Briefly, cardiomyocytes were fixed by incubating in 4% paraformaldehyde in PBS at 37 °C for 30 m, then washed with PBS and blocked for 1 h at room temperature in 50% SEA BLOCK (Thermo Fisher Scientific Waltham, MA) and 0.5% w/v Triton X-100 in PBS (blocking buffer). Several antibodies were used to image proteins in the myocyte: MTs were probed with a rat (Harlan, Indianapolis, IN, MAS 077) or mouse (Sigma, St. Louis, MO, T-9026) anti-tubulin antibody and mouse anti-EB1 antibody (BD transduction, San Jose, CA, 610534). The jSR was probed with anti-BIN1 (Santa Cruz Labs, SC13575), anti-Ca<sub>v</sub>1.2 $\alpha$  (gift from Catterall lab), anti-Ca<sub>v</sub>1.2 $\beta$ <sub>2</sub> (gift from Catterall lab), anti-CLIP170 (Santa Cruz Lab, SC12799) antibodies. Kinesin-1 was probed with anti-Kif5B (Santa Cruz Labs, SC13356) antibody. All primary antibodies were diluted to 1  $\mu$ g/mL in blocking buffer and cells were incubated overnight at 4 °C. Cells were washed extensively with 20% Sea Block three times. Cells were then incubated for 1 h at room temperature with donkey anti-goat Alexa Fluor 647, chicken anti-rabbit Alexa Fluor 647, goat anti-rabbit Alexa Fluor 568, chicken anti-goat Fluor 568, or donkey anti-mouse Alexa Fluor 488 in blocking buffer. Myocytes were washed with 20% Sea Block three times and then mounted with PBS and sealed with nail polish.

#### 4.2.5. Viral expression system

Two Adeno-associated viruses serotype 9 (AAV9), one expressing a marker of microtubule heads (AAV9-EB3-EGFP) and one expressing a dominant negative version of the kinesin 1 motor tagged with RFP (AAV9-Kif5B-DN-RFP), were generated by Vector Biolabs (Inagaki, Fuess et al. 2006, Bish, Morine et al. 2008). Mice were anesthetized by isoflurane and injected retro-orbitally with AAV9. To allow expression of the proteins, experiments were performed at least 3 weeks after virus injection.

#### 4.2.6. Imaging and fluorescent indicators

Ventricular myocytes were imaged using an Olympus FluoView 1000 confocal microscope equipped with an Olympus 60x (NA = 1.49) oil immersion lens (Drum, Dixon et al. 2014). In some myocytes, 10  $\mu$ M di-8-ANEPPS was loaded into the cells by 20 min incubation, 10 min pellet, and resuspension in Tyrode's solution in order to visualize the T-tubules. T-tubule power was calculated by taking a Fourier transform of the T-tubule image and quantifying the first harmonic peak, which is a measure of the consistency of distance between segments (Wei, Guo et al. 2010).

#### 4.2.7. Image analysis

Colocalization was analyzed using the ImageJ plugin “JaCoP” after applying a threshold to eliminate noise.

For quantification of live MT dynamics: each cell was scanned in the z-axis and recorded at a plane where the predominant number of MTs could be seen and tracked, usually in the midsection of the cell. MTs were tracked manually by generating a kymograph for each MT with strict parameters. For readers not familiar with this, kymographs can be conceptualized as an x-t scan, where the intensity along a given line is plotted for all images of a stack. We constructed kymographs by tracing the path of an MT throughout the image stack to form the x-axis of the kymograph image. The lines are then stacked along the y-axis for all frames in the image stack. In this paradigm, a growing MT will appear as a line oriented downward and to the right and a shrinking MT will appear as a line oriented downward and to the left. A catastrophe would be seen as a left facing angle (>) and a rescue is seen as a right facing angle (<). A pause is visualized as a vertical line (Drum, Yuan et al. 2016).

Growth and shrinkage were evaluated only in linear circumstances ( $R^2 < 0.85$  in linear regression analysis) as seen in many other studies (Tirnauer, O'Toole et al. 1999, Kosco, Pearson et al. 2001, Tanaka, Kitamura et al. 2007). MT pause was characterized by a MT tip moving less than 0.5  $\mu\text{m}$  in 30 s (Kline-Smith and

Walczak 2002). Catastrophe and rescue were counted if: (1) they persisted for more than 15 s; (2) clear growth, shrinkage, or pause could be seen surrounding the event; and (3) movement exceeded that of pausing conditions. MTs were analyzed blind to experimental condition via name randomization (Labbe, Maddox et al. 2003, Peris, Wagenbach et al. 2009). EB3-monitored dynamics was measured by counting the number of EB3-marked MTs in a given cell area, corrected for photobleaching using the Histogram Matching feature of Photocorrection in ImageJ (Montenegro Gouveia, Leslie et al. 2010, Drum, Yuan et al. 2016).

#### 4.2.8. Electrophysiology

All electrophysiological recordings were performed while cells were superfused with saline solutions at room temperature ( $\approx 22$  °C). Pipettes were pulled using a Flaming-Brown type puller (Sutter Instruments) with nominal resistance of 1-2 M $\Omega$  and filled with solutions as described below. To record  $I_{Ca}$ , membrane potential was controlled via the patch-clamp technique using an Axopatch 200B amplifier (Molecular Devices). Data were acquired at 10 kHz and low-pass filtered at 2 kHz. Ventricular myocytes were continuously perfused with Tyrode's solution. Once whole-cell configuration was successfully established in myocytes, an extracellular solution with the following constituents (mM) was exchanged: 140 NMDG, 5 CsCl<sub>2</sub>, 2 CaCl<sub>2</sub>, 1 MgCl<sub>2</sub>, 10 glucose, 10 HEPES; pH 7.4 with HCl, and 10  $\mu$ M tetrodotoxin was added to block sodium channels. The

pipette solution used in experiments designed to record  $I_{Ca}$  during EC coupling contained (mM): 130 CsCl, 10 TEA-Cl, 5 Mg-ATP and 10 HEPES; pH 7.2 with CsOH.  $I_{Ca}$  was evoked by 200 ms long depolarization pulses from -80 mV to potentials ranging from -40 to +60 mV (10 mV increment). Current integrals were calculated by summing the area under the curve created by the current trace.

#### 4.2.9. Co-immunoprecipitation Western blotting

Protein expression for Kif5B and  $Ca_v1.2\beta_2$  co-immunoprecipitation was determined by Western blot, performed as previously described (Cheng, Yuan et al. 2011). Briefly, proteins were extracted from control and MI mice left ventricle or cardiomyocytes and run on SDS-PAGE. To check Kif5B and  $Ca_v1.2\beta_2$  colocalization in cardiomyocytes, we immunoprecipitated Kif5B and anti- $Ca_v1.2\beta_2$  antibody and  $Ca_v1.2\beta_2$  with anti-Kif5B antibody in order to verify protein-protein interaction. IgG was used as a negative control. Cardiomyocyte protein lysates were incubated with anti-Kif5B or anti- $Ca_v1.2\beta_2$  antibody at 4°C for 2 hours and protein-antibody complexes were precipitated with protein-A/G-coupled agarose beads (Santa Cruz Biotech, Dallas, TX) at 4°C for overnight. The agarose beads were washed 4 times with IP-buffer and proteins were eluted by incubation at 100°C for 10 min in 2 × Laemmli sample buffer (Bio-Rad, Hercules, CA) supplemented with 5% 2-mercaptoethanol. The supernatants were then run on SDS-PAGE and proteins were transferred to PVDF membranes. After blocking with 5% normal donkey serum (Jackson ImmunoResearch, West

Grove, PA), membranes were probed with anti-Kif5B or anti-Ca<sub>v</sub>1.2β<sub>2</sub> antibody at room temperature for 2 h, followed by incubation with donkey anti-mouse or donkey anti-goat IgG alkaline phosphatase conjugated secondary antibody (Jackson ImmunoResearch) at room temperature for 1 h. The blots were developed with ECF (Amersham Biosciences, Piscataway, NJ) and imaged with Bio-Rad ChemiDoc XRS+ system.

#### 4.2.10. Statistics

Data are presented as mean ± standard error of the mean (S.E.M.). Two-sample comparisons were made using a Student's *t* test (\**P* < 0.05, \*\**P* ≤ 0.01).

### 4.3. Results

#### 4.3.1. BIN1 colocalizes with other proteins in T-tubules.

We directly visualized BIN1 in cardiomyocytes using immunohistochemistry and compared its expression to that of several other proteins (Figure 4.1). BIN1 had a periodic signal at a frequency of  $\approx 2 \mu\text{m}$ , indicating some relationship with the Z-lines or T-tubules. Using the technique of dual-antibody staining, we were able to image BIN1 with several other proteins, including the  $\alpha$  subunit of  $\text{Ca}_v1.2$ , the  $\beta$  subunit of  $\text{Ca}_v1.2$ , CLIP170, and Kif5B. Both the  $\alpha$  and  $\beta$  subunits of  $\text{Ca}_v1.2$  colocalize to the T-tubules directly opposite the jSR. CLIP170 is a MT plus-end-tracking protein abundantly expressed in the heart, implicated in the control of MT dynamics and stability, which requires EB1 to bind to growing MT ends (Akhmanova, Mausset-Bonnefont et al. 2005, Bieling, Kandels-Lewis et al. 2008). Lastly, Kif5B is the heavy chain protein composing kinesin-1.

We determined the Pearson's coefficient of the BIN1 fluorescence signal with the signal from these proteins (the merged images in Figure 4.1) to provide a quantitative analysis of the degree of overlap between these proteins. The Pearson co-efficient ranges from 0 (for non co-localized) to 1 (for fully co-localized) fluorescent signals. Indeed, we found that the Pearson's coefficient between BIN1 and the  $\alpha$  subunit of  $\text{Ca}_v1.2$  was  $0.7 \pm 0.1$  ( $n = 4$ ), indicating that at the level of resolution of our confocal microscope ( $\sim 250 \text{ nm}$ )

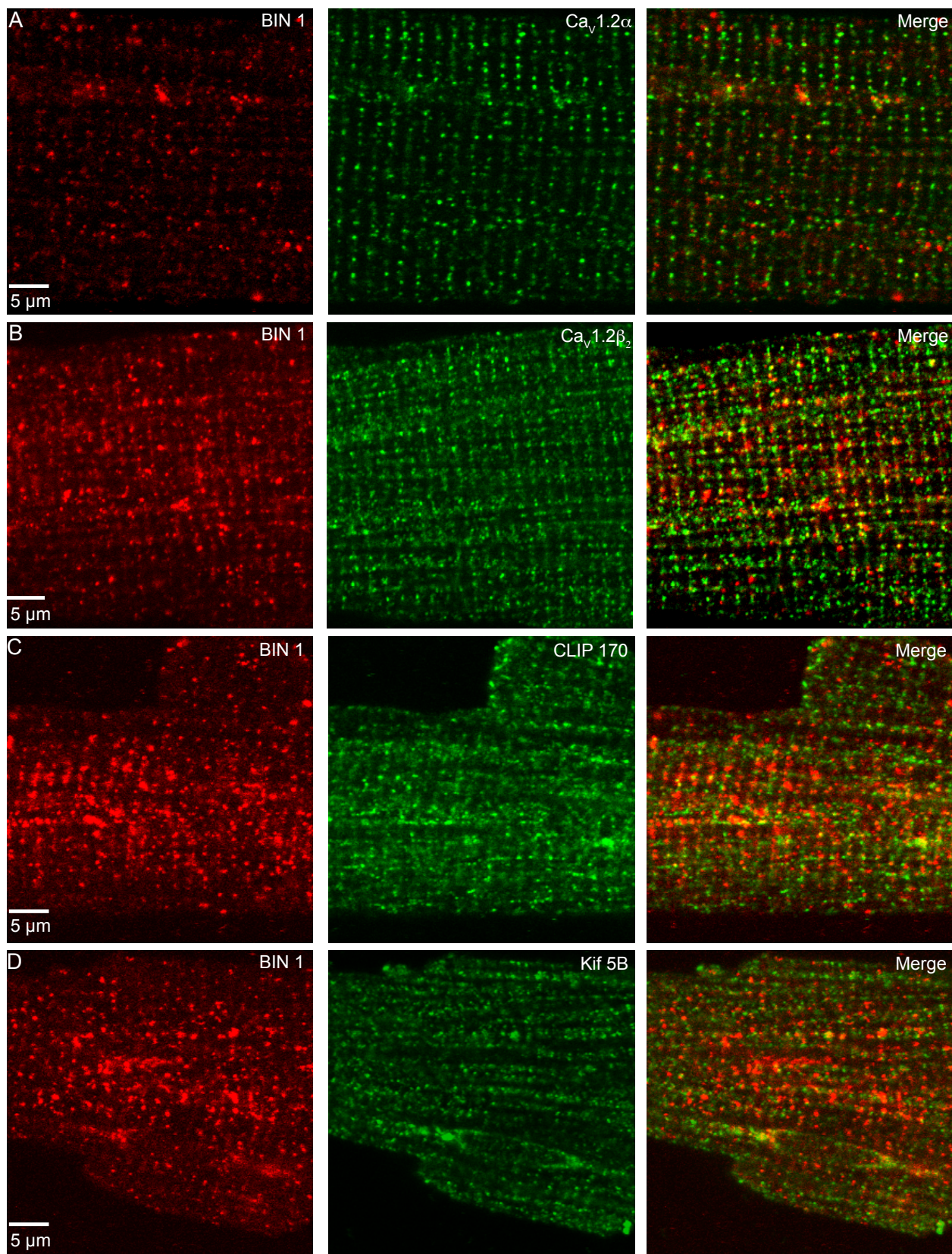


**Figure 4.1.** BIN1 colocalizes with several proteins in ventricular myocytes.

**A**, an exemplary ventricular myocyte dual-labeled with anti-BIN1 tagged with Alexa568 (left) and anti-Ca<sub>v</sub>1.2 $\alpha$  tagged with Alexa647 (middle), merged image shown (right); scale bar = 5  $\mu$ m. **B**, an exemplary ventricular myocyte dual-labeled with anti-BIN1 tagged with Alexa568 (left) and anti-Ca<sub>v</sub>1.2 $\beta$ <sub>2</sub> tagged with Alexa647 (middle), merged image shown (right); scale bar = 5  $\mu$ m. **C**, an exemplary ventricular myocyte dual-labeled with anti-BIN1 tagged with Alexa647 (left) and anti-CLIP170 tagged with Alexa568 (middle), merged image shown (right); scale bar = 5  $\mu$ m. **D**, an exemplary ventricular myocyte dual-labeled with anti-BIN1 tagged with Alexa647 (left) and anti-Kif5B tagged with Alexa647 (middle), merged image shown (right); scale bar = 5  $\mu$ m.

these two proteins have a high degree of co-localization in ventricular myocytes, as most both proteins can be found at the T-tubules (Figure 4.1A). The Pearson's coefficient between BIN1 and the  $\beta$  subunit of Ca<sub>v</sub>1.2 was similar ( $0.7 \pm 0.1$ ; n = 4) (Figure 4.1B). Surprisingly, CLIP170 also localized to the jSR and had a similar Pearson's coefficient with BIN1 ( $0.6 \pm 0.1$ ; n = 4) (Figure 4.1C). Lastly the Kif5B signal had a smaller overlap with BIN1 as measured with Pearson's coefficient ( $0.4 \pm 0.1$ ; n = 4) (Figure 4.1D). As Kif5B could be found anywhere along the MT rather than at the jSR, this finding is expected. Taken together, these findings indicate that BIN1, Ca<sub>v</sub>1.2 $\alpha$ , Ca<sub>v</sub>1.2 $\beta$ <sub>2</sub>, and CLIP170 all localize to the dyad and that Kif5B may approach the dyad periodically.

#### 4.3.2. Cultured ventricular myocytes exhibit increased MT dynamic disruptions.

Considering the expression of BIN1 and CLIP170 on the T-tubules and our hypothesis that these molecules might be implicated in MT stability around the T-tubules, these imaging results in fixed tissue emphasizing the importance of the

T-tubules led us to experimental strategies designed to disrupt or abolish T-tubules in order to assay MT dynamics in real time (Figure 4.2). It has been established that mouse ventricular myocytes lose their T-tubules and structure after being cultured (O'Connell, Ni et al. 2003). We cultured myocytes and assayed their structure and T-tubules by taking a Fourier transform of the T-tubule image acquired by dyeing with di-8-ANEPPS and quantifying the first harmonic peak, which is a measure of the consistency of distance between segments (Wei, Guo et al. 2010). We quantified this peak as T-Tubule power (Figure 4.2.E). We previously quantified MT dynamics in ventricular myocytes using an adeno-associated virus expressing EB3, a marker of MT (+) ends (AAV9-EB3-GFP) (Drum 2016). We used this same method to examine MT dynamics (Figure 4.2A-D). Figure 4.2A shows two kymographs from a representative myocyte showing MT growth under control conditions (top) and after 72 hours of culture (bottom). Labels show areas of growth, rescue, and catastrophe. Under control conditions, this MT grew at a rate that ranged from  $0.05\text{-}0.07\ \mu\text{m}\cdot\text{s}^{-1}$ . The MT recorded after 72 h in culture a similar rate of growth ( $0.06\ \mu\text{m}\cdot\text{s}^{-1}$ ) than the control, but was much more unstable and underwent catastrophe and rescue at much higher rates.

We used analysis from several kymographs generated from images of MTs to quantify multiple MT dynamics: growth rate and distance, shrinkage rate and distance, catastrophe rate, and rescue rate (Figure 4.2 B-D). MT growth rate and shrink rate were unchanged, as was growth distance. Shrink distance was

increased in cultured myocytes. Lastly, catastrophe rate rescue rate were also increased. These data show that, after being cultured, myocytes exhibit increased MT instability (Figure 4.2 B-D).

We assayed T-tubule power over time in culture and found that T-tubule decreased after every 24 h measurement, confirming the loss of T-tubules in our

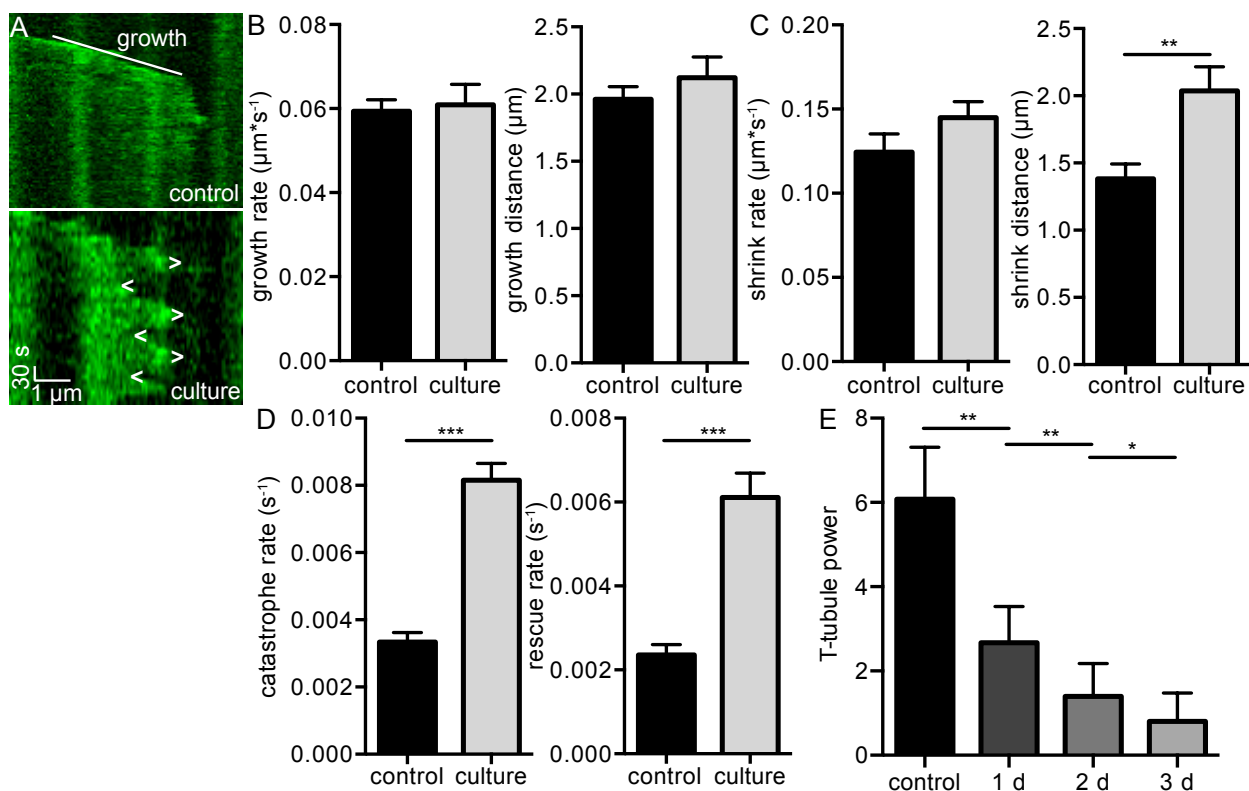


**Figure 4.2.** Live imaging of microtubules in cultured ventricular myocytes.

**A**, representative kymographs of a MT taken from a control myocyte (*above*) and a myocyte recorded after 72 h in culture (*below*), scale bars = 1  $\mu\text{m}$  horizontally and 30 s vertically. Growth directions indicated by line, catastrophe indicated by ">" and rescue indicated by "<". **B**, bar plots of the mean  $\pm$  S.E.M. of growth rate (*left*) and growth distance (*right*) of MTs from control myocytes (*black*) and myocytes after 72 h culture (*grey*). **C**, bar plots of the mean  $\pm$  S.E.M. of shrink rate (*left*) and shrink distance (*right*) of MTs from control myocytes (*black*) and myocytes after 72 h culture (*grey*). **D**, bar plots of the mean  $\pm$  S.E.M. of catastrophe rate (*left*) and rescue rate (*right*) of MTs from control myocytes (*black*) and myocytes after 72 h culture (*grey*). **E**, bar plot of the mean  $\pm$  S.E.M.

of T-tubule power from control myocytes and myocytes after 24 h, 48 h, and 72 h in culture.

culture cell model (Figure 4.2E). In addition, there were fewer horizontally moving MTs after 72 h culture (63%) compared to control (80%). Rather than moving horizontally, many of the MTs (34%) moved diagonally, perhaps due to the absence of T-tubules. The lack of T-tubules may have also been responsible for the increased distance of shrinkage exhibited by MTs from cultured cells (Figure 4.2C).

#### **4.3.3. Atrial myocytes have distinct expression of BIN1 and EB1 compared to ventricular myocytes.**

Another myocyte model of decreased T-tubules is in atrial myocytes, as most mouse atrial myocytes lack T-tubules, instead opting for Z-tubules, invaginations of the SR towards the plasma membrane (Bootman, Smyrniak et al. 2011). Using dual-label antibody staining, we compared the expression patterns of BIN1 and EB1, a marker of MT (+) ends, in isolated ventricular and atrial myocytes (Figure 4.3). As shown previously, EB1 expresses on the Z-lines as well as along the length of MTs and BIN1 expresses along the T-tubules in ventricular myocytes, thus leading to significant overlap (Figure 4.3A) (Drum, Yuan et al. 2016).

Indeed, the Pearson coefficient between these proteins in ventricular myocytes was  $0.6 \pm 0.1$ ;  $n = 4$ . However, the expression of these proteins in atrial myocytes was markedly different. Although BIN1 was still somewhat present along the Z-lines, its periodic signal was far weaker. Rather, it seemed as there were clusters

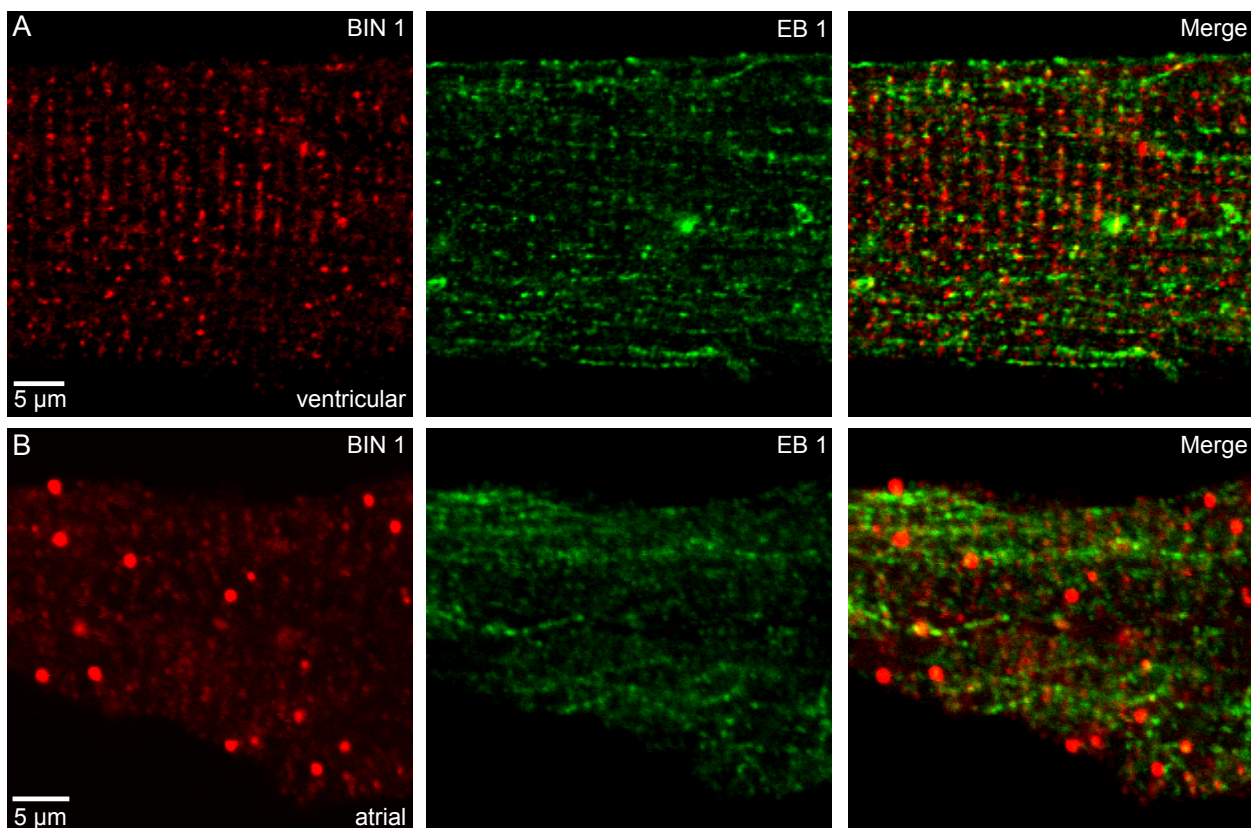


**Figure 4.3.** BIN1 and EB1 have variable expression in ventricular vs. atrial myocytes.

**A**, an exemplary ventricular myocyte dual-labeled with anti-BIN1 tagged with Alexa568 (left) and anti-EB1 tagged with Alexa647 (middle), merged image shown (right); scale bar = 5  $\mu$ m. **B**, an exemplary atrial myocyte dual-labeled with anti-BIN1 tagged with Alexa568 (left) and anti-EB1 tagged with Alexa647 (middle), merged image shown (right); scale bar = 5  $\mu$ m.

of BIN1 throughout the atrial myocyte, concentrated to the periphery of the cell (42%). These clusters were almost 1  $\mu$ m in diameter (Figure 4.3). EB1, seemed to lose all of its periodicity, instead expressing almost exclusively along MTs. Accordingly, the Pearson coefficient between these proteins in atrial myocytes was much lower ( $0.3 \pm 0.1$ ;  $n = 4$ ), coinciding with the probability that a MT was present along a section of the cell with a strong BIN1 periodic signal or BIN1 cluster.

#### 4.3.4. Atrial myocytes exhibit increased MT dynamic disruptions.

Having found dramatic differences in BIN1 and EB1 in these cell types, we assayed live MT dynamics in atrial myocytes. Figure 4.4A shows two kymographs from a representative ventricular (top) and atrial myocyte (bottom). Labels show areas of growth, rescue, and catastrophe. The MT recorded from the atrial myocyte was much more unstable and underwent catastrophe and rescue at much higher rates compared to the ventricular myocyte. In addition, the atrial myocyte did not pause, whereas the ventricular myocyte was paused for the majority of the recording.

We used analysis from several kymographs generated from images of MTs to quantify multiple MT dynamics: growth rate and distance, shrinkage rate and distance, catastrophe rate, and rescue rate (Figure 4.4B-D). MT growth rate and shrink rate was reduced in atrial myocytes, but growth distance and shrink distance were unchanged. Lastly, catastrophe rate rescue rate were also increased. These data show that atrial myocytes exhibit increased MT instability (Figure 4.4B-D). There were two other attributes of MTs in atrial myocytes that were different compared to ventricular myocytes. First, atrial myocytes spent little time in pause (10%) compared to ventricular myocytes (56%). Rather, atrial myocytes are usually growing and almost always alternating between growth and shrink (Figure 4.4E). Second, whereas the vast majority (80%) of MTs in ventricular myocytes moved horizontally, in atrial myocytes, just as many MTs

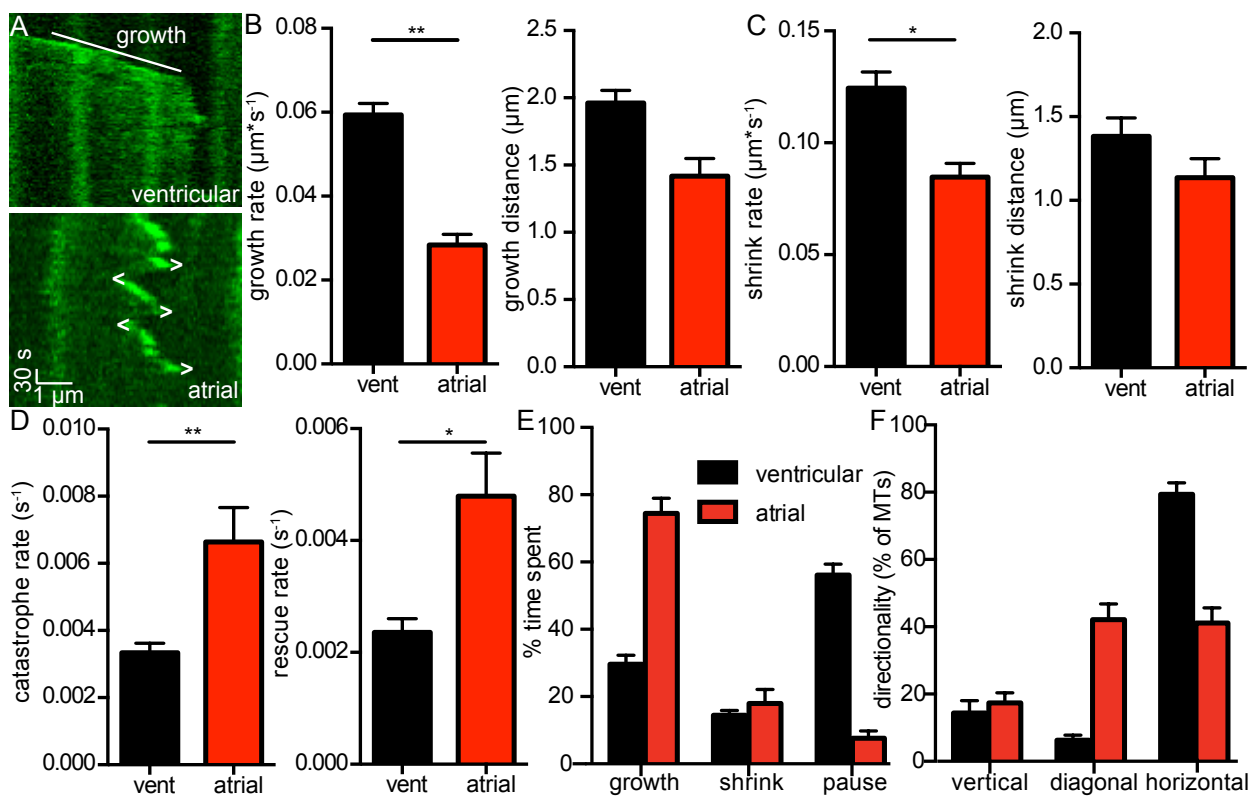


**Figure 4.4.** Live imaging of microtubules in atrial myocytes.

**A**, representative kymographs of a MT taken from a ventricular (*above*) and atrial (*below*) myocyte, scale bars =  $1\mu\text{m}$  horizontally and 30 s vertically. Growth directions indicated by line, catastrophe indicated by “>” and rescue indicated by “<”. **B**, bar plots of the mean  $\pm$  S.E.M. of growth rate (*left*) and growth distance (*right*) of MTs from ventricular (*black*) and atrial (*red*) myocytes. **C**, bar plots of the mean  $\pm$  S.E.M. of shrink rate (*left*) and shrink distance (*right*) of MTs from ventricular (*black*) and atrial (*red*) myocytes. **D**, bar plots of the mean  $\pm$  S.E.M. of catastrophe rate (*left*) and rescue rate (*right*) of MTs from ventricular (*black*) and atrial (*red*) myocytes. **E**, bar plot of the mean  $\pm$  S.E.M. of the percentage of time spent in growth, shrink, and pause from ventricular (*black*) and atrial (*red*) myocytes. **F**, bar plot of the mean  $\pm$  S.E.M. of the directionality of MTs in ventricular (*black*) and atrial (*red*) myocytes.

moved diagonally as they did horizontally (41% vs. 40%, respectively) (Figure 4.4F).

#### 4.3.5. Kif5B colocalizes with other proteins in T-tubules.

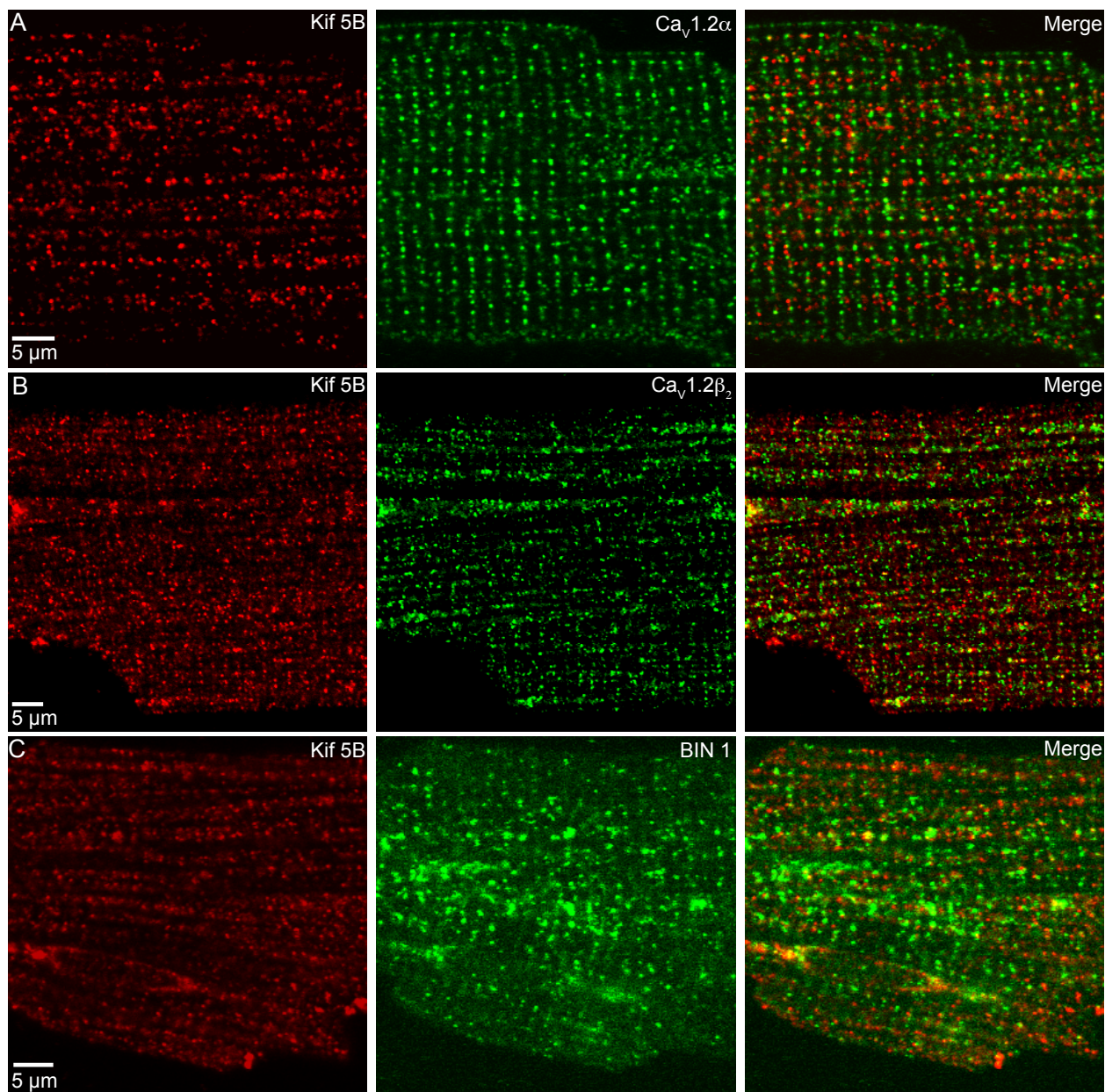


**Figure 4.5.** Kif5B colocalizes with several proteins in ventricular myocytes.

**A**, an exemplary ventricular myocyte dual-labeled with anti-Kif5B tagged with Alexa568 (left) and anti-Ca<sub>v</sub>1.2α tagged with Alexa488 (middle), merged image shown (right); scale bar = 5 μm. **B**, an exemplary ventricular myocyte dual-labeled with anti-Kif5B tagged with Alexa568 (left) and anti-Ca<sub>v</sub>1.2β<sub>2</sub> tagged with Alexa647 (middle), merged image shown (right); scale bar = 5 μm. **C**, an exemplary ventricular myocyte dual-labeled with anti-Kif5B tagged with Alexa568 (left) and anti-BIN1 tagged with Alexa647 (middle), merged image shown (right); scale bar = 5 μm.

Whereas in ventricular myocytes  $Ca_v1.2$  is distributed along the periphery of the cell as well as throughout the T-tubules, in atrial myocytes,  $Ca_v1.2$  is limited to the cell periphery (Bootman, Smyrniak et al. 2011). It has also been shown that BIN1 is important in trafficking  $Ca_v1.2$  to the membrane (Hong, Smyth et al. 2010). Given the differences in BIN1 expression in atrial myocytes, we tested the hypothesis that Kif5B colocalizes with proteins in the dyad.

Thus, we directly visualized BIN1 in cardiomyocytes using immunohistochemistry and compared its expression to that of several other proteins (Figure 4.5). Using the technique of dual-antibody staining, we were able to image Kif5B with several other proteins, including the  $\alpha$  subunit of  $Ca_v1.2$ , the  $\beta$  subunit of  $Ca_v1.2$ , and BIN1. Although Kif5B did not colocalize extremely well with  $Ca_v1.2\alpha$  (Pearson coefficient =  $0.5 \pm 0.1$  ( $n = 4$ )) or BIN1 (Pearson coefficient =  $0.5 \pm 0.1$  ( $n = 4$ )), Kif5B showed high overlap with  $Ca_v1.2\beta_2$  (Pearson coefficient =  $0.7 \pm 0.1$  ( $n = 4$ )) (Figure 4.5A-C). Taken together, these findings indicate that Kif5B may approach the dyad periodically and that it may be associated in the trafficking of the  $\beta_2$  subunit to the dyad.

#### 4.3.6. Kinesin-1 is the motor responsible for $Ca_v1.2\beta_2$ trafficking

We created an adeno-associated virus, AAV9-Kif5B-DN-RFP, which expressed a dominant negative form of the Kif5B heavy chain, thus disabling the kinesin-1 motor. Using this motor, we were able to evaluate the effect of Kif5B on  $Ca^{2+}$  currents in ventricular myocytes. We found that  $I_{Ca}$  was dramatically decreased in

both current density and integral upon expression of Kif5B-DN (Figure 4.6A-C), indicating that a defect in kinesin-1 function impacted  $\text{Ca}^{2+}$  current. We performed a co-immunoprecipitation and found that Kif5B and  $\text{Ca}_v1.2\beta_2$  reciprocally co-precipitated (Figure 4.6D). Taken together, these findings indicate that Kif5B is responsible for trafficking  $\text{Ca}_v1.2\beta_2$  to the membrane, and impairment of this trafficking leads to defects in  $I_{\text{Ca}}$ .

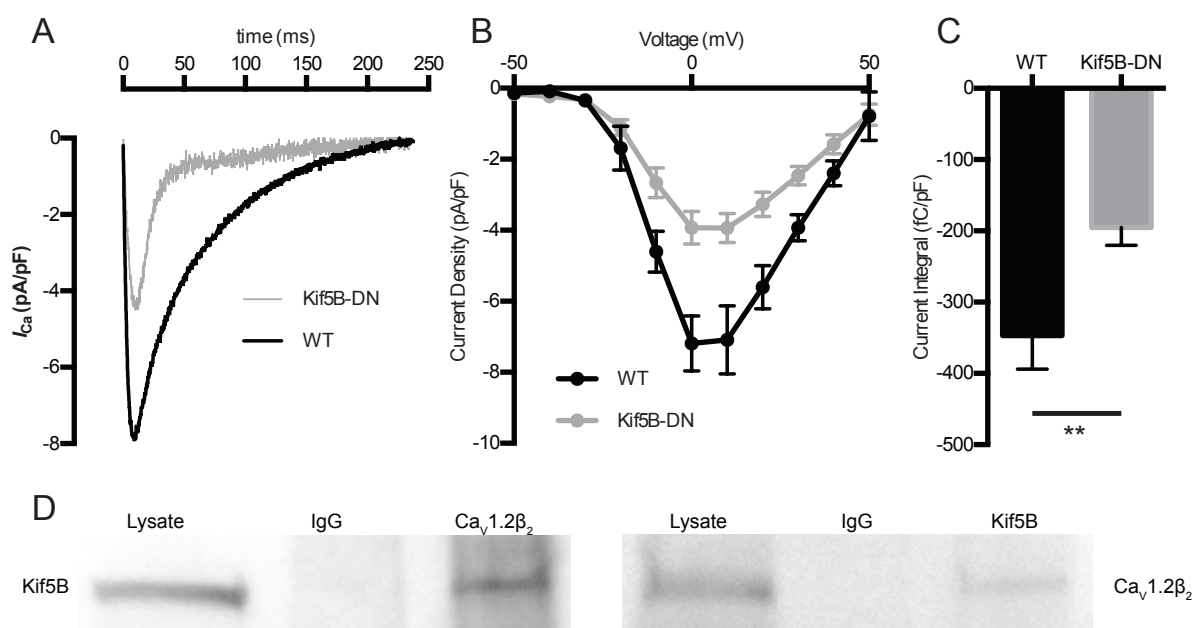


**Figure 4.6.** Kif5B is the motor transporting  $\text{Ca}_v1.2\beta_2$ .

**A**, representative  $I_{\text{Ca}}$  records normalized to peak from WT (black) and Kif5B-DN (grey) myocytes. Currents were evoked by a voltage step from -50 mV to 0 mV in the presence of 2 mM external  $\text{Ca}^{2+}$ . **B**, mean  $\pm$  S.E.M. of current-voltage relationship of  $I_{\text{Ca}}$  on negative y-axis, for both WT (black) and Kif5B-DN (grey) myocytes. **C**, bar plot of the mean  $\pm$  S.E.M. of the current integral (fC/pF) in WT (black) and Kif5B-DN (grey) myocytes. **D**, Co-immunoprecipitation Western blot Kif5B expression in lysate (positive control) (lane 1), IgG (negative control) (lane 2), and bound to anti- $\text{Ca}_v1.2\beta_2$  (lane 3) (left). Right, co-immunoprecipitation Western blot  $\text{Ca}_v1.2\beta_2$  expression in lysate (positive control) (lane 1), IgG (negative control) (lane 2), and bound to anti-Kif5B (lane 3).

#### 4.4. Discussion

This study expands previous work exploring MT dynamics in atrial myocytes and linking MT dynamics to  $\text{Ca}^{2+}$  signaling. To summarize, we have discovered five novel observations relating to cardiac physiology: 1) BIN1, EB1, and CLIP170 all colocalize to the dyad; 2) T-tubules are important for anchoring and stabilizing cardiac MTs; 3) BIN1 expresses in clusters and EB1 is not expressed on the Z-lines in atrial cells; 4) MTs have more varied directionality and lack pausing in atrial myocytes; and 5) kinesin-1 is the molecular motor responsible for trafficking  $\text{Ca}_v1.2\beta_2$  to the membrane in ventricular myocytes. These findings increase current knowledge of both ventricular and atrial physiology in the context of both the composition of the T-tubules as well as MT dynamics. In particular, this is the first study to link MT proteins, namely CLIP170 and EB1, with those of  $\text{Ca}^{2+}$  signaling, BIN1 and  $\text{Ca}_v1.2\beta_2$ .

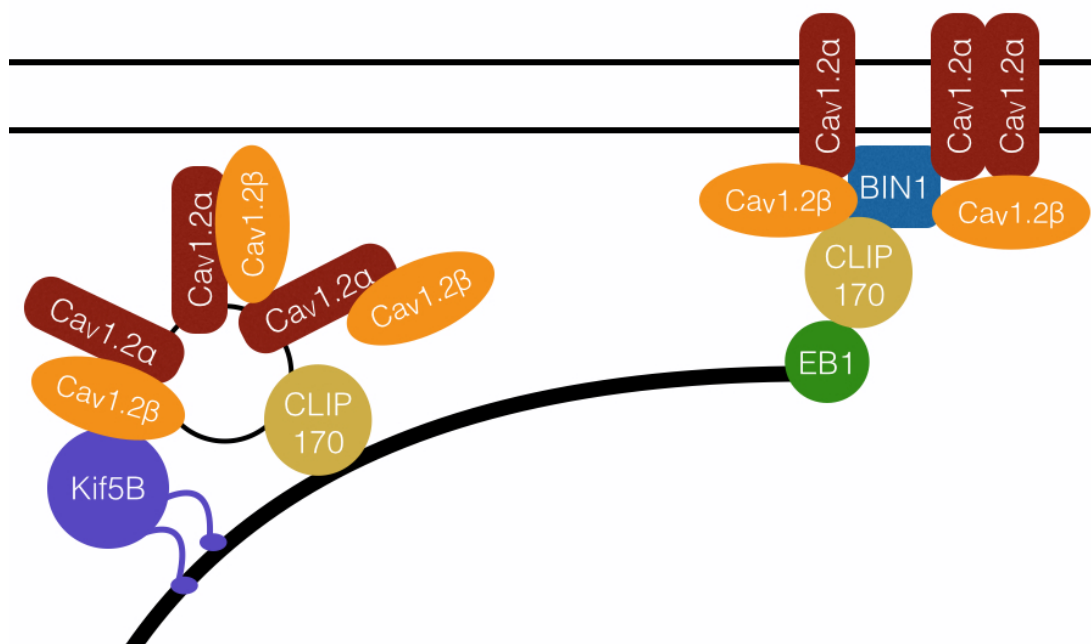


**Figure 4.7.** Proposed model of Ca<sub>v</sub>1.2 transport.

Kinesin 1 walks along MTs towards the plus-end carrying an endosome of Ca<sub>v</sub>1.2 subunits. The microtubule end is anchored to the T-tubule via EB1-CLIP170-BIN1 complex.

From these findings, we can propose a model of this MT-Ca<sup>2+</sup> machinery interaction. Kinesin-1 is the molecular motor that associates with Ca<sub>v</sub>1.2β<sub>2</sub>, and it moves processively towards the MT plus-end, potentially in an endosome.

Although it is unclear, given that the β subunit is required for Ca<sub>v</sub>1.2α expression and given the expression profile of Ca<sub>v</sub>1.2α and Kif5B, we hypothesize that Ca<sub>v</sub>1.2α also travels in this endosome. CLIP170 associates periodically with MTs, although it requires EB1 to tip track, so it is possible that CLIP170 helps anchor the endosome to the MT. At the sarcolemma, Ca<sub>v</sub>1.2α and Ca<sub>v</sub>1.2β are functional and cluster with BIN1, which creates the T-tubule and serves as the anchor for the MT via an EB1-CLIP170-BIN1 complex.

This model is hypothetical and still needs validation in some specific areas. For example, more work needs to be done establishing how Ca<sub>v</sub>1.2α associates with the β subunit, and whether CLIP170 aids in transport. On the T-tubule end, definitive proof of BIN1 interacting with CLIP170 more than just a co-localization would be highly informative. To that end, one avenue would be to explore the presence of SxIP domains in BIN1, which is a common method to explore whether a protein interacts with EB1. This would show whether CLIP170 is needed for BIN1 to interact with EB1 or if the two can interact together. A preliminary search shows some SxIP domains in BIN1, which is not a traditional SxIP domain but has been shown to interact with EB1 (Jiang, Toedt et al. 2012).

More research needs to be done here, perhaps transfecting BIN1 into cultured cells and assaying if it tip tracks and, if it does, mutating the SSLP to attempt to negate tip tracking.

This research briefly addresses the possible role of CLIP170, but again, more work needs to be done here. Meunier et al recently performed research on CLIP170 in HeLa cells and found that BIN1 and CLIP170 associate and; moreover, CLIP170 is essential for formation of T-tubules by BIN1. They suggest that BIN1 may be the anchoring point for CLIP170 on the plasma membrane (Meunier, Quaranta et al. 2009). Confirming these findings in cardiac tissue would be highly informative. In addition, CLIP170 often associates with dyneins more than kinesins, so it is possible that dyneins may be involved in transporting proteins in the dyad (Coquelle, Caspi et al. 2002). In addition, CLIP170 has been shown to pull on/anchor microtubules, which could explain the stabilization and pausing of MTs on T-tubules (Tai, Dujardin et al. 2002). One experiment could be to look at expression of CLIP170 in atrial myocytes, as this is a cell type that does not have MT pausing. In addition, CLIP170 is regulated by phosphorylation and it is possible to disrupt its function with non-phosphorylatable mutants, although this would likely require the production of an AAV9 construct (Kakeno, Matsuzawa et al. 2014).

Similarly, more work needs to be done addressing the role of BIN1. Our research highlights the importance of T-tubules in MT stabilization and implicates BIN1 in

trafficking via colocalization imaging, but does not clearly establish the influence of BIN1 on MT stabilization. One possible experiment would be to image BIN1 in cultured cells and see how BIN1 changes as the myocyte loses its T-tubules. We hypothesize that, as BIN1 is essential for T-tubule formation, that cultured myocytes experience a loss in BIN1 corresponding with the increase in MT dynamic disruption. In addition, perhaps a better experiment would be to inject a BIN1 heterozygous mouse with EB3-GFP to assay MT dynamics in ventricular myocytes.

We visualized and quantified live MT dynamics in atrial myocytes for the first time. Very little is known about MTs in cardiac tissue and about atrial myocytes in general, so the intersection of these two research areas is currently sparse. Our work is the first to image BIN1 and EB1 in atrial myocytes, showing a distinct break from the patterns of expression seen in ventricular myocytes. Notably, EB1 does not express along the Z-lines in atrial myocytes, indicating that EB1 binds to proteins on the T-tubules rather than the jSR. This coincides with our hypothesis that BIN1 binds to CLIP170 which binds to EB1 on T-tubules. BIN1 also expressed differently, seeming to express in large clusters largely localized to the cell periphery with far less expression on the Z-lines. More research needs to be done exploring these clusters; however, Smyrniak et al recently imaged  $Ca_v1.2$  in atrial myocytes and found that the channels expressed mainly around the periphery of the cell with only small patches of staining within the center of the myocyte (Smyrniak, Mair et al. 2010). Thus, it is perhaps expected that BIN1 is

notably less prevalent in the center of atrial myocytes. Lastly, the lack of T-tubules and differences in BIN1 expression seem to have a direct impact on MT dynamics. Not only were catastrophe and rescue rates increased in atrial myocytes, but the MTs no longer were directionally preferenced toward the horizontal orientation and lost the ability to pause. More research needs to be done determining what causes the directionality preference of MTs in ventricular myocytes.

Lastly, our findings highlight the importance of the  $\beta_2$  subunit in  $Ca_v1.2$  localization. Previous studies indicate that  $Ca_v\beta$  enhances  $Ca_v\alpha$  localization by exposing ER export signals on  $Ca_v1.2$  when it is newly synthesized and preventing  $Ca_v\alpha$  degradation when  $Ca_v1.2$  is on the membrane (Birnbaumer, Qin et al. 1998). In addition,  $Ca_v\beta$  enhances  $Ca_v1.2$  overall current. Our research shows that kinesin-1 is the molecular motor responsible for  $Ca_v\beta$  trafficking. Loss of kinesin-1 function by expression of a dominant-negative kinesin to compete resulted in a loss of current density in  $Ca_v1.2$ . It is unknown if this decrease was due to loss of the  $Ca_v\beta$  subunit on the channel or due to loss of  $Ca_v1.2\alpha$  subunits as well. More research teasing out this issue, for example, conducting a surface biotinylation Western blot on  $Ca_v1.2\alpha$  in mice injected with Kif-5B-DN compared to control, would elucidate this issue.

## Chapter 5: Elucidating the biogenesis and role of junctional sarcoplasmic reticulum motility in normal and pathological $\text{Ca}^{2+}$ signaling

### 5. Summary

Excitation-contraction (EC) coupling is the coordinated process by which an action potential (AP) triggers cell contraction. It is initiated in specialized regions (called “dyads”) where the junctional SR (jSR) comes into close apposition (20-30 nm) to the sarcolemma of cardiac myocytes. Activation of sarcolemmal voltage-gated  $\text{Ca}_v1.2$  channels during the AP causes a small influx of  $\text{Ca}^{2+}$  that activates ryanodine receptors (RyR) expressed in the nearby jSR via the mechanism of  $\text{Ca}^{2+}$ -induced  $\text{Ca}^{2+}$  release (CICR). Previous work has led to the formulation of a model of EC coupling in which the communication between  $\text{Ca}_v1.2$  and RyR channels via local  $\text{Ca}^{2+}$  signals is critically dependent on the spatial organization of the sarcolemma and jSR. A central tenet of this model is that dyads must be stable in order to ensure the fidelity and strength of EC coupling, and even small changes in the separation between RyR and  $\text{Ca}_v1.2$  channels can induce dramatic changes in EC coupling (Gomez, Valdivia et al. 1997, Soeller and Cannell 1997).

We tested a key aspect of this model: whether dyads are static subcellular structures. To do this, we developed a novel strategy to monitor, for the first time, jSR motility in living, acutely dissociated adult ventricular myocytes. By injecting

mice with an adeno-associated virus serotype 9 (AAV9) expressing the jSR protein triadin tagged with a photo-activatable enhanced GFP, we tracked jSR-associated fluorescence. We found that the jSR is not static. Instead, our data are consistent with a model in which the reproducibility of EC coupling results from the activation of a temporally averaged number of SR  $\text{Ca}^{2+}$  release units forming and dissolving SR-sarcolemmal junctions. We discovered multiple modalities of SR motility and jSR biogenesis. We investigated the mechanisms controlling SR mobility as well as its implications under physiological and pathological conditions. The molecular motors dynein and kinesin-1 are active participants in jSR formation and stability. Furthermore, uncoupling the jSR from the T-tubules leads to dysfunctional  $\text{Ca}^{2+}$  signaling. Lastly, we found that the jSR motility increases following myocardial infarction (MI). Taken in totality, these findings challenge the long-held view that the jSR is an immobile structure, elucidate the mechanisms underlying sarcoplasmic reticulum (SR) motility in ventricular myocytes, and discover how these mechanisms alter excitation-contraction (EC) coupling in these cells.

## 5.1. Introduction

The function of the heart is to pump blood into the pulmonary and systemic circulation. To achieve this, each of the four chambers of the heart must contract in a specific sequence. The trigger for cardiac contraction is an action potential (AP). Under physiological conditions, each cardiac cycle starts in the sinoatrial node, where a specialized group of cells spontaneously fire APs. This AP propagates from SA node cells to atrial muscle cells and, with a delay, eventually reaches the ventricles through the atrio-ventricular node. For a 72-year-old human, this cycle would have repeated itself a total of 2-3 billion times.

The chain of events that couple an AP to contraction is collectively known as excitation-contraction (EC) coupling. Classical biophysics state that the strength of cardiac contraction is determined by multiple factors including  $\text{Ca}^{2+}$  influx, sarcoplasmic reticulum (SR)  $\text{Ca}^{2+}$  release, and the sensitivity of contractile proteins to cytosolic  $\text{Ca}^{2+}$ . The reproducibility of the heartbeat given these variations in EC coupling is remarkable. To provide a quantitative measurement of EC coupling reproducibility, we determined the coefficient of variation (COV) of the  $[\text{Ca}^{2+}]_i$  transient during EC coupling. The COV is defined as the standard deviation divided by the mean. We found that the COV of the AP-evoked intracellular  $\text{Ca}^{2+}$  ( $[\text{Ca}^{2+}]_i$ ) transient is approximately 0.12. It is worth noting that the electrical signals produced by rod cells in the retina, generally considered a highly reliable detector of single photons, in response to light have a COV of

about 0.3 (Field and Rieke 2002). This is much smaller than the COV expected for a process composed of first-order processes, such as the open-close transition of an ion channel. Thus, under physiological conditions, EC coupling in cardiac muscle is remarkably reproducible.

To provide insights into the potential mechanisms underlying the reproducibility of the  $[Ca^{2+}]_i$  transient, it is pertinent to review key events during EC coupling. Activation of sarcolemmal voltage-gated calcium channels ( $Ca_v1.2$ ) during the AP causes a small influx of  $Ca^{2+}$  that activates ryanodine receptors (RyRs) in the nearby junctional SR (jSR) via the mechanism of calcium induced calcium release. The small distance and volume separating  $Ca_v1.2$  and RyR channels ensures that even brief openings of  $Ca_v1.2$  channels allow enough  $Ca^{2+}$  to enter the cell and increase local  $[Ca^{2+}]_i$  high enough to activate nearby RyRs. A corollary of this model is that the fidelity of local EC coupling is critically dependent on the structural stability of the dyad and hence the separation between RyR and  $Ca_v1.2$  channels. However, contrary to this view, we find that the network and junctional SR (jSR) are highly dynamic.

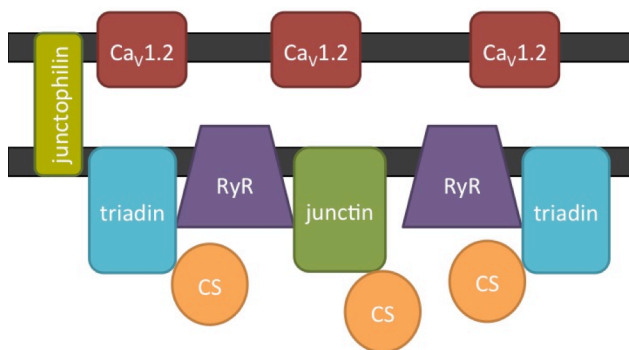


**Figure 5.1.** Cartoon of the proposed structure of the jSR.

The jSR is a complex structure with several proteins contributing to its architecture and function. Figure 5.1 shows a cartoon of the proposed protein composition of the jSR, which we will use to give the reviewer background information about this structure. Let us start with junctophilin. Junctophilin is a protein that is anchored to the jSR in its C-terminus and contacts the T-tubules through lipid-interacting motifs in its N-terminus (Garbino and Wehrens 2010). These proteins are hypothesized to provide a molecular bridge between the jSR and the T-tubules. Calsequestrin (CS) is a  $\text{Ca}^{2+}$ -binding protein that ensures high concentration of  $\text{Ca}^{2+}$  close to RyRs (Rossi, Barone et al. 2008). Two proteins, junctin and triadin, anchor CS to the SR membrane. Because these proteins contain binding sites for the RyR as well as for CS, they allow conformational coupling between the  $\text{Ca}^{2+}$ -binding protein and the  $\text{Ca}^{2+}$  release channel (Beard, Laver et al. 2004). Both triadin and junctin knockout mice show changes in the jSR architecture, and, with RyRs and CS, form the “core complex of proteins required for  $\text{Ca}^{2+}$  release” (Zhang, Kelley et al. 1997, Glover, Quinn et al. 2002). We targeted triadin as a marker of jSR because it is hypothesized to maintain dyad structure, contribute to healthy EC coupling, recruit microtubules and molecular motors, and is localized to only the jSR (Fourest-Lieuvain, Rendu et al. 2012).

New research shows that changes in the T-tubule sarcolemma-SR junction can likely contribute to  $\text{Ca}^{2+}$  instability during pathology. Zhang *et al* found that T-tubules and SR physically uncouple in human heart failure (Zhang, Li et

al. 2013). Furthermore, Louch *et al.* showed that, in heart failure, dyssynchronous  $\text{Ca}^{2+}$  transients are a result of T-tubule disorganization (Louch, Hake et al. 2013). Song *et al* found that remodeled T-tubules move away from the Z-lines in heart failure, leading to loss of local control and  $\text{Ca}^{2+}$  instability (Song, Sobie et al. 2006). Recently, Zhang *et al* has shown that microtubule densification is implicated in T-tubule remodeling and disruption of dyadic proteins in heart failure (Zhang, Chen et al. 2014). Similar studies have been done in other pathological states besides heart failure. Wagner *et al*, for example, used STED nanoscopy to assay T-tubule remodeling post-myocardial infarction (MI) and found proliferative membrane changes, early EC uncoupling, and SR network fracturing (Wagner, Lauterbach et al. 2012).

In the following chapter, by elucidating the role of the SR in normal physiology, I uncover a new potential mechanism by which the cell could regulate  $\text{Ca}^{2+}$  signaling. We tested a new model for  $\text{Ca}^{2+}$  signaling in which the T-tubule sarcolemma-SR junction is dynamic and plays a significant role in cardiac physiology. This model represents a departure from long-standing models of  $\text{Ca}^{2+}$  signaling in which the T-tubule sarcolemma-SR junction is thought to be static. jSR motility is a new fundamental phenomenon with profound implications in cardiac pathophysiology. The dynamic jSR creates another place of regulation in  $\text{Ca}^{2+}$  signaling; moreover, this regulation could display exquisitely local precision. Evidence that the jSR and T-tubules are disrupted in pathology such

as heart failure and MI suggests that restoring or protecting the T-tubule sarcolemma-SR junction could reduce aberrancies in  $\text{Ca}^{2+}$  signaling and protect cardiac function.

## 5.2. Methods

### 5.2.1. Isolation of mouse ventricular myocytes

Mice were euthanized with a lethal dose of sodium pentobarbital administered intra-peritoneally as approved by the University of Washington Institutional Animal Care and Use Committee. Ventricular myocytes were isolated using a Langendorff perfusion apparatus as previously described (Drum, Dixon et al. 2014). The isolated ventricular myocytes were kept either at room temperature (22 °C) or at 37 °C in Tyrode's solution containing (mM): 140 NaCl, 5 KCl, 10 HEPES, 10 glucose, 2 CaCl<sub>2</sub>, and 1 MgCl<sub>2</sub>; pH = 7.4 with NaOH, and used 0.5–8 h after isolation.

### 5.2.2. Myocardial infarction

The myocardial infarction model was produced as described previously (Kolk, Meyberg et al. 2009). Briefly, mice were anesthetized by isoflurane and non-invasively intubated. A left lateral thoracotomy was performed to expose the heart and the associated vasculature. The left ascending coronary artery was permanently ligated with a silk ligature and the thoracotomy was then closed. The infarct was obvious upon gross examination and myocytes were isolated from the left ventricle 48-72 h after the procedure.

### 5.2.3. Viral expression system

Adeno-associated virus serotype 9 (AAV9) expressing EB3-EGFP was generated by Vector Biolabs. Mice were anesthetized by isoflurane and injected retro-orbitally with AAV9s encoding the following: TRD tagged with AGFP (AAV9-TRD-AGFP); a SR/ER retention signal tagged with RFP (AAV9-SR-RFP); an shRNA disruption expression of dynein tagged with RFP (AAV9-Dync1h1-shRNA-RFP); and a dominant negative version of the kinesin 1 motor tagged with RFP (AAV9-Kif5B-DN-RFP) (Inagaki, Fuess et al. 2006, Bish, Morine et al. 2008). The photo-activatable GFP is a protein that fluoresces only after brief illumination with 405 nm light (Patterson and Lippincott-Swartz 2002). After activation, AGFP can be excited with 473 nm light and has an emission peak around 510 nm. The peak of the excitation and emission spectra of RFP is 560 nm and 590 nm, respectively. To allow expression of the proteins and shRNA, experiments were performed at least 3 weeks after virus injection.

#### 5.2.4. Immunocytochemistry and imaging

Ventricular myocytes were imaged using an Olympus FluoView 1000 confocal microscope equipped with an Olympus 60x (NA = 1.49) oil immersion lens (Drum, Dixon et al. 2014). Experiments were performed while the Zero-Drift Control (ZDC) module of our Olympus FV1000 confocal was activated, continuously correcting for drifts and thus maintaining a focal point throughout the duration of the experiment. In some myocytes, 10  $\mu$ M di-8-ANEPPS was

loaded into the cells by 20 min incubation, 10 min pellet, and resuspension in Tyrode's solution in order to visualize the T-tubules.

Super-resolution imaging was performed as described previously (Mercado, Baylie et al. 2014, Dixon, Moreno et al. 2015). Briefly, cardiomyocytes were fixed by incubating in 4% paraformaldehyde in PBS at 37 °C for 30 m, then washed with PBS and blocked for 1 h at room temperature in 50% SEA BLOCK (Thermo Fisher Scientific Waltham, MA) and 0.5% w/v Triton X-100 in PBS (blocking buffer). Cells were probed with an anti-Ca<sub>v</sub>1.2 $\alpha$  antibody (Millipore, Darmstadt, Germany, MAB13170) and anti-triadin antibody (Santa Cruz Labs. SC33393) diluted to 1  $\mu$ g/mL in blocking buffer by incubating overnight at 4 °C. Cells were washed extensively with 20% Sea Block three times. Cells were then incubated for 1 h at room temperature with donkey anti-goat Alexa Fluor 647 and chicken anti-mouse Alexa Fluor 568 in blocking buffer. Myocytes were washed with 20% Sea Block three times and then mounted for imaging. The cells were mounted with imaging buffer containing: MEA-GLOX (MEA is cysteamine, GLOX is 0.56 mg/mL glucose oxidase, 34  $\mu$ g/mL catalase, 10% w/v glucose), TN buffer (50 mM Tris pH 8.0, 10 mM NaCl). Slides were sealed with Twinsil (Picodent, Wiperfürth, Germany) sealant.

GSD super-resolution images of MTs and EB1 in fixed ventricular myocytes were generated with a Leica SR GSD 3D system consisting of a Leica DMI6000 B TIRF microscope equipped with a Leica oil-immersion HC PL APO 160x (NA =

1.43) objective, four laser lines (405 nm/30 mW, 488 nm/300 mW, 532 nm/500mW, and 642 nm/600mW), and an Andor iXon3 EM-OCD. Images were collected in TIRF mode with a 100 Hz frame rate for 20,000-100,000 frames using Leica Application Suite (LAS AF) software.

#### 5.2.5. Image analysis

For nearest neighbor distance, GSD image files were thresholded and converted to binary and merged together. Clusters were identified and area of overlap was calculated and straight lines were drawn from central  $Ca_v1.2$  signal to each TRD signal in the cluster. Overlapped areas, seen as yellow, were considered 0.

For recordings of virally-expressed TRD, each cell was scanned in the z-axis and recorded at a plane where the predominant number of TRDs could be seen and tracked, usually at the cell surface. Many precautions were taken to ensure these areas are indeed dynamic and not mere changes in fluorescence. There are many possible reasons why fluorescence may decrease; a change in the absorption/extinction coefficient, a change in quantum yield, a change in laser power, focus, or other microscope settings, or a decrease in the number of fluorescent molecules may all affect the signal. While the quantum yield and fluorescent coefficients are constant within a fluorophore, the other two variables could change in experimental design. To control for experimental manipulation variability, once an experiment was started, none of the laser settings were

changed. Thus, only the number of fluorescent molecules could change in our experimental paradigm, either by a change in SR movement or by photobleaching. Although photobleaching could potentially confound our analysis, its uniform nature in decreasing the fluorescence signal helps differentiate it from SR segment movement. Myocytes were corrected for photobleaching using the Histogram Matching feature of Photocorrection in ImageJ (Montenegro Gouveia, Leslie et al. 2010). In order to verify that disappearing SR segments are true changes in the dyad and not artifacts of photobleaching, the SR segment must either 1) be completely surrounded by other segments that do not change, or change in a different way than the SR segment in question, or 2) increase in fluorescence later in the recording. Cells were analyzed blind to experimental condition via name randomization (Labbe, Maddox et al. 2003, Peris, Wagenbach et al. 2009).

#### 5.2.6. Real Time qRT-PCR

For this study, dynein mRNA was quantified using real time quantitative RT-PCR as previously described (Amberg, Bonev et al. 2003, Amberg and Santana 2003). Total RNA was purified from mouse left ventricle using TRIzol reagent (Invitrogen, Waltham, MA) and RNeasy Mini Kit (Qiagen). The RNA was reverse transcribed using Super Script III First-Strand Synthesis System (Invitrogen). qPCR was used to confirm the expression of dynein and compared using GAPDH as a reference.

### 5.2.7. Detubulation

Myocytes were detubulated by applying 10 mM formamide to experimental dish during recording. Organization of the SR and T-tubules before and after detubulation by taking a fast Fourier transform of the data and quantifying the first harmonic peak (referred to here as SR or T-tubule power), which is a measure of the consistency of distance between segments.

### 5.2.8. Statistics

Data are presented as mean  $\pm$  standard error of the mean (S.E.M.). Two-sample comparisons were made using a Student's *t* test (\**P* < 0.05, \*\**P*  $\leq$  0.01).

### 5.3. Results

#### 5.3.1. Triadin and Ca<sub>v</sub>1.2 colocalize under super-resolution imaging

We used super-resolution nanoscopy to image two proteins in the dyad: Ca<sub>v</sub>1.2 on the sarcolemma and triadin on the jSR. On TIRF microscopy, the signals completely overlapped in areas that were approximately 2 μm apart, indicating T-tubule periodicity as expected (Figure 5.2A). Upon switching to super-resolution

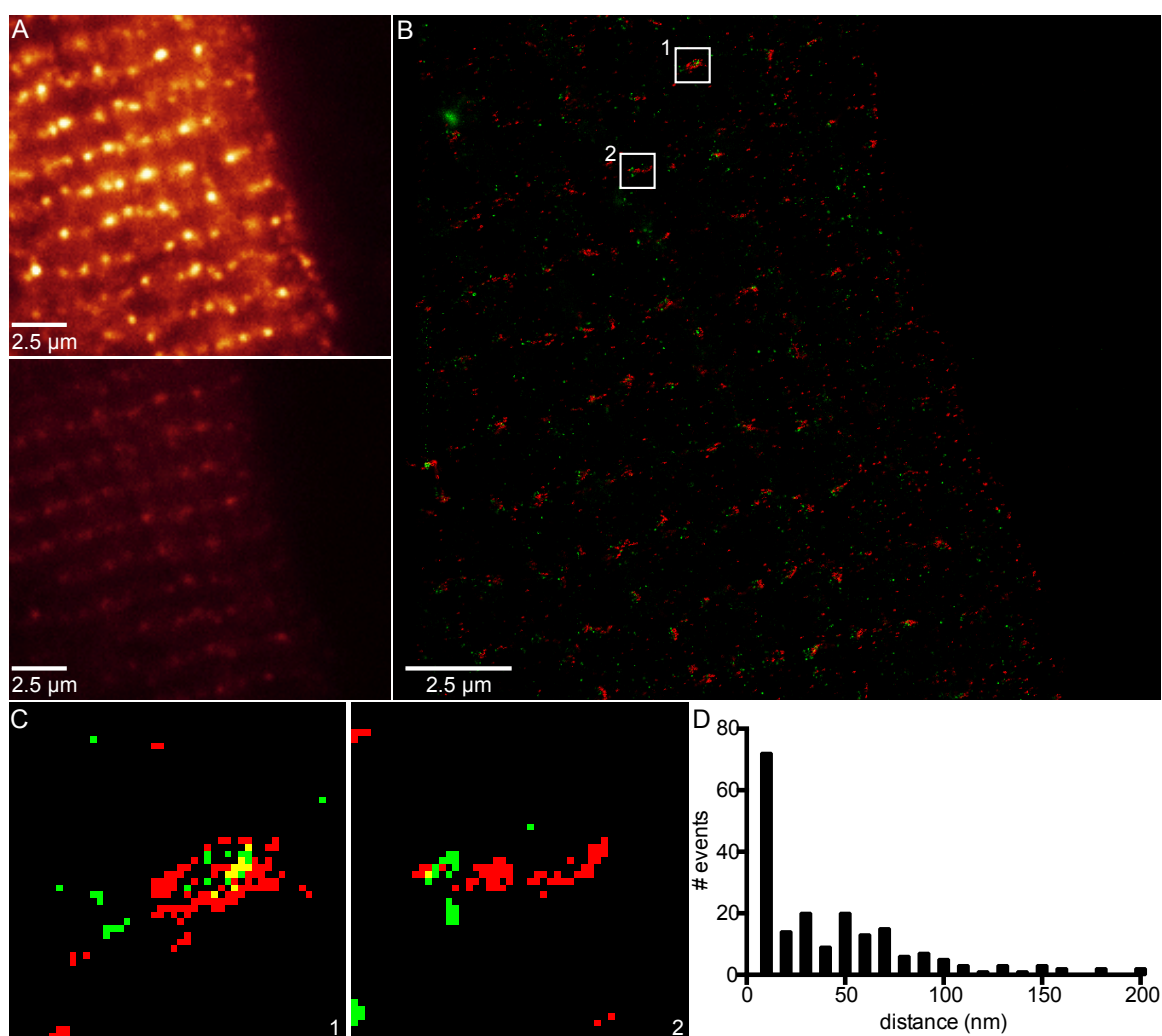


**Figure 5.2.** Triadin and Ca<sub>v</sub>1.2 clustering visualized by GSD.

**A**, TIRF image of myocyte dual-labeled with anti-Ca<sub>v</sub>1.2α tagged with Alexa Fluor 647 (*top*) and anti-triadin tagged with Alexa Fluor 568 (*below*), scale bar = 2.5 μm. **B**, GSD super-resolution of same myocyte dual-labeled with anti-

Ca<sub>v</sub>1.2α tagged with Alexa Fluor 647 (*red*) and anti-triadin tagged with Alexa Fluor 568 (*green*). **C**, two zoomed-in images of Ca<sub>v</sub>1.2 and triadin clustering from boxes seen in B. **D**, histogram of distance between Ca<sub>v</sub>1.2 and triadin fluorescence, showing vast majority of fluorescent signals are less than 10 nm apart.

nanoscopy, the seemingly uniform clusters revealed themselves as distinct clusters of proteins rather than completely overlapping signals (Figure 5.2B-C). The signals remained very close together and would overlap even at this higher resolution. Using our GSD nanoscope, we were able to calculate the nearest neighbor distance between Ca<sub>v</sub>1.2 and triadin signals and found that the vast majority of signals in the cluster were less than 10 nm apart (Figure 5.2D). This confirms that the jSR is part of the dyad and is sufficiently close to Ca<sub>v</sub>1.2 channels to be impacted by their Ca<sup>2+</sup> influx.

### 5.3.2. Virally-expressed TRD colocalizes with T-tubules and with the SR

We designed two AAV9s. One expresses triadin tagged with a photo-activatable GFP (AAV9-TRD-AGFP) and the other a constitutively fluorescent RFP with a retention signal for the SR lumen (SR-RFP). Ventricular myocytes were isolated from the hearts of mice at least 3 weeks after injection of these viruses. Myocytes expressing TRD-AGFP (TRD) were exposed to the potentiometric fluorescent indicator di-8-ANNEPs (di-8) to identify the sarcolemma and T-tubular membrane (Figure 5.3A-B). We detected high levels of TRD signal and di-8 fluorescence in puncta separated by ≈2 μm. These signals co-localize, showing that the TRD signal is in close proximity to the T-tubules (Figure 5.3C). Figure

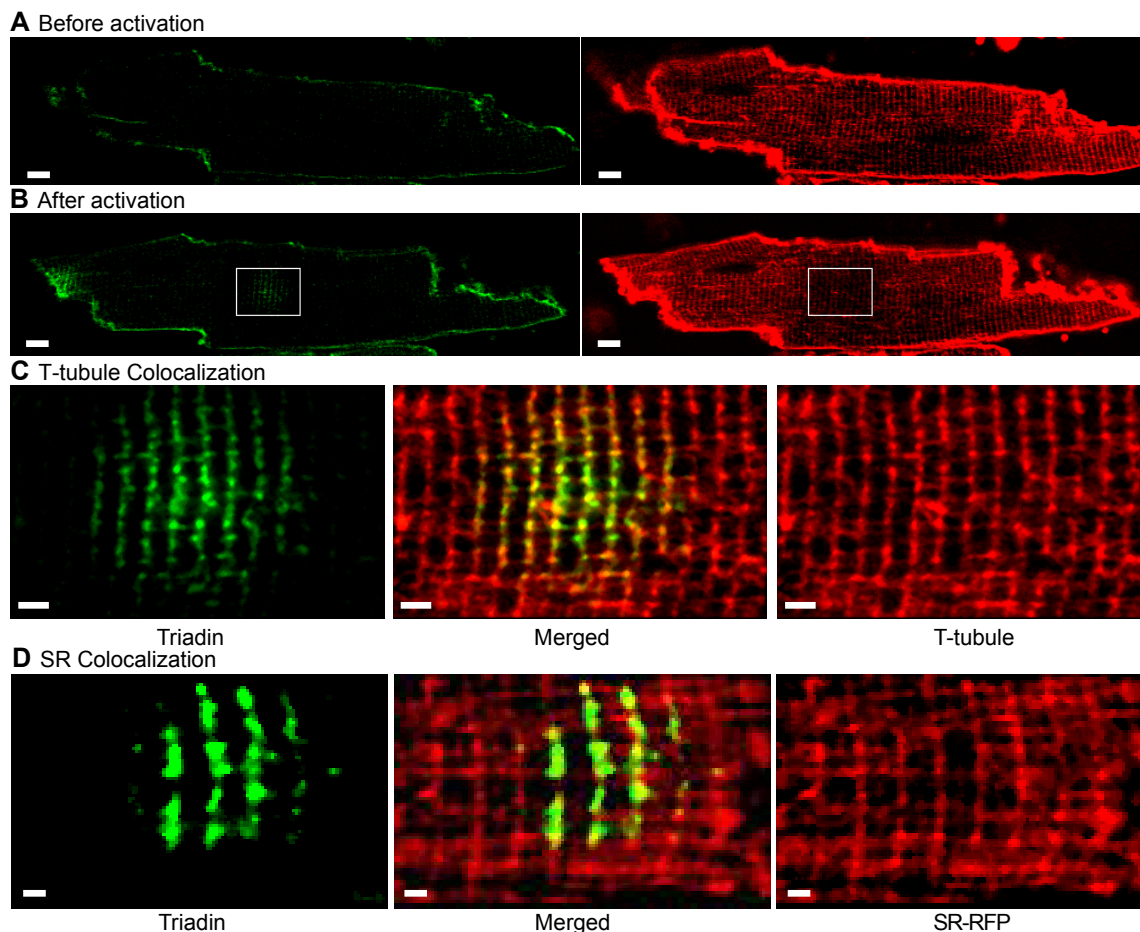


**Figure 5.3.** Photoactivation of AGFP-TRD in a live myocyte.

**A** and **B**: a myocyte before (**A**) and after (**B**) activation. The myocyte was activated using a 405 nm laser directed at the circle where activation occurred. Left panels display the AGFP signal; right panels display the di-8 signal. Scale bar = 5  $\mu$ m. **C**: magnified view of the area boxed in **A** and **B**. Scale bar = 2  $\mu$ m. **D**: magnified view of a different myocyte expressing TRD (left) and SR-RFP (right) co-localizing (center). Scale bar = 1  $\mu$ m.

5.3D shows confocal images of a ventricular myocyte expressing TRD-AGFP and SR-RFP. As described before, SR-RFP is broadly expressed in the lumen of the SR, showing that this organelle forms a vast network that extends throughout the cell (Vega and Santana 2011). TRD fluorescence was also observed at opposing ends of SR expressing SR-RFP. In summary, the TRD signal

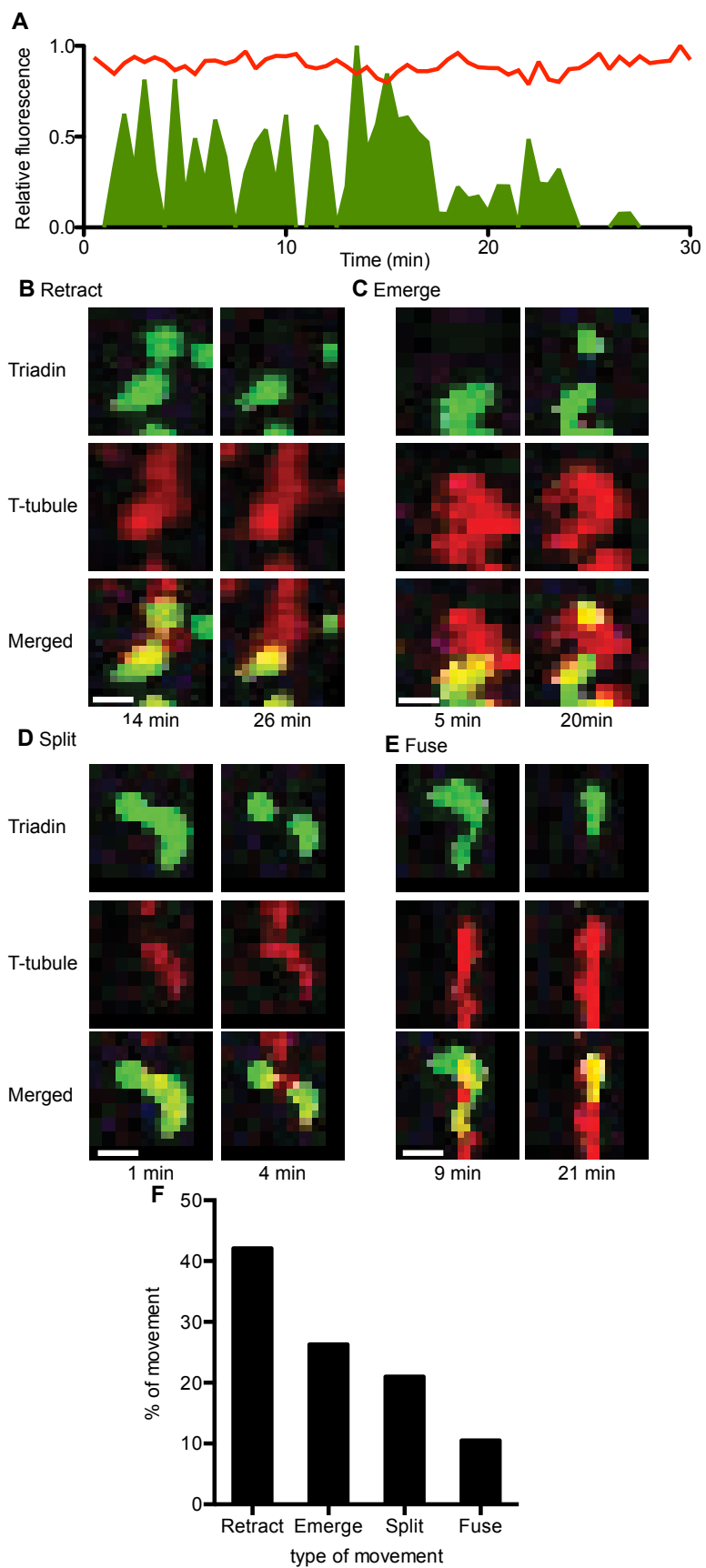


**Figure 5.4.** Dynamic profiles of motile jSR segments.

**A:** Red trace shows fluorescence of di-8 stain of T-tubules. Green trace shows fluorescence of AGFP tracking the jSR as it approaches and retracts from the T-tubules. **B:** A segment of jSR retracts from the T-tubules. **C:** A new segment of jSR emerges to interact with the T-tubules. **D:** A segment of jSR splits to create two junctions. **E:** An extension of SR fuses and centralizes into another segment. Scale bar = 0.5  $\mu\text{m}$  for all **B-E**. **F:** Quantification of % of modalities shown in **B-E**.

overlapped with both SR-RFP and di-8 fluorescence. These data show that TRD is expressed and properly targeted to the jSR.

**5.3.3. The jSR is mobile and has several modalities of mobility.**

We photo-activated TRD in a small region of the cell and tracked its fluorescence over time. Confocal images were acquired at a frequency of 1 Hz for a period of 5 minutes. During analysis, we measured the averaged fluorescence intensity in 0.2  $\mu\text{m}$  diameter regions of interest within the region of the cell where TRD was activated. Di-8 fluorescence was relatively constant during this experiment, suggesting that the T-tubules were stable and that the focal plane did not change during the experiment. Interestingly we detected relatively large TRD fluorescence fluctuations in specific regions of the cell. In the example shown in Figure 5.4, TRD decreased by over 80% and, within tens of seconds, increased again to its original level. Because newly synthesized TRD is not fluorescent before activation with 405 nm light, these fluctuations likely represent changes in the number and/or localization of TRD proteins we previously activated in the experiment.

Careful examination of the confocal images of TRD-AGFP obtained during preliminary experiments has revealed four seemingly different patterns of jSR biogenesis and motility. Figure 5.4B-E shows exemplary segments of SR that either: 1) retract to withdraw from the T-tubule; 2) emerge to approach the T-tubule; 3) split to become two distinct segments; or 4) fuse to become a single segment. Figure 5.4F quantifies these movements. The majority of movement (42%) seen is retraction from the T-tubule. 27% of the movement seen is emergence of a jSR area towards the T-tubules. Splitting (21%) and fusion (11%) of jSR puncta are less common.

#### 5.3.4. **Dynein and kinesin 1 regulate jSR motility.**

Work from our lab and others implicates the molecular motors dynein and kinesin 1 (Kif5b) in SR motility (Vega and Santana 2011, Zhang, Chen et al. 2014). However, the role of these proteins in jSR mobility is unknown. We packaged a motorless Kif5B into an adeno-associated virus, AAV9-Kif5bDN-TRFP for live cell imaging. We also generated a virus, AAV9-Dnchc1-shRNA-TRFP, which expresses an shRNA directed against dynein. Expression of this virus reduces mRNA expression of dynein by 62% (Figure 5.5A). We injected these viruses retro-orbitally into mice akin to our method of triadin tagging. We confirmed successful expression of these viruses by assaying for TRFP fluorescence. We found that these mice will have more stable SR segments. We calculated the percentage of dynamic SR segments per cell and compare this ratio between

WT, Kif5bDN, Dnchc1, and Kif5bDN-Dnchc1 (double knockdown) models (Figure 5B).

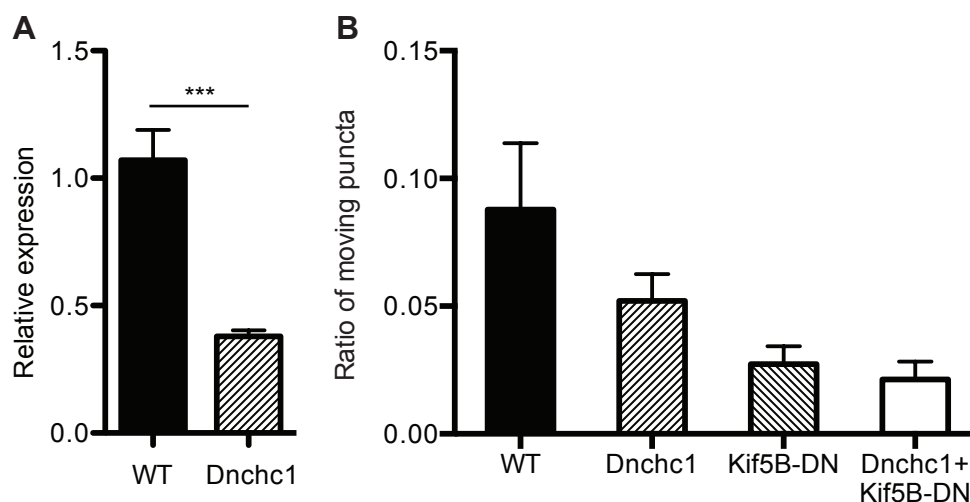


**Figure 5.5.** Dynein and kinesin are implicated in jSR mobility.

**A:** Injection of Dnchc1-shRNA into mice decreases expression of dynein by 62%, as shown by real time qRT-PCR transcript. **B:** Ratio of moving jSR puncta in WT, Dnchc1, Kif5B-DN, and Dnchc1+Kif5B-DN constructs.

### 5.3.5. The jSR and T-tubules can be uncoupled, leading to defects in Ca<sup>2+</sup> signaling.

It was unknown whether the SR and T-tubules move together or if they are regulated by different mechanisms. We used formamide to induce chemical detubulation in live myocytes (Figure 5.6A) (Brette, Komukai et al. 2002, Fowler, Dobson et al. 2004). We measured the organization of the SR and T-tubules before and after detubulation by taking a fast Fourier transform of the data and quantifying the first harmonic peak (referred to here as SR or T-tubule power), which is a measure of the consistency of distance between segments (Vega and Santana 2011).

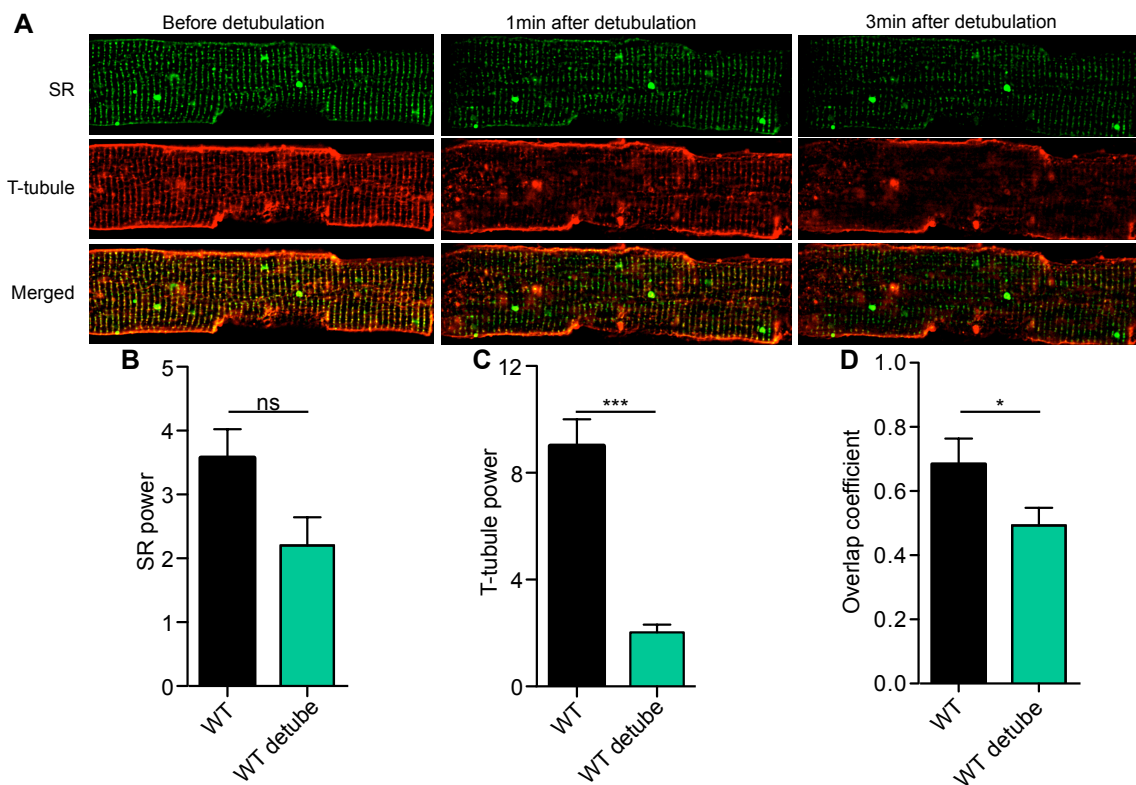


**Figure 5.6.** Detubulation results in uncoupling the jSR from the T-tubules.

**A:** Confocal image of a cardiomyocyte expressing TRD-AGFP (top) and stained with di-8-ANEPPS (middle) before detubulation (left), 1 min after application of 10 mM formamide (middle), and 3 min after application of formamide (right). Merged signal is shown below. **B:** SR power before and after application of formamide. **C:** T-Tubule power before and after application of formamide. **D:** Overlap coefficient of SR and T-tubules before and after application of formamide.

We also quantified the relationship between the T-tubules and the SR by conducting a colocalization analysis on ImageJ and measuring the overlap coefficient. We found that while detubulation did not significantly change the SR structure, it did result in loss of T-tubule power, showing that the jSR can be uncoupled from T-tubules (Figure 5.6B-C). Indeed, the overlap coefficient significantly decreased after detubulation (Figure 5.6D). Disrupting the T-tubule sarcolemma-SR junction also disrupted global  $\text{Ca}^{2+}$  signaling. We were unable to evoke field transients after complete detubulation.

### 5.3.6. The jSR is disrupted and highly mobile after MI.

We induced MI in the left ventricle of mice injected with TRD-AGFP and isolated ventricular myocytes 48 hours post-infarct (Figure 5.7A). As expected, T-tubules were disorganized and damaged post-MI, yielding low T-tubule power (Figure 5.7C). SR power was also decreased, but not significantly (Figure 5.7B). We found that jSR is disrupted and highly mobile after MI by comparing these myocytes to wild-type cells. These cells showed increased jSR segment mobility. These data are consistent with the hypothesis that the dyads are disorganized post-MI.

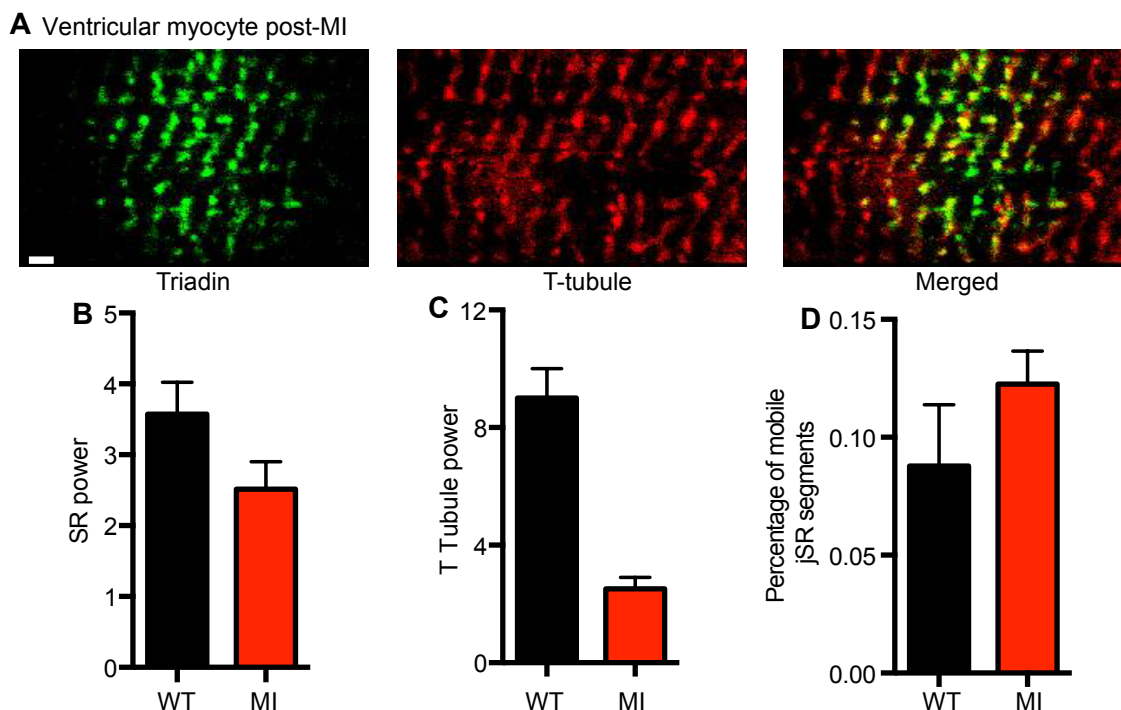


**Figure 5.7.** jSR mobility is decreased after MI.

**A:** Confocal image of a cardiomyocyte expressing TRD-AGFP (left) and stained with di-8-ANEPPS (middle), merged signal shown right. **B:** SR power before and after MI. **C:** T-Tubule power before and after MI. **D:** Overlap coefficient of SR and T-tubules before and after MI.

#### 5.4. Discussion

This study is the first of its kind to visualize and characterize movement of the jSR in real time. To summarize, we have discovered four novel observations relating to cardiac physiology: 1) the jSR is dynamic and moves in several modalities; 2) this movement is dependent on molecular motors; 3) the dyad can be uncoupled using chemical reagents which impacts  $\text{Ca}^{2+}$  signaling; and 4) the dyad is disrupted in MI and jSR mobility is increased. These findings stand in opposition to traditional dogma that the jSR is static in order to maximize the reproducibility of the myocyte's response to an AP. Instead, we see a complex system of potential regulation, where jSR segments may move in and out locally based on the movement of molecular motors. The reproducibility of the heartbeat, then, is perpetuated by the local control theory of  $\text{Ca}^{2+}$  signaling, which hypothesizes that a sum of thousands of local  $\text{Ca}^{2+}$  events contributes to contraction in the myocyte.

Because the jSR is mobile, this suggests it can be regulated, and adjusted in pathology. Indeed, we found increased jSR mobility after MI. Given the change in T-tubule structure after MI, it is possible that the increase in mobility helps the myocyte reconnect jSR segments to be in close apposition with T-tubules and maximize  $\text{Ca}^{2+}$  signaling after MI by removing jSR segments that have been orphaned by T-tubules. jSR mobility and structural remodeling may be a part of

normal physiology, based on the local  $\text{Ca}^{2+}$  load of the SR, attempting to maximize  $\text{Ca}^{2+}$  release.

Another interesting finding is the implication of the microtubule network in jSR protein trafficking. Due to the limited cell division of myocytes, the cardiac microtubule network has been understudied and its purposes are still largely unknown. The images we do have of the microtubule network suggest it to be a vast, dynamic entity (Oddoux, Zaal et al. 2013, Zhang, Chen et al. 2014). What is the fidelity of the microtubule network, and how does it develop? Based on this study, it seems that the microtubule network must be in place at least in some capacity to allow formation of the jSR. How dynamic is this network, and how does it recover in pathology? Microtubule-mediated defects in junctophilin-2 trafficking has been implicated in  $\text{Ca}^{2+}$  handling dysfunction and heart failure (Zhang, Chen et al. 2014). From this study, the molecular motors kinesin and dynein could hold promise of therapeutic targets if they are specific in their cardiac roles.

Our findings suggest that the jSR plays a vital role in normal physiology, and that loss of jSR organization can lead to pathology. Vega *et al* (Vega and Santana 2011) found that SR “boutons” expressing functional RyRs can move throughout the cell, approaching or moving away from the sarcolemma of ventricular myocytes. The questions of exactly how dynamic the jSR is, as well as how jSR movement is regulated, remain unanswered.

The chemical decoupling of T-tubules and jSR, where the T-tubules have disorganized but the jSR remains structured, demonstrates that jSR movement is unique from T-tubule movement. While this observation is correlated and not causative, as many processes could lead to different time courses of disorganization, it would be interesting to establish differences in time course in pathological uncoupling and determine the initial steps in the pathogenesis of dyad disruption. Finding mechanisms to stabilize the jSR and keep it in tight proximity to the T-tubules would increase ECC coupling and improve myocyte  $\text{Ca}^{2+}$  signaling. If kinesin-1 and dynein are responsible for SR remodeling, then we expect an increase in kinesin-1 and dynein activity post-MI. More research is needed to answer these questions.

In conclusion, the jSR is a dynamic entity, capable of approaching and withdrawing from the dyad, and adjust to the dyad after injury. We hypothesize that this mobility can impact and regulate EC coupling due to the high concentration of calcium needed for faithful RyR opening, although more research is needed to elucidate the role of jSR movement in EC coupling.

## Chapter 6: Concluding Remarks

In this dissertation, I have researched new concepts in cardiac physiology through the lens of two causes of cardiac arrhythmia, TS and MI. I have studied the importance of the intracellular calcium environment and how a calcium-overloaded cell is prone to arrhythmia. Similarly, I studied oxidative stress and how its presence after MI signals MT disruption and disruption of channel trafficking, which can lead to arrhythmia. Both of these projects are attempts to understand pathology that disrupts the fidelity of the heartbeat. In my last project, I further explored the fidelity of the heartbeat and made a case for regulation of the heartbeat via jSR mobility.

In Chapter 2, I provided a comprehensive study of  $\text{Ca}^{2+}$  signaling in a mouse model of TS. I found that in TS, the resting and diastolic  $\text{Ca}^{2+}$  concentration was increased by a factor of 1.4. In addition,  $\text{Ca}_v1.2$ -TS channels increased sarcolemmal  $\text{Ca}^{2+}$  leak,  $\text{Ca}^{2+}$  transients,  $\text{Ca}^{2+}$  sparks, as well as SR load. Increased SR  $\text{Ca}^{2+}$  release in TS myocytes increased the rate of  $\text{Ca}^{2+}$  inactivation to a high, persistent level, limiting the amount of influx during EC coupling. Depolarization of WT myocytes with a TS AP waveform increased but did not equalize  $\text{Ca}^{2+}$  transient levels compared to depolarization of TS myocytes with the same waveform. Likewise, depolarization of TS myocytes with a WT AP waveform decreased but did not equalize  $\text{Ca}^{2+}$  transient levels compared to depolarization of WT myocytes with the same waveform. Thus, I concluded that

both the increase in AP duration as well as the increased  $\text{Ca}^{2+}$  in the cytosol and SR work together to create a  $\text{Ca}^{2+}$  overloaded state that increases the rate of arrhythmia. Further research should explore the roles other proteins, particularly CaMKII, have in further augmenting SR leak and abnormal  $\text{Ca}^{2+}$  signaling in TS, as well as explore the phenotype TS has in atrial myocytes given the differential expression of  $\text{Ca}_v1.2$  in these cells. Additionally, research could be done exploring if disrupting kinesin-1 could help rescue the abnormal  $\text{Ca}^{2+}$  signaling by decreasing  $\text{Ca}_v1.2$  trafficking.

In Chapter 3, I visualized and quantified live MT dynamics in ventricular myocytes for the first time. I exposed the temperature-sensitive nature of these dynamics and quantified growth and shrink rate and distance, catastrophe and rescue rates, and directionality, presenting evidence that MTs appear to be stabilized at the Z line. I showed that oxidative stress during MI disrupts these dynamics, increasing catastrophe and growth rates, and that this disruption impacts protein trafficking. In particular, I showed that  $\text{K}_v4.2$  and  $\text{K}_v4.3$  channels were unable to properly traffic to the sarcolemma, resulting in a decrease in  $I_{to}$ . Further studies should continue examining the importance of MTs in cardiac tissue. It is currently unclear why MT growth appears to be stereotypically directional. Oddoux et al recently speculated that dystrophin may serve to guide MT growth, and proposed that MT pathology may be implicated in muscular dystrophy (Oddoux 2013). In addition, the mechanism of ROS disruption of MT dynamics can be more fully elucidated. Future studies could examine MT

dynamics during myocyte contraction and continue investigating MT-mediated protein trafficking.

In Chapter 4, I present evidence that BIN1 interacts with MTs to anchor and stabilize them on the T-tubules, enabling kinesin-1 to traffic  $Ca_v1.2\beta_2$  to the dyad. I recorded MT dynamics in both atrial myocytes as well as cultured ventricular myocytes lacking intact T-tubules and saw increases in catastrophe rate and rescue rate. In addition, in atrial myocytes, MTs lacked the stereotypical pausing and horizontal directionality seen in ventricular myocytes. Although BIN1 is expressed with T-tubule periodicity in ventricular myocytes, BIN1 seemed to associate in clusters surrounding the periphery of the cell in atrial myocytes. Dual-antibody staining showed that BIN1 colocalized with T-tubule-associated proteins  $Ca_v1.2\alpha$  and  $Ca_v1.2\beta_2$  in addition to MT-associated proteins EB1 and CLIP170, providing evidence that it could serve as a mediator between MTs and T-tubules. Lastly, I found that kinesin-1 is the molecular motor responsible for trafficking  $Ca_v1.2\beta_2$  to the sarcolemma. This study is one of the first to link MTs with the machinery of EC coupling, and more work needs to be done expanding the interface of these fields. Further work should examine the role of CLIP170, search for SxIP domains in BIN1 as a molecular mechanism of interaction with EB1, and explore the trafficking of  $Ca_v1.2\alpha$ . Long-term goals include researching atrial MT dynamics and their impact on protein trafficking.

In Chapter 5, I visualized the jSR in acute, dissociated myocytes and found that the jSR undergoes dynamic changes and mobility in these cells. This is in stark contrast to existing dogma that states that the dyad is a static subcellular structure. I discovered multiple modalities of jSR mobility and implicated the motors dynein and kinesin-1 in jSR formation and stability. I also showed that detubulating myocytes effectively uncouples the dyad, eliminating EC coupling. Lastly, I found that the jSR becomes increasingly mobile after MI, presumably remodeling itself after the loss of T-tubules. This study is one of the first of its kind to suggest that the dyad is not static. More work exploring the roles of kinesin-1 and dynein in this mobility would be highly informative, especially in states where increased jSR movement occurs such as in MI. Indeed, future work should delve deeper into how the jSR remodels after pathology using time points to catch remodeling in action. Lastly, repeating these studies under higher resolution imaging such as TIRF would be highly informative.

In conclusion, this thesis represents a broad spectrum of cardiac research. I have looked at pathology mechanistically, at the level current density or surface expression of ion channels. In these projects, I have also needed to take into account the environment of the entire cell, both the calcium overload in TS and oxidative stress in MI. I have used conventional techniques such as Western blot, patch clamping, and fluorescent imaging, in addition to novel techniques such as ground state depletion and adeno-associated viral transfections to illuminate previously unknown mechanisms of heart physiology. Lastly, I have pushed

against existing dogma, establishing roles for MTs in myocytes and movement in the jSR. Moving forward, these kinds of studies will continue to fascinate me. By looking at the behavior of the entire cell and reducing it down to single mechanisms, one is able to reduce the complexity of complicated problems into manageable sections.

## References

- Adachi-Akahane, S., L. Cleemann and M. Morad (1996). "Cross-signaling between L-type Ca<sup>2+</sup> channels and ryanodine receptors in rat ventricular myocytes." J Gen Physiol **108**(5): 435-454.
- Akhmanova, A., A. L. Mausset-Bonnefont, W. van Cappellen, N. Keijzer, C. C. Hoogenraad, T. Stepanova, K. Drabek, J. van der Wees, M. Mommaas, J. Onderwater, H. van der Meulen, M. E. Tanenbaum, R. H. Medema, J. Hoogerbrugge, J. Vreeburg, E. J. Uringa, J. A. Grootegoed, F. Grosveld and N. Galjart (2005). "The microtubule plus-end-tracking protein CLIP-170 associates with the spermatid manchette and is essential for spermatogenesis." Genes Dev **19**(20): 2501-2515.
- Akhmanova, A. and M. O. Steinmetz (2008). "Tracking the ends: a dynamic protein network controls the fate of microtubule tips." Nat Rev Mol Cell Biol **9**: 309-322.
- Amberg, G. C., A. D. Bonev, C. F. Rossow, M. T. Nelson and L. F. Santana (2003). "Modulation of the molecular composition of large conductance, Ca<sup>2+</sup> activated K<sup>+</sup> channels in vascular smooth muscle during hypertension." J Clin Invest **112**(5): 717-724.
- Amberg, G. C. and L. F. Santana (2003). "Downregulation of the BK channel beta1 subunit in genetic hypertension." Circ Res **93**(10): 965-971.
- Aquila-Pastir, L. A., N. R. DiPaola, R. G. Matteo, N. G. Smedira, P. M. McCarthy and C. S. Moravec (2002). "Quantitation and distribution of beta-tubulin in human cardiac myocytes." J Mol Cell Cardiol **34**(11): 1513-1523.

- Arakel, E. C., S. Brandenburg, K. Uchida, H. Zhang, Y. W. Lin, T. Kohl, B. Schrul, M. S. Sulkin, I. R. Efimov, C. G. Nichols, S. E. Lehnart and B. Schwappach (2014). "Tuning the electrical properties of the heart by differential trafficking of KATP ion channel complexes." J Cell Sci **127**(Pt 9): 2106-2119.
- Baddeley, D., I. D. Jayasinghe, L. Lam, S. Rossberger, M. B. Cannell and C. Soeller (2009). "Optical single-channel resolution imaging of the ryanodine receptor distribution in rat cardiac myocytes." Proc Natl Acad Sci U S A **106**(52): 22275-22280.
- Balke, C. W., T. M. Egan and W. G. Wier (1994). "Processes that remove calcium from the cytoplasm during excitation- contraction coupling in intact rat heart cells." J Physiol **474**(3): 447-462.
- Barrett, C. F. and R. W. Tsien (2008). "The Timothy syndrome mutation differentially affects voltage- and calcium-dependent inactivation of CaV1.2 L-type calcium channels." Proc Natl Acad Sci U S A **105**(6): 2157-2162.
- Beard, N. A., D. R. Laver and A. F. Dulhunty (2004). "Calsequestrin and the calcium release channel of skeletal and cardiac muscle." Pro Biophys Mol Biol **85**(1): 33-69.
- Belanto, J. J., T. L. Mader, M. D. Eckhoff, D. M. Strandjord, G. B. Banks, M. K. Gardner, D. A. Lowe and J. M. Ervasti (2014). "Microtubule binding distinguishes dystrophin from utrophin." Proc Natl Acad Sci U S A **111**(15): 5723-5728.

- Bers, D. M., J. W. Bassani and R. A. Bassani (1993). "Competition and redistribution among calcium transport systems in rabbit cardiac myocytes." Cardiovasc Res **27**(10): 1772-1777.
- Bieling, P., S. Kandels-Lewis, I. A. Telley, J. van Dijk, C. Janke and T. Surrey (2008). "CLIP-170 tracks growing microtubule ends by dynamically recognizing composite EB1/tubulin-binding sites." J Cell Biol **183**(7): 1223-1233.
- Birnbaumer, L., N. Qin, R. Olcese, E. Tareilus, D. Platano, J. Costantin and E. Stefani (1998). "Structures and functions of calcium channel beta subunits." J Bioenerg Biomembr **30**: 357-375.
- Bish, L. T., K. Morine, M. M. Sleeper, J. Sanmiguel, D. Wu, G. Gao, J. M. Wilson and H. L. Sweeney (2008). "Adeno-Associated Virus (AAV) Serotype 9 Provides Global Cardiac Gene Transfer Superior to AAV1, AAV6, AAV7, and AAV8 in the Mouse and Rat." Hum Gene Ther **19**: 1359-1368.
- Bodi, I., G. Mikala, S. E. Koch, S. A. Akhter and A. Schwartz (2005). "The L-type calcium channel in the heart: the beat goes on." J Clin Invest **115**(12): 3306-3317.
- Bonow, R. O., D. L. Mann, D. P. Zipes and P. Libby (2011). Genesis of cardiac arrhythmias, electrophysiologic considerations. Braunwald's Heart Disease: A Textbook of Cardiovascular Medicine. Philadelphia, PA, Elsevier.

- Bootman, M. D., D. R. Higazi, S. Coombes and H. L. Roderick (2006). "Calcium signalling during excitation-contraction coupling in mammalian atrial myocytes." J Cell Sci **119**: 3915-3925.
- Bootman, M. D., I. Smyrniak, R. Thul, S. Coombes and H. L. Roderick (2011). "Atrial cardiomyocyte calcium signalling." Biochim Biophys Acta **1813**: 922-934.
- Boyle, M. P. and H. F. Weisman (1993). "Limitation of infarct expansion and ventricular remodeling by late reperfusion." Circulation **88**(2872-83).
- Bradshaw, J. M., Y. Kubota, T. Meyer and H. Schulman (2003). "An ultrasensitive Ca<sup>2+</sup>/calmodulin-dependent protein kinase II-protein phosphatase 1 switch facilitates specificity in postsynaptic calcium signaling." Proc Natl Acad Sci U S A **100**(18): 10512-10517.
- Bretschneider, S., C. Eggeling and S. W. Hell (2007). "Breaking the Diffraction Barrier in Fluorescence Microscopy by Optical Shelving." Phys Rev Lett **98**: 218103-218107.
- Brette, F., K. Komukai and C. H. Orchard (2002). "Validation of formamide as a detubulation agent in isolated rat cardiac cells." Am J Physiol **283**: H1720-H1728.
- Brette, F. and C. H. Orchard (2003). "T-tubule function in mammalian cardiac myocytes." Circ Res **92**: 1182-1192.
- Cannell, M. B., H. Cheng and W. J. Lederer (1995). "The control of calcium release in heart muscle." Science **268**(5213): 1045-1049.

- Cannell, M. B. and C. H. T. Kong (2012). "Local control in cardiac E-C coupling." J Mol Cell Cardiol **52**(2): 298-303.
- Carl, S. L., K. Felix, A. H. Caswell, N. R. Brandt, W. J. Ball Jr., P. L. Vaghy, G. Meissner and D. G. Ferguson (1995). "Immunolocalization of sarcolemmal dihydropyridine receptor and sarcoplasmic reticular triadin and ryanidine receptor in rabbit ventricle and atrium." J Cell Biol **129**: 672-682.
- Cartelli, D., C. Ronchi, M. G. Maggioni, S. Rodighiero, E. Giavini and G. Cappelletti (2010). "Microtubule dysfunction precedes transport impairment and mitochondria damage in MPP<sup>+</sup>-induced neurodegeneration." J Neurochem **115**(1): 247-258.
- Catterall, W. A. (2000). "Structure and regulation of voltage-gated Ca<sup>2+</sup> channels." Annu Rev Cell Dev Biol **16**: 521-555.
- Catterall, W. A. (2011). "Voltage-gated calcium channels." Cold Spring Harb Perspect Biol **3**(8): a003947.
- Cens, T., M. Rousset, J.-P. Leyris, P. Fesquet and P. Charnet (2006). "Voltage and calcium dependent inactivation in high voltage-gated Ca<sup>2+</sup> channels." Pro Biophys Mol Biol **90**(1-3): 104-117.
- Chen-Izu, Y., S. L. McCulle, C. W. Ward, C. Soeller, B. M. Allen, C. Rabang, M. B. Cannell, C. W. Balke and L. T. Izu (2006). "Three-dimensional distribution of ryanodine receptor clusters in cardiac myocytes." Biophys J **91**(1): 1-13.
- Cheng, E. P., C. Yuan, M. F. Navedo, R. E. Dixon, M. Nieves-Cintrón, J. D. Scott and L. F. Santana (2011). "Restoration of normal L-type Ca<sup>2+</sup> channel

- function during Timothy syndrome by ablation of an anchoring protein." Circ Res **109**(3): 255-261.
- Cheng, H., M. R. Lederer, W. J. Lederer and M. B. Cannell (1996). "Calcium sparks and  $[Ca^{2+}]_i$  waves in cardiac myocytes." Am J Physiol **270**(1 Pt 1): C148-159.
- Cheng, H. and W. J. Lederer (2008). "Calcium sparks." Physiol Rev **88**(4): 1491-1545.
- Cheng, H., W. J. Lederer and M. B. Cannell (1993). "Calcium sparks: elementary events underlying excitation-contraction coupling in heart muscle." Science **262**(5134): 740-744.
- Cheng, H. and S. Q. Wang (2002). "Calcium signaling between sarcolemmal calcium channels and ryanodine receptors in heart cells." Front Bios **7**: 1867-1878.
- Choi, B.-R., F. Burton and G. Salama (2002). "Cytosolic  $Ca^{2+}$  triggers early afterdepolarizations and torsade de pointes in rabbit hearts with type 2 long QT syndrome." J Physiol **543**(Pt 2): 615-631.
- Chu, P. J., J. F. Rivera and D. B. Arnold (2006). "A role for Kif17 in transport of Kv4.2." J Biol Chem **281**(1): 365-373.
- Chung, Y. S. and A. Guarne (2008). "Crystallization and preliminary X-ray diffraction analysis of SeqA bound to a pair of hemimethylated GATC sites." Acta Crystallogr Sect F Struct Biol Cryst Commun **64**(Pt 6): 567-571.

- Colecraft, H. M., B. A. Alseikhan, S. X. Takahashi, D. Chaudhuri, S. Mittman, V. Yegnasubramanian, R. S. Alvania, D. C. Johns, E. Marban and D. T. Yue (2002). "Novel functional properties of Ca(2+) channel beta subunits revealed by their expression in adult rat heart cells." J Physiol **541**(Pt 2): 435-452.
- Cooper, P. J., C. Soeller and M. B. Cannell (2010). "Excitation-contraction coupling in human heart failure examined by action potential clamp in rat cardiac myocytes." J Mol Cell Cardiol.
- Coquelle, F. M., M. Caspi, F. P. Cordelieres, J. P. Dompierre, D. L. Dujardin, C. Koifman, P. Martin, C. C. Hoogenraad, A. Akhmanova, N. Galjart, J. R. De Mey and O. Reiner (2002). "LIS1, CLIP-170's key to the dynein-dynactin pathway." Mol Cell Biol **22**(9): 3089-3102.
- de Zwaan, C., M. J. Daemen and W. T. Hermens (2001). "Mechanisms of cell death in acute myocardial infarction: pathophysiological implications for treatment." Neth Heart J **9**(1): 30-44.
- Desai, A. and T. J. Mitchison (1997). "Microtubule polymerization dynamics." Annu Rev Cell Dev Biol **13**: 83-117.
- Diaz, M. E., C. O'Neill S and D. A. Eisner (2004). "Sarcoplasmic reticulum calcium content fluctuation is the key to cardiac alternans." Circ Res **94**(5): 650-656.
- Diaz-Munoz, M., M. A. Alvarez-Perez, L. Yanez, S. Vidrio, L. Martinez, G. Rosas, M. Yanez, S. Ramirez and V. C. de Sanchez (2006). "Correlation between oxidative stress and alteration of intracellular calcium handling in

- isoproterenol-induced myocardial infarction." Mol Cell Biochem **289**(1-2): 125-136.
- Dixit, R., B. Barnett, J. E. Lazarus, M. Tokito, Y. E. Goldman and E. L. Holzbaur (2009). "Microtubule plus-end tracking by CLIP-170 requires EB1." Proc Natl Acad Sci U S A **106**(2): 492-497.
- Dixon, R. E., C. M. Moreno, C. Yuan, X. Opitz-Araya, M. D. Binder, M. F. Navedo and L. F. Santana (2015). "Graded  $Ca^{2+}$ /calmodulin-dependent coupling of voltage-gated  $Ca_v1.2$  channels." Elife **4**.
- Dixon, R. E., C. Yuan, E. P. Cheng, M. F. Navedo and L. F. Santana (2012). "Ca<sup>2+</sup> signaling amplification by oligomerization of L-type  $Ca_v1.2$  channels." Proc Natl Acad Sci U S A **109**(5): 1749-1754.
- Drake, R. L., W. Vogl and A. W. M. Mitchell (2005). Anatomy for Students. Philadelphia, Churchill Livingstone.
- Drum, B. M., R. E. Dixon, C. Yuan, E. P. Cheng and L. F. Santana (2014). "Cellular mechanisms of ventricular arrhythmias in a mouse model of Timothy syndrome (long QT syndrome 8)." J Mol Cell Cardiol **66**: 63-71.
- Drum, B. M., C. Yuan, L. Li, Q. Liu, L. Wordeman and L. F. Santana (2016). "Oxidative stress decreases microtubule growth and stability in ventricular myocytes." J Mol Cell Cardiol **93**: 32-43.
- Erleben, C., Y. Liao, S. Gentile, D. Chin, C. Gomez-Alegria, Y. Mori, L. Birnbaumer and D. L. Armstrong (2006). "Cyclosporin and Timothy syndrome increase mode 2 gating of  $Ca_v1.2$  calcium channels through

- aberrant phosphorylation of S6 helices." Proc Natl Acad Sci U S A **103**(10): 3932-3937.
- Fabiato, A. (1983). "Calcium-induced release of calcium from the cardiac sarcoplasmic reticulum." Am J Physiol **245**(1): C1-14.
- Field, G. D. and F. Rieke (2002). "Mechanisms Regulating Variability of the Single Photon Responses of Mammalian Rod Photoreceptors." Neuron **35**: 733-747.
- Fischmeister, R., L. R. Castro, A. Abi-Gerges, F. Rochais, J. Jurevicius, J. Leroy and G. Vandecasteele (2006). "Compartmentation of cyclic nucleotide signaling in the heart: the role of cyclic nucleotide phosphodiesterases." Circ Res **99**(8): 816-828.
- Forbes, M. S. and N. Sperelakis (1983). "The membrane systems and cytoskeletal elements of mammalian myocardial cells." Cell Muscle Motil **3**: 89-155.
- Fourest-Lieuvain, A., J. Rendu, A. Osseni, K. Pernet-Gallay, D. Rossi, S. Oddoux, J. Brocard, V. Sorrentino, I. Marty and J. Faure (2012). "Role of triadin in the organization of reticulum membrane at the muscle triad." J Cell Sci **125**: 3443-3453.
- Fowler, M. R., R. S. Dobson, C. H. Orchard and S. M. Harrison (2004). "Functional consequences of detubulation of isolated rat ventricular myocytes." Cardiovasc Res **62**: 529-537.

- Franzini-Armstrong, C., F. Protasi and V. Ramesh (1999). "Shape, size, and distribution of Ca<sup>2+</sup> release units and couplons in skeletal and cardiac muscles." Biophys J **77**(3): 1528-1539.
- Frolov, R. V., I. I. Ignatova and S. Singh (2011). "Inhibition of hERG Potassium Channels by Celecoxib and its mechanism." PLoS ONE **6**(10): e26344.
- Ganem, N. J. and D. A. Compton (2004). "The KinI kinesin Kif2a is required for bipolar spindle assembly through a functional relationship with MCAK." J Cell Biol **166**(4): 473-478.
- Garbino, A. and X. H. Wehrens (2010). "Emerging role of junctophilin-2 as a regulator of calcium handling in the heart." Acta Pharma Sinica **31**: 1019-1021.
- Gelfand, V. I. and A. D. Bershadsky (1991). "Microtubule dynamics: mechanism, regulation, and function." Annu Rev Cell Biol **7**: 93-116.
- Ginkel, L. M. and L. Wordeman (2000). "Expression and partial characterization of kinesin-related proteins in differentiating and adult skeletal muscle." Mol Biol Cell **11**(12): 4143-4158.
- Glover, L., S. Quinn, M. Ryan, D. Pette and K. Ohlendieck (2002). "Supramolecular casequestrin complex." Eur J Biochem **269**: 4607-4616.
- Gold, M. G., F. Stengel, P. J. Nygren, C. R. Weisbrod, J. E. Bruce, C. V. Robinson, D. Barford and J. D. Scott (2011). "Architecture and dynamics of an A-kinase anchoring protein 79 (AKAP79) signaling complex." Proc Natl Acad Sci U S A **108**(16): 6426-6431.

- Gomez, A. M., H. H. Valdivia, H. Cheng, M. R. Lederer, L. F. Santana, M. B. Cannell, S. A. McCune, R. A. Altschuld and W. J. Lederer (1997). "Defective excitation-contraction coupling in experimental cardiac hypertrophy and heart failure." Science **276**(5313): 800-806.
- Graham, E. L., C. Balla, H. Franchino, Y. Melman, F. del Monte and S. Das (2013). "Isolation, culture, and functional characterization of adult mouse cardiomyocytes." J Vis Exp **79**: e50289.
- Grynkiewicz, G., M. Poenie and R. Y. Tsien (1985). "A new generation of  $\text{Ca}^{2+}$  indicators with greatly improved fluorescence properties." J Biol Chem **260**(6): 3440-3450.
- Gu, C., W. Zhou, M. A. Puthenveedu, M. Xu, Y. N. Jan and L. Y. Jan (2006). "The microtubule plus-end tracking protein EB1 is required for Kv1 voltage-gated  $\text{K}^+$  channel axonal targeting." Neuron **52**(5): 803-816.
- Guatimosim, S., K. Dilly, L. F. Santana, M. Saleet Jafri, E. Sobie and W. Lederer (2002). "Local  $\text{Ca}^{2+}$  Signaling and EC Coupling in Heart:  $\text{Ca}^{2+}$  Sparks and the Regulation of the  $[\text{Ca}^{2+}]_i$  Transient." J Mol Cell Cardiol **34**(8): 941.
- Guo, T., T. Zhang, R. Mestral and D. M. Bers (2006). " $\text{Ca}^{2+}$ /Calmodulin-dependent protein kinase II phosphorylation of ryanodine receptor does affect calcium sparks in mouse ventricular myocytes." Circ Res **99**(4): 398-406.
- Heinemann, S. H., H. Terlau, W. Stuhmer, K. Imoto and S. Numa (1992). "Calcium channel characteristics conferred on the sodium channel by single mutations." Nature **356**(6368): 441-443.

- Heling, A., R. Zimmermann, S. Kostin, Y. Maeno, S. Hein, B. Devaux, E. Bauer, W. P. Klovekorn, M. Schlepper, W. Schaper and J. Schaper (2000). "Increased expression of cytoskeletal, linkage, and extracellular proteins in failing human myocardium." Circ Res **86**(8): 846-853.
- Hell, S. W. and M. Kroug (1995). "Ground-state-depletion fluorescence microscopy: a concept for breaking the diffraction resolution limit." Appl Phys B **60**: 495-497.
- Herman, N. and B. K. Shelton (2010). "QT Prolongation: Implications for Oncology Nurses." Acute & Critical Care **21**(1).
- Hess, P., J. B. Lansman and R. W. Tsien (1984). "Different modes of Ca channel gating behaviour favoured by dihydropyridine Ca agonists and antagonists." Nature **311**(5986): 538-544.
- Hinshaw, D. B., M. T. Miller, G. M. Omann, T. F. Beals and P. A. Hyslop (1993). "A cellular model of oxidant-mediated neuronal injury." Brain Res **615**: 13-26.
- Hong, T. T., J. W. Smyth, D. Gao, K. Y. Chu, J. M. Vogan, T. S. Fong, B. C. Jensen, H. M. Colecraft and R. M. Shaw (2010). "BIN1 Localizes the L-Type Calcium Channel to Cardiac T-Tubules." PLoS Biol **8**(2): 1-14.
- Hong, T. T., H. Yang, S. Zhang, H. C. Cho, M. Kalashnikova, B. Sun, H. Zhang, A. Bhargava, M. Grabe, J. Olgin, J. Gorelik, E. Marban, L. Y. Jan and R. M. Shaw (2014). "Cardiac BIN1 folds T-tubule membrane, controlling ion flux and limiting arrhythmia." Nat Med **20**(6): 624-632.

- Hori, M. and K. Nishida (2009). "Oxidative stress and left ventricular remodelling after myocardial infarction." Cardiovasc Res **81**: 457-464.
- Howard, J. and A. A. Hyman (2003). "Dynamics and mechanics of the microtubule plus end." Nature **422**: 753-758.
- Hu, W. and Q. Lu (2014). "Impact of oxidative stress on the cytoskeleton of pancreatic epithelial cells." Exp Ther Med **8**: 1428-1442.
- Huang, G. N., W. Zeng, J. Y. Kim, J. P. Yuan, L. Han, S. Muallem and P. F. Worley (2006). "STIM1 carboxyl-terminus activates native SOC, I(crac) and TRPC1 channels." Nat Cell Biol **8**(9): 1003-1010.
- Huffaker, R., S. T. Lamp, J. N. Weiss and B. Kogan (2004). "Intracellular calcium cycling, early afterdepolarizations, and reentry in simulated long QT syndrome." Heart Rhythm **1**(4): 441-448.
- Inagaki, K., S. Fuess, T. A. Storm, G. A. Gibson, C. F. Mictiernan, M. A. Kay and H. Nakai (2006). "Robust Systemic Transduction with AAV9 Vectors in Mice: Efficient Global Cardiac Gene Transfer Superior to that of AAV8." Mol Ther **14**(1): 45-53.
- Iwai, K., M. Hori, A. Kitabatake, H. Kurihara, K. Uchida, M. Inoue and T. Kamada (1990). "Disruption of microtubules as an early sign of irreversible ischemic injury. Immunohistochemical study of in situ canine hearts." Circ Res **67**(3): 694-706.
- Izu, L. T., T. Banyasz, C. W. Balke and Y. Chen-Izu (2007). "Eavesdropping on the social lives of Ca(2+) sparks." Biophys J **93**(10): 3408-3420.

- Jiang, K., G. Toedt, S. Montenegro Gouveia, N. E. Davey, S. Hua, B. van der Vaart, I. Grigoriev, J. Larsen, L. B. Pedersen, K. Bezstarosti, M. Lince-Faria, J. Demmers, M. O. Steinmetz, T. J. Gibson and A. Akhmanova (2012). "A Proteome-wide screen for mammalian SxIP motif-containing microtubule plus-end tracking proteins." Curr Biol **22**(19): 1800-1807.
- Jones, L. R., L. Zhang, K. Sanborn, A. O. Jorgensen and J. Kelley (1995). "Purification, primary structure, and immunological characterization of the 26-kDa calsequestrin binding protein (junctin) from cardiac junctional sarcoplasmic reticulum." J Biol Chem **270**(51): 30787-30796.
- Kakeno, M., K. Matsuzawa, T. Matsui, H. Akita, I. Sugiyama, F. Ishidate, A. Nakano, S. Takashima, H. Goto, M. Inagaki, K. Kaibuchi and T. Watanabe (2014). "Plk1 phosphorylates CLIP-170 and regulates its binding to microtubules for chromosome alignment." Cell Struct Funct **39**(1): 45-59.
- Kalyanaraman, B., V. Darley-Usmar, K. J. A. Davies, P. A. Dennery, H. J. Forman, M. B. Grisham, G. E. Mann, K. Moore, L. J. I. Roberts and H. Ischiropoulos (2012). "Measuring reactive oxygen and nitrogen species with fluorescent probes: challenges and limitations." Free Radic Biol Med **52**(1): 1-6.
- Kawai, M., M. Hussain and C. H. Orchard (1999). "Excitation-contraction coupling in rat ventricular myocytes after formamide-induced detubulation." Am J Physiol **277**(2 Pt 2): H603-609.

- Kerfant, B. G., G. Vassort and A. M. Gomez (2001). "Microtubule disruption by colchicine reversibly enhances calcium signaling in intact rat cardiac myocytes." Circulation research **88**(7): E59-65.
- Kim, K. C., A. H. Caswell, J. A. Talvenheimo and N. R. Brandt (1990). "Isolation of a terminal cisterna protein which may link the dihydropyridine receptor to the junctional foot protein in skeletal muscle." Biochemistry **29**(39): 9281-9289.
- Klabunde, R. E. (2005). Cardiovascular Physiology Concepts. Philadelphia, Lippincott, Williams, & Wilkins.
- Kline-Smith, S. L. and C. E. Walczak (2002). "The microtubule-destabilizing kinesin XKCM1 regulates microtubule dynamic instability in cells." Mol Biol Cell **13**(8): 2718-2731.
- Kolk, M. V., D. Meyberg, T. Deuse, K. R. Tang-Quan, R. C. Robbins, H. Reichenspurner and S. Schrepfer (2009). "LAD-ligation: a murine model of myocardial infarction." J Vis Exp(32).
- Kosco, K. A., C. G. Pearson, P. S. Maddox, P. J. Wang, I. R. Adams, E. D. Salmon, K. Bloom and T. C. Huffaker (2001). "Control of Microtubule Dynamics by Stu2p Is Essential for Spindle Orientation and Metaphase Chromosome Alignment in Yeast." Mol Biol Cell **12**: 2870-2880.
- Kratzer, E., Y. Tian, N. Sarich, T. Wu, A. Meliton, A. Leff and A. A. Birukova (2012). "Oxidative stress contributes to lung injury and barrier dysfunction via microtubule destabilization." Am J Respir Cell Mol Biol **47**(5): 688-697.

- Kukielka, G. L., C. W. Smith, A. M. Manning, K. A. Youker, L. H. Michael and M. L. Entman (199). "Induction of interleukin-6 synthesis in the myocardium. Potential role in postreperfusion inflammatory injury." Circulation **92**: 1866-1875.
- Labbe, J., P. S. Maddox, E. D. Salmon and B. Goldstein (2003). "PAR Proteins Regulate Microtubule Dynamics at the Cell Cortex in *C. elegans*." Curr Biol **13**: 707-714.
- Lacerda, A. E., H. S. Kim, P. Ruth, E. Perez-Reyes, V. Flockerzi, F. Hofmann, L. Birnbaumer and A. M. Brown (1991). "Normalization of current kinetics by interaction between the alpha 1 and beta subunits of the skeletal muscle dihydropyridine-sensitive Ca<sup>2+</sup> channel." Nature **352**(6335): 527-530.
- Le Grand, M., A. Rovini, V. Bourgarel-Rey, S. Honore, S. Bastonero, D. Braguer and M. Carre (2014). "ROS-mediated EB1 phosphorylation through Akt/GSK3beta pathway: implication in cancer cell response to microtubule-targeting agents." Oncotarget **5**(10): 3408-3423.
- Lederer, W. J., E. Niggli and R. W. Hadley (1990). "Sodium-calcium exchange in excitable cells: fuzzy space." Science **248**(4953): 283.
- Lee, A., R. E. Westenbroek, F. Haeseleer, K. Palczewski, T. Scheuer and W. A. Catterall (2002). "Differential modulation of Ca(v)2.1 channels by calmodulin and Ca<sup>2+</sup>-binding protein 1." Nat Neurosci **5**(3): 210-217.
- Lee, C., C. Liu, R. Hsieh and Y. Wei (2005). "Oxidative Stress-Induced Depolymerization of Microtubules and Alteration of Mitochondrial Mass in Human Cells." Ann N Y Acad Sci **1042**: 246-254.

- Liao, P. and T. W. Soong (2010). "CaV1.2 channelopathies: from arrhythmias to autism, bipolar disorder, and immunodeficiency." Pflugers Arch **460**(2): 353-359.
- Ljubojevic, S., S. Walther, M. Asgarzoei, S. Sedej, B. Pieske and J. Kockskamper (2011). "In situ calibration of nucleoplasmic versus cytoplasmic Ca<sup>2+</sup> concentration in adult cardiomyocytes." Biophys J **100**(10): 2356-2366.
- Loewen, M. E., Z. Wang, J. Eldstrom, A. Dehghani Zadeh, A. Khurana, D. F. Steele and D. Fedida (2009). "Shared requirement for dynein function and intact microtubule cytoskeleton for normal surface expression of cardiac potassium channels." Am J Physiol Heart Circ Physiol **296**(1): H71-83.
- López-López, J. R., P. S. Shacklock, C. W. Balke and W. G. Wier (1995). "Local calcium transients triggered by single L-type calcium channel currents in cardiac cells." Science **268**(5213): 1042-1045.
- Louch, W. E., J. Hake, H. K. Mork, K. Hougen, B. Skrbic, D. Ursu, T. Tonnessen, I. Sjaastad and O. M. Sejersted (2013). "Slow Ca<sup>2+</sup> sparks de-synchronize Ca<sup>2+</sup> release in failing cardiomyocytes: Evidence or altered configuration of Ca<sup>2+</sup> release units?" Journal of Molecular and Cellular Cardiology **58**: 41-52.
- Louch, W. E., H. K. Mork, J. Sexton, T. A. Stromme, P. Laake, I. Sjaastad and O. M. Sejersted (2006). "T-tubule disorganization and reduced synchrony of Ca<sup>2+</sup> release in murine cardiomyocytes following myocardial infarction." J Physiol **574**(2): 519-533.

- Lukyanenko, V. and S. Gyorke (1999). "Ca<sup>2+</sup> sparks and Ca<sup>2+</sup> waves in saponin-permeabilized rat ventricular myocytes." J Physiol **521 Pt 3**: 575-585.
- Lyon, A. R., K. T. MacLeod, Y. Zhang, E. Garcia, G. K. Kanda, M. J. Lab, Y. E. Korchev, S. E. Harding and J. Gorelik (2009). "Loss of T-tubules and other changes to surface topography in ventricular myocytes from failing human and rat heart." Proc Natl Acad Sci U S A **106**(16): 6854-6859.
- Mackenzie, L., M. D. Bootman, M. J. Berridge and P. Lipp (2001). "Predetermined recruitment of calcium release sites underlies excitation-contraction coupling in rat atrial myocytes." J Physiol **530**: 417-429.
- Mackenzie, L., H. L. Roderick, M. J. Berridge, S. J. Conway and M. D. Bootman (2004). "The spatial pattern of atrial cardiomyocyte calcium signalling modulates contraction." J Cell Sci **117**: 6327-6337.
- Maier, L. S., T. Zhang, L. Chen, J. DeSantiago, J. H. Brown and D. M. Bers (2003). "Transgenic CaMKII $\delta$ C overexpression uniquely alters cardiac myocyte Ca<sup>2+</sup> handling: reduced SR Ca<sup>2+</sup> load and activated SR Ca<sup>2+</sup> release." Circ Res **92**(8): 904-911.
- Maravall, M., Z. F. Mainen, B. L. Sabatini and K. Svoboda (2000). "Estimating intracellular calcium concentrations and buffering without wavelength ratioing." Biophys J **78**(5): 2655-2667.
- Mercado, J., R. Baylie, M. F. Navedo, C. Yuan, J. D. Scott, M. T. Nelson, J. E. Brayden and L. F. Santana (2014). "Local control of TRPV4 channels by AKAP150-targeted PKC in arterial smooth muscle." J Gen Physiol **143**(5): 559-575.

- Meunier, B., M. Quaranta, L. Daviet, A. Hatzoglou and C. Leprince (2009). "The membrane-tubulating potential of amphiphysin 2/BIN1 is dependent on the microtubule-binding cytoplasmic linker protein 170 (CLIP-170)." Eur J Cell Biol **88**(2): 91-102.
- Mitchison, T. and M. Kirschner (1984). "Dynamic instability of microtubule growth." Nature **312**(5991): 237-242.
- Montenegro Gouveia, S., K. Leslie, L. C. Lapitein, R. M. Buey, I. Grigoriev, M. Wagenbach, I. Smal, E. Meijering, C. C. Hoogenraad, L. Wordeman, M. O. Steinmetz and A. Akhmanova (2010). "In vitro reconstitution of the functional interplay between MCAK and EB3 at microtubule plus ends." Curr Biol **20**(19): 1717-1722.
- Muller, A. J., J. F. Baker, J. B. DuHadaway, K. Ge, G. Farmer, P. S. Donover, R. Meade, C. Reid, R. Grzanna, A. H. Roach, N. Shah, A. P. Soler and G. C. Prendergrast (2003). "Targeted disruption of the murine Bin1/Amphiphysin II gene does not disable endocytosis but results in embryonic cardiomyopathy with aberrant myofibril formation." Mol Cell Biol **23**(12): 4295-4306.
- Muller, M. J. I., S. Klumpp and R. Lipowsky (2008). "Motility states of a molecular motors engaged in a stochastic tug-of-war." J Stat Phys **133**: 1059-1081.
- Murphy, C. T., R. S. Rock and J. A. Spudich (2002). "A myosin II mutation uncouples ATPase activity from motility and shortens step size." Nat Cell Biol **3**: 311-315.

- Nabauer, M., D. J. Beuckelmann and E. Erdmann (1993). "Characteristics of transient outward current in human ventricular myocytes from patients with terminal heart failure." Circ Res **73**(2): 386-394.
- Navedo, M. F., G. C. Amberg, V. S. Votaw and L. F. Santana (2005). "Constitutively active L-type  $\text{Ca}^{2+}$  channels." Proc Natl Acad Sci U S A **102**(31): 11112-11117.
- Navedo, M. F., E. P. Cheng, C. Yuan, S. Votaw, J. D. Molkenin, J. D. Scott and L. F. Santana (2010). "Increased coupled gating of L-type  $\text{Ca}^{2+}$  channels during hypertension and Timothy syndrome." Circ Res **106**(4): 748-756.
- Nerbonne, J. M. and R. S. Kass (2005). "Molecular physiology of cardiac repolarization." Physiol Rev **85**(4): 1205-1253.
- Newton, C. N., M. Wagenbach, Y. Ovechkina, L. Wordeman and L. Wilson (2004). "MCAK, a Kin I kinesin, increases the catastrophe frequency of steady-state HeLa cell microtubules in an ATP-dependent manner in vitro." FEBS Lett **573**(1-3): 80-84.
- Niggli, E. and W. J. Lederer (1990). "Voltage-independent calcium release in heart muscle." Science **250**(4980): 565-568.
- O'Connell, T. D., Y. G. Ni, K.-M. Lin, H. Han and Z. Yan (2003). "Isolation and culture of adult mouse cardiac myocytes for signaling studies." AfCS Res Rep **1**(5): 1-9.
- Oddoux, S., K. J. Zaal, V. Tate, A. Kenea, S. A. Nandkeolyar, E. Reid, W. Liu and E. Ralston (2013). "Microtubules that form the stationary lattice of

- muscle fibers are dynamic and nucleated at Golgi elements." J Cell Biol **203**(2): 205-213.
- Oliveria, S. F., M. L. Dell'Acqua and W. A. Sather (2007). "AKAP79/150 anchoring of calcineurin controls neuronal L-type Ca<sup>2+</sup> channel activity and nuclear signaling." Neuron **55**(2): 261-275.
- Parker, A. L., M. Kavallaris and J. A. McCarroll (2014). "Microtubules and their role in cellular stress in cancer." Front Onco **4**: 1-19.
- Parker, I. and W. G. Wier (1997). "Variability in frequency and characteristics of Ca<sup>2+</sup> sparks at different release sites in rat ventricular myocytes." J Physiol **505**(Pt 2): 337-344.
- Pasek, M., J. Simurda and G. Christe (2006). "The functional role of cardiac T-tubules explored in a model of rat ventricular myocytes." Philos Trans A Math Phys Eng Sci **364**: 1187-1206.
- Patterson, G. H. and J. Lippincott-Swartz (2002). "A Photoactivatable GFP for Selective Photolabeling of Proteins and Cells." Science **297**: 1873-1877.
- Peris, L., M. Wagenbach, L. Lafanechere, J. Brocard, A. T. Moore, F. Kozielski, D. Job, L. Wordeman and A. Andrieux (2009). "Motor-dependent microtubule disassembly driven by tubulin tyrosination." J Cell Biol **185**(7): 1159-1166.
- Picht, E., A. V. Zima, L. A. Blatter and D. M. Bers (2007). "SparkMaster: automated calcium spark analysis with ImageJ." Am J Physiol Cell Physiol **293**(3): C1073-1081.

- Pierce, G. F., D. Brown and T. A. Mustoe (1991). "Quantitative analysis of inflammatory cell influx, procollagen type I synthesis, and collagen cross-linking in incisional wounds: influence of PDGF-BB and TGF-beta 1 therapy." J Lab Clin Med **117**: 373-382.
- Pierce, G. F., T. A. Mustoe, J. Lingelbach, V. R. Masakowski, G. L. Griffin and S. R. M. (1989). "Platelet-derived growth factor and transforming growth factor- beta enhance tissue repair activities by unique mechanisms." J Cell Biol **109**: 429-440.
- Reichenbach, H., E. M. Meister and H. Theile (1992). "The heart-hand syndrome. A new variant of disorders of heart conduction and syndactylia including osseous changes in hands and feet." Kinderarztl Prax **60**(2): 54-56.
- Robu, V. G., E. S. Pfeiffer, S. L. Robia, R. C. Balijepalli, Y. Pi, T. J. Kamp and J. W. Walker (2003). "Localization of functional endothelin receptor signaling complexes in cardiac transverse tubules." J Biol Chem **278**: 48154-48161.
- Rossi, D., V. Barone, E. Giacomello, V. Cusimano and V. Sorrentino (2008). "The Sarcoplasmic Reticulum: An Organized Patchwork of Specialized Domains." Traffic **9**: 1044-1049.
- Rossow, C. F., K. W. Dilly and L. F. Santana (2006). "Differential Calcineurin/NFATc3 Activity Contributes to the I<sub>to</sub> Transmural Gradient in the Mouse Heart." Circ Res **98**: 1306-1313.
- Rossow, C. F., K. W. Dilly, C. Yuan, M. Nieves-Cintron, J. L. Cabarrus and L. F. Santana (2009). "NFATc3-dependent loss of I<sub>to</sub> gradient across the left

- ventricular wall during chronic beta adrenergic stimulation." J Mol Cell Cardiol **46**(2): 249-256.
- Rubart, M. and D. P. Zipes (2005). "Mechanisms of sudden cardiac death." J Clin Invest **115**(9): 2305-2315.
- Santana, L. F., H. Cheng, A. M. Gomez, M. B. Cannell and W. J. Lederer (1996). "Relation between the sarcolemmal  $Ca^{2+}$  current and  $Ca^{2+}$  sparks and local control theories for cardiac excitation-contraction coupling." Circ Res **78**(1): 166-171.
- Sato, D., L. H. Xie, A. A. Sovari, D. X. Tran, N. Morita, F. Xie, H. Karagueuzian, A. Garfinkel, J. N. Weiss and Z. Qu (2009). "Synchronization of chaotic early afterdepolarizations in the genesis of cardiac arrhythmias." Proc Natl Acad Sci U S A **106**(9): 2983-2988.
- Saucerman, J. J. and D. M. Bers (2008). "Calmodulin mediates differential sensitivity of CaMKII and calcineurin to local  $Ca^{2+}$  in cardiac myocytes." Biophys J **95**(10): 4597-4612.
- Schliwa, M. and G. Woehlke (2003). "Molecular motors." Nature **422**: 759-764.
- Shah, R. V. and M. A. Fifer (2007). Chapter: 9 Heart Failure. Philadelphia, Lippincott Williams & Wilkins.
- Shaw, R. M., A. J. Fay, M. A. Puthenveedu, M. von Zastrow, Y. N. Jan and L. Y. Jan (2007). "Microtubule plus-end-tracking proteins target gap junctions directly from the cell interior to adherens junctions." Cell **128**(3): 547-560.
- Shepherd, N. and H. B. McDonough (1998). "Ionic diffusion in transverse tubules of cardiac ventricular myocytes." Am J Physiol **275**(H852-H860).

- Shioya, T. (2007). "A simple technique for isolating healthy heart cells from mouse models." J Physiol Sci **57**(6): 327-335.
- Sipido, K. R., P. G. Volders, M. A. Vos and F. Verdonck (2002). "Altered Na/Ca exchange activity in cardiac hypertrophy and heart failure: a new target for therapy?" Cardiovasc Res **53**(4): 782-805.
- Sironi, L., J. Solon, C. Conrad, T. Mayer, D. Brunner and J. Ellenberg (2011). "Automatic Quantification of Microtubule Dynamics Enables RNAi-screening of New Mitotic Spindle Regulators." Cytoskeleton **68**: 266-278.
- Slep, K. C. and R. D. Vale (2007). "Structural basis of microtubule plus end tracking by XMAP215, CLIP-170, and EB1." Mol Cell **27**(6): 976-991.
- Smyrniak, I., W. Mair, D. Harzheim, S. A. Walker, H. L. Roderick and M. D. Bootman (2010). "Comparison of the T-tubule system in adult rat ventricular and atrial myocytes and its role in excitation-contraction coupling and inotropic stimulation." Cell Calcium **47**: 210-223.
- Smyth, J. W., T. T. Hong, D. Gao, J. M. Vogan, B. C. Jensen, T. S. Fong, P. C. Simpson, D. Y. Stainier, N. C. Chi and R. M. Shaw (2010). "Limited forward trafficking of connexin 43 reduces cell-cell coupling in stressed human and mouse myocardium." J Clin Invest **120**(1): 266-279.
- Soeller, C. and M. B. Cannell (1997). "Numerical simulation of local calcium movements during L-type calcium channel gating in the cardiac diad." Biophys J **73**(1): 97-111.

- Soldatov, N. M. and M. B. Cannell (1997). "Numerical simulation of local calcium movements during L-type calcium channel gating in the cardiac diad." Biophys J **73**(1): 97-111.
- Soldatov, N. M., M. Oz, K. A. O'Brien, D. R. Abernethy and M. Morad (1998). "Molecular determinants of L-type Ca<sup>2+</sup> channel inactivation. Segment exchange analysis of the carboxyl-terminal cytoplasmic motif encoded by exons 40-42 of the human alpha1C subunit gene." J Biol Chem **273**(2): 957-963.
- Soldatov, N. M., R. D. Zuhlke, A. Bouron and H. Reuter (1997). "Molecular structures involved in L-type calcium channel inactivation." J Biol Chem **273**(2): 957-963.
- Song, L., E. A. Sobie, S. L. McCulle, W. J. Lederer, C. W. Balke and H. Cheng (2006). "Orphaned ryanodine receptors in the failing heart." Proc Natl Acad Sci U S A **103**(11): 4305-4310.
- Song, Q., J. J. Saucerman, J. Bossuyt and D. M. Bers (2008). "Differential integration of Ca<sup>2+</sup>-calmodulin signal in intact ventricular myocytes at low and high affinity Ca<sup>2+</sup>-calmodulin targets." J Biol Chem **283**(46): 31531-31540.
- Splawski, I., K. W. Timothy, N. Decher, P. Kumar, F. B. Sachse, A. H. Beggs, M. C. Sanguinetti and M. T. Keating (2005). "Severe arrhythmia disorder caused by cardiac L-type calcium channel mutations." Proc Natl Acad Sci U S A **102**(23): 8089-8096; discussion 8086-8088.

- Splawski, I., K. W. Timothy, L. M. Sharpe, N. Decher, P. Kumar, R. Bloise, C. Napolitano, P. J. Schwartz, R. M. Joseph, K. Condouris, H. Tager-Flusberg, S. G. Priori, M. C. Sanguinetti and M. T. Keating (2004). "Ca(V)1.2 calcium channel dysfunction causes a multisystem disorder including arrhythmia and autism." Cell **119**(1): 19-31.
- Stotz, S. C. and G. W. Zamponi (2001). "Identification of Inactivation Determinants in the Domain IIS6 Region of High Voltage-activated Calcium Channels." J Biol Chem **276**(35): 33001-33010.
- Stout, J. R., A. L. Yount, J. A. Powers, C. LeBlanc, S. C. Ems-McClung and C. E. Walczak (2011). "Kif18B interacts with EB1 and controls astral microtubule length during mitosis." Mol Biol Cell **22**(17): 3070-3080.
- Swift, F., T. A. Stromme, B. Amundsen, O. M. Sejersted and I. Sjaastad (2006). "Slow diffusion of K<sup>+</sup> in the T tubules of rat cardiomyocytes." J Appl Physiol **101**(1170-1176).
- Swinne, C. J., E. P. Shapiro, S. D. Lima and J. L. Fleg (1992). "Age-associated changes in left ventricular diastolic performance during isometric exercise in normal subjects." Am J Cardiol **69**(8): 823-826.
- Tadross, M. R. and D. T. Yue (2010). "Systematic mapping of the state dependence of voltage- and Ca<sup>2+</sup>-dependent inactivation using simple open-channel measurements." J Gen Physiol **135**(3): 217-227.
- Tagawa, H., M. Koide, H. Sato, M. R. Zile, B. A. Carabello and G. t. Cooper (1998). "Cytoskeletal role in the transition from compensated to

- decompensated hypertrophy during adult canine left ventricular pressure overloading." Circ Res **82**(7): 751-761.
- Tai, C. Y., D. L. Dujardin, N. E. Faulkner and R. B. Vallee (2002). "Role of dynein, dynactin, and CLIP-170 interactions in LIS1 kinetochore function." J Cell Biol **156**(6): 959-968.
- Tanaka, K., E. Kitamura, Y. Kitamura and T. U. Tanaka (2007). "Molecular mechanisms of microtubule-dependent kinetochore transport toward spindle poles." J Cell Biol **178**(2): 269-281.
- Temple, J., P. Frias, J. Rottman, T. Yang, Y. Wu, E. E. Verheijck, W. Zhang, C. Siprachanh, H. Kanki, J. B. Atkinson, P. King, M. E. Anderson, S. Kupersmidt and D. M. Roden (2005). "Atrial fibrillation in KCNE1-null mice." Circ Res **97**(1): 62-69.
- Thiel, W. H., B. Chen, T. J. Hund, O. M. Koval, A. Purohit, L. S. Song, P. J. Mohler and M. E. Anderson (2008). "Proarrhythmic defects in Timothy syndrome require calmodulin kinase II." Circulation **118**(22): 2225-2234.
- Tirnauer, J. S., E. O'Toole, L. Berrueta, B. E. Bierer and D. Pellman (1999). "Yeast Bim1p Promotes the G1-specific Dynamics of Microtubules." J Cell Biol **145**(5): 993-1007.
- Treinys, R. and J. Jurevicius (2008). "L-type Ca<sup>2+</sup> channels in the heart: structure and regulation." Medicina **44**(7): 491-499.
- Trudeau, M. C. (2012). "Unlocking the mechanisms of HCN channel gating with locked-open and locked-closed channels." J Gen Physiol **140**(5): 457-461.

- Tsien, R. W., B. P. Bean, P. Hess, J. B. Lansman, B. Nilius and M. C. Nowycky (1986). "Mechanisms of calcium channel modulation by beta-adrenergic agents and dihydropyridine calcium agonists." J Mol Cell Cardiol **18**(7): 691-710.
- Tsutsui, H., K. Ishihara and G. t. Cooper (1993). "Cytoskeletal role in the contractile dysfunction of hypertrophied myocardium." Science **260**(5108): 682-687.
- Valen, G., A. Sonden, J. Vaage, E. Malm and B. T. Kjellstrom (1999). "Hydrogen peroxide induces endothelial cell atypia and cytoskeleton depolymerization." Free Radic Biol Med **26**(11/12): 1480-1488.
- Vaughan, J. C., S. Jia and X. Zhuang (2012). "Ultrabright photoactivatable fluorophores created by reductive caging." Nat Methods **9**: 1181-1184.
- Vega, A. L. and L. F. Santana (2011). "Dynamic Changes in Sarcoplasmic Reticulum Structure in Ventricular Myocytes." Journal of Biomedicine and Biotechnology **2011**: 1-14.
- von Knethen, A., D. Callsen and B. Brune (1999). "Superoxide attenuates macrophage apoptosis by NF-kappa B and AP-1 activation that promotes cyclooxygenase-2 expression." J Immunol **163**(2858-66).
- Wagner, E., M. A. Lauterbach, T. Kohl, V. Westphal, G. S. B. Williams, J. H. Steinbrecher, J. Streich, B. Korff, H. M. Tuan, B. Hagen, S. Luther, G. Hasenfuss, U. Parlitz, M. S. Jafri, S. W. Hell, W. J. Lederer and S. E. Lehnart (2012). "Stimulated Emission Depletion Live-Cell Super-Resolution Imaging Shows Proliferative Remodeling of T-Tubule

- Membrane Structures After Myocardial Infarction." Circ Res **111**(4): 402-414.
- Wagner, M., D. Goltz, C. Stucke, A. P. Schwoerer, H. Ehmke and T. Volk (2007). "Modulation of the transient outward K<sup>+</sup> current by inhibition of endothelin-A receptors in normal and hypertrophied rat hearts." Pflugers Arch **454**(4): 595-604.
- Wei, S., A. Guo, B. Chen, W. J. Kutschke, Y. P. Xie, K. Zimmerman, R. M. Weiss, M. E. Anderson, H. Cheng and L. S. Song (2010). "T-Tubule Remodeling During Transition From Hypertrophy to Heart Failure." Circ Res.
- Weiss, J. N., M. Nivala, A. Garfinkel and Z. Qu (2011). "Alternans and Arrhythmias." Circ Res **108**(1): 98-112.
- Woodruff, M. L., A. P. Sampath, H. R. Matthews, N. V. Krasnoperova, J. Lem and G. L. Fain (2002). "Measurement of cytoplasmic calcium concentration in the rods of wild-type and transducin knock-out mice." J Physiol **542**(Pt 3): 843-854.
- Wride, M. A., P. H. Lapchak and E. J. Sanders (1994). "Distribution of TNF-alpha like proteins correlates with some regions of programmed cell death in the chick embryo." Int J Dev Biol **38**: 673-682.
- Xie, J., X. Zhou, X. Hu and H. Jiang (2013). "H<sub>2</sub>O<sub>2</sub> Evokes Injury of Cardiomyocytes Through Upregulating HMGB1." Hellenic J Cardiol **54**: 101-106.

- Yarotsky, V., G. Gao, B. Z. Peterson and K. S. Elmslie (2009). "The Timothy syndrome mutation of cardiac CaV1.2 (L-type) channels: multiple altered gating mechanisms and pharmacological restoration of inactivation." J Physiol **587**(Pt 3): 551-565.
- Yazawa, M., B. Hsueh, X. Jia, A. M. Pasca, J. A. Bernstein, J. Hallmayer and R. E. Dolmetsch (2011). "Using induced pluripotent stem cells to investigate cardiac phenotypes in Timothy syndrome." Nature **471**(7337): 230-234.
- Zachariah, J. P., R. S. Vasan and R. B. D'Agostino (2011). Chapter 2. The Burden of Increasing Worldwide Cardiovascular Disease. Hurst's The Heart.
- Zadeh, A. D., Y. Cheng, H. Xu, N. Wong, Z. Wang, C. Goonasekara, D. F. Steele and D. Fedida (2009). "Kif5b is an essential forward trafficking motor for the Kv1.5 cardiac potassium channel." J Physiol **587**(Pt 19): 4565-4574.
- Zhang, C., B. Chen, A. Guo, Y. Zhu, J. D. Miller, S. Gao, C. Yuan, W. Kutschke, K. Zimmerman, R. M. Weiss, X. H. Wehrens, J. Hong, F. L. Johnson, L. F. Santana, M. E. Anderson and L. Song (2014). "Microtubule-Mediated Defects in Junctophilin-2 Trafficking Contribute to Myocyte T-Tubule Remodeling and Ca<sup>2+</sup> Handling Dysfunction in Heart Failure." Circ Res.
- Zhang, D., K. D. Grode, S. Stewman, D. Diaz, E. Liebling, U. Rath, T. Riera, J. Currie, D. W. Buster, A. B. Asenjo, H. J. Sosa, J. Ross, A. Ma, S. L. Rogers and D. J. Sharp (2011). "Drosophila Katanin is a microtubule depolymerase that regulates cortical-microtubule plus-end interactions and cell migration." Nat Cell Biol **13**(4): 361-370.

- Zhang, H., R. Li, M. Xu, S. Xu, Y. Lai, H. Wu, X. Xie, W. Gao, H. Ye, Y. Zhang, X. Meng and S. Wang (2013). "Ultrastructural uncoupling between T-tubules and sarcoplasmic reticulum in human heart failure." Cardiovasc Res **98**(2): 269-276.
- Zhang, J. F., P. T. Ellinor, R. W. Aldrich and R. W. Tsien (1994). "Molecular determinants of voltage-dependent inactivation in calcium channels." Nature **372**(6501): 97-100.
- Zhang, L., J. Kelley, G. Schmeisser, Y. M. Kobayashi and L. R. Jones (1997). "Complex formation between junctin, triadin, calsequestrin, and the ryanodine receptor. Proteins of the cardiac junctional sarcoplasmic reticulum membrane." J Biol Chem **272**(23389-23397).
- Zhang, S. and R. M. Shaw (2013). "Multilayered regulation of cardiac ion channels." Biochim Biophys Acta **1833**: 876-885.
- Zielonk, J., J. Vasquez-Vivar and B. Kalyanaraman (2008). "Detection of 2-hydroxyethidium in cellular systems: a unique marker product of superoxide and hydroethidine." Nat Protoc **3**(1): 8-21.
- Zimetbaum, P. J. and M. E. Josephson (2008). Pathophysiology of the long QT syndrom. UpToDate. Waltham, MA.

## Curriculum Vitae

### Benjamin Mark Loren Drum

bdrum@uw.edu  
4911 Evanston Ave N  
Seattle WA, 98103  
(971) 998-7386

#### EDUCATION

- University of Washington**, Seattle, WA June 2018
- Expected Degrees: M.D. and Ph. D. (Physiology and Biophysics)
  - Graduate Student in the lab of Dr. Santana
  - Rotations in the Rieke, Perkel, and Santana labs
  - Preceptorships in family medicine, internal medicine, psychiatry, sports medicine, and pediatric cardiology
  - Step One Score: 247
- University of Washington**, Seattle, WA June 2010
- B.S. Neurobiology & B.A. English (Creative Writing) with minor in Chemistry
  - University Honors Program, GPA: 3.93, graduated magna cum laude
  - Completed honors thesis in Neurobiology in lab of Dr. Zagotta
  - Designed & taught GEN ST 197: Exploring Paths in Health Careers, a freshman seminar
  - MCAT Score: 39Q (Physical Sciences 13, Verbal Reasoning 11, Biological Sciences 15)

#### FELLOWSHIPS

2015-2018 NIH F30 HL126249-01  
2014 AHA Predoctoral Fellowship 14PRE20460098  
2012-2014 ARCS Foundation Fellow, UW  
2012 Turner Society Endowed Fellow, UW  
2008 NSI Undergraduate Fellow, OHSU

#### PRESENTATIONS

2016 Biophysical Society Annual Meeting  
2014 Patton Symposium  
2011 Rotation talk, Perkel lab  
2010 Rotation talk, Rieke lab  
2010 Undergraduate Research Symposium (UW)  
2010 Spring Celebration of Leadership (UW)  
2009 Undergraduate Research Symposium (UW)  
2008 Neurological Sciences Institute Research Colloquium (OHSU)  
2008 Undergraduate Research Symposium (UW)  
2008 Honors Research Colloquium (UW)

#### AWARDS

2016 Biophysical Society Travel Award Recipient  
2014 Neurobiology Training Grant (received and declined)  
2010 Mary Gates Leadership Scholar  
2009 Mary Gates Research Scholar  
2008 Mary Gates Research Scholar

CONFERENCE ABSTRACTS

**BM Drum**, C Yuan, L Li, Q Liu, L Wordeman, & LF Santana "Oxidative Stress in Myocardial Infarction Disrupts Microtubule Trafficking, Reducing Transient Outward Current Density" *Biophysical Journal* 2016 Feb; 110(3):129a.

AE Carlson, **BM Drum**, & WN Zagotta "Deletion of the Amino-Terminus Uncovers an Inactivated State in Eag1 channels" *Biophysical Journal* 2011 Feb; 100(3):30a

C Gonzalez, HP Koch, **BM Drum**, & HP Larsson "Strong Negative Cooperativity Between Subunits in Voltage-Gated Proton Channels" *Biophysical Journal*, 2010 Jan; 98(3):314a.

PUBLICATIONS

**BM Drum**, C Yuan, L Li, Q Liu, L Wordeman, & LF Santana "Oxidative stress decreases microtubule growth and stability in ventricular myocytes" *J Mol Cell Cardiol* 2016 Apr; 93: 32-43.

**BM Drum** & LF Santana "The long and winding road home: How junction and triadin find their way to the junction SR" *J Mol Cell Cardiol*, 2015 Apr; 81:15-17.

**BM Drum**, RE Dixon, C Yuan, EP Cheng, & LF Santana "Cellular mechanisms of ventricular arrhythmias in a mouse model of Timothy syndrome (long QT syndrome 8)" *J Mol Cell Cardiol.* 2014 Jan; 66:63-71.

C Gonzalez, HP Koch, **BM Drum**, & HP Larsson "Strong negative cooperativity between subunits in voltage-gated proton channels" *Nat Struct Mol Biol.* 2010 Jan; 17(1):51-6.